

## LA-UR-18-31854

Approved for public release; distribution is unlimited.

Title: PHASE-SPACE MANIPULATIONS OF ELECTRON BEAMS FOR X-RAY FREE-ELECTRON LASERS AND INVERSE COMPTON SCATTERING SOURCES.

Author(s): Malyzhenkov, Alexander

Intended for: PhD Dissertation

Issued: 2018-12-20

---

**Disclaimer:**

Los Alamos National Laboratory, an affirmative action/equal opportunity employer, is operated by Triad National Security, LLC for the National Nuclear Security Administration of U.S. Department of Energy under contract 89233218CNA000001. By approving this article, the publisher recognizes that the U.S. Government retains nonexclusive, royalty-free license to publish or reproduce the published form of this contribution, or to allow others to do so, for U.S. Government purposes. Los Alamos National Laboratory requests that the publisher identify this article as work performed under the auspices of the U.S. Department of Energy. Los Alamos National Laboratory strongly supports academic freedom and a researcher's right to publish; as an institution, however, the Laboratory does not endorse the viewpoint of a publication or guarantee its technical correctness.

## ABSTRACT

### PHASE-SPACE MANIPULATIONS OF ELECTRON BEAMS FOR X-RAY FREE-ELECTRON LASERS AND INVERSE COMPTON SCATTERING SOURCES.

A. V. Malyzhenkov, PhD  
Department of Physics  
Northern Illinois University, 2018  
Philippe Piot, Director

This dissertation describes advanced techniques of phase space manipulations of the electron beam for improving performance and efficiency of high brightness X-ray light sources based on the free-electron Laser (FEL) and inverse-Compton scattering (ICS) processes. In particular, it first discusses a novel bunch-compression scheme based on a double transverse-to-longitudinal phase-space exchanger – dubbed emittance exchanger (EEX) – separated by a demagnifying transverse-optics system. While the outline of the scheme is quite sophisticated, the basic physics behind it is quite straight-forward. The benefits and disadvantages of these scheme are compared to the conventional approach of compressing a bunch using a magnetic bunch-compression chicane.

The second scheme discussed in this dissertation is a novel beamline for imposing and removing the energy slew along the bunch also known as chirping and dechirping the beam in the accelerator community. This scheme consists of transverse deflecting cavities separated by drifts and relies on imposing and removing the transverse-longitudinal correlations on the electron beam. The benefits of this alternative method are compared with standard schemes of chirping and dechirping the beam via an off-crest acceleration. Finally, a novel

6-dimensional theory of the ICS source concludes this dissertation. It derives the photon distribution in 6D phase space describing radiation produced in the process of scattering a laser pulse off a relativistic electron beam as a function of electron distribution in the phase space using the Wigner function formalism. This result opens up the possibility for the optimization of the brightness of an ICS source via imposing transverse-longitudinal correlations on the beam.

NORTHERN ILLINOIS UNIVERSITY  
DE KALB, ILLINOIS

DECEMBER 2018

**PHASE-SPACE MANIPULATIONS OF ELECTRON BEAMS FOR X-RAY  
FREE-ELECTRON LASERS AND INVERSE COMPTON SCATTERING  
SOURCES.**

BY

A. V. MALYZHENKOV  
© 2018 A. V. Malyzhenkov

A DISSERTATION SUBMITTED TO THE GRADUATE SCHOOL  
IN PARTIAL FULFILLMENT OF THE REQUIREMENTS  
FOR THE DEGREE  
DOCTOR OF PHILOSOPHY

DEPARTMENT OF PHYSICS

Dissertation Director:  
Philippe Piot

## ACKNOWLEDGEMENTS

I would like to thank my scientific adviser at Northern Illinois University, Prof. Philippe Piot<sup>1</sup>, for valuable scientific discussions, patience, flexibility and tremendous support of my scientific career. I would also like to thank my mentors at Los Alamos National Laboratory, Dr. Bruce Carlsten, Dr. Nikolai Yampolsky, and Dr. Alonso Castro, for their bright ideas, leadership, encouragement and for providing the financial and scientific opportunity to work on the cutting edge research projects. In addition, I would like to acknowledge my colleagues and friends: Dr. Petr Anisimov, Dr. Alexander Scheinker, Dr. Evgenya Simakov, Dr. Quinn Marksteiner and Dr. Joshua Bartlett at LANL, Dr. Sergey Arsenyev, Dr. Dmitry Shchegolkov and Dr. Vyacheslav Lebedev formerly at LANL, Dr. Timofey Zolkin at Fermi National Accelerator Laboratory, Prof. Luis Elias at University of Hawaii at Manoa (retired), for important scientific discussions, moral support and help. Moreover, I would like to thank the United States Particle Accelerator Program (USPAS) leaded by Prof. William Barletta (MIT) and him personally for the unique opportunity of continuing education in the field of particle accelerators and light sources leaded by the true genii of the field. Next, I want to thank my family and friends in Russian Federation and all across the globe for their support and encouragement. Finally, I would like to thank my good friend, Stephanie Gershon, for the infinite support in all aspects of life.

I would like to thank the United States Department of Energy and, specifically, the Laboratory Directed Research and Development (LDRD) foundation at Los Alamos National Laboratory (LANL) for the financial support of the major part of the research.

---

<sup>1</sup>Also at Fermi National Accelerator Laboratory.

## **DEDICATION**

To Humanity and to the Universe, and, perhaps, to my lovely dogs and horses...

# TABLE OF CONTENTS

	Page
LIST OF TABLES . . . . .	vii
LIST OF FIGURES. . . . .	ix
Chapter	
1 INTRODUCTION . . . . .	1
1.1 X-radiation and X-ray light sources overview . . . . .	1
1.2 Phase space evolution of the electron beam: the matrix formalism, important quantities and particle tracking codes. . . . .	8
1.3 Working principles of a Free Electron Laser and requirements on the driving electron beam . . . . .	30
1.4 Inverse Compton scattering source working principles and requirements on driving electron beam . . . . .	35
1.5 Organization structure of the dissertation . . . . .	37
2 DOUBLE EMITTANCE EXCHANGER AS A BUNCH COMPRESSOR . . . . .	39
2.1 Working principle of a chicane-based bunch compressor . . . . .	40
2.2 Eigen emittance formalism. . . . .	53
2.3 Double EEX bunch compressor: design . . . . .	57
2.4 Double EEX bunch compressor: simulation studies. . . . .	69
2.4.1 Linear effects . . . . .	69
2.4.2 Real dynamics: nonlinear and CSR effects . . . . .	70
2.5 Extremum seeking. . . . .	75

Chapter	Page
2.6 Minimizing emittance growth . . . . .	79
2.6.1 Twiss parameters optimization . . . . .	79
2.6.2 Optimization of beamline elements: unsymmetrical DEEX . . . . .	81
2.6.3 Dependence of the phase space degradation from the input beam parameters . . . . .	84
2.6.4 CSR effects compensation in the low charge regime . . . . .	88
2.7 2EEX BC optimum designs for another FELs . . . . .	98
2.8 Alternative emittance exchanger (AEEX) design with two bending magnets .	101
2.9 Summary . . . . .	105
3 CHIRPER AND DECHIRPER DESIGN BASED ON TRANSVERSE DEFLECT- ING CAVITIES . . . . .	107
3.1 Standard Chirper configurations . . . . .	108
3.2 Chirper design using transverse deflecting cavities . . . . .	111
3.3 Design optimization for the MaRIE linac . . . . .	116
3.4 Transverse deflecting cavity models in ELEGANT . . . . .	118
3.5 Nonlinear effects and its optimization for 250 MeV Chirper . . . . .	122
3.5.1 Optimization of the Twiss parameters . . . . .	125
3.5.2 Suppressing linear correlations . . . . .	128
3.5.3 Longitudinal space charge effects . . . . .	133
3.5.4 Nonlinear optics for correction of the longitudinal emittance . . . . .	136
3.6 Chirper at 1 GeV beam energy . . . . .	142
3.7 Dechirper design using transverse deflecting cavities . . . . .	151
3.7.1 Linear design . . . . .	151
3.7.2 Dechirper design for the MaRIE Injector test stand . . . . .	152
3.7.3 Dechirper design for the MaRIE linac at 1 GeV . . . . .	159

Chapter	Page
3.7.4 Summary . . . . .	165
4 6D PHOTON PHASE SPACE OF AN ICS SOURCE USING THE WIGNER FUNCTION APPROACH . . . . .	176
4.1 The Wigner function formalism and brightness . . . . .	177
4.2 Radiation emitted by a moving electron . . . . .	179
4.3 The single-electron Wigner function: simple approximations . . . . .	181
4.3.1 The continuous plane wave approximation . . . . .	181
4.3.2 The time-limited plane wave approximation . . . . .	182
4.4 The single-electron Wigner function: arbitrary laser pulse . . . . .	186
4.4.1 Total emitted radiation as a superposition of single modes . . . . .	186
4.4.2 The single-electron Wigner function . . . . .	188
4.5 The Gaussian approximation of the laser pulse . . . . .	193
4.6 The Wigner function of radiation emitted by the electron bunch . . . . .	204
4.6.1 Representing single-electron Wigner function in 6D form . . . . .	206
4.6.2 Convolution of the single-electron Wigner function with an arbitrary electron distribution in 6D phase space . . . . .	213
4.7 Peak Brightness for the on-axis observer . . . . .	216
4.8 Summary . . . . .	217
5 CONCLUSION . . . . .	219
5.1 Importance of this work for electron-beam-driven light sources . . . . .	219
5.2 Discussion . . . . .	222
REFERENCES . . . . .	224

## LIST OF TABLES

Table		Page
2.1	Parameters of the components of DEEX BC for the initial design and two optimized designs optimized for MaRIE beam parameters I and II listed in Table 2.2. . . . .	69
2.2	Desirable (I) and acceptable (II) beam parameters for MaRIE XFEL at the entrance of the second BC at 1 GeV. . . . .	70
2.3	Initial and final beam parameters (rms) in the DEEX bunch compressor in different approximations of the particle dynamics: linear single particle dynamics (LSP), non-linear single-particle dynamics (NSP) and multi-particle dynamics including CSR effects for 100 pC bunch charge (MP). . . . .	74
2.4	Initial (i) and final (f) beam parameters (rms) in the DEEX bunch compressor for the unoptimized symmetrical design (SD), the symmetrical design with the optimized Twiss parameters (OSD) and the optimized unsymmetrical design (OUD). The simulations are performed for the multi-particle dynamics accounting for the CSR effects at 100 pC bunch charge. . . . .	85
2.5	Parameters of the elements of DEEX BCs: initial unoptimized design, design II optimized for beam parameters of Set II listed in Table 2.2, design III optimized for the same beam parameters with an exception of the reduced bunch charge of $q = 20$ pC. . . . .	89
2.6	Initial (I), after the first EEX module (M) and final (F) beam parameters (rms) in the DEEX bunch compressor for the optimized unsymmetrical design. The simulations are performed for the multi-particle dynamics accounting for CSR effects for 20 pC bunch charge. . . . .	90
2.7	European XFEL and LCLS-II beam parameters on the entrance of the bunch compressor used in our simulations [80]. Listed twiss parameters are found during optimization. . . . .	98
2.8	Parameters of the optimized 2EEX BCs for European XFEL and LCLS-II for the input beam parameters listed in Table 2.7. . . . .	99

Table	Page
2.9 Parameters of the DEEX beamline for LCLS-II and fold increase of emittances for different compression ratios. . . . .	100
3.1 Parameters of the TDC-based chirper for MaRIE x-ray FEL. . . . .	118
3.2 Emittance degradation in the 250 MeV chirper accounting for the LSC effects for different bunch charges. . . . .	137
3.3 Parameters of the TDC-based dechirper beamline for MITS . . . . .	153
3.4 Parameters of the TDC-based dechirper beamline at 1 GeV for MaRIE . . . .	162

## LIST OF FIGURES

Figure		Page
2.1	Schemes of the C-chicane (a), S-chicane (b), and double-chicane (c) consisting of four, six and eight bending magnets, respectively. Green and blue rectangles represent different dipole magnets.. . . . .	49
2.2	(a) A scheme of an exact EEX up (A). (b) A conceptual scheme of a double EEX bunch compressor at 1 GeV for MaRIE XFEL electron beam. Bending magnets are represented by green rectangles, the deflecting cavity is represented by the yellow rectangle with red borders.. . . . .	62
2.3	Telescope scheme: two triplets and the “superlense” are combined together to compress and reshape the beam in $(x, x')$ phase space, as it is described by the telescope matrix $R_T$ in Eq. (2.53). Red and blue ovals symbolize focusing and defocussing quadrupole magnets in respect to the $(x, x')$ phase space.. . . . .	66
2.4	Normalized rms emittance (a) and normalized eigen-emittance (b) evolution from the distance along the path in the DEEX BC beamline. The elements are represented by the color scheme as follows: green is for the bending magnets, yellow is for the TDCs, gray is for the drifts and pink is for the telescope. The TDCs and dipole magnet lengths are enlarged on the scheme to be visualized better. . . . .	71
2.5	Evolution of eigen emittances evolution from the distance along the beam-path in the DEEX BC: (a) nonlinear dynamics without CSR effects and (b) nonlinear dynamics with CSR effects ( $q = 100$ pC). The elements of the beamline are represented by the color scheme as follows: green is for the bending magnets, yellow is for the TDCs, gray is for the drifts and pink is for the telescope. The TDCs and dipole magnet lengths are enlarged on the scheme to be better visualized. . . . .	72
2.6	Transverse (left) and longitudinal (right) phase spaces for the linear (a-b) and nonlinear (c-d) single-particle dynamics, and the nonlinear dynamics with the CSR effects for $q = 100$ pC (e-f) at the exit of DEEX BC.. . . .	73

Figure	Page
2.7 Dependence of the $\Sigma$ -matrix determinant fold-increase (left) and the compression factor of the beam length after the 1st EEX (right) from the Twiss parameters. . . . .	81
2.8 Evolution of the ES optimization from the iteration number $n$ over 800 steps: (a) $\text{cost} = \det(\Sigma)_f / \det(\Sigma)_i$ ; (b) $(\epsilon_{n_x})_f / (\epsilon_{n_x})_i$ ; (c) the compression ratio after EEX up; (d) the Twiss parameters; (e) parameters of EEX up; (f) parameters of EEX down. . . . .	91
2.9 Transverse, longitudinal and $(z, x')$ phase spaces (from left to right) for the linear (a-c) and nonlinear (d-f) single particle dynamics, and for the nonlinear dynamics with the CSR effects for $q = 100$ pC on the exit of the optimized DEEX BC (Design I, set I). Real dynamics results in approximately 10-fold increase of $\epsilon_{n_x}$ and 2-fold increase of $\epsilon_{n_z}$ . . . . .	92
2.10 Transverse, longitudinal and $(z, x')$ phase spaces (from left to right) for the different cases of beam dynamics at the end of the optimized DEEX BC (Design II, set II): (a-c) the linear single-particle dynamics; (d-f) the nonlinear single-particle dynamics (1.89-fold increase of $\epsilon_{n_x}$ , $\epsilon_{n_z}$ does not change); (g-i) the multi-particle dynamics with the CSR effects for $q = 100$ pC (3.44-fold increase of $\epsilon_{n_x}$ , 1.16-fold increase of $\epsilon_{n_z}$ ). . . . .	93
2.11 Left: dependence of the emittance fold increase from the compression factor $m$ for Designs I and Design II of DEEX BC. Initial longitudinal parameters of the beam are adjusted to achieve the same beam size at the end of the compressor as expected for $m = 25$ : $\sigma'_z = \sigma_z \cdot m/25$ and $\Delta E' = \Delta E \cdot 25/m$ . Right: dependence of the emittance fold increase in DEEX BC (Design I and II) from the bunch charge $q$ . Points are marking the beam parameters for which each design was optimized. . . . .	94
2.12 Dependence of the fold emittance increase from the initial transverse normalized emittances at different initial energy spreads for Design I and II (left). Dependence of the fold emittance increase from the initial energy spread for Design I and II (right). Points are marking the beam parameters for which each design was optimized. . . . .	94
2.13 Dependence of the fold emittance increase from the beam energy for Design I: $\epsilon_{n_x, n_y} = 0.10 \mu\text{m}$ , $\Delta E = 25 \text{ keV}$ ; and Design II: $\epsilon_{n_x, n_y} = 0.19 \mu\text{m}$ , $\Delta E = 70 \text{ keV}$ . Points are marking the beam parameters for which each design was optimized. . . . .	95

- 2.14 Transverse, longitudinal and  $(z, x')$  phase spaces at the exit of the optimized DEEX (Design III, set III) from left to right: (a-c) the linear single-particle dynamics; (d-f) the nonlinear single-particle dynamics resulting in 1.7-fold increase of  $\epsilon_{nx}$ , 1.01-fold increase of  $\epsilon_{nz}$ ; (g-i) the nonlinear dynamics with CSR for  $q = 20$  pC resulting in 1.35-fold increase of  $\epsilon_{nx}$ , 1.01-fold increase of  $\epsilon_{nz}$  (bottom). Real dynamics with the CSR effects, for which this design was optimized, results in better transverse beam quality than nonlinear dynamics without CSR. . . . . 96
- 2.15 Evolution of the fold increase of eigen emittances after each beam element ( $k$ ) from the distance along the beamline in the optimized DEEX BC design III: (a)  $\det(\Sigma)$  and eigen-emittance  $\lambda_2$ , corresponding to  $\epsilon_x$  on the entrance/exit of the beamline; (b) eigen-emittance  $\lambda_3$ , corresponding to  $\epsilon_z$ , and eigen-emittance  $\lambda_1$ , corresponding to  $\epsilon_y$ . The elements of the beamline are represented by the color scheme as follows: green is for the bending magnets, yellow is for the TDCs, gray is for the drifts and pink is for the telescope. The TDCs and dipole magnet lengths are enlarged on the scheme to be better visualized. . . . . 97
- 2.16 RMS beam sizes evolution through optimized DEEX BC: (a)  $\sigma_x$ ; (b)  $\sigma_y$  and  $\sigma_z$ . . . . . 97
- 2.17 The ratio of final and initial emittances for transverse and longitudinal phase spaces from the compression ratio  $m$ . The beamline and the Twiss parameters are individually optimized for each compression ratio and summarized in Table 2.9, while other input beam parameters remain invariant. . . . . 100
- 2.18 (a) Emittance Exchanger configuration with reduced number of bending magnets. (b) A bunch compressor, combined from two alternative EEX configurations, has a similar topology as a chicane with inserted transverse deflecting cavities. Yellow symbols represent TDCs, green rectangles represent dipole magnets, and blue and red ovals represent focusing and defocussing quadrupoles in respect to  $(x, x')$  phase space. The negative drift sections are highlighted blue, while the regular drift sections are gray. . . . . 104

3.1	The schematics of the TDC-based chirper beamline (above) consisting of three TDCs for imposing longitudinal energy chirp in relativistic bunches. Subplots below show the $(x, z)$ bunch distribution inside each TDC. Green arrows in these plots show $z$ -dependent deflection provided by each cavity and color shows the particle energy at the corresponding location: the red color corresponds to the highest energy and the blue color to the lowest energy in the bunch. . . . .	114
3.2	The layout of TDCs inside the cryomodules for the MaRIE linac. The design shows the TDC-based chirper consisting of twenty four total 13-cell cavities within two cryomodules at 250 MeV (above) and at 1 GeV with thirty two total 13-cell cavities within four cryomodules (below). The cryomodule contours are represented by blue ovals, each 13-cell TDC is represented by a yellow rectangle, and the black arrows point along the direction of the beam propagation. . . . .	117
3.3	Transverse and longitudinal emittances and eigen emittances along the beamline for the input Twiss parameters $\beta_x = \beta_y = 5$ m and $\alpha_x = \alpha_y = 0$ . Each 13-cell cavity is marked as a yellow rectangle representing its actual geometric length and position within the beamline. The ordinate $s = 0$ m corresponds to the entrance of the beamline. . . . .	123
3.4	Phase spaces at the exit of the TDC-based chirper at 250 MeV for nonlinear single-particle dynamics $\beta_x = \beta_y = 5$ m and $\alpha_x = \alpha_y = 0$ . . . . .	124
3.5	Beam parameters at a distance $s$ along the beamline in TDC-based chirper at 250 MeV ( $\beta_{x,y} = 5$ m and $\alpha_{x,y} = 0$ ): (a) $\sigma_x$ and $\sigma_y$ ; (b) $\sigma_z$ ; (c) the total energy spread; (d) the chirp. The ordinate $s = 0$ m corresponds to the entrance of the beamline. . . . .	125
3.6	Transverse and longitudinal emittances and eigen emittances from the input beta-function $\beta_x$ at $\beta_y = 5$ m and $\alpha_x = \alpha_y = 0$ . . . . .	127
3.7	Transverse and longitudinal emittances and eigen emittances from the Beta-function $\beta_x$ for different $\alpha_x$ ( $\beta_y = 5$ m and $\alpha_y = 0$ ). . . . .	128
3.8	Beam parameters at a distance $s$ along the beamline in TDC-based chirper at 250 MeV with the optimized Twiss parameters $\beta_x = \beta_y = 59$ m and $\alpha_x = \alpha_y = 2.1$ : (a) $\sigma_x$ and $\sigma_y$ together; (b) $\sigma_y$ on the different scale; (c) the total energy spread; (d) the energy chirp. The longitudinal beam profile remains identical to the previous case and is not shown. . . . .	129

Figure	Page
3.9 Transverse and longitudinal emittances and eigen emittances along the beam-line for the optimum input Twiss parameters $\beta_x = \beta_y = 59$ m and $\alpha_x = \alpha_y = 2.1$ . . . . .	130
3.10 Phase spaces at the exit of the TDC-based chirper at 250 MeV for the non-linear single-particle dynamics for the optimal Twiss parameters $\beta_{x,y} = 59$ m and $\alpha_{x,y} = 2.1$ . . . . .	131
3.11 Normalized emittances at the exit of the TDC-based chirper at 250 MeV with the optimized Twiss parameters in respect to the applied chirp at the end of the beamline. The upper horizontal axes relate the imposed chirp to the final correlated energy spread of the beam. . . . .	132
3.12 Transverse and longitudinal emittances and eigen emittances from the voltage in the last TDC at the Twiss parameters values of $\beta_{x,y} = 59$ m and $\alpha_{x,y} = 2.1$ . The dotted vertical line demonstrates the optimal voltage when the minimum of the transverse emittance is reached, which happens when the longitudinal regular and eigen emittances match. . . . .	133
3.13 Phase spaces at the exit of the TDC-based chirper at 250 MeV for nonlinear single-particle dynamics at $\beta_{x,y} = 59$ m and $\alpha_{x,y} = 2.1$ with the tuned voltage ( $\Delta V = +26.5$ kV) in the last TDC. . . . .	134
3.14 Phase spaces at the exit of the TDC-based chirper at 250 MeV for nonlinear single-particle dynamics with tuned voltage ( $\Delta V = +26.5$ kV) in the last TDC for the new optimal set of the input Twiss parameters $\beta_{x,y} = 150$ m and $\alpha_{x,y} = -1.3$ . . . . .	135
3.15 Transverse and longitudinal emittances and eigen emittances along the beam-line with the adjusted voltage in the last TDC at the new optimal Twiss parameters $\beta_{x,y} = 150$ m and $\alpha_{x,y} = -1.3$ . . . . .	136
3.16 LSC effects on the final longitudinal phase space in the TDC-based chirper at 250 MeV for different bunch charges: (a) 0 pC; (b) 100 pC; (c) 10 nC and (d) 20 nC. . . . .	138
3.17 Phase spaces in the middle of the TDC-based chirper at 250 MeV with tuned voltage in the last TDC and Twiss parameters: $\beta_x = \beta_y = 150$ m and $\alpha_x = \alpha_y = -1.3$ . . . . .	139
3.18 Phase spaces in the middle of the TDC-based chirper at 250 MeV after the sextupole with $k_1 = 4.5$ m <sup>-3</sup> . The voltage in the last TDC is up-shifted and the input Twiss parameters are $\beta_x = \beta_y = 150$ m and $\alpha_x = \alpha_y = -1.3$ . . . . .	140

3.19	Transverse and longitudinal eigen emittances along the beamline: (a,b) one sextupole $k_1 = 4.5 \text{ m}^{-3}$ adjusted to suppress quadratic correlations in $(z', x')$ , $(x, x')$ and $(z, x')$ phase spaces in the middle of the beamline; (b,c) three sextupoles $k_1 = 5.6 \text{ m}^{-3}$ , $k_2 = -21.5 \text{ m}^{-3}$ and $k_3 = -22 \text{ m}^{-3}$ adjusted to minimize the longitudinal eigen emittance with the previously optimized Twiss parameters $\beta_{x,y} = 150 \text{ m}$ and $\alpha_{x,y} = -1.3$ ; (e,f) the same sextupole configuration with re-optimized Twiss parameters $\beta_{x,y} = 589 \text{ m}$ and $\alpha_{x,y} = 35$ . The black lines mark the actual positions of the sextupoles within the beamline. . . . .	141
3.20	Normalized emittances at the exit of the TDC-based chirper at 1 GeV in respect to the applied chirp. The upper horizontal axes relate the imposed chirp to the final correlated energy spread of the beam. . . . .	143
3.21	Transverse and longitudinal emittances and eigen emittances along the beamline of the TDC-based chirper at 1 GeV for the input Twiss parameters $\beta_x = \beta_y = 175 \text{ m}$ and $\alpha_x = \alpha_y = 0.3$ . . . . .	144
3.22	Beam parameters at a distance $s$ along the beamline for the optimized Twiss parameters $\beta_x = \beta_y = 175 \text{ m}$ and $\alpha_x = \alpha_y = 0.3$ : (a) $\sigma_x$ and $\sigma_y$ ; (b) $\sigma_z$ ; (c) the total energy spread; (d) the energy chirp. The ordinate $s = 0 \text{ m}$ corresponds to the entrance of the beamline. . . . .	145
3.23	Phase spaces at the exit of the TDC-based chirper at 1 GeV with the non-linear dynamics accounting for the LSC at $q=100 \text{ pC}$ , $\beta_x = \beta_y = 175 \text{ m}$ and $\alpha_x = \alpha_y = 0.3$ . . . . .	146
3.24	Transverse and longitudinal emittances and eigen emittances along the beamline of the TDC-based chirper at 1 GeV with sextupoles ( $k_1 = 0 \text{ m}^{-3}$ , $k_2 = -2.5 \text{ m}^{-3}$ , $k_3 = -12 \text{ m}^{-3}$ ) tuned to preserve the longitudinal phase space. Twiss parameters are $\beta_x = \beta_y = 1472.5 \text{ m}$ and $\alpha_x = \alpha_y = 40$ . . . . .	147
3.25	Beam parameters: (a) $\sigma_x$ and $\sigma_y$ ; (b) $\sigma_z$ ; (c) the total energy spread; (d) the energy chirp, at a distance $s$ along the beamline of the TDC-based chirper at 1 GeV with sextupoles $k_1 = 0 \text{ m}^{-3}$ , $k_2 = -2.5 \text{ m}^{-3}$ , and $k_3 = -12 \text{ m}^{-3}$ tuned to preserve the quality of the longitudinal phase space. The Twiss parameters are $\beta_x = \beta_y = 1472.5 \text{ m}$ and $\alpha_x = \alpha_y = 40$ . . . . .	148
3.26	Phase spaces at the exit of the TDC-based chirper at 1 GeV with sextupoles tuned to preserve the longitudinal phase space. The simulations use nonlinear dynamics accounting for the LSC at $q=100 \text{ pC}$ and input Twiss parameters $\beta_x = \beta_y = 1472.5 \text{ m}$ and $\alpha_x = \alpha_y = 40$ . . . . .	150

Figure	Page
3.27 The layout of TDC-based dechirper inside the cryomodule for MITS. Each 13-cell cavity is represented by a yellow rectangle with a red border, while the focusing and defocussing quadrupoles in respect to the $(x, x')$ phase space are represented respectively by the blue and red ovals. The large blue rectangular contour with smoothed corners represents the cryomodule boundary. . . . .	152
3.28 Longitudinal phase spaces on the exit of the TDC-based dechirper for MITS for the nonlinear particle dynamics accounting for the LSC effects for different bunch charges: (a) 0 pC; (b) 100 pC; (c) 1 nC; (d) 10 nC. The beam has zero chirp on the entrance of the beamline, and gains a negative chirp in the dechirper. . . . .	154
3.29 Evolution of the normalized emittances (a,b) and related to them eigen emittances (c,d) at a distance $s$ along the beamline of the TDC-based dechirper at 250 MeV. The ordinate $s = 0$ m corresponds to the entrance of the beamline. The Twiss parameters are $\beta_{x,y} = 4.16$ m and $\alpha_{x,y} = -1$ . . . . .	155
3.30 Beam parameters: (a) $\sigma_x$ and $\sigma_y$ ; (b) $\sigma_z$ ; (c) the total energy spread; (d) the energy chirp, at a distance $s$ along the beamline of the TDC-based dechirper at 250 MeV. The ordinate $s = 0$ m corresponds to the entrance of the beamline. The input Twiss parameters are $\beta_{x,y} = 4.2$ m and $\alpha_{x,y} = -1$ . . . . .	156
3.31 Phase spaces at the exit of the TDC-based dechirper for MITS. Simulations account for nonlinear dynamics with LSC-effects at a 100 pC bunch charge. The beam has zero chirp on the entrance of the beamline. . . . .	157
3.32 Evolution of the normalized emittances (a,b) and related to them eigen emittances (c,d) at a distance $s$ along the beamline of the TDC-based dechirper at 250 MeV for the optimal Twiss parameters $\beta_x = 28.8$ m $\beta_y = 9.8$ m, $\alpha_x = -7$ , and $\alpha_y = 1$ . . . . .	158
3.33 Beam parameters: (a) $\sigma_x$ and $\sigma_y$ ; (b) $\sigma_z$ ; (c) the total energy spread; (d) the energy chirp, at a distance $s$ along the beamline of the TDC-based dechirper at 250 MeV. The ordinate $s = 0$ m corresponds to the entrance of the beamline. The Twiss parameters are $\beta_x = 28.8$ m $\beta_y = 9.8$ m, $\alpha_x = -7$ , and $\alpha_y = 1$ . . . . .	159
3.34 Phase spaces at the exit of the TDC-based dechirper with optimized input Twiss parameters for MITS. . . . .	160

- 3.35 The layout of TDC-based dechirper at 1 GeV fitting inside of six cryomodules for MaRIE. The cryomodules one, two, three and six contain a single TDC beamline each. The TDCs are combined from sixteen 13-cell cavities. Each 13-cell cavity is represented by a yellow rectangle with a red border. The TDCs are shifted towards each other in cryomodules three (CRM-1') and four (CRM-1'') to keep the same gap between 13-cell cavities. The cryomodules two and five contain the negative drift beamlines combined from focusing (blue) and defocussing (red) quadrupoles in respect to the  $(x, x')$  phase space. . . . . 161
- 3.36 Longitudinal phase spaces at the exit of the TDC-based dechirper at 1 GeV for MaRIE for the nonlinear dynamics accounting for the LSC effects for different bunch charges: (a) 0 pC; (b) 40 pC; (c) 100 pC; (d) 1 nC. The beam has a chirp at the entrance of the beamline, which is removed in the dechirper. . . . . 163
- 3.37 Evolution of the normalized emittances (a,b) and related to them eigen emittances (c,d) at a distance  $s$  along the beamline of the TDC-based dechirper at 1 GeV for the optimal Twiss parameters  $\beta_x = 95$  m,  $\beta_y = 56$  m,  $\alpha_x = -3.1$ , and  $\alpha_y = 2$ . Each TDC, comprised of sixteen 13-cell cavities, is represented by a yellow rectangle, while focusing and defocussing quadrupoles in respect to  $(x, x')$  phase space are marked by blue and red lines respectively. The ordinate  $s = 0$  m corresponds to the entrance of the beamline. . . . . 168
- 3.38 Beam parameters: (a)  $\sigma_x$  and  $\sigma_y$ ; (b)  $\sigma_z$ ; (c) the total energy spread; (d) the energy chirp, at a distance  $s$  along the beamline of the TDC-based dechirper at 1 GeV. Twiss parameters are  $\beta_x = 95$  m,  $\beta_y = 56$  m,  $\alpha_x = -3.1$ , and  $\alpha_y = 2.0$ . . . . . 169
- 3.39 Evolution of eigen emittances at a distance  $s$  along the beamline with a sextupole ( $k_1 = 35.5 \text{ m}^{-3}$ ) added in the middle of the scheme (marked by a black line) for the different bunch charges: (a,b) 0 pC; (c,d) 100 pC. The optimal Twiss parameters for this configuration of the scheme are  $\beta_x = 70.0$  m,  $\beta_y = 62.1$  m,  $\alpha_x = -3.7$ , and  $\alpha_y = 1.6$ . . . . . 170
- 3.40 Phase spaces at the exit of the TDC-based dechirper at 1 GeV with the sextupole  $k_1 = 35.5 \text{ m}^{-3}$  in the middle of the scheme and the optimized input Twiss parameters  $\beta_x = 70.0$  m,  $\beta_y = 62.1$  m,  $\alpha_x = -3.7$ , and  $\alpha_y = 1.6$  in the approximation of the nonlinear single-particle dynamics. . . . . 171

## Figure

## Page

3.41	Phase spaces at the exit of the TDC-based dechirper at 1 GeV with the sextupole ( $k_1 = 35.5 \text{ m}^{-3}$ ) in the middle of the scheme with the optimized input Twiss parameters $\beta_x = 70.0 \text{ m}$ , $\beta_y = 62.1 \text{ m}$ , $\alpha_x = -3.7$ , and $\alpha_y = 1.6$ in the approximation of the nonlinear dynamics with the LSC effects ( $q=100 \text{ pC}$ ). . . . .	172
3.42	Dependence of the output energy spread of the beam from the input energy spread in the TDC-based dechirper at 1 GeV with the sextupole $k_1 = 35.5 \text{ m}^{-3}$ in the middle of the scheme. The case without the LSC effects is presented on the left and the case accounting for the LSC effects ( $q=100 \text{ pC}$ ) is on the right. The upper horizontal axes relate the initial chirp to the initial correlated energy spread of the beam. The right vertical axes relate the final chirp to the final correlated energy spread. . . . .	173
3.43	Dependence of the final emittances from the initial chirp in the TDC-based dechirper for the nonlinear single particle dynamics on the left and for the nonlinear dynamics with LSC effects ( $q = 100 \text{ pC}$ ) on the right. The upper horizontal axes relate the initial chirp to the initial correlated energy spread of the beam. The voltage in all TDCs was adjusted to exactly compensate for the initial chirp in the approximation of the linear single-particle dynamics. .	174
3.44	Dependence of the final emittances and their related eigen emittances from the voltage in the last TDC for the nonlinear single particle dynamics on the top and the for nonlinear dynamics with LSC effects ( $q = 100 \text{ pC}$ ) on the bottom. The dotted vertical lines demonstrate the optimal voltage minimizing the transverse emittance for both cases. . . . .	175
4.1	The numerically calculated Wigner function (solid-green) and its time-limited plane wave approximation (dashed-brown) at $r_n = 0$ : for the weak focusing regime ( $\sigma_x > \gamma\sigma_z$ ) on the top and for the special case, $\sigma_x = \gamma\sigma_z$ , on the bottom. The chosen values of the Lorentz factor ( $\gamma$ ) respectively correspond to the electron energies of 3.5 MeV, 35 MeV and 350 MeV. . . . .	199
4.2	The numerically calculated Wigner function at $r_n = 0$ in the weak focusing regime ( $\sigma_{x_n} = 200$ and $\sigma_{x_z} = 20$ ) for different electron velocities $\beta c$ represented by distinct colors. . . . .	200
4.3	The numerically calculated Wigner function (solid-green) versus its time-limited plane-wave approximation (dashed-brown) in the extreme focusing regime for different parameters of the laser pulse. . . . .	202

4.4 The numerically calculated normalized Wigner function (solid-green) versus its time-limited plane-wave approximation (dashed-brown) in the moderate focusing regime for different parameters of the laser pulse. . . . . 203

# CHAPTER 1

## INTRODUCTION

### 1.1 X-radiation and X-ray light sources overview

X-rays are a type of electromagnetic radiation whose wavelength lies in the range extending from 10 pm ( $3 \times 10^{19}$  Hz and  $\sim 124$  keV) to 10 nm ( $3 \times 10^{16}$  Hz and  $\sim 124$  eV). This region is surrounded by ultraviolet (UV) radiation and gamma ( $\gamma$ ) radiation on the upper and lower wavelength boundaries, respectively<sup>1</sup>. Sometimes, the X-ray region is subdivided in two regions: soft X-ray, spanning from 200 pm to 10 nm, and hard X-ray, spanning from 10 pm to 200 pm. X-radiation was named and characterized by Wilhelm Röntgen in 1895. Interestingly, in the same year, Alfred Nobel wrote and signed his last will establishing the series of prizes to recognize “the greatest benefit on mankind” in several scientific disciplines including physics, chemistry, physiology or medicine, literature, and peace, which is known today as the Nobel prize. Ultimately, Röntgen’s discovery and systematic studies of X-rays was recognized with the first Nobel prize in physics in 1901. Röntgen studied the radiation emanating from Crookes tubes [1], which are known as the first man-made source of X-ray radiation. A Crookes tube is a partial vacuum ( $\sim 10^{-5}$  Torr) discharge glass tube where electrons are created by the ionization of residual air by a high DC voltage. This voltage also accelerates the electrons towards the anode, a positively charged electrode. If the applied voltage is large enough ( $>5$  kV), electrons, hitting the anode or a glass wall, emit X-ray radiation. This radiation can be caused by two conceptually different mechanisms. The first

---

<sup>1</sup>There are no strict boundaries between those regions. The borders have mostly phenomenological character motivated by the convenience of radiation description.

mechanism is X-ray fluorescence, where the free electrons strike orbital electrons of an atom within a material and excite its electrons to a higher state [2]. The atom then spontaneously emits radiation when transitioning to a lower energy state. The second mechanism of producing X-rays in Crookes tubes is bremsstrahlung radiation, where a free electron trajectory is bent by the atomic nucleus<sup>2</sup> [3]. Both mechanisms of X-ray production described above rely on the presence of a moving electron, whether bound by an atom or free.

Historically, the first studied X-rays were produced by man-made sources, however there are several natural sources of X-radiation which we briefly review next. Cosmic X-rays (and gamma rays) are subjects of study in X-ray astronomy [7]. They are formed in stars and in other extremely high-temperature cosmic gases, rarely reach the Earth, and are mostly observed within the Earth's atmosphere. Natural terrestrial X-ray sources are primarily associated with radioactive elements. Radioactive decay is the process by which an unstable atom decays into another atom called a daughter by emitting an  $\alpha$  (Helium-4 nucleus) or  $\beta$  (electron) particle. This process often results in a daughter nucleus in an excited state. The excited nucleus decays to the lower energy state emitting an X-ray or  $\gamma$ -ray photon depending on the transition energy.

Crookes tubes were not intentionally designed to produce X-rays. Similarly, the first particle accelerators were built for acceleration purposes without the intention of producing X-rays. Classical electrodynamics suggests that a charged particle moving on a circular trajectory emits synchrotron radiation. This was first derived for the non-relativistic case by Joseph Larmor in 1897 [8] and extended to the relativistic case by Alfred-Marie Lienard in 1912 [9], long before particle accelerators began to operate. Energy-loss due to radiation questioned the existent atomic model and motivated a new stream of research seeking for a new model. The atomic structure based on quantum theory was soon proposed by Niels Bohr

---

<sup>2</sup>Bound atomic electrons affect the rate and other properties of the bremsstrahlung radiation [4,5], moreover this radiation is also possible via scattering of two electrons [5,6]

in 1913 and recognized with the Nobel Prize in 1922. Despite this fact, the energy-loss due to synchrotron radiation in particle accelerators received proper attention only after the first betatron<sup>3</sup> was built in 1940 with an operating energy of 2.3 MeV [9]. Ivanenko and Pomeranchuk estimated that the synchrotron radiation limits the maximum achievable energy in a betatron to  $\sim 0.5$  GeV in 1944. A year later, McMillan predicted the rate [12] and Schwinger predicted the spectrum of synchrotron radiation [13]. The significant radiation losses were experimentally observed in a 100 MeV betatron in 1946. Radiation was detected as a visible light in a 70 MeV synchrotron in 1947 [13]. This opened the era of first generation light sources also known as parasitic operation: prior to this accelerators were primarily dedicated to high energy and nuclear physics research. The synchrotron is a circular accelerator proposed by McMillan in 1945. Its design was inspired by the cyclotron invented by Lawrence in 1930 [14] and constructed by him and his graduate student, Livingston, in 1932 [15]. In the cyclotron, the charged particle beam oscillates in the constant magnetic field of an H-shaped solenoid and is accelerated by the radio-frequency (RF) field of D-shaped electrodes [16]. The RF is in resonance with the cyclotron frequency, characterizing circular particle motion in magnetic field,  $B$ :

$$\omega_{cycl} = \frac{qB}{\gamma mc} \quad , \quad (1.1)$$

where  $q$  and  $m$  are the particle charge and mass respectively,  $c$  is the speed of light, and  $\gamma$  is the Lorentz factor of the moving particle:

$$\gamma = \frac{1}{\sqrt{1 - v^2/c^2}} \quad , \quad (1.2)$$

---

<sup>3</sup>A betatron is a circular machine accelerating electrons by magnetic induction. Its working principles are similar to a transformer, where an external time-varying current in the magnetic coil (the first loop) drives the electron beam traveling in the circular vacuum tube (the second loop) [10, 11].

where  $v$  is the particle velocity. The constant frequency of the RF field maintains synchronization with a charged particle's oscillations during acceleration<sup>4</sup> as long as the particle remains in the non-relativistic regime ( $\gamma \sim 1$ ). Upon reaching the relativistic regime, the Lorentz factor increases and the cyclotron frequency decreases, coming out of resonance with the RF field. McMillan [17] and Veksler [18] independently proposed to fix this issue by varying the RF field which is known as the synchronous acceleration principle. This led to a synchronous cyclotron and later to a synchrotron. In the synchrotron, the magnetic guiding and the RF acceleration are separated in space and realized by bending magnets and linear acceleration sections, respectively. Synchrotrons are followed by storage rings in which the beam continuously circulates providing higher fluxes of radiation. Once realized, synchrotron and storage ring radiation became actively used for material science research.

The first synchrotrons had relatively small currents as they were dedicated predominantly for charged particle collision experiments. The Synchrotron Radiation Source (SRS) was the first accelerator specifically designed and constructed as a source of radiation in 1970. This opened the era of second generation light sources [9]. X-ray spectroscopy experiments actively conducted during that time required higher spectral brightness than was previously available for improving spatial and temporal resolution. Brightness, a conserved quantity in ideal optical systems, is defined as the photon flux ( $F$ ) per unit area ( $\Delta A$ ) per unit solid angle ( $\Delta\Omega$ ) [19]. The radiation emitted in the narrow bandwidth is more valuable for spectroscopy experiments and can be achieved by using a monochromator. Conversely, such a radiation can be characterized by spectral brightness also referred as brilliance [19]:

$$B = \frac{F}{\Delta A \Delta\Omega (\Delta\omega/\omega)} \quad , \quad (1.3)$$

---

<sup>4</sup>The radius of the particle trajectory grows linearly with its momentum.

where  $\omega$  is the radiation frequency, and  $\Delta\omega$  is the bandwidth interval. This motivated a new stream of research towards periodic magnetic devices called undulators and wigglers, for bending electron trajectories and enhancing the synchrotron radiation. These structures were inserted in the straight sections of the existing storage rings. The total power of radiation emitted by an electron in a bending magnet with magnetic field amplitude,  $B$ , is:

$$P_{bend} = \frac{e^4 \gamma^2 B^2}{6\pi \epsilon_0 c m_e^2} \quad , \quad (1.4)$$

and in an undulator with the same magnetic field amplitude:

$$P_{und} = \frac{e^4 \gamma^2 B^2}{12\pi \epsilon_0 c m_e^2} \quad , \quad (1.5)$$

where  $\epsilon_0$  is the dielectric permittivity of vacuum,  $e$  and  $m_e$  are the electron charge and mass, respectively, and  $\gamma$  is the electron Lorentz factor. The radiation power in the undulator differs only by a factor of two from its bending magnet counterpart. Indeed, the radiation power from each magnet of the periodic structure is proportional to  $B^2$ , and this value averaged over the undulator period is equal to  $B^2/2$ . However, the spectral brightness of the radiation from an undulator is much higher, because its bandwidth is:

$$\Delta\omega_{rad} \approx \frac{\omega_{rad}}{N_u} \quad , \quad (1.6)$$

where  $N_u$  is the number of the undulator periods and  $\omega_{rad}$  is the frequency of the undulator radiation:

$$\omega_{rad} \approx \frac{4\pi \gamma^2 c}{\lambda_u} \quad , \quad (1.7)$$

where  $\lambda_u$  is the undulator period<sup>5</sup>. By contrast, the spectrum of the synchrotron radiation in a bending magnet is continuous up to the critical frequency [20]:

$$\omega_c = \frac{3c\gamma^3}{2R} \quad , \quad (1.8)$$

where  $R$  is the radius of curvature. The radiation from a particle moving on a curved trajectory is emitted at a  $\sim 1/\gamma$  angle centered along the tangent to the particle trajectory at each point. The angular distribution of the overall radiation from a periodic structure is defined by the maximum angle of the particle trajectory with respect to the axis:

$$\theta_{max} \approx \frac{K}{\gamma} \quad , \quad (1.9)$$

where  $K$  is the dimensionless undulator parameter:

$$K = \frac{eB\lambda_u}{2\pi m_e c} \quad . \quad (1.10)$$

Periodic magnetic structures are typically divided in two types with respect to the value of the undulator parameter: undulators ( $K \leq 1$ ) and wigglers ( $K \gg 1$ ). Thus, the radiation from an electron wiggled by the different poles in an undulator incoherently sums up and is emitted in a narrow angle along the axis, resulting in the narrow bandwidth spectrum.

After the electron “shaking” mechanism was optimized using periodic magnetic structures in the existing particle accelerators, the electron beam distribution became the main limiting factor of synchrotron radiation brightness. Electrons in the beam of any real machine are not identical to each other coordinate- or speed-wise. As a result, individual electrons in the beam travel on the distinct trajectories and emit photons in different directions and different times. Increasing the radiation brightness further required better quality of the electron

---

<sup>5</sup>The undulator period is the distance between two closest equal poles.

beam characterized by lower emittances<sup>6</sup>. Hence, design of new storage rings capable of providing low-emittance electron beams became an active area of research. This started the epoch of the third generation light sources. Among the first were the European Synchrotron Radiation Facility (ESRF) in 1994 and the Advanced Photon Source (APS) in 1996. Both successfully operate to this day<sup>7</sup> providing powerful radiation over a wide spectrum range for users conducting research in the fields of material science, crystallography, spectroscopy, and many more.

Above, we predominantly discussed X-ray light sources based on circular accelerators, which, however, stopped their evolution brightness-wise in the third generation. An alternative concept of a light source, the Free Electron Laser<sup>8</sup> (FEL), was proposed by John Madey at Stanford University in 1971 [22] and was later built by him and his colleagues [23,24]. The FEL is conceptually different from previous generation light sources, by actually operating in a manner similar to a laser. Different electrons in a FEL bunch radiate coherently, whereas the 3rd generation light sources produce non-coherent radiation. Similar to a synchrotron, a FEL relies on the presence of the electron beam and the undulator section. The FEL requirements for a low-emittance<sup>9</sup>, low-energy-spread, and high-charge-density beam cannot be satisfied in circular accelerators [20]. Therefore, all high brightness FELs are driven by high brightness, high energy electron beams from linear accelerators (linacs). Moreover, the undulator section in FELs is significantly long. Thus, electrons in a FEL become grouped in a train of several bunches in the field of the emitted radiation, if the length of the undulator is more than several gain lengths. The gain length is the distance along the undulator in which the power of the emitted radiation grows  $e$  times in the exponential growth regime [20]. The distance between any of the two consequent “wagons” is equal to the wavelength of the

---

<sup>6</sup>We will introduce the definition of the beam emittance in the next section.

<sup>7</sup>Both facilities went through several upgrades since they were initially built.

<sup>8</sup>LASER is actually an acronym, meaning light amplification by stimulated emission of radiation, which became a narrative term [21].

<sup>9</sup>We introduce the emittance concept and other important characteristics of the beam in the next section

emitted radiation. Therefore, these bunches, continuing oscillations in the magnetic field of the undulator, start emitting coherent radiation with respect to each other. We discuss a FEL's working principles in more detail, especially those which are closely related to the work described in this dissertation in Section 1.3. In the next section, we present the standard formalism used in the community to describe a beam propagating in an accelerator by introducing the phase space concept, emittances, energy spread, and other important characteristics of the beam. We also provide an overview of the most popular beam tracking codes and discuss the physics behind their subroutines for quantifying complex effects of the particle-particle interactions within an accelerator structure via electrostatic forces and electromagnetic radiation.

## **1.2 Phase space evolution of the electron beam: the matrix formalism, important quantities and particle tracking codes.**

The electron beam is often characterized by a reference particle<sup>10</sup> with an averaged coordinate and velocity over the ensemble, and the beam phase space – the particle distribution of the coordinates and velocities with respect to the reference particle. The longitudinal coordinate can be written using the evolution variable  $s$  and the time of propagation  $t$ :  $z = s - ct$ , and typically describes the relative distance between a particle in the bunch to its center, while its average value  $\langle z \rangle = 0$ . The  $z$ -axis is typically aligned with the instantaneous beam trajectory. The coordinate system follows the beam along its path in the accelerator, in such a way that the bunch always moves along the  $s$ -direction and the transverse phase space instantaneously follows the path curvature and torsion [25]. This approach is convenient

---

<sup>10</sup>The reference or “test” particle is a virtual particle which is not necessary present in the beam

in accelerator physics to describe the propagation of the beam through a beamline<sup>11</sup>. The transverse distribution of the beam of charged particles is often quantitatively characterized by its emittance<sup>12</sup> [26]:

$$\epsilon_x = \sqrt{\langle x^2 \rangle \langle x'^2 \rangle - \langle xx' \rangle^2} , \quad (1.11)$$

$$\epsilon_y = \sqrt{\langle y^2 \rangle \langle y'^2 \rangle - \langle yy' \rangle^2} , \quad (1.12)$$

where  $\langle \dots \rangle$  denotes the average over the ensemble, and  $x' = dx/ds \approx v_x/v_z$  and  $y' = dy/ds \approx v_y/v_z$  are the slopes with respect to the instantaneous tangent to the particle trajectory. Analogously, the longitudinal distribution of the beam is characterized by the longitudinal emittance:

$$\epsilon_z = \sqrt{\langle z^2 \rangle \langle z'^2 \rangle - \langle zz' \rangle^2} , \quad (1.13)$$

where  $z' = \frac{\gamma - \gamma_0}{\gamma_0} = \frac{\delta\gamma}{\gamma_0}$  is the coordinate characterizing energy distribution of the electron beam, while  $\gamma_0$  is the average normalized energy of the beam (the Lorentz factor) and  $\gamma$  is the normalized energy of a given particle in the beam distribution.

The beam dynamics of charged particles in an accelerator is typically described by tracking the central position and speed of the bunch and the evolution of its phase space<sup>13</sup>. In general, there are two types of interactions affecting the phase space evolution of charged particles: the interaction of an individual particle with an electromagnetic field of the accelerator structure, and the interaction of particles with each other, which is also known as collective effects in the accelerator community. The actual collisions of heavy charged particles, protons or ions, of two counter-propagating beams are observable in particle col-

---

<sup>11</sup>In Chapter 4 we choose the coordinate system differently to simplify the new 6-dimensional formalism of the beam interaction with a laser pulse.

<sup>12</sup>This definition comes from Statistical Mechanics.

<sup>13</sup>In principal, a similar approach can be used for describing the propagation of a beam of neutral atoms with non-zero magnetic moment in a magnetic guide [27], the propagation of liquids in hydrodynamics [28], the evolution of quantum state in time [29], etc.

liders, making possible the experimental apparatus for High Energy Physics (HEP) research. However, in this dissertation we predominantly discuss acceleration of electrons in the same direction. Since the probabilities of actual collisions between the electrons are very low, we can neglect all of the related interactions between them, except those relying on particle interactions through electromagnetic fields. Since characteristic sizes of the variation of the electromagnetic fields in accelerator structures are small in comparison to the typical bunch sizes, the phase space evolution to the first order can be described using a linear matrix formalism with good accuracy [16, 25]. In such a description, each beam element of an accelerator (a drift space, a bending dipole magnet, a quadrupole magnet, etc.) is represented by a matrix derived from the linearization of the relativistic dynamics of a charged particle relative to the reference particle. The acceleration of a charged particle is defined by the action of the Lorentz force via the Newton equation. Alternatively, it can be derived from the linearization of the Hamiltonian equations of motions of a charged particle in an electromagnetic field. For example, consider a 1D problem of the motion of a particle with coordinate  $q$  and momentum  $p$  influenced by the force  $F(q, p; t)$ , where  $t$  is the evolution variable. This motion is described according to the equations:

$$\frac{dq}{dt} = p \quad , \quad (1.14)$$

$$\frac{dp}{dt} = F(q, p; t) \quad . \quad (1.15)$$

Assuming that the force and momentum are constant within the small interval from  $t_0$  to  $t_0 + \Delta t$  for simplicity, we find the coordinate and momentum at the end of this time interval from the corresponding values at the beginning of the interval:

$$q_f = p_i \Delta t + q_i \quad , \quad (1.16)$$

$$p_f = F(q, p; t_0) \Delta t + p_i \quad . \quad (1.17)$$

Now, we introduce the reference particle characterized by the coordinate  $q_0$  and momentum  $p_0$ . The coordinate and momentum of a particle of interest relative to the reference particle are respectively  $\Delta q$  and  $\Delta p$ . If the force slightly changes on the scale of the relative coordinate and momentum we can rewrite these equations as following:

$$q_{0_f} + \Delta q_f = p_{0_i} \Delta t + q_{0_i} + \Delta p_i \Delta t + \Delta q_i \quad , \quad (1.18)$$

$$p_{0_f} + \Delta p_f = \left( F(q_0, p_0; t_0) + \frac{\partial F}{\partial q} \Delta q_i + \frac{\partial F}{\partial p} \Delta p_i \right) \Delta t + p_{0_i} + \Delta p_i \quad . \quad (1.19)$$

We group the terms related to the reference particle and the particle of interest and find the propagation of the reference particle:

$$q_{0_f} = p_{0_i} \Delta t + q_{0_i} \quad , \quad (1.20)$$

$$p_{0_f} = F(q_0, p_0; t_0) \Delta t + p_{0_i} \quad , \quad (1.21)$$

and for the particle of interest we obtain:

$$\Delta q_f = \Delta t \Delta p_i + \Delta q_i \quad , \quad (1.22)$$

$$\Delta p_f = \left( \frac{\partial F}{\partial q} \Delta t \right) \Delta q_i + \left( \frac{\partial F}{\partial p} \Delta t + 1 \right) \Delta p_i \quad . \quad (1.23)$$

One can rewrite the last equations for the particle of interest in the matrix form:

$$\begin{pmatrix} \Delta q \\ \Delta p \end{pmatrix}_f = \begin{pmatrix} 1 & \Delta t \\ \frac{\partial F}{\partial q} \Delta t & \frac{\partial F}{\partial p} \Delta t + 1 \end{pmatrix} \cdot \begin{pmatrix} \Delta q \\ \Delta p \end{pmatrix}_i. \quad (1.24)$$

The approximation of constant force within the time interval is redundant. In addition the momentum in equation (1.14) can be generalized as an arbitrary function  $G(q, p; t)$ . Indeed, for continuous<sup>14</sup> functions  $F$  and  $G$ , we can switch the order of integration over time and the partial differentiation over variables  $q$  and  $p$ , and find the transport matrix:

$$T(t_1, t_0) = \begin{pmatrix} 1 + \int_{t_0}^{t_1} \frac{\partial G}{\partial q}(q_0(t), p_0(t); t) dt & \int_{t_0}^{t_1} \frac{\partial G}{\partial p}(q_0(t), p_0(t); t) dt \\ \int_{t_0}^{t_1} \frac{\partial F}{\partial q}(q_0(t), p_0(t); t) dt & 1 + \int_{t_0}^{t_1} \frac{\partial F}{\partial p}(q_0(t), p_0(t); t) dt \end{pmatrix}, \quad (1.25)$$

which describes the evolution of the particle of interest in time as:

$$\begin{pmatrix} \Delta q(t_1) \\ \Delta p(t_1) \end{pmatrix} = T(t_1, t_0) \cdot \begin{pmatrix} \Delta q(t_0) \\ \Delta p(t_0) \end{pmatrix}. \quad (1.26)$$

The equations of motion in the case of Hamiltonian dynamics described by  $H(q, p; t)$ :

$$\frac{dq}{dt} = \frac{\partial H}{\partial p}, \quad (1.27)$$

$$\frac{dp}{dt} = -\frac{\partial H}{\partial q}, \quad (1.28)$$

simply result in  $G(q, p; t) = \frac{\partial H}{\partial p}$  and  $F(q, p; t) = -\frac{\partial H}{\partial q}$ . The linear matrix formalism holds if terms with higher order derivatives of the functions  $F$  and  $G$  are much smaller than the first derivatives:  $\frac{\partial^2 F}{\partial q^2} \Delta q \ll \frac{\partial F}{\partial q}$ ,  $\frac{\partial^2 F}{\partial q \partial p} \Delta p \ll \frac{\partial F}{\partial q}$ , etc. If terms of the second order or higher orders are not negligible and have to be taken into account, then the evolution of the particle

---

<sup>14</sup>This is a valid approximation within a single beam element of an accelerator.

vector  $(q, p)$  can be written in tensor form (see [16, 25] for more details). Correspondingly, the motion of an electron in a real 3-dimensional space in an accelerator is described by a 6-dimensional vector:

$$\boldsymbol{\xi}^T = (x, x', y, y', z, z') \quad . \quad (1.29)$$

This vector at the exit of a beam element can be found as the product (on the left) of the  $6 \times 6$  transport matrix of the beam element with the electron vector at its entrance in the approximation of linear single-particle dynamics:

$$\boldsymbol{\xi}_1 = R \cdot \boldsymbol{\xi}_0 \quad , \quad (1.30)$$

which in matrix form is written as:

$$\begin{pmatrix} x \\ x' \\ y \\ y' \\ z \\ z' \end{pmatrix}_1 = \begin{pmatrix} R_{11} & R_{12} & R_{13} & R_{14} & R_{15} & R_{16} \\ R_{21} & R_{22} & \dots & \dots & \dots & \dots \\ \dots & \dots & R_{33} & \dots & \dots & \dots \\ \dots & \dots & \dots & R_{44} & \dots & \dots \\ \dots & \dots & \dots & \dots & R_{55} & \dots \\ R_{61} & R_{62} & \dots & \dots & \dots & R_{66} \end{pmatrix} \cdot \begin{pmatrix} x \\ x' \\ y \\ y' \\ z \\ z' \end{pmatrix}_0 \quad . \quad (1.31)$$

A nondissipative Hamiltonian system requires symplectic behavior of the canonical variables. The evolution of such a system can be represented as a canonical transformation of the coordinates:  $\boldsymbol{\xi}_0 = (\mathbf{q}, \mathbf{p}) \rightarrow \boldsymbol{\xi}_1 = (\mathbf{Q}, \mathbf{P})$ . The canonical transformations can be described by the Jacobian Matrix, the elements of which are  $R_{ij} = \frac{\partial \xi_{1i}}{\partial \xi_{0j}}$  [16]. This imposes the symplectic condition on the transport matrix, so that the following property is satisfied:

$$J = R^T J R \quad , \quad (1.32)$$

where  $J$  is the unit block-diagonal antisymmetric symplectic matrix<sup>15</sup>:

$$J = \begin{pmatrix} 0 & 1 & 0 & 0 & 0 & 0 \\ -1 & 0 & 0 & 0 & 0 & 0 \\ 0 & 0 & 0 & 1 & 0 & 0 \\ 0 & 0 & -1 & 0 & 0 & 0 \\ 0 & 0 & 0 & 0 & 0 & 1 \\ 0 & 0 & 0 & 0 & -1 & 0 \end{pmatrix}. \quad (1.33)$$

This matrix has a property that  $J^2 = -I$ , where  $I$  is the identity matrix:

$$I = \begin{pmatrix} 1 & 0 & 0 & 0 & 0 & 0 \\ 0 & 1 & 0 & 0 & 0 & 0 \\ 0 & 0 & 1 & 0 & 0 & 0 \\ 0 & 0 & 0 & 1 & 0 & 0 \\ 0 & 0 & 0 & 0 & 1 & 0 \\ 0 & 0 & 0 & 0 & 0 & 1 \end{pmatrix}. \quad (1.34)$$

The symplectic condition in equation (1.32) can be illustrated in the 1D example (2D phase space) discussed above<sup>16</sup>. The Hamiltonian equations (1.27-1.28) can be rewritten in matrix form using antisymmetric symplectic matrix  $J_1$ :

$$\frac{d}{dt} \begin{pmatrix} q \\ p \end{pmatrix} = \begin{pmatrix} 0 & 1 \\ -1 & 0 \end{pmatrix} \begin{pmatrix} \frac{\partial H}{\partial q} \\ \frac{\partial H}{\partial p} \end{pmatrix} = J_1 \begin{pmatrix} \frac{\partial H}{\partial q} \\ \frac{\partial H}{\partial p} \end{pmatrix}. \quad (1.35)$$

---

<sup>15</sup>Indeed,  $R = J$  satisfies the condition in equation (1.32).

<sup>16</sup>We follow the derivation presented in [16] for the 6-dimensional phase space simplifying it for the 2-dimensional phase space.

The Hamiltonian equations are valid in the old coordinates ( $q_0 = q_t$ ,  $p_0 = p_t$ ), corresponding to a particle at the entrance of the beam element, and new coordinates ( $q_1 = q_{t+\Delta t}$ ,  $p_1 = p_{t+\Delta t}$ ) at the exit of the beam element. These coordinates are related through the corresponding linear transformation described by matrix  $R$  in Eq. (1.31), which is at the same time is the Jacobian matrix describing a canonical transformation in the Hamiltonian mechanics [16, 30]:

$$\begin{pmatrix} q_1 \\ p_1 \end{pmatrix} = \begin{pmatrix} \frac{\partial q_1}{\partial q_0} & \frac{\partial p_1}{\partial q_0} \\ \frac{\partial q_1}{\partial p_0} & \frac{\partial p_1}{\partial p_0} \end{pmatrix} \begin{pmatrix} q_0 \\ p_0 \end{pmatrix} = R \begin{pmatrix} q_0 \\ p_0 \end{pmatrix} \quad (1.36)$$

The partial derivatives of the Hamiltonian over  $q_1(q_0, p_0)$  and  $p_1(q_0, p_0)$  can be written in a convenient matrix form in coordinates  $q_0$  and  $p_0$ :

$$\begin{pmatrix} \frac{\partial H}{\partial q_1} \\ \frac{\partial H}{\partial p_1} \end{pmatrix} = \begin{pmatrix} \frac{\partial q_0}{\partial q_1} & \frac{\partial p_0}{\partial q_1} \\ \frac{\partial q_0}{\partial p_1} & \frac{\partial p_0}{\partial p_1} \end{pmatrix} \begin{pmatrix} \frac{\partial H}{\partial q_0} \\ \frac{\partial H}{\partial p_0} \end{pmatrix} = (R^{-1})^T \begin{pmatrix} \frac{\partial H}{\partial q_0} \\ \frac{\partial H}{\partial p_0} \end{pmatrix} = (R^{-1})^T J_1^{-1} \frac{d}{dt} \begin{pmatrix} q_0 \\ p_0 \end{pmatrix} , \quad (1.37)$$

where the last step is accomplished using Eq. (1.35) for  $(q_0, p_0)$ . By putting the result of Eq. (1.37) in Eq. (1.35) for canonical pair  $(q_1, p_1)$ , we find:

$$\frac{d}{dt} \begin{pmatrix} q_1 \\ p_1 \end{pmatrix} = \begin{pmatrix} 0 & 1 \\ -1 & 0 \end{pmatrix} \begin{pmatrix} \frac{\partial H}{\partial q_1} \\ \frac{\partial H}{\partial p_1} \end{pmatrix} = J_1 (R^{-1})^T J_1^{-1} \frac{d}{dt} \begin{pmatrix} q_0 \\ p_0 \end{pmatrix} . \quad (1.38)$$

One can switch the order of differentiation over  $t$  and matrix multiplication, while differentiating both sides of Eq. (1.36) over  $t$ , since the transport matrix of a beam element from the beginning to the end is independent<sup>17</sup> of the evolution variable  $t$ . Comparing this result with one in Eq. (1.38) one can find:

$$R = J_1 (R^{-1})^T J_1^{-1} , \quad (1.39)$$

---

<sup>17</sup>The evolution through the beam element depends only on its actual length or the duration of the evolution in time  $\Delta t$  in this particular example.

which can be transformed to a similar form as equation (1.32):

$$(R^T J_1) \cdot R = (R^T J_1) \cdot J_1 (R^{-1})^T J_1^{-1} = -R^T I (R^{-1})^T J_1^{-1} = -J_1^{-1} = J_1 \quad , \quad (1.40)$$

The derivation of the symplectic property of the transport matrix can be generalized for the 6-dimensional Hamiltonian beam dynamics<sup>18</sup>, and can be found in detail in references [16,25]. The symplectic condition in equation (1.32) immediately leads to  $\det(R)=1$ . This can be shown by taking the determinant on both sides of the equation and using the matrix property  $\det(A \cdot B) = \det(A) \cdot \det(B)$ . This condition is equivalent to the well-known Liouville's theorem in Hamiltonian mechanics stating the conservation of phase space volume.

The symplectic property of the transport matrix holds for many beam elements used in particle accelerators: drift sections, bending magnets, quadrupole magnets, etc. in the approximation of the linear dynamics. Two or more consecutive beam elements  $(R_1, R_2, \dots, R_n)$  result in the overall matrix  $R$  describing transport through this beamline:

$$\xi_n = R_n \cdot R_{n-1} \cdot \dots \cdot R_2 \cdot R_1 \cdot \xi_0 = R \cdot \xi_0 \quad , \quad (1.41)$$

where the overall matrix is a product of its components in the reverse order. This is due to the transport matrix of first beam element being applied to the vector-column first, and hence places the last in the product of matrices, etc.

There are non symplectic beam elements, whose matrices do not satisfy this condition because the beam dynamics in them are not Hamiltonian (i.e dissipative). However, such dynamics can still be described by first order matrices since the formalism resulting in equation (1.25) presented above still holds. Typically a beam element is described by the transport matrix within it and the matrices on the borders of the element. Since the elec-

---

<sup>18</sup>This is obviously holds for the  $2n$ -dimensional Hamiltonian dynamics, where  $n$  is any integer number.

tromagnetic fields can be discontinuous at the element edges, this approach is often quite convenient in the field of particle accelerators.

The distribution in phase space of a beam in a particle accelerator is characterized by the symmetric matrix of the second order momenta known as  $\Sigma$ -matrix [16, 25]. Such a matrix can be found as an ensemble-averaged product of the 6-dimensional vector-column on the 6-dimensional vector-row of an electron<sup>19</sup>:

$$\langle \boldsymbol{\xi} \boldsymbol{\xi}^T \rangle = \Sigma = \begin{pmatrix} \langle x^2 \rangle & \langle xx' \rangle & \langle xy \rangle & \langle xy' \rangle & \langle xz \rangle & \langle xz' \rangle \\ \langle xx' \rangle & \langle x'^2 \rangle & \langle x'y \rangle & \langle x'y' \rangle & \langle x'z \rangle & \langle x'z' \rangle \\ \langle xy \rangle & \langle x'y \rangle & \langle y^2 \rangle & \langle yy' \rangle & \langle yz \rangle & \langle yz' \rangle \\ \langle xy' \rangle & \langle x'y' \rangle & \langle yy \rangle & \langle y'^2 \rangle & \langle y'z \rangle & \langle y'z' \rangle \\ \langle xz \rangle & \langle x'z \rangle & \langle yz \rangle & \langle y'z \rangle & \langle z^2 \rangle & \langle zz' \rangle \\ \langle xz' \rangle & \langle x'z' \rangle & \langle yz' \rangle & \langle y'z' \rangle & \langle zz' \rangle & \langle z'^2 \rangle \end{pmatrix}. \quad (1.42)$$

This observation suggests that the evolution of the  $\Sigma$ -matrix in a beam element can be described via its transport matrix as following:

$$\Sigma_1 = \langle \boldsymbol{\xi}_1 \boldsymbol{\xi}_1^T \rangle = \langle R \boldsymbol{\xi}_0 (R \boldsymbol{\xi}_0)^T \rangle = R \langle \boldsymbol{\xi}_0 \boldsymbol{\xi}_0^T \rangle R^T = R \Sigma_0 R^T, \quad (1.43)$$

where the averaging over the ensemble was permuted with the multiplication on the transport matrix  $R$  since the latter is independent of an individual particle. The determinant of the  $\Sigma$ -matrix characterizes the 6-dimensional phase space volume of the beam. It is conserved in the case of symplectic linear single-particle dynamics:

$$\det(\Sigma_1) = \det(R) \det(\Sigma_0) \det(R^T) = \det(\Sigma_0). \quad (1.44)$$

---

<sup>19</sup>The particle is an electron in this particular example relevant to this dissertation, while in general for an accelerator it can be a proton, an ion, etc. It can be even a neutral particle outside of the field of particle accelerators.

The 6-dimensional phase space, uncorrelated between different cross planes  $(x, x')$ ,  $(y, y')$  and  $(z, z')$ , results in the block-diagonal  $\Sigma$ -matrix. Such a beam can be properly characterized by the transverse emittances introduced in equations (1.11-1.12) and longitudinal emittances introduced in equation (1.13) which appear to be the determinants of the corresponding 2-dimensional blocks of the  $\Sigma$ -matrix. The transverse phase spaces of such a beam are often characterized via the corresponding Twiss parameters. For example, for the horizontal phase space they are defined according to the equation:

$$\Sigma_1 = \begin{pmatrix} \langle x^2 \rangle & \langle xx' \rangle \\ \langle xx' \rangle & \langle x'^2 \rangle \end{pmatrix} = \det(\Sigma_1) \begin{pmatrix} \beta & -\alpha \\ -\alpha & \gamma \end{pmatrix} = \epsilon_x^2 \begin{pmatrix} \beta_x & -\alpha_x \\ -\alpha_x & \gamma_x \end{pmatrix} , \quad (1.45)$$

where  $\beta_x$ ,  $\alpha_x$ ,  $\gamma_x$  are the Twiss parameters of the  $(x, x')$  phase space and  $\beta\gamma - \alpha^2 = 1$ . Therefore,  $\beta_x = \langle x^2 \rangle / \epsilon_x$  has the dimension of meters in International System of Units (SI units) and  $\alpha_x = \langle xx' \rangle / \epsilon_x$  is the dimensionless Twiss parameter.

The normal (Gaussian) distribution of the beam<sup>20</sup> is described as the exponential of the product of the  $\Sigma$ -matrix with the 6-dimensional vector  $\boldsymbol{\xi}$  on both sides:

$$N(\boldsymbol{\xi}) = N_0 \cdot (2\pi)^{-3/2} \sqrt{\det(\Sigma^{-1})} \cdot e^{-\frac{\boldsymbol{\xi}^T \Sigma^{-1} \boldsymbol{\xi}}{2}} , \quad (1.46)$$

where  $N_0$  is the total number of particles in the bunch, which is large enough so one may consider  $N(\boldsymbol{\xi})$  as a continuous function. The root-mean-square<sup>21</sup> (rms) transverse sizes of the beam are respectively:

$$\sigma_x = \sqrt{\langle x^2 \rangle} , \quad (1.47)$$

---

<sup>20</sup>Alternatively, in some cases the beam can be represented by a flat-top distribution, which means a uniform particle distribution within the particle intervals bounded by the beam geometry in the phase space described by the  $\Sigma$ -matrix

<sup>21</sup>The root-mean-square width of a 1-dimensional Gaussian distribution is equivalent to its standard deviation.

and

$$\sigma_y = \sqrt{\langle y^2 \rangle} \quad , \quad (1.48)$$

and the rms longitudinal beam size is:

$$\sigma_z = \sqrt{\langle z^2 \rangle} \quad , \quad (1.49)$$

where the phase space coordinates are considered with respect to the reference particle meaning that  $\langle x \rangle = \langle y \rangle = \langle z \rangle = 0$ . Another important characteristic of the beam characterizing the longitudinal phase space are the total energy spread:

$$\sigma_{z'} = \sqrt{\langle z'^2 \rangle} \quad , \quad (1.50)$$

and the bunch “chirp” which is a linear energy slope along the bunch length:

$$h = \frac{\langle zz' \rangle}{\langle z^2 \rangle} = \frac{\langle zz' \rangle}{\sigma_z^2} \quad . \quad (1.51)$$

It is convenient in some cases to separate the total energy spread into uncorrelated ( $\sigma_{z'_u}$ ) and correlated ( $\sigma_{z'_c} = h\sigma_z$ ) energy spreads:

$$\sigma_{z'} = \sqrt{\frac{\epsilon_z^2}{\sigma_z^2} + \frac{\langle zz' \rangle^2}{\sigma_z^2}} = \sqrt{\frac{\epsilon_z^2}{\sigma_z^2} + h^2 \sigma_z^2} = \sqrt{\sigma_{z'_u}^2 + \sigma_{z'_c}^2} \quad . \quad (1.52)$$

The total energy spread is equal to the uncorrelated energy spread if the bunch has zero chirp.

The majority of beam elements used in accelerators can impose higher order effects on the particle dynamics which under some circumstances can be significant and have to be taken into account. Therefore, in addition to the transport matrix  $M$ , the beam elements

are characterized by tensors of higher orders whose components describe the higher order derivative terms in equations (1.22-1.23). The  $i$ -component of the 6-dimensional electron vector at the exit of the beam element can then be found as:

$$\xi_{1_i} = \sum_j R_{ij} \xi_{0_j} + \sum_{j,k} T_{ijk} \xi_{0_j} \xi_{0_k} + \sum_{j,k,m} P_{ijk m} \xi_{0_j} \xi_{0_k} \xi_{0_m} + \dots \quad , \quad (1.53)$$

where  $R_{ij}$  are the matrix elements of the linear transport matrix  $R$ ,  $T_{ijk}$  are the elements of the tensor  $T$  describing effects of the second order, etc. The linear dynamics is a preferable choice of particle dynamics in traditional particle accelerators because of the simplicity of control and description. In order to compensate for undesired higher order effects unavoidably coming from linear optics<sup>22</sup>, nonlinear optics elements, such as sextupoles, octupoles, etc., are sometimes integrated within the beamline. Linear matrices of these elements are equivalent to the matrix of a drift section associated with its geometrical length along the beam propagation. Nonlinear elements of the second order can impose effects of the third order which then can be compensated by the nonlinear effects of the third order and so on. The higher order effects in this approach should be compensated for until one reaches an order in which they are negligible for the beam dynamics of interest. These effects can be calculated analytically using the matrix/tensor formalism. While performing matrix multiplications is still easily achievable manually, tensor operations accounting for the higher order effects are often realized with the help of beam tracking codes and other computer software<sup>23</sup>.

The actual purpose of powerful beam tracking codes is the necessity to predict collective effects of particle dynamics in an accelerator, which are nearly impossible to estimate and

---

<sup>22</sup>Beam optics and beam lenses are the specific terminology often used in the accelerator community to describe the diversity of the beamline elements originally coming from the light optics.

<sup>23</sup>Recent development of powerful mathematical software such as Mathematica [31] which operates with symbols and formulas and MATLAB [32] which operates with large sets of data numerically allows calculation of high order beam dynamics without using beam tracking codes.

implement within the linear or higher order dynamics of the beam interaction with an accelerator structure<sup>24</sup>. Among others, the interaction between charged particles due to the Coulomb forces is probably the most straightforward and understandable collective effect. Indeed, charged particles of the same charge sign push each other away in a static beam. The relativistic motion of the beam imposes different behavior of the transverse and longitudinal space charge forces with respect to the propagation direction of the beam. These effects are known as the transverse space charge effects (TSC) and longitudinal space charge effects (LSC) in the particle accelerator community. These effects depend on the bunch charge  $q$ , the shape of the beam phase space, and its energy<sup>25</sup>. In addition, the presence of the beam structure or simply a beam pipe can influence the space charge effects. The space charge forces are typically calculated in two steps. First, the electromagnetic fields initiated by the presence of the beam and its motion are calculated using Maxwell's equations. Second, the action of the Lorentz force from this field on each individual particle in the beam is calculated using the relativistic Newton equations. For calculating the TSC forces we consider a cylindrically symmetrical electron beam moving along the  $z$ -direction with speed  $\beta c$  [16]. In addition, we assume a uniformly distributed long bunch in the longitudinal direction and the radial dependence  $\rho(r)$ . From the Maxwell equations in vacuum:

$$\nabla \cdot (\epsilon_0 \mathbf{E}) = \rho \quad , \quad (1.54)$$

$$\nabla \times \left( \frac{\mathbf{B}}{\mu_0} \right) = \mathbf{j} + \frac{\partial(\epsilon_0 \mathbf{E})}{\partial t} \quad , \quad (1.55)$$

---

<sup>24</sup>While it is possible to construct a linear transport matrix accounting for collective effects in some cases, such a matrix typically strongly depends on the beam parameters in contrast to the transport matrix describing the beam interaction with an accelerator structure.

<sup>25</sup>Although  $q$  was used in equation (1.1) as a charge of the particle, in this dissertation it is predominantly used for characterizing the bunch charge of the electron beam unless otherwise stated.

where  $\mu_0 = 1/(\epsilon_0 c^2)$  is the permeability of vacuum. With the proposed symmetry of the beam we can find the radial component of the electric field<sup>26</sup>:

$$E_r = \frac{1}{\epsilon_0 r} \int_0^r r \rho(r) dr \quad , \quad (1.56)$$

and the angular component of the magnetic field<sup>27</sup> arising from the motion of a charged bunch<sup>28</sup>:

$$B_\phi = \frac{\beta}{c \epsilon_0 r} \int_0^r r \rho(r) dr \quad . \quad (1.57)$$

The resulting Lorentz force acting on each ring of the beam depends on the radial coordinate:

$$F_r(r) = \frac{e}{\epsilon_0 r} (1 - \beta^2) \int_0^r r \rho(r) dr \quad , \quad (1.58)$$

where  $e < 0$  is the charge of a single electron. Since  $e \rho(r) > 0$  and  $\beta < 1$  we clarify that the overall force is repulsive. We also admit that for the highly relativistic electron beams the attractive magnetic component of the Lorentz force nearly compensates its repulsive electric counterpart. Therefore, the TSC force in this simple model scales as  $1/\gamma^2$ , where  $\gamma$  is the average Lorentz factor of the beam. For a beam with a Gaussian distribution in the radial direction and a bunch length  $l$ :

$$\rho(r) = \frac{q}{2\pi l \sigma^2} \cdot e^{-\frac{r^2}{2\sigma^2}} \quad , \quad (1.59)$$

---

<sup>26</sup>In the cylindrical coordinate the divergence of the vector field  $\mathbf{A}$  is  $\nabla \cdot \mathbf{A} = \frac{1}{r} \frac{\partial(r A_r)}{\partial r} + \frac{1}{r} \frac{\partial A_\phi}{\partial \phi} + \frac{\partial A_z}{\partial z}$  .

<sup>27</sup>In the cylindrical coordinate the curl of the vector field  $\mathbf{A}$  is  $\nabla \times \mathbf{A} = \left( \frac{1}{r} \frac{\partial A_z}{\partial \phi} - \frac{\partial A_\phi}{\partial z} \right) \hat{\mathbf{r}} + \left( \frac{\partial A_r}{\partial z} - \frac{\partial A_z}{\partial r} \right) \hat{\phi} + \frac{1}{r} \left( \frac{\partial(r A_\phi)}{\partial r} - \frac{\partial A_r}{\partial \phi} \right) \hat{\mathbf{z}}$  .

<sup>28</sup>Here we used  $\mathbf{j} = j_z \cdot \hat{\mathbf{z}} = \rho(r) \beta c \cdot \hat{\mathbf{z}}$  .

where  $q = Ne < 0$  is the total charge of the electron bunch of  $N$  particles. We can evaluate the integral in equation (1.58):

$$F_r(r) = \frac{Ne^2}{2\pi l \epsilon_0} (1 - \beta^2) \frac{1 - e^{-\frac{r^2}{2\sigma^2}}}{r} . \quad (1.60)$$

The force is zero at the center of the beam  $r = 0$ . The maximum of the radial force is reached at  $r \approx 1.58\sigma$  and results in  $F_{r_{max}} \approx \frac{0.45}{2\pi} \frac{Ne^2}{\epsilon_0 l \sigma \gamma^2}$ . The TSC force in this simple model scales linearly with the bunch charge  $q$  or the number of particles in the bunch  $N$ , and scales quadratically with the charge of the particle  $e$ .

Next, we discuss the simple model beyond the calculation of the longitudinal space charge forces. In the previous model we discussed a very long uniformly distributed beam in the longitudinal direction. Such a model would result in a lack of LSC forces. Conversely, a uniformly distributed beam in the radial direction from 0 to  $a$  with a parabolic profile in the longitudinal direction  $N(z) = \frac{3N}{2l} \left(1 - \left(\frac{2z}{l}\right)^2\right)$  results in a longitudinal force [16]:

$$F_z = \frac{3(1 + 2 \ln(b/a))}{\pi} \frac{Ne^2}{\epsilon_0 l^3 \gamma^2} z , \quad (1.61)$$

where  $b$  is the radius of the beam pipe. This repulsive force is compensated at the center of the bunch and linearly depends on the coordinate along the bunch reaching its maximum  $F_{z_{max}} \approx \frac{3}{2\pi} \frac{Ne^2}{\epsilon_0 l^2 \gamma^2}$  at the ends of the bunch<sup>29</sup>. The electric component of the transverse force in Eq. (1.60) is  $\gamma^2$  times bigger than its longitudinal counterpart in Equation (1.61), however the presence of the attractive magnetic component in the transverse force results in both forces being of the same order. The major difference between them can be due to the various beam sizes in the transverse ( $\sigma$ ) and longitudinal ( $l$ ) directions. In these simple approximations, the action of the space charge forces can be presented via the linear transport matrices

---

<sup>29</sup>The approximation  $a = b$  was used here for simplicity.

depending on the beam parameters<sup>30</sup>, while for more sophisticated beam distributions the use of beam tracking codes to account for space charge forces is required.

There are a variety of codes capable of tracking electron bunches from an injector to an undulator accounting for the space charge effects such as PARMELA [33], ASTRA [34], GTR [36], ELEGANT [37], etc. Despite the wide variety of the available beam elements and routines for calculating collective effects, we predominantly used ELEGANT for all simulation studies discussed in this dissertation. The self-generated longitudinal fields are accounted for in the LSDRIFT routine via longitudinal space charge impedance in free space in the frequency domain per unit length [38, 39]:

$$Z_{LSC}(k) = \frac{iZ_0}{\pi k \sigma_r^2} \left( 1 - \frac{k \sigma_r^2}{\gamma} K_1 \left( \frac{k \sigma_r^2}{\gamma} \right) \right) , \quad (1.62)$$

where  $Z_0 = 377 \, \Omega$  is the free space impedance,  $\sigma_r^2 = \sigma_x^2 + \sigma_y^2$  is the transverse size of the beam,  $K_1(\dots)$  is the first modified Bessel function of the second kind<sup>31</sup>, and  $k = 2\pi/\lambda$ , where  $\lambda$  is the modulation wavelength. Equation (1.62) is valid only for short bunches, when their lengths in the beam frame is much smaller than the beam pipe radius. The impedance is used to integrate the LSC kick given by  $Z_{LSC} L_{eff}$  through a section of a lattice<sup>32</sup>. The LSCDRIFT routine relies on the preceding beam element CHARGE used to define the bunch charge  $q$  in pC. If  $q = 0$  pC in the CHARGE element or LSC=0 in the LSCDRIFT routine, then the beam element acts as a regular drift<sup>33</sup>, similar to the different ELEGANT element DRIF realized as a matrix up to the second order [38].

There is no direct routine in ELEGANT for calculating transverse space charge effects in linacs. Moreover, the only routine available in ELEGANT for TSC is the SCMULT designed for

---

<sup>30</sup>The second order effects for TSC are zero, while the third and higher order effects can be accounted via the related tensor.

<sup>31</sup> $K_\alpha(x) = \int_0^\infty e^{-x \cosh(t)} \cosh(\alpha t) dt$

<sup>32</sup>If the impedance and the beam current distribution is known in a small region, one can calculate the voltage and its action on the particle propagation.

<sup>33</sup>It acts as the second order drift at  $q = 0$ .

calculations in rings [40]. However, simulating TSC effects in this dissertation is redundant. Indeed, we predominantly discuss highly relativistic electron beams with a bunch charge not more than 100 pC at beam energies:  $E = 1$  GeV ( $\gamma \sim 2000$ ) for the Matter-Radiation Interactions in Extremes Facility (MaRIE) at Los Alamos National Laboratory (LANL) and  $E = 1.6$  GeV ( $\gamma \sim 3200$ ) for the Linac Coherent Light Source II (LCLS-II) at Stanford Linear Accelerator Center (SLAC) in Chapter 2, and in addition to those, for  $E = 250$  MeV ( $\gamma \sim 500$ ) for the MaRIE linac and MaRIE Injector Test Stand (MITS) in Chapter 3. For these parameters the transverse and longitudinal space charge forces appear to be negligible if the beam distribution is smooth on the scale of its transverse and longitudinal sizes. The last condition can be easily compromised in the longitudinal direction because of effects known in the accelerator community as the microbunching instabilities. There is a possibility of amplifying noise in the longitudinal direction due to the LSC-induced microbunching instabilities. Briefly, the noise, always present in the density distribution of the electron beam, can be transferred to the energy domain via the LSC forces. If the dynamics appear due to a highly dispersive element, the energy modulations are transferred back to the density distribution along the bunch amplifying the initial noise. This is similar to the principles of a klystron amplifier [41]. A more detailed explanation of the LSC-induced microbunching instabilities related to the beam dynamics can be found in Chapter 2.

Another collective effect which can amplify the initial noise present in the electron beam is coherent synchrotron radiation (CSR) [39]. CSR effects themselves<sup>34</sup> are more “dangerous” for beam dynamics in dispersive elements such as a bunch compressor discussed in Chapter 2. They may result in the significant transverse emittance growth [42]. Minimal transverse emittances are extremely critical for the FEL performance as we will discuss in Section 1.3. Therefore, it is important to properly account for the CSR effects’ impact on beam dynamics.

---

<sup>34</sup>The LSC-induced microbunching instabilities are typically much larger in comparison to the CSR-induced microbunching instabilities [39].

As mentioned earlier, a beam moving on a curved trajectory emits synchrotron radiation, which can be described by the Lienard-Wiechert formula [43]:

$$E(L, \mathbf{n}) = \frac{e}{\gamma^2} \frac{\mathbf{n} - \boldsymbol{\beta}'}{L^2(1 - \mathbf{n}\boldsymbol{\beta}')^3} + \frac{e}{c^2} \frac{\mathbf{n} \times [(\mathbf{n} - \boldsymbol{\beta}') \times \mathbf{g}']}{L(1 - \mathbf{n}\boldsymbol{\beta}')^3} \quad , \quad (1.63)$$

where  $L$  is the distance and  $\mathbf{n}$  is the unit vector directed to the observer,  $\boldsymbol{\beta}'$  is the instant normalized velocity of the particle emitting the radiation, and  $\mathbf{g}'$  its instant acceleration whose amplitude is equal to  $g' = \frac{(\beta'c)^2}{r^2}$  for a particle moving on a circular orbit of radius  $r$ . While this effect is extremely important and useful for light sources, its appearance in the accelerator beamline delivering the beam to an undulator of a FEL<sup>35</sup> should be minimized and/or its impact on the beam dynamics should be compensated. There are two possible mechanisms. The first is quantum excitation, a random process of energy loss by a particle in a beam due to radiation which is carried away in portions by photons. This process is also known as incoherent synchrotron radiation (ISR) due to different particles in the beam emitting with random phases. Typically, the impact of this radiation on other particles in the bunch is negligible, and hence often omitted. However, the phase space distribution of a beam moving on a curved trajectory is affected since different particles in the bunch lose energy randomly. Moreover, if the propagation happens in a dispersive element, such as a bending magnet, the energy modulations result in variations of the transverse slopes in the bending plane, which increases transverse emittance of the beam. These effects can be accounted for in the ELEGANT routine CSBEND<sup>36</sup> describing the propagation in a sector dipole magnet accounting for symplectic beam dynamics up to the 18th pole moment [38]. The ISR effects' impact on beam dynamics is typically much less than from the CSR effects.

---

<sup>35</sup>Also consider an undulator of a synchrotron and the place of interaction with a laser pulse for the inverse Compton scattering source.

<sup>36</sup>The parameter “ISR” should be set to one to include the ISR effects [38].

Particles in very short electron bunches traveling through a dipole magnet emit radiation coherently at a wavelength comparable to the size of the bunch. The interaction of such radiation emitted by the tail of the beam with the head of the beam is critical for the beam dynamics in the longitudinal direction and also impacts the transverse phase space in a dispersive element as mentioned above. The CSR effects' impact on beam dynamics in bends were estimated in references [42, 44] motivated by growing interest in X-ray FEL sources and high energy particle colliders. Next, Saldin *et al.* [45] developed an analytical 1D formalism describing CSR effects in bends and downstream drifts starting from the Lienard-Wiechert formula written in equation (1.63). The first term in the right-hand side of the equation describes the Coulomb field (velocity field), while the second term is known as a radiation or an acceleration field. The action of this field on an electron is accounted for via the Lorentz force resulting in the energy change of the previous one. The angle  $\phi$  between the normalized velocity vector  $\beta'$  and the direction to the second electron is known as the retarded angle, which is small in the ultrarelativistic approximation. The distance between two electrons interacting via radiation, also known as the slippage length, can be represented as:

$$\Delta s = s - s' \approx (1 - \beta')r\phi + \frac{r\phi^3}{24} \quad , \quad (1.64)$$

where the first term on the right-hand side is due to the difference between the speed of an electron and the speed of light, and the second term is due to the difference between the arc length (the trajectory of an electron) and the chord (the trajectory of a photon). The singularity appearing in the Coulomb term at zero distance, which is equal to the zero retarded angle for circular motion, is compensated for by the renormalization of the Coulomb term via subtracting the related term for the motion of two electrons on a straight line<sup>37</sup>. The renormalized Coulomb term of the force acting on the electron at short distance

---

<sup>37</sup>Basically, the LSC forces of the straight motion are artificially excluded from this CSR formalism and can be added in the following drift element as a kick if necessary.

( $\phi \ll 1/\gamma$ ) scales as  $\frac{-2e^2\gamma^4}{r^2}$ , while the acceleration terms scale as  $\frac{2e^2\gamma^4}{3r^2}$ . Therefore, the overall radiative force is decelerative at short distances. At large retarded angle  $\phi \gg 1/\gamma$ , resulting in  $\Delta S \gg r/\gamma^3$ , the Coulomb force is negligible and the overall radiation force is accelerative. Hence, CSR radiation results in a longitudinal wakefield along the bunch, known as the CSR wake<sup>38</sup>. In the 1D approximation, the overall CSR wake is calculated for the known longitudinal distribution of the electron beam and its action on the electrons along the beam can be calculated. This model does not account for the shielding of the CSR radiation within a vacuum tube or effects on the transverse distribution of the beam. However, these effects based on the presented formalism can be accounted for in the beam tracking codes.

The 1D formalism presented in reference [45] is implemented in the `ELEGANT` beam elements `CSRBEND` and `CSRDRIFTS` [46]. `CSRBEND` is the extension of the `CSBEND` element discussed above with added CSR effects. The beam propagation in the sector magnet is divided into several regions, whose number can be specified by the user. At the end of each region, the CSR wake is calculated along the beamline and the CSR energy kicks are applied to the electron distribution. Since canonical integration through each region includes transport to all orders, the dispersive CSR effects on the dynamics in the transverse phase space in the bending plane are accounted for automatically. This routine also accounts for transient effects happen when a CSR-wake enters and exits the magnet based on the model presented in reference [47]. Since the approximation of a stationary wakefield does not hold in the short bending magnets, this is included as an additive transient force, which disappears for long bending magnets [46]. The CSR radiation can exit the dipole magnet and keep acting on the beam in the downstream elements. Such an action is accounted for by `CSRDRIFT` elements during free space propagation [38] based on the 1D CSR model [45, 47]. The CSR

---

<sup>38</sup>The CSR wake emitted by the particles in the tail of the beam acts on the particles in front of the beam, because in the relativistic regime the radiation is emitted predominantly in the cone  $1/\gamma$  along the direction of the beam propagation. By contrast, a typical wakefield in an accelerator initiated by particles in the head of the bunch acts on the particles propagating behind it.

effects within different elements are calculated in a downstream CSRDRIFT element<sup>39</sup>. The 1D model realized in ELEGANT neglects the effects of the transverse beam distribution while calculating CSR, neither does it include the variation of the CSR wake across the bunch. This 1D approximation is legitimate if the Derbenev *et al.* criteria is satisfied [44]:

$$\frac{\sigma_r}{\sigma_s} \ll \left( \frac{r}{\sigma_s} \right)^{1/3}, \quad (1.65)$$

where  $\sigma_r$  and  $\sigma_s$  are respectively transverse and longitudinal rms beam sizes. This condition can be checked directly in the CSRDRIFT routine in ELEGANT within a bending magnet by setting the related parameter “DERBENEV\_CRITERION\_MODE=evaluate.” The CSR effects accounting for the transverse and longitudinal distribution of the beam are implemented in a different beam tracking code, CSRTRACK [48], based on the formalism presented in references [49, 50]. The 3D CSR effects do not appear to be important in the scope of the work presented in this dissertation, so we skip the description of the model realized in CSRTRACK here.

Summarizing this section, beam propagation through a beamline of a linear accelerator is described via the evolution of its phase space with respect to a reference particle. The beam interaction with the electromagnetic fields of the beamline elements can be described via linear matrix formalism, while effects of the second and higher orders can be accounted for via tensors of related orders. The collective effects, which are the interactions between different particles in the beam during the propagation, such as CSR and SC, can be described by simple 1D models and can be simulated with good accuracy in beam tracking codes. CSR and LSC effects can significantly impact beam dynamics and result in the degradation of the transverse and longitudinal emittances and the overall beam phase space. These effects can

---

<sup>39</sup>If the action of the LSC effects is expected to be critical within an element, for example in a bending magnet simulated by a CSRBEND routine, the element of interest can be split into several regions and the LSCDRIFT elements can be added between those regions [38].

be critical for an electron beam to effectively drive a free electron laser and produce high quality X-ray radiation as we will discuss in the next section.

### 1.3 Working principles of a Free Electron Laser and requirements on the driving electron beam

The Linac Coherent Light Source (LCLS) at SLAC, which produced its first light in 2009, started a new era of 4th generation X-ray light sources [51]. Since then, many X-Ray FEL facilities<sup>40</sup> have been commissioned and are now in operation: Spring-8 Angstrom Compact Free-electron Laser (SACLA) at Harima, Japan in 2012 [53], European X-ray free-electron Laser (EXFEL) at DESY in Hamburg, Germany 2017 [54], and SwissFEL at Paul Scherrer Institute (PSI) in Villigen, Switzerland in 2017<sup>41</sup> [56]. Some X-ray FELs are still in the design and construction stage such as LCLS-2 at SLAC [57] and MaRIE at Los Alamos National Laboratory (LANL) [58].

Scientists at Los Alamos National Laboratory are considering a light source with extreme capabilities, such as an ultrashort wavelength of 0.02 nm, high brightness, high repetition rate, and much more as a main part of the Matter-Radiation Interactions in Extremes Facility (MaRIE) at LANL<sup>42</sup>. Such extreme capabilities for a hard X-ray light source can be realized only as a Free Electron Laser. The wavelength of the radiation in a FEL near the undulator axis<sup>43</sup> is:

$$\lambda_{x-ray} = \frac{\lambda_u}{2\gamma^2} \left( 1 + \frac{K^2}{2} + \gamma^2 \theta^2 \right) , \quad (1.66)$$

---

<sup>40</sup>Close to the X-Ray region, FLASH FEL at The Deutsches Elektronen-Synchrotron (DESY) started operation in 2005 [52] It covers the wavelength range from 4 to 90 nm among two undulators, which are driven by a single linac.

<sup>41</sup>The first pilot experiment at SwissFEL was conducted in 2017 [55], while user's operations are expected to start in the end of 2018.

<sup>42</sup>The MaRIE project was approved as Critical Decision-0 (CD-0) in 2016.

<sup>43</sup>Assuming the beam is injected in the undulator parallel to the undulator axis.

where  $K$  is the undulator parameter defined in Eq. (1.10),  $\gamma$  is the electron Lorentz factor,  $\lambda_u$  is the undulator period and  $\theta$  is the radiation emission angle with respect to the undulator axis. The shortest possible undulator period is  $\sim 1$  cm, achievable without losing the accuracy of the geometric structure and, as a result, necessary magnetic field precision over a few hundred meter long undulator. For the undulator parameter  $K \sim 1$  and on-axis observer ( $\theta = 0$ ), this suggests that a beam energy of  $\sim 10$  GeV is required to drive this FEL for generating sub-angstrom radiation. In addition, the electron beam emittance limitation for a free electron laser is<sup>44</sup> [19, 20]:

$$\epsilon_{n_x, n_y} \leq \frac{\beta \gamma \lambda_{x-ray}}{4\pi} , \quad (1.67)$$

where  $\epsilon_{n_x, n_y} = \beta \gamma \epsilon_{x, y}$  are normalized emittances and  $\beta = v/c$  is the normalized electron velocity, which is  $\sim 1$  in the highly relativistic regime. Equation (1.67) suggests emittance of  $\sim 0.03 \mu\text{m}$  for the discussed MaRIE parameters:  $\lambda \sim 0.02$  nm and  $\gamma \sim 2 \times 10^5$ . Effective lasing strongly depends on the electron beam satisfying this condition, however typically emittances a few times bigger are still acceptable in high gain FELs. For example, the anticipated beam emittance for MaRIE is  $\sim 0.3 \mu\text{m}$  meaning that this FEL will be operating in the emittance-dominated regime and 3D effects of the electron beam dynamics in an undulator have to be taken into account. Moreover, using a beam with bigger emittances results in an increased FEL gain length and, as a result, the overall undulator length. As will be discussed further in Chapter 2, the normalized emittances can only grow during beam propagation in an accelerator. Stochastic cooling [59] is the only technique known to decrease the overall phase space volume of the beam<sup>45</sup>. However, it has never been experimentally

---

<sup>44</sup>This condition is the limitation of the electron phase space area in respect to the produced radiation phase space volume, since FEL work principles rely on the proper interaction of the electron beam with produced radiation. In the Rayleigh approximation of the Gaussian laser radiation, the equivalent photon beam emittance is  $\sim \lambda/4$ .

<sup>45</sup>Here we assume the normalized phase space volume taking into account the acceleration.

realized in the linacs of any existing FELs to the best of our knowledge. Nevertheless, the ultra-cold electron beam has to be produced and injected in the linac of a FEL. State-of-the-art high brightness photo-injectors are capable of producing such beams. Their emittances are limited by transverse space charge forces and scale with bunch charge,  $q$ , as [60,61]:

$$\epsilon_{n_x, n_y} \sim 1 \mu m \cdot (q/nC)^{1/2} . \quad (1.68)$$

This results in  $\epsilon_{n_x, n_y} \sim 0.3 \mu m$  for a  $q = 100$  pC bunch. This bunch charge emphasizes the limitation on the bunch length in undulator(  $\sim 10$  fs) to reach the required high current (  $\sim 10$  kA) for FEL lasing. In addition, the longitudinal space charge forces at the injector and at the earlier stages of acceleration reinforce to produce long bunches with as small-as possible transverse emittances and energy-spread on the photo-cathode, and enhance their peak current using one or several bunch compressors once the beam becomes highly relativistic. A bunch compressor is a specific line of beam elements which compresses the beam in the longitudinal direction. As discussed earlier, the overall phase space volume cannot be decreased. Therefore, compressing the beam typically results in an enlarged beam energy spread<sup>46</sup>.

A FEL relies on proper synchronization between the electrons traveling in an undulator and the produced X-ray radiation. The average beam energy and the undulator period,  $\lambda_u$ , define the resonant wavelength of the produced radiation. Meanwhile, the energy deviation of electrons in the beam defines the bandwidth of the instantaneously produced X-ray radiation and the overall efficiency of lasing. The actual (*e.g* not normalized) beam energy spread is defined here as:

$$\sigma_\gamma = \sqrt{\langle \gamma^2 \rangle - \langle \gamma \rangle^2} , \quad (1.69)$$

---

<sup>46</sup>The beam in a typical bunch compressor is reshaped in the longitudinal phase space.

the condition for proper lasing is:

$$\sigma_\gamma \leq 0.5 \rho_{FEL} \quad , \quad (1.70)$$

where  $\rho_{FEL}$  is the FEL parameter also known as the Pierce parameter [19, 20]:

$$\rho_{FEL} = \frac{\lambda_u}{4\sqrt{3}\pi L_g} \quad , \quad (1.71)$$

where  $L_g$  is the effective gain length defined in one-dimensional FEL theory, not accounting for 3D effects. Summarizing the above, a bunch compressor (BC) is one of the key elements in any X-ray FEL. Ideally, the beam traveling through it should be compressed, while the input beam quality should be preserved, particularly in terms of the transverse and longitudinal emittances. Moreover, residual correlations between transverse and longitudinal phase spaces at the exit of a BC should be minimized (as we will discuss in Chapter 2).

The most commonly used type of a bunch compressor in a FEL linac is realized via a combination of a chicane, a chirper and a dechirper. Without going into much detail<sup>47</sup>, a chicane usually consists of four bending magnets separated by drift spaces. Such a beamline imposes a pathlength dependence on energy: it takes longer for lower energy particles to go through the chicane. Thus, if the beam at the entrance of the chicane has correlations in the longitudinal phase space, such that electrons in front of the beam have lower energy than electrons in the tail of the beam (a chirp), the chicane will compress it. Chirping the beam is usually realized via an off-crest acceleration, which unavoidably results in a lower acceleration gradient<sup>48</sup>. Therefore, it can be beneficial to realize a BC as a combination of transverse deflecting cavities, separated by drifts, as we will discuss in Chapter 3. We will

---

<sup>47</sup>See Chapter 2 for more details.

<sup>48</sup>A larger slope is required for shorter bunches, resulting in bigger off-crest phase and bigger gradient loss. See Chapter 3 for details.

also demonstrate that this scheme can be modified to remove the imposed energy slew along the beam after the chicane, which is typically also realized by an off-crest acceleration.

Typically, bunch compression in a FEL linac is realized via multiple compression modules placed at different locations along the beamline, and, as a result, at different energies of the electron beam. The multistage scheme is defined by the fact that often a high compression ratio ( $\sim 100$ ) is required, and it is almost impossible to realize as a single chicane-type bunch compressor in the approximation of realistic energy chirps. There are several factors which degrade the quality of an electron beam traveling through a bunch compressor, such as space charge effects and coherent synchrotron radiation. Moreover, these effects can amplify the current density noise always present in an electron beam. Such effects are known as longitudinal space charge induced micro-bunch instabilities, mentioned above, and CSR-induced microbunching instabilities. All of these are collective effects, by nature arising from interactions between different particles in the beam via electromagnetic forces. For a homogeneous beam of  $\sim 100$  pC bunch charge, space charge effects dominate at energies  $\leq 300$  MeV, while CSR effects are dominant at energies of  $\geq 300$  MeV. Following the outlines of existing FELs, the original plan is to have two chicane-type bunch compressors at 250 MeV and 1 GeV for the MaRIE XFEL linac to minimize SC and CSR effects and satisfy the design needs of  $\sim 600$  compression ratio. Preliminary studies have shown that a standard chicane-type bunch compressor at 1 GeV strongly distorts and dilutes the transverse phase space of the electron beam, increasing its emittances due to CSR effects. In addition, LSC-induced microbunching instabilities are another bottleneck of this BC critical for effective FEL lasing. In finding an alternative solution, we propose realizing a second bunch compressor as a double emittance exchanger (EEX)<sup>49</sup> and a telescope in Chapter 2. Previously, schemes based on a single EEX were discussed, which would switch the longitudinal and transverse phase space

---

<sup>49</sup>Principles of operation of an emittance exchanger and the physics behind it are explained in details in Chapter 2.

of the beam to reach a desired bunch size. However, the quality of the transverse phase space of the electron beam is also important for effective FEL lasing. In addition, initial transverse and longitudinal emittances are produced with very different values in a photocathode injector. Therefore, the schemes based on a single EEX did not improve the beam quality compared to the standard chicane-type bunch compressor. In the newly proposed design, the initial phase spaces are preserved in the approximation of ideal exchange, while the longitudinal bunch size is compressed by transverse optics elements in the telescope located between two EEX modules. If the emittance growth due to CSR effects in this scheme is comparable with the chicane-type counterpart, the scheme will be beneficial due to suppression of the microbunching instabilities, and thereby is an improvement over the chicane-type bunch compressor. Finally, there are almost no limitations on transverse optics, which is why such a scheme may reach high compression ratio and substitute for both compressors at once.

## 1.4 Inverse Compton scattering source working principles and requirements on driving electron beam

Inverse Compton scattering (ICS), scattering photons off relativistic electron beams, was discovered and explained in 1923 by Arthur H. Compton [62]. The lower energy limit of Compton scattering, Thompson scattering was demonstrated even before that [63]. Since then, the physics of inverse Compton scattering (ICS) has been explored in many different systems. It has practical applications in different types of devices, one of which is an ICS X-ray light source. In such a source, a relativistic electron bunch collides with a counter-propagating laser pulse. Each electron oscillates in the electromagnetic field of the laser pulse and generates backscattered radiation at the up-shifted frequency ( $\sim 4\gamma^2\omega$ , where  $\gamma$  is

the relativistic Lorentz factor for electron) relatively to the laser frequency ( $\omega$ ). From this perspective, an ICS is similar to undulator radiation in which electrons are oscillating in a periodic magnetic field. The photons produced by electrons in an ICS source have random phases and, hence, sum up incoherently with each other. The lack of a proper bunching mechanism for an ICS source results in a brightness of  $10^{20} - 10^{22}$  ph/mm<sup>2</sup>/mrad<sup>2</sup>/s/0.1% BW, which is typically ten orders of magnitude lower than the brightness of FELs, where self-bunching of electrons develops. As a result, ICS sources, based on current technology, cannot fully compete with FELs. On the other hand, ICS sources do not require such high energy electrons as FELs to produce photons of the same energy, due to the short laser wavelength ( $0.4 - 10 \mu\text{m}$ ) compared to an undulator period in FELs ( $1 - 10 \text{ cm}$ ). Hence, ICS X-ray sources do not require long accelerators such of those used for FELs. They can be very compact if driven by high-gradient accelerators, such as Plasma Wakefield accelerator (PWA) or Dielectric Wakefield accelerator [64,65]. Understanding the limitations on brightness in ICS sources is of large interest to the scientific community. The brightness of ICS sources is limited by the nonlinear frequency shift at high laser intensity and by the electron beam quality since electrons traveling at different angles with different energies produce photons with different energies. In Chapter 4 of this dissertation we focus on the fact that spectral brightness of the source depends on the 6D electron phase space distribution and the laser beam parameters. The peak brightness of the ICS source can be maximized if the electron phase space is reshaped so that all electrons scatter off X-ray photons at the same frequency in the same direction. However, the existing theoretical models of ICS are not able to quantitatively estimate this effect, since they do not account for possible correlations between the electron positions in the phase space [66,67]. In Chapter 4, we demonstrate that the parameters of ICS can be found for an arbitrary distribution of electrons using the Wigner function approach [68–72]. A similar approach has been used in previous research to describe the transverse brightness of light sources [73–78].

## 1.5 Organization structure of the dissertation

In the second chapter, we discuss an alternative scheme of bunch compression based on the double emittance exchanger (EEX) for a FEL-driving linac. The idea behind this scheme is quite simple. First, the transverse and the longitudinal phase spaces are exchanged by the first EEX. Then, the new transverse phase space is reshaped by transverse beam optics elements, such as quadrupole magnets (quads) and free space propagation elements (drifts), resulting in compression of the beam along the  $x$ -direction. Finally, the reshaped transverse and longitudinal phase spaces are exchanged back in the second EEX, delivering a longitudinally compressed beam. In comparison to a standard well-studied chicane-based BC, such a scheme does not require an additional chirper and dechirper. Specifically, we propose a novel asymmetrical double emittance exchange scheme. By optimizing this beamline, we demonstrate that the new scheme allows to suppress CSR and nonlinear effects which critically demolish performance of its symmetrical counterpart.

In the third chapter, we propose and describe a new scheme for chirping and dechirping the beam based on using transverse deflecting cavities (TDCs) separated by drifts. Such schemes mix transverse and longitudinal phase spaces for the sake of imposing/removing energy correlations along the bunch. These schemes predominantly rely on the transverse beam size in the middle cavity, in comparison to off-crest acceleration for imposing and removing energy slew along the bunch, which both depend efficiency-wise on the longitudinal bunch size within the accelerating cavity. Since the transverse beam size is much more flexible and can be changed using a diverse pool of transverse optics elements in comparison to the longitudinal size, typically fixed in linacs, such schemes are more cost and energy effective. We discuss potential applications of these schemes for compressing the beam as parts of the chicane-based bunch compressors in FEL linacs.

In the fourth chapter, we propose and develop the novel 6-dimensional theory of an ICS source based on the Wigner function approach. Initially, this theory was motivated by an idea to maximize brightness of an ICS source by reshaping the electron beam in phase space, while existing theoretical models were not capable of predicting the impact of arbitrary correlations in the electron phase space. Since the analytical dependence of the photon phase space of the produced radiation from the electron beam phase space can be analytically derived, this theory opens up the possibility for non-invasive diagnostics of the 6D phase space of the electron beam via the diagnostics of the produced radiation during beam propagation in an undulator or during the inverse Compton scattering process.

## CHAPTER 2

# DOUBLE EMITTANCE EXCHANGER AS A BUNCH COMPRESSOR

In this chapter, we discuss an advanced scheme of a bunch compressor (BC), based on the double emittance exchange. As it was discussed in Sec. 1.3, modern FELs requires high current and low emittance beam to reach high peak brightness of the X-ray photons. While state-of-the-art photocathodes are able to produce cold (low emittance) beam, its bunch charge is limited by the space charge forces, especially dominating at low beam energies. Therefore, accelerators driving FELs typically have several bunch compressors to reach the required high current. The longitudinal beam size is shortened multiple times ( $\times 10 - 20$ ) in each BC, which usually leads to the increased energy spread<sup>1</sup>.

This chapter is organized as follows. First, we discuss a standard chicane-based bunch compressor scheme. It relies on passing a beam with imposed energy slew (or chirped beam) through the dispersive beam line, chicane. Typically beam is chirped, while being priorly accelerated off-crest. There are some alternative schemes, as it will be discussed in Chapter 3. Nevertheless, removing of the imposed correlated energy spread is required at the exit of the chicane before the beam enters an undulator section. The latest can be realized by a long free space propagation or by applying a dechirper (see Chapter 3 for more details). Second in this chapter, we introduce an alternative scheme of a bunch compressor, which does not rely on a beam being chirped<sup>2</sup>. It is based on using two emittance exchange modules separated

---

<sup>1</sup>Linear beam dynamics has several invariants of motion as discussed in Sec. 2.2. It results in that the 6-dimensional beam phase space in a bunch compressor cannot be cooled overall, but only reshaped. Compressing beam along one coordinate in the phase space typically leads to expanding it along another canonically conjugated coordinate.

<sup>2</sup>In principal, it can also effectively work for beams with non-zero correlated energy spread.

by a transverse “telescope”. For this scheme, we present numerical studies of the beam dynamics, including the nonlinear and CSR effects. We then demonstrate how these effects can be minimized by simultaneously tuning the beam optics and beam line parameters. Finally in this chapter, we discuss an alternative EEX beamline with a reduced number of bending magnets (two instead of four), and demonstrate that the overall CSR dynamics in a bunch compressor does not necessary scale with a number of the CSR-imposing elements.

## 2.1 Working principle of a chicane-based bunch compressor

A typical bunch compressor is realized via a chicane with four bending magnets or C-chicane (Fig. 2.1 (a)) resulting in the non-zero  $R_{56}$  element. Its matrix in 6D  $(x, x', y, y', z, z')$  phase space is<sup>3</sup>:

$$R_{chicane} = \begin{pmatrix} 1 & L_x & 0 & 0 & 0 & 0 \\ 0 & 1 & 0 & 0 & 0 & 0 \\ 0 & 0 & R_{33} & R_{34} & 0 & 0 \\ 0 & 0 & R_{43} & R_{44} & 0 & 0 \\ 0 & 0 & 0 & 0 & 1 & R_{56} \\ 0 & 0 & 0 & 0 & 0 & 1 \end{pmatrix} . \quad (2.1)$$

This matrix can be found as a matrix product of its structural components: two doglegs shifting up and down<sup>4</sup> separated by a free space propagation section:

$$R_{chicane} = R_{dogleg}(\eta) R_{Drift}(L_2) R_{dogleg}(-\eta) . \quad (2.2)$$

---

<sup>3</sup>In this chapter,  $z$  and  $z'$  are referred to the canonical coordinates:  $s - ct$  and  $\delta\gamma/\gamma$ , respectively as introduced in Sec. 1.2.

<sup>4</sup>The bending plane  $(x, z)$  is referred as the vertical plane here.

A dogleg beamline is represented by the following transfer matrix [16]:

$$R_{dogleg}(\eta) = \begin{pmatrix} 1 & L_{eff} & 0 & 0 & 0 & \eta \\ 0 & 1 & 0 & 0 & 0 & 0 \\ 0 & 0 & R'_{33} & R'_{34} & 0 & 0 \\ 0 & 0 & R'_{43} & R'_{44} & 0 & 0 \\ 0 & \eta & 0 & 0 & 1 & \psi \\ 0 & 0 & 0 & 0 & 0 & 1 \end{pmatrix}, \quad (2.3)$$

where  $\eta$  is the dispersion. The matrix of a free space propagation (drift) of a length  $L$  for the highly relativistic beam ( $\gamma \gg 1$ ) is:

$$R_{Drift}(L) = \begin{pmatrix} 1 & L & 0 & 0 & 0 & 0 \\ 0 & 1 & 0 & 0 & 0 & 0 \\ 0 & 0 & 1 & L & 0 & 0 \\ 0 & 0 & 0 & 1 & 0 & 0 \\ 0 & 0 & 0 & 0 & 1 & 0 \\ 0 & 0 & 0 & 0 & 0 & 1 \end{pmatrix}. \quad (2.4)$$

A dogleg is a sequence of two identical but oppositely oriented bending magnets separated by drift. This beamline shifts the beam in the bending plane and imposes transverse-longitudinal correlations. Each bending magnet can be represented by the transfer matrix

under the assumption that the beam trajectory is orthogonal to the edge surfaces of the magnet [16]:

$$R_{bend}(r, \theta) = \begin{pmatrix} \cos \theta & r \sin \theta & 0 & 0 & 0 & r(1 - \cos \theta) \\ r^{-1} \sin \theta & \cos \theta & 0 & 0 & 0 & \sin \theta \\ 0 & 0 & 1 & r\theta & 0 & 0 \\ 0 & 0 & 0 & 1 & 0 & 0 \\ -\sin \theta & -r(1 - \cos \theta) & 0 & 0 & 1 & r(\sin \theta - \theta) \\ 0 & 0 & 0 & 0 & 0 & 1 \end{pmatrix}, \quad (2.5)$$

where  $\theta$  is the bending angle and  $r$  is the bending radius, and  $D = r\theta$  is the length of the bending magnet along the beam path. For instance,  $\theta < 0$  and  $r < 0$  for bending a trajectory up and vice versa. Focusing or defocussing effects by the edge of the magnet appear, if the beam arrives to/leaves the bending magnet under an angle  $\alpha$  relatively to the normal vector to the edge surface. This can be described by the following transfer matrix [16]:

$$R_{edge}(r, \alpha) = \begin{pmatrix} 1 & 0 & 0 & 0 & 0 & 0 \\ r^{-1} \tan \alpha & 1 & 0 & 0 & 0 & 0 \\ 0 & 0 & 1 & 0 & 0 & 0 \\ 0 & 0 & -r^{-1} \tan \alpha & 1 & 0 & 0 \\ 0 & 0 & 0 & 0 & 1 & 0 \\ 0 & 0 & 0 & 0 & 0 & 1 \end{pmatrix}. \quad (2.6)$$

The total transfer matrix of a bending magnet with equal edge angles  $\alpha$  can be found as:

$$R_{bend'}(r, \theta, \alpha) = R_{edge}(r, \alpha) R_{bend}(r, \theta) R_{edge}(r, \alpha) \quad . \quad (2.7)$$

If  $\alpha = \theta/2$  for each bending magnet<sup>5</sup>, the combination of two bending magnets accounting for the edge focusing effects separated by the drift  $L_1$  results in the transfer matrix of a dogleg shifting the trajectory up as presented in equation (2.3):

$$R_{dogleg}(r, \theta, L_1) = R_{bend'}(r, \theta, \frac{\theta}{2}) R_{Drift}(L_1) R_{bend'}(-r, -\theta, -\frac{\theta}{2}) \quad , \quad (2.8)$$

Parameters of the dogleg can be found as follows. The dogleg dispersion is:

$$\eta = -2(L_1 + r \sin \theta) \tan \left( \frac{\theta}{2} \right) \quad , \quad (2.9)$$

and its  $R_{56}$  matrix element is equal to the expression below:

$$\psi = -2r(\theta + \sin \theta) + 8r \tan \left( \frac{\theta}{2} \right) + 4L_1 \tan^2 \left( \frac{\theta}{2} \right) \quad . \quad (2.10)$$

The effective length for the vertical dynamics happening in the bending plane is:

$$L_{eff} = L_1 + 2r \sin \theta \quad , \quad (2.11)$$

and the horizontal dynamics elements in Equation (2.3) can be found as<sup>6</sup>:

$$R'_{33} = R'_{44} = 1 - \tan \frac{\theta}{2} \left( \theta \tan \frac{\theta}{2} - 2 \right) \left( \frac{L_1}{r} \left( \theta \tan \frac{\theta}{2} - 1 \right) - 2\theta \right) \quad , \quad (2.12)$$

$$R'_{34} = \left( \theta \tan \frac{\theta}{2} - 1 \right) \left( L_1 \left( \theta \tan \frac{\theta}{2} - 1 \right) - 2r\theta \right) \quad , \quad (2.13)$$

$$R'_{43} = \frac{R'^2_{33} - 1}{R'_{34}} \quad , \quad (2.14)$$

---

<sup>5</sup>Such a configuration is often referred as a sector magnet.

<sup>6</sup>The only difference between matrices of dogleg up and dogleg down is in the sign of the dispersion  $\pm\eta$ , while all other matrix elements are the same.

Finally, parameters of the chicane can be written down based on the presented formalism.

The chicane strength is equal to:

$$R_{56} = 2\psi \quad , \quad (2.15)$$

and the effective chicane length in the vertical plane ( $x, x'$ ) is:

$$L_x = 2L_{eff} + L_2 \quad , \quad (2.16)$$

where  $L_2$  is the free space propagation length in between of two doglegs. The matrix elements describing ( $y, y'$ ) dynamics can be found from their dogleg counterparts as following:

$$R_{33} = R_{44} = R_{33}'^2 + L_2 R_{33}' R_{43}' + R_{34}' R_{43}' \quad , \quad (2.17)$$

$$R_{34} = R_{33}' (L_2 R_{33}' + 2R_{34}') \quad , \quad (2.18)$$

$$R_{43} = \frac{R_{33}'^2 - 1}{R_{34}'} \quad . \quad (2.19)$$

The linear beam dynamics within the elements of a chicane is coupled in 4-dimensional ( $x, x', z, z'$ ) phase space, while the transverse dynamics along ( $y, y'$ ) phase space is uncoupled. The chicane acts on the longitudinal coordinate of a particle in the bunch as:

$$z_f = z_i + R_{56} \cdot z_i' \quad , \quad (2.20)$$

which literally means that particles with smaller energy than the reference particle will travel through the chicane longer and vice versa. According to the equations (1.42,1.43) for an ensemble of particles, we find:

$$\sigma_{z_f}^2 = \sigma_{z_i}^2 + R_{56}^2 \langle z'^2 \rangle_i + 2R_{56} \langle z z' \rangle_i \quad . \quad (2.21)$$

Since  $R_{56}^2 > 0$ , the equation (2.21) results that a bunch has to have a nonzero correlated energy spread ( $R_{56}\langle zz'\rangle_i < 0$ ) to be compressed in the chicane. Next, by using equation (1.13) for the longitudinal emittance, we find:

$$\sigma_{z_f}^2 = \sigma_{z_i}^2 + R_{56}^2 \frac{\epsilon_z^2}{\sigma_{z_i}^2} + R_{56}^2 \frac{\langle zz'\rangle_i^2}{\sigma_{z_i}^2} + 2R_{56}\langle zz'\rangle_i \quad . \quad (2.22)$$

Analyzing the expression on the right-hand part of equation (2.22), we find that the minimum bunch length is reached when:

$$\langle zz'\rangle_i = -\sigma_{z_i}^2 / R_{56} \quad (2.23)$$

and equal to:

$$\min(\sigma_{z_f}^2) = R_{56}^2 \frac{\epsilon_z^2}{\sigma_{z_i}^2} = -\frac{R_{56}}{\langle zz'\rangle_i} \epsilon_z^2 = \frac{\sigma_{z_i}^2}{\langle zz'\rangle_i^2} \epsilon_z^2 \quad , \quad (2.24)$$

where we assumed that the longitudinal emittance remains constant once one imposed a correlated energy spread on the beam. Hence, we find the maximum compression ratio:

$$m_{max} = \max\left(\frac{\sigma_{z_i}}{\sigma_{z_f}}\right) = \frac{|\langle zz'\rangle_i|}{\epsilon_z} \quad , \quad (2.25)$$

which justifies that one needs to maximize the uncorrelated energy spread to maximize the compression. In addition, the equation (2.25) suggests that it is easier to compress beams with smaller longitudinal emittance than beams with larger emittance in a chicane-based

BC. The correlated energy spread before the chicane can be imposed via an element (or a beamline) known as a chirper<sup>7</sup>:

$$R_{chirp} = \begin{pmatrix} 1 & L_c & 0 & 0 & 0 & 0 \\ 0 & 1 & 0 & 0 & 0 & 0 \\ 0 & 0 & 1 & L_c & 0 & 0 \\ 0 & 0 & 0 & 1 & 0 & 0 \\ 0 & 0 & 0 & 0 & 1 & 0 \\ 0 & 0 & 0 & 0 & R_{65} & 1 \end{pmatrix}, \quad (2.26)$$

where  $R_{65} < 0$ . The chirper does not affect the longitudinal beam size  $\sigma_{z_1} = \sigma_{z_0}$ , while the correlated energy spread on its exit is<sup>8</sup>:

$$\langle zz' \rangle_1 = R_{65} \cdot \sigma_{z_0}^2, \quad (2.27)$$

and the uncorrelated energy spread is respectively:

$$\langle z'^2 \rangle_1 = \langle z'^2 \rangle_0 + R_{65}^2 \cdot \sigma_{z_0}^2. \quad (2.28)$$

The longitudinal beam size after the chicane becomes:

$$\sigma_{z_2}^2 = (1 + R_{56}R_{65})^2 \sigma_{z_0}^2 + R_{56}^2 \langle z'^2 \rangle_0 \quad (2.29)$$

---

<sup>7</sup>In the following matrix the effective vertical and horizontal lengths are chosen to be identical for simplicity but can vary for the chirper  $L_c$  and the dechirper  $L_d$ . This condition is redundant.

<sup>8</sup>The coordinates of the beam on the entrance of the chirper are referred with index 0, at the exit of it as 1, and etc.

and the correlated energy spread can be found as following:

$$\langle zz' \rangle_2 = R_{65}(1 + R_{56}R_{65})\sigma_{z_0}^2 + R_{56}\langle z'^2 \rangle_0, \quad (2.30)$$

while the energy spread remains unchanged  $\langle z'^2 \rangle_2 = \langle z'^2 \rangle_1$ . One needs to complete the scheme with a dechirper in order to remove the correlated energy spread  $\langle zz' \rangle_2$  after the chicane. The dechirper is described by the matrix in equation (2.26) with  $R'_{65} > 0$  and  $R_{12} = R_{34} = L_d$ . Up to now matrix elements  $R_{56}$  of the chicane and  $R_{65}$  of the chirper could have been independent of the beam parameters unless ones aims to maximize the compression ratio according to equation (2.23). However, the longitudinal beam size got changed (as intended) due to the action of the chicane, hence  $R'_{65}$  of the dechirper depends not only on the parameters of the chirper  $R_{65}$  and the chicane  $R_{56}$ , but also on the initial beam parameters:

$$R'_{65} = -\frac{\langle zz' \rangle_2}{\sigma_{z_2}^2} = -\frac{R_{65}(1 + R_{56}R_{65})\sigma_{z_0}^2 + R_{56}\langle z'^2 \rangle_0}{(1 + R_{56}R_{65})^2\sigma_{z_0}^2 + R_{56}^2\langle z'^2 \rangle_0}. \quad (2.31)$$

Therefore, the final matrix of the chicane-based bunch compressor is specific for each set of the longitudinal beam parameters and can be found as:

$$R_{BC} = \begin{pmatrix} 1 & L_{BC_x} & 0 & 0 & 0 & 0 \\ 0 & 1 & 0 & 0 & 0 & 0 \\ 0 & 0 & R''_{33} & R''_{34} & 0 & 0 \\ 0 & 0 & R_{43} & R''_{44} & 0 & 0 \\ 0 & 0 & 0 & 0 & 1 + R_{56}R_{65} & R_{56} \\ 0 & 0 & 0 & 0 & \frac{R_{56}\langle z'^2 \rangle_0}{(1+R_{56}R_{65})^2\sigma_{z_0}^2 + R_{56}^2\langle z'^2 \rangle_0} & \frac{(1+R_{56}R_{65})\sigma_{z_0}^2}{(1+R_{56}R_{65})^2\sigma_{z_0}^2 + R_{56}^2\langle z'^2 \rangle_0} \end{pmatrix}, \quad (2.32)$$

where  $L_{BC_x} = L_c + L_x + L_d$ , and the elements describing the transverse dynamics in  $(y, y')$  phase space are  $R''_{33} = R_{33} + L_d R_{43}$ ,  $R''_{44} = R_{33} + L_c R_{43}$  and  $R''_{34} = (L_c + L_d)R_{33} + R_{34} + L_c L_d R_{43}$ . The impact of the chicane ( $R_{56} > 0$ ) on the longitudinal dynamics is equivalent to the impact of the free space propagation ( $R_{12} > 0$ ) on the transverse dynamics. Therefore, the chicane has to be accompanied by at least two other elements, a chirper ( $R_{65} < 0$ ) and a dechirper ( $R_{65} > 0$ ), to complete a bunch compressor for a beam with given longitudinal parameters. The chirper and dechirper are longitudinal analogs of focusing and defocussing transverse elements, respectively. Therefore, the resulting chicane-based beam line compresses the beam in the longitudinal phase space, similar to how a two-quad telescope compresses the beam in the transverse phase space  $(x, x')$ :

$$R_{T_{xx'}} = \begin{pmatrix} 1 & 0 \\ 1/f_2 & 1 \end{pmatrix} \cdot \begin{pmatrix} 1 & d_1 \\ 0 & 1 \end{pmatrix} \cdot \begin{pmatrix} 1 & 0 \\ 1/f_1 & 1 \end{pmatrix} = \begin{pmatrix} 1 + \frac{d_1}{f_1} & d_1 \\ \frac{d_1 + f_1 + f_2}{f_1 f_2} & 1 + \frac{d_1}{f_2} \end{pmatrix} . \quad (2.33)$$

One needs at least two drifts and two quads to combine a transverse telescope for an arbitrary beam:

$$R_{\tilde{T}_{xx'}} = \begin{pmatrix} 1 & d_2 \\ 0 & 1 \end{pmatrix} \cdot \begin{pmatrix} 1 & 0 \\ 1/f_2 & 1 \end{pmatrix} \cdot \begin{pmatrix} 1 & d_1 \\ 0 & 1 \end{pmatrix} \cdot \begin{pmatrix} 1 & 0 \\ 1/f_1 & 1 \end{pmatrix} = \begin{pmatrix} -\frac{d_2}{d_1} & 0 \\ 0 & -\frac{d_1}{d_2} \end{pmatrix} , \quad (2.34)$$

where the requested conditions on focal distances are  $f_1 = d_1 d_2 / (d_1 + d_2) - d_1$  and  $f_2 = -f_1 - d_1$ . Similarly, one needs at least two chicanes, a chirper and a dechirper to make a universal beam-independent bunch compressor  $R_{66} = R_{55}^{-1} = m > 1$ , where  $m$  is the compression factor<sup>9</sup>.

The standard approach to impose/remove the correlated energy spread is realized via an off-crest acceleration. Briefly, this method leads to the reduced acceleration gradient in

---

<sup>9</sup>Such schemes are not widely used in FEL driven linacs. The universality of a BC for an arbitrary beam is sacrificed towards the simplicity of the scheme.

comparison to the on-crest acceleration. This loss is discussed in details and quantified in Chapter 3. A novel scheme for chirping/dechirping the bunch based on transverse deflecting cavities is also introduced in Chapter 3. Meanwhile, there are several modifications of a standard chicane, for example, an S-chicane combined from six bending magnets (Fig. 2.1 (b)), where two pairs of magnets are located on the opposite sides of the  $x$ -axis [79]. The more advanced scheme of a chicane-based BC relies on a double-chicane, requiring eight bending magnets (Fig. 2.1 (c))<sup>10</sup>. This is considered as a primary compressing scheme for the MaRIE XFEL beamline [80]. It is combined from two oppositely oriented chicanes<sup>11</sup> to compensate a time-dependent dispersion from the CSR wakefield and, as a result, to minimize the transverse emittance degradation caused by it.

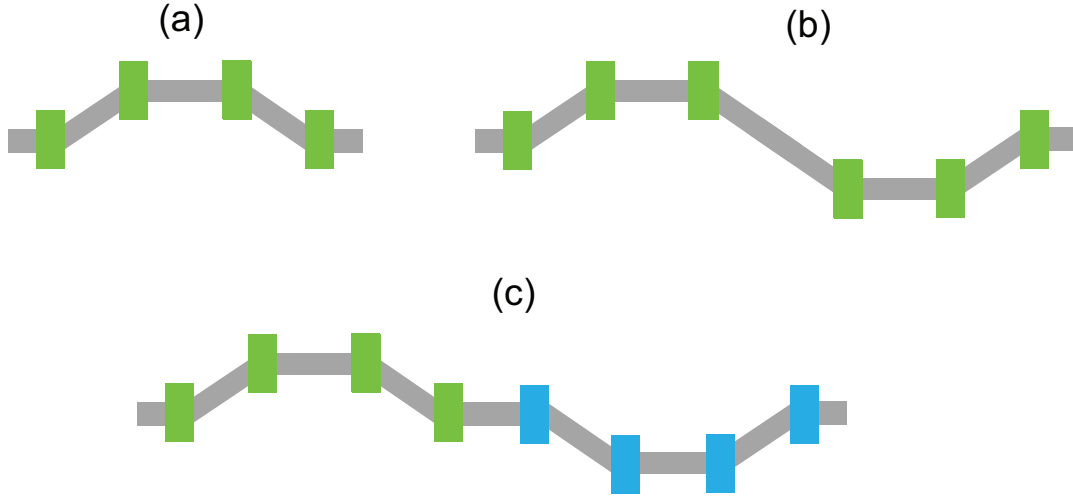


Figure 2.1: Schemes of the C-chicane (a), S-chicane (b), and double-chicane (c) consisting of four, six and eight bending magnets, respectively. Green and blue rectangles represent different dipole magnets.

<sup>10</sup>Different colors of dipole magnets represent that each chicane can have different bending magnets resulting in the different  $R_{56}$  matrix elements.

<sup>11</sup>In general, chicanes are not identical and each of them can have different bending magnets and drifts.

At high electron-beam energies, all chicane-based BCs suffer from CSR effects in bends and following them elements. As we promptly discussed in Section 1.2, particles in front of a bunch interacts with a CSR wake emitted by the tail of the bunch while the beam moves on the curved trajectory. This results in the transverse emittance enlargement [42, 44, 45, 81]. Another factor limiting beam quality is the microbunching instabilities caused by collective effects of the multi-particle dynamics: predominantly by the longitudinal space charge (LSC) forces [82, 83] and less by the CSR effects [84]. Current and energy modulations on the noise level are always present in the electron beam. Saldin *et al.* predicted that a noise in the longitudinal direction will be amplified by the LSC space charge forces in the chicane-based BC comparing this effect with a working principles of a klystron amplifier [41]. Following the formalism of this paper, we assume that the beam upstream of the bunch compressor has a current modulation:

$$I_1(z) = I_0(1 + \rho_0 \cos(kz)) \quad , \quad (2.35)$$

where  $k = \omega/c$ ,  $\rho_0$  and  $\omega$  is respectively the modulation density and frequency. While the bunch passes through the long drift or/and accelerator section, LSC forces amplify this noise resulting in the strong energy modulations along the beam:

$$\Delta\gamma(z) = \Delta\gamma_m \cos(kz) \quad , \quad (2.36)$$

and its amplitude can be found as:

$$\Delta\gamma_m = \frac{|Z(k)|}{Z_0} \frac{I_0}{I_A} \rho_i \quad , \quad (2.37)$$

where  $I_A = 17$  kA is the Alfven current,  $Z_0 = 377 \Omega$  is the vacuum impedance, and  $Z(k)$  is the longitudinal impedance characterizing the action of longitudinal wakefields<sup>12</sup>. Due

---

<sup>12</sup>For example, equation (1.62) describes  $Z(k)$  for the beam with a parabolic longitudinal profile.

to a non-zero  $R_{56}$  matrix element in a chicane, these energy modulations results in the modulations of the current at the exit of the chicane. This current in the approximation of the initial DC current beam ( $\sigma_z \rightarrow \infty$ ) with the Gaussian energy spread and linear energy chirp along the bunch  $\langle zz' \rangle / \sigma_z^2$  can be found as [41]:

$$I_2(z) = CI_0 \left( 1 + 2 \sum_{n=1}^{\infty} J_n \left( nCkR_{56} \frac{\Delta\gamma_m}{\gamma_0} \right) e^{-\frac{n^2 C^2 k^2 R_{56}^2 \langle z'^2 \rangle}{2}} \cos(nCkz) \right) , \quad (2.38)$$

where  $C = (1 + \langle zz' \rangle R_{56} / \sigma_z^2)^{-1}$  is the compression factor. For  $nCkR_{56} \frac{\Delta\gamma_m}{\gamma_0} \ll 1$ , by keeping only the linear harmonic term one can find<sup>13</sup>:

$$I_2(z) = CI_0 + CI_0 \cos(Ckz) \cdot CkR_{56} \frac{\Delta\gamma_m}{\gamma_0} e^{-\frac{C^2 k^2 R_{56}^2 \langle z'^2 \rangle}{2}} = CI_0 (1 + \rho_{ind} \cos(Ckz)) , \quad (2.39)$$

where  $\rho_{ind}$  is the induced density modulation in the chicane<sup>14</sup>. Analyzing the second term on the right-hand part of equation (2.39), we find that if  $\langle z'^2 \rangle \gg \Delta\gamma_m / \gamma_0$  the harmonic component becomes negligible, otherwise chicane can significantly amplify initial density and energy modulations along the bunch at the exit of the BC. This would eventually lead to the possible loss of FEL performance [85–88].

There are several methods to suppress the microbunching instabilities in the chicane-based bunch compressors. For example, the uncorrelated energy spread can be increased in a superconducting wiggler, where the ICS radiation is induced [86]. Heating the electron beam with a laser in an undulator before the chicane is another well-developed technique aiming to increase the uncorrelated energy spread within the FEL tolerance (see equation (1.70)). The laser heater induces rapid energy modulations on the optical frequency which wash out the short wave modulation in the chicane. Both techniques result in that the exponent in equation (2.39) suppresses the growing harmonic current proportional to  $\Delta\gamma_m$

<sup>13</sup>We also used the linearization of the Bessel function  $J_1(x) \approx x/2$  at  $x \ll 1$ .

<sup>14</sup>The ratio between the induced  $\rho_{ind}$  and initial  $\rho_i$  density modulations is referred as the instabilities gain.

at large uncorrelated energy spread  $\sqrt{\langle z'^2 \rangle}$  [85, 86]. The alternative approaches are based on transverse-longitudinal mixing realized via adding transverse deflecting cavities [87] and bending magnets [88] to the chicane. Applying additional elements to the chicane to initiate transverse mixing intuitively suggests to search for an alternative compression scheme, which would mix density and energy modulations ideally overall 6-dimensional phase space. This can potentially results in suppressed microbunch instabilities. Yet such a scheme must match the best chicane-based BC in an aspect of the emittance growth due to nonlinear single particle dynamics and CSR effects.

Among all chicane-based BCs, the double chicane [89] scheme (Fig. 2.1 (c)) shows the best simulation results in an aspect of preserving transverse beam quality and transverse emittances required for MaRIE XFEL while accounting for nonlinear and CSR effects. As expected, a laser heater (or an alternative method) is required to suppress LSC induced micro-bunch instabilities. In addition, chicane-based schemes rely on a beam being chirped at the entrance of the compressor. In Chapter 3, dedicated to chirping/dechirping schemes, we will demonstrate that the off-crest acceleration, a standard technique used to impose a correlated energy spread on the beam, results in losing the significant portion of the accelerating gradient in comparison to the on-crest acceleration, and hence the length of the accelerator section should be increased, while the significant portion of the RF power is wasted. Finally, a significant space downstream of the chicane is required to dechirp the beam, where the electron beam brightness might be further reduced due to additional nonlinear and collective effects. Arguments presented above eventually resulted in that an alternative BC scheme without using a chicane was proposed for the MaRIE XFEL. It was initially based on using a single emittance exchange (EEX) beamline [90]. The transverse and longitudinal phase spaces are exchanged at the end of the ideal EEX beamline resulting in the absence of correlations between  $(x, x')$ ,  $(y, y')$  and  $(z, z')$  phase-spaces. However, during the exchange itself these phase-spaces can be highly coupled. It results in that emittances

can grow up to several orders even without nonlinear or/and collective effects. Other words, emittances become an ineffective measure to quantify the real dynamics effects within such a beamline. Therefore, we introduce eigen emittances, the invariants of the linear dynamics, in the next section.

## 2.2 Eigen emittance formalism

As we discussed in Section 1.2 the beam distribution in linear accelerators is characterized by the matrix of the second order momentums,  $\Sigma$ -matrix (see equation (1.42)). The elements on the main diagonal represent transverse  $\langle x^2 \rangle = \sigma_x^2$ ,  $\langle y^2 \rangle = \sigma_y^2$  and longitudinal  $\langle z^2 \rangle = \sigma_z^2$  bunch sizes, beam divergences  $\langle x'^2 \rangle = \sigma_x'^2$ ,  $\langle y'^2 \rangle = \sigma_y'^2$  and the normalized energy spread  $\langle z'^2 \rangle = \sigma_z'^2$ . The elements off the main diagonal describe linear correlations between different coordinates of the 6D phase space. Transverse and longitudinal emittances introduced in equations (1.11-1.13) are proper characteristics of the beam only if the motion between the corresponding degrees of freedom is decoupled, meaning that the  $\Sigma$ -matrix remains block diagonal through a beamline<sup>15</sup>. In general, emittances in chosen coordinates are not always conserved. Perhaps, they will change during the acceleration. For example, transverse momentums are invariant  $p_x = p_{x0}$ ,  $p_y = p_{y0}$ , but the absolute momentum changes  $p(t) = \gamma\beta mc = -eEt + p(0)$  in a constant electric field  $\mathbf{E} = -E\hat{\mathbf{z}}$ . The last equation is also valid for the average beam momentum  $p_0(t)$ . This results in that the divergences  $x' \approx p_x/p_0$  and  $y' \approx p_y/p_0$  are decreased proportionally to  $(\gamma\beta)^{-1}$  when the electron beam is accelerated in the longitudinal direction. Since transverse coordinates  $x$  and  $y$  remain unchanged, transverse emittances are reduced proportionally to the factor  $\sim (\gamma\beta)^{-1}$ . Another important quantities, canonical emittances, can be defined in any canonical coordinates of the Hamiltonian motion.

---

<sup>15</sup>If the motion is coupled within a beamline, but uncoupled at the entrance and at the exit of the beamline, emittances associated to each degree of freedom still can be used.

For example for the spatial and momentum canonical coordinates  $(\mathbf{r}, \mathbf{p}) = (x, p_x, y, p_y, z, p_z)$  defined relatively to the reference particle, one can find:

$$\epsilon_i = \frac{1}{mc} \sqrt{\langle r_i^2 \rangle \langle p_i^2 \rangle - \langle x_i p_i \rangle^2} \quad , \quad (2.40)$$

where  $i = x, y, z$ . Transverse canonical emittances are invariant under the linear acceleration as it is clear from the discussion above. The longitudinal emittance also remains unchanged. Indeed, the longitudinal momentum of a particle of interest changes on the same quantity as the reference particle counterpart. If the particle deviations of the design trajectory are small, the transverse slopes  $x'$  and  $y'$  are convenient momentum coordinates of the beam and one can introduce normalized emittance, which for  $(x, x')$  phase space can be found as:

$$\epsilon_{n_x} = \gamma\beta \sqrt{\langle x^2 \rangle \langle x'^2 \rangle - \langle x x' \rangle^2} = \gamma\beta \epsilon_x \quad , \quad (2.41)$$

where the averaged momentum of the beam  $p_0$  is factored out from equation (2.40) resulting in the factor  $\gamma\beta$  before the square root. Similarly one can find  $\epsilon_{n_y} = \gamma\beta \epsilon_y$  and  $\epsilon_{n_z} = \gamma\beta \epsilon_z$ . Normalized emittances are invariants of motion in the paraxial approximation<sup>16</sup> since the phases-space coordinates  $(x, x', y, y', z, z')$  then become canonical [16]. In this dissertation, we predominantly discuss the phase space manipulations not involving acceleration of the overall beam. However, the normalized emittances are still handy to use since we discuss inserting the beamlines of interest at several locations along the linac beamline resulting in the different beam energies.

An advanced analysis is needed for the phase space manipulations where the motion between different degrees of freedom is coupled, since neither regular nor normalized emittances are conserved. For instance, this is necessary to optimize a complicated beamline such as an EEX, where transverse and longitudinal phase spaces are coupled resulting in

---

<sup>16</sup>Literally, when the transverse slopes are small.

the multiple correlations in the  $\Sigma$ -matrix elements off the diagonal blocks in the process of exchange. The electron beam matrix is block diagonal at the entrance and at the exit of the beamline in the case of the ideal exchange in the approximation of the linear single-particle dynamics. However, the nonlinear and CSR effects may result in undesirable correlations in  $\Sigma$ -matrix off the diagonal blocks even after the “exact” exchange is completed. Therefore, a special technique is needed to describe beam propagation through the advanced schemes often relying on the transverse-longitudinal mixing<sup>17</sup>. The Hamiltonian motion of a beam has three conserved moments, which can be chosen as the quantities known as the eigen emittances  $\lambda_j$ , introduced by A. Dragt [91,92]:

$$\det(J\Sigma - i\lambda_j I) = 0, \quad (2.42)$$

where  $J$  is the unit block-diagonal antisymmetric symplectic matrix introduced in equation (1.33) and  $I$  is an identity matrix introduced in equation (1.34).

Eigen emittances are practically set at the beam source, a photo-cathode injector, an electron gun, etc. In the case of uncoupled motion each eigen-emittance corresponds to a physical emittance along one plane. The eigen emittances are invariant even as the beam propagates in coupled lattice, where physical emittances change. Typically regular emittances get enlarged in the case of the coupled single particle dynamics relatively to the corresponding eigen emittances. The majority of the FEL/ICS theories rely on the approximation of the uncoupled beam<sup>18</sup> and characterize the radiation properties relatively to the regular emittances. In the frame of these conventional models the remaining correlations between different planes will most likely enlarge the regular emittances and provide with radiation of worse quality.

---

<sup>17</sup>In principal, this technique is useful for any beamline where beam dynamics is coupled between two or more phase spaces. For example, beam dynamics is also coupled in each bending magnet of a chicane.

<sup>18</sup>There are some exceptions, for example the model of an ICS source which will be discussed in Chapter 4.

The concept of eigen-emittance provides a convenient tool for designing a coupled beamline capable of swapping emittances such as the EEX beamline investigated in this chapter. It can especially be used to explore the impact of non-ideal and collective effects on the phase-space degradation and emittance swapping. In the case of an EEX design, first, eigen emittances have to be compared with real emittances under the assumption of linear and single-particle beam dynamics, in order to ensure the design is correct. Then, the same procedure is repeated taking into account nonlinear and collective effects to check whether emittances are still matching with eigen emittances. If both grow, then the optimization of the input Twiss parameters might be useful in order to find an optimal profile along the beamline. Such a profile would result in that the nonlinear effects in different elements along the beamline can compensate each other<sup>19</sup> (see Sec. 2.6.1). High order elements, such as sextupoles, octupoles, etc., might be also needed to additionally correct the nonlinear dynamics along the beamline<sup>20</sup>. However, if eigen emittances remain the same but normalized emittances grow, then nonlinear or/and collective effects somehow breach the ideal exchange configuration in the first order resulting in the residual linear correlations at the exit of the scheme which are present in the  $\Sigma$ -matrix elements off the diagonal blocks. In this case, it might be possible to fix the issue by slightly adjusting parameters of the beam elements already present in the scheme or by inserting additional linear elements (quads, bends, drifts, etc.) in order to remove these residual correlations. Summarizing this section, we emphasize that eigen emittances make understanding of a “magical” EEX straightforward: beam optics of an ideal exchange flips the projection directions of eigen emittances, invariants of a linear beam dynamics, to emittances.

---

<sup>19</sup>Another bright example validating this statement for the different beamline relying on the transverse-longitudinal mixing is discussed in Sec. 3.5.1.

<sup>20</sup>This approach did not bring any significant improvement for the EEX beamline because the emittance degradation was predominantly defined by the CSR effects, in contrast as discussed in Sec. 3.5.4 the approach is very efficient for the beamlines where nonlinear effects are dominating factor enlarging emittances.

### 2.3 Double EEX bunch compressor: design

The first emittance exchange (EEX) scheme was proposed in 2002 [93]. It was realized as a chicane with inserted transverse deflecting cavity between its doglegs. Although such a scheme highly couples transverse and longitudinal phase spaces, the exchange between the corresponding emittances is not exact and only works if the conditions between beam parameters  $4 < x'^2 > < z'^2 > \eta^2 \ll \epsilon_x^2, \epsilon_z^2$  are satisfied, where  $\eta$  is a dogleg dispersion. Since then, various schemes have been developed which are capable to swap transverse and longitudinal phase space. The exact in the first order EEX is realized as two identical doglegs oriented in the same direction separated by a transverse deflecting cavity (TDC) (Fig. 2.2 (a)) [94]. The main disadvantage of this scheme in comparison to its chicane-type counterpart is that such a configuration shifts the beam from its original trajectory, and requires some additional beam optics to return it back.

The working principles of this exact EEX scheme can be explained by analyzing the transfer matrices of its structural components<sup>21</sup>. We start from rewriting the 4D part of the transfer matrix of a dogleg in equation (2.3) describing the motion in 4D  $(x, x', z, z')$  phase space:

$$R_{dogleg}(\eta) = \begin{pmatrix} 1 & L_{eff} & 0 & \eta \\ 0 & 1 & 0 & 0 \\ 0 & \eta & 1 & \psi \\ 0 & 0 & 0 & 1 \end{pmatrix}. \quad (2.43)$$

This matrix suggests that the transverse and longitudinal motions are partially coupled. In particular, the transverse coordinate  $x$  is affected by the energy  $z'$  proportional to a dogleg dispersion  $\eta$ . In addition, the longitudinal coordinate  $z$  is affected by the divergence  $x'$ ,

---

<sup>21</sup>We will demonstrate that an alternative exact EEX scheme can be constructed as a combination of two TDCs and one modified dogleg in Section (2.8).

also proportional to a dogleg dispersion<sup>22</sup>. Another element is required to provide with a back action. In such an element the initial coordinates ( $z$  and  $x$ ) should affect the final momentums of the motions in the opposite degree of freedom (respectively divergence  $x'$  and energy spread  $z'$ ). The proper matching element is a transverse deflecting cavity (TDC). Its transfer matrix in the “thin-lens” approximation can be written as:

$$R_{TDC}(\kappa) = \begin{pmatrix} 1 & 0 & 0 & 0 \\ 0 & 1 & \kappa & 0 \\ 0 & 0 & 1 & 0 \\ \kappa & 0 & 0 & 1 \end{pmatrix} . \quad (2.44)$$

Briefly a TDC is an RF cavity operating in a dipole mode  $TM_{110}$ . Thus, transverse components of the electric field are not present  $E_x = E_y = 0$ , while the longitudinal electric field varies linearly with transverse distance from the axis ( $x \ll a$ ):

$$E_z = E_0 \frac{x}{a} \cos(\omega t) \quad , \quad (2.45)$$

where  $a$  is a constant characteristic of the cavity dimensions. The longitudinal electric field vanishes at  $x = 0$  meaning that there is no action of the electric field on the reference particle. The action of this field on the particle off axis via the Lorentz force results in the induced energy spread depending on  $x$ :

$$z'(x) = \frac{eV_0}{E} \frac{x}{a} \cos(\omega t) \approx \frac{eV_0}{E} \frac{x}{a} \quad , \quad (2.46)$$

---

<sup>22</sup>The second condition immediately coming along due to the transfer matrix is symplectic, see equation (1.32) for details.

where we used approximation  $\omega t \ll 1$  which is valid if the reduced wavelength of the RF field much shorter than a bunch length  $\lambda_{RF}/2\pi \ll \sigma_z$ . We introduce the cavity strength parameter:

$$\kappa = \frac{eV_0}{Ea} \quad . \quad (2.47)$$

Next, we find the element of the TDC transfer matrix  $R_{61} = \kappa$  by using equations (2.46-2.47).

The only non-zero magnetic field component present in the TDC:

$$B_y = \frac{E_0}{a\omega} \sin(\omega t) \approx \frac{E_0 t}{a} \quad , \quad (2.48)$$

results in the additional deflection angle  $x'(z)$  described by the element  $R_{25}$  of the transfer matrix<sup>23</sup>. The additional physics behind the TDC including the effects due to its non-zero thickness is discussed in Chapter 3 in more details.

The matrix of a dogleg-TDC combination can be found as:

$$R = R_{TDC}(\kappa) \cdot R_{dogleg}(\eta) = \begin{pmatrix} 1 + \kappa\eta & L_{eff} & \kappa L_{eff} & \eta \\ 0 & 1 & \kappa & 0 \\ \kappa\psi & \eta & 1 + \kappa\eta & 0 \\ \kappa & 0 & 0 & 1 \end{pmatrix} \quad . \quad (2.49)$$

A combination of two elements is not yet enough to completely couple transverse and longitudinal phase spaces. However, it starts to demonstrate an important feature. If the cavity strength is chosen such that  $\kappa = -1/\eta$  then some matrix elements on the main diagonal disappear:  $R_{11} = R_{55} = 0$ . This means that the transverse and longitudinal sizes at the exit of the scheme are independent of their corresponding values at the entrance of the scheme.

---

<sup>23</sup>Here one has to use  $z = ct$  and  $x' = \beta_x/\beta_z$ .

If one then complete the scheme with an extra dogleg identical to the first one and oriented in the same direction, the overall transfer matrix becomes:

$$R_{EEX} = \begin{pmatrix} 0 & 0 & -\frac{L_{eff}}{\eta} & \eta - \frac{L_{eff}}{\eta} \\ 0 & 0 & -\frac{1}{\eta} & -\frac{\psi}{\eta} \\ -\frac{\psi}{\eta} & \eta - \frac{L_{eff}}{\eta} & 0 & 0 \\ -\frac{1}{\eta} & -\frac{L_{eff}}{\eta} & 0 & 0 \end{pmatrix}, \quad (2.50)$$

where the condition  $\kappa = -1/\eta$  was implemented. The matrix elements in the main diagonal blocks completely vanished (became zero). This means that transverse and longitudinal phase spaces at the exit of this scheme are completely independent from their corresponding initial values. Moreover, the initial transverse and longitudinal emittances at the exit of the scheme correspond to the initial counterparts<sup>24</sup>.

For comparison, we evaluate the transfer matrix of the chicane-type EEX presented in the original work by Cornacchia *et al.* [93] as  $R_{EEX'} = R_{dogleg}(\eta) \cdot R_{TDC}(\kappa) \cdot R_{dogleg}(-\eta)$  and immediately find:

$$R_{EEX'} = \begin{pmatrix} 1 + \kappa\eta & 2L_{eff} & \kappa L_{eff} & \kappa(L_{eff}\psi - \eta^2) \\ 0 & 1 - \kappa\eta & \kappa & \kappa\psi \\ \kappa\psi & \kappa(L_{eff}\psi - \eta^2) & 1 + \kappa\eta & 2\psi \\ \kappa & \kappa L_{eff} & 0 & 1 - \kappa\eta \end{pmatrix}, \quad (2.51)$$

It is clear that the ideal exchange cannot be satisfied in this configuration for an arbitrary beam since the condition on the elements  $R_{11} = R_{55} = 0$  and  $R_{22} = R_{66} = 0$  are mutually exclusive. Depending on the parameters of the beam one can choose the cavity parameter

---

<sup>24</sup>The emittances are exchanged in this scheme, while the phase space shapes are not exactly exchanged. Hence, the scheme was named as an emittance exchanger, emphasizing its action on the beam.

$\kappa = \pm 1/\eta$  to uncouple either the final beam sizes or divergence and energy spread from their initial values.

The idea to use a single EEX as a bunch compressor was discussed by Carlsten *et al.* in the beginning of 2011 [90]. The main advantage of the proposed scheme is that the final longitudinal phase space is decoupled from the initial longitudinal phase space and, in addition, it does not require any initial and residual energy-phase compensation as a chicane-based scheme. Hence, such a scheme should be less affected by the LSC induced micro-bunch instabilities in the final longitudinal phase space. However, since an emittance exchange only swap the projections of eigen emittances between transverse and longitudinal phase spaces [61,95], this configuration either requires all initial emittances to be of the same order ( $\epsilon_{n_x} \sim \epsilon_{n_y} \sim \epsilon_{n_z}$ ), or needs an additional emittance exchange. Since transverse emittances from the ultra-bright photo-cathodes are typically of the same order and significantly different from the longitudinal emittance, the idea of the single EEX based bunch compressor transformed into a double EEX with a transverse telescope [96]. First, transverse  $(x, x')$  phase space is exchanged with the longitudinal phase space. Then, a telescope, combined from the transverse optics elements (quads and drifts), is applied to compress the beam in the new  $(x, x')$  phase-space, which is the old  $(z, z')$  phase-space. Finally, second EEX switches transverse and longitudinal phase spaces back, returning the beam compressed in  $z$ -direction with enlarged energy spread. The LSC induced microbunch instabilities in an EEX-based schemes are expected to be smaller than in chicane based BCs. Instabilities are not amplified along one particular direction, because the beam phase space is constantly mixed <sup>25</sup> [97]. However, CSR effects in the dipole magnets in this scheme are still expected to be critical, similarly to the chicane-based scheme. Further in this chapter, we quantita-

---

<sup>25</sup>The quantitative investigation of this question is left beyond the scope of this dissertation. LSC imposed microbunching instabilities for the double EEX beam optics can be theoretically analyzed by solving microbunching integral equation in [83] similar to how it is accomplished for the chicane with extra bending magnets in [88]. In addition, it can be added in simulations by imposing the initial modulations on the electron beam distribution.

tively investigate if they can be minimized to preserve the transverse beam quality, which is extremely important for the effective lasing in the undulator section as was discussed in Sec. 1.3.

A. Zholents and M. Zolotarev proposed using chicane-type EEX modules with inserted along the beamline focusing and defocussing quadrupole magnets in respect to  $(x, x')$  phase space to adjust the beam parameters in the original design of DEEX-based BC [96]. In contrast, we discuss the exact EEX modules: unidirectional doglegs up-up or down-down in this dissertation. We also invert the direction of the second EEX module of the bunch compressor, so the electron beam travels back to its original path (Fig. 2.2 (b)). For this configuration, the phase space position coordinate should be mirrored in the telescope, e.g.  $x \rightarrow -x$ , which is easy to realize. We avoid any transverse optics elements to correct the beam in the EEX parts, by adding it in the advanced telescope design, if required. Summarizing

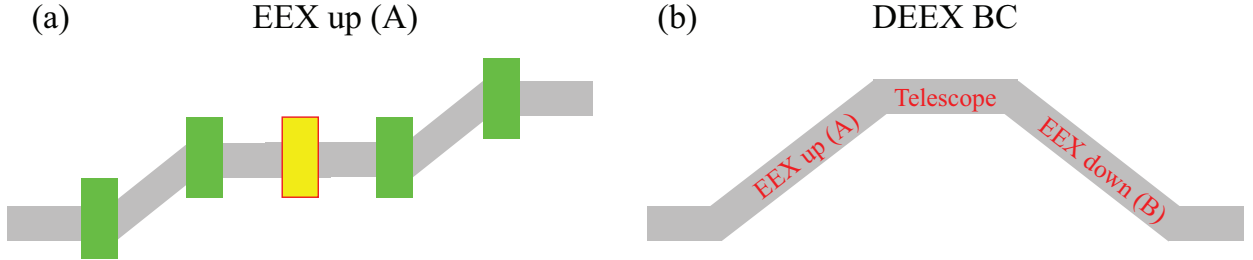


Figure 2.2: (a) A scheme of an exact EEX up (A). (b) A conceptual scheme of a double EEX bunch compressor at 1 GeV for MaRIE XFEL electron beam. Bending magnets are represented by green rectangles, the deflecting cavity is represented by the yellow rectangle with red borders.

above, we get the design represented in Fig. 2.2, where EEX up/down and telescope modules

are described by the matrices in  $(xx'zz')$  4D phase space while the dynamics in  $(y, y')$  phase space is uncoupled:

$$R_{EEX^\pm} = \mp \begin{pmatrix} 0 & 0 & \frac{L_{eff}}{\eta} & \frac{L_{eff}\psi}{\eta} - \eta \\ 0 & 0 & \frac{1}{\eta} & \frac{\psi}{\eta} \\ \frac{\psi}{\eta} & \frac{L_{eff}\psi}{\eta} - \eta & 0 & 0 \\ \frac{1}{\eta} & \frac{L_{eff}}{\eta} & 0 & 0 \end{pmatrix}, \quad (2.52)$$

$$R_T = \begin{pmatrix} m - \left(\frac{1}{m} + m\right)q & L_{eff}(-1 + q)\left(\frac{1}{m} + m\right) & 0 & 0 \\ \frac{\left(\frac{1}{m} + m\right)q}{L_{eff}} & \frac{1}{m} - \left(\frac{1}{m} + m\right)q & 0 & 0 \\ 0 & 0 & 1 & 0 \\ 0 & 0 & 0 & 1 \end{pmatrix}, \quad (2.53)$$

and the parameters for EEX are defined according to the relations<sup>26</sup>:

$$\psi = -2D \theta \csc \theta + \sec \theta (2D + S_1 \tan^2 \theta) \quad , \quad (2.54)$$

$$\eta = -(S_1 \cos \theta + S_1 + D \cos(2\theta) + D) \sec^3 \theta \tan(\theta/2) \quad , \quad (2.55)$$

$$L_{eff} = (D + D \cos(2\theta) + S_1) \sec^3 \theta + S_2 \quad , \quad (2.56)$$

where  $D = r \sin \theta$  is the length of the bending magnet along the  $z$ -axis in the laboratory frame and  $\theta$  is the bend angle,  $S_1$  and  $S_2$  are respectively separations between two magnets and magnet - deflecting cavity, and cavity strength  $\kappa = -1/\eta$  is chosen to satisfy the condition of the exact emittance exchange. The telescope matrix is then defined via the parameter  $q = \psi L_{eff}/\eta^2$ ,  $L_{eff}$  and the compression factor  $m$ .

---

<sup>26</sup>Note that parameters  $\psi$ ,  $\eta$ ,  $L_{eff}$  here vary from their values in equation (2.50) which are defined in equations (2.9-2.11) for the dogleg with equal edge angles of each bending magnet ( $\alpha_1 = \alpha_2 = \theta/2$ ). Here each dogleg is combined in such a way that the edge angles of the first magnet are  $\alpha_1 = 0$  and  $\alpha_2 = \theta$  and for the second magnet  $\alpha_1 = \theta$  and  $\alpha_2 = 0$ . In addition,  $L_{eff}$  has an extra length  $S_2$  due to two doglegs and the TDC are separated by drifts in this design.

The telescope configuration can be realized using drifts, focusing and defocussing lenses, and, in our design, it is constructed as a combination of two negative drifts and a “super-lens” (Fig. 2.3). In principal, the telescope matrix has only three independent elements in  $(x, x')$  block, because the fourth element is fixed by the condition on the matrix determinant  $\det(T)=1$ . Hence, theoretically, three transverse optics elements should be enough to realize an arbitrary telescope matrix. This is valid if beam dynamics along the  $y$ -axis is not important. However, while there are focusing and defocussing quadrupole magnets, free space propagation elements (drifts) are restricted to be positive ( $R_{12} = R_{34} = d \geq 0$ ). Indeed, negative drift ( $R_{12} \leq 0$  and  $R_{34} \geq 0$ ) is a virtual element in beam optics which describes the back propagation along one axis (the  $x$ -axis here) and the direct propagation along another axis (the  $y$ -axis here). For example, a negative drift along the  $x$ -axis can be constructed as a combination of two triplets. Each triplet is combined from two focusing ( $f_1 < 0$ ) and one defocussing quadrupoles<sup>27</sup> in respect to the  $x$ -axis which are separated by equal drifts ( $d_1 = -f_1$ ). We rewrite matrices of the triplet components in 4-dimensional  $(x, x', y, y')$  representation<sup>28</sup>:

$$R_Q(f) = \begin{pmatrix} 1 & 0 & 0 & 0 \\ 1/f & 1 & 0 & 0 \\ 0 & 0 & 1 & 0 \\ 0 & 0 & -1/f & 1 \end{pmatrix}, \quad R_{Drift}(d) = \begin{pmatrix} 1 & d & 0 & 0 \\ 0 & 1 & 0 & 0 \\ 0 & 0 & 1 & d \\ 0 & 0 & 0 & 1 \end{pmatrix}. \quad (2.57)$$

The overall triplet matrix then can be found as:

$$R_{Tr}(d_1) = R_Q(-d_1) \cdot R_{Drift}(d_1) \cdot R_Q(d_1) \cdot R_{Drift}(d_1) \cdot R_{Q_1}(-d_1) \quad , \quad (2.58)$$

---

<sup>27</sup>Here, we use the thin-lens approximation for quadrupoles, thick lens can be presented as the combination of drift, thin lens and another drift.

<sup>28</sup>Longitudinal dynamics is not affected by quads and drifts for highly relativistic beam ( $\gamma \gg 1$ ).

and we finally obtain:

$$R_{Tr}(d_1) = \begin{pmatrix} -1 & 3d_1 & 0 & 0 \\ 0 & -1 & 0 & 0 \\ 0 & 0 & 1 & d_1 \\ 0 & 0 & 0 & 1 \end{pmatrix}. \quad (2.59)$$

The combination of two triplets results in the negative drift along the  $x$ -axis and the positive drift along the  $y$ -axis:

$$R_{L-}(d_1) = R_{Tr}(d_1) \cdot R_{Tr}(d_1) = \begin{pmatrix} 1 & -6d_1 & 0 & 0 \\ 0 & 1 & 0 & 0 \\ 0 & 0 & 1 & 2d_1 \\ 0 & 0 & 0 & 1 \end{pmatrix}. \quad (2.60)$$

In this dissertation we define the “superlens” as a virtual lens focusing beam in one direction, combined from quads and drifts:

$$R_S(f) = \begin{pmatrix} -1 & 0 & 0 & 0 \\ 1/f & -1 & 0 & 0 \\ 0 & 0 & -1 & 0 \\ 0 & 0 & 0 & -1 \end{pmatrix}. \quad (2.61)$$

Combination of two triplets and the superlens  $R_T = R_{Tr}(d_2) \cdot R_S(f) \cdot R_{Tr}(d_1)$ , results in the desired telescope matrix  $R_T$  in Eq. (2.53), if the next conditions between the parameters of the components are satisfied:

$$f = \frac{L_{eff}}{q(m + 1/m)} , \quad (2.62)$$

$$3d_1 = \frac{q(m + 1/m) - 1/m - 1}{q(m + 1/m)} L_{eff} , \quad (2.63)$$

$$3d_2 = \frac{q(m + 1/m) - m - 1}{q(m + 1/m)} L_{eff} . \quad (2.64)$$

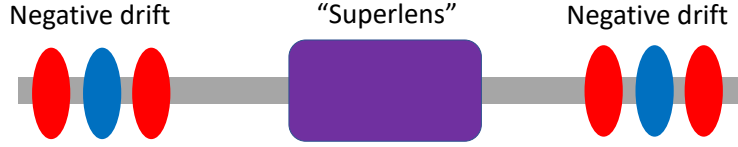


Figure 2.3: Telescope scheme: two triplets and the “superlense” are combined together to compress and reshape the beam in  $(x, x')$  phase space, as it is described by the telescope matrix  $R_T$  in Eq. (2.53). Red and blue ovals symbolize focusing and defocussing quadrupole magnets in respect to the  $(x, x')$  phase space.

The final DEEX bunch compressor scheme is described by a first-order transport matrix, derived as a sequence of its elements in  $(x, x', z, z')$  4D phase space:

$$R_{BC} = R_{EX-} \cdot R_T \cdot R_{EX+} = \begin{pmatrix} 1 - \frac{2L_{eff}\epsilon}{\eta^2} & 2L_{eff} \left(1 - \frac{L_{eff}\epsilon}{\eta^2}\right) & 0 & 0 \\ -\frac{2\epsilon}{\eta^2} & 1 - \frac{2L_{eff}\epsilon}{\eta^2} & 0 & 0 \\ 0 & 0 & 1/m & 0 \\ 0 & 0 & 0 & m \end{pmatrix}. \quad (2.65)$$

The beam dynamics in  $(y, y')$  plane is uncoupled and the associated transfer matrix for the BC can found as a combination of its structural components:

$$R_{BC_{yy'}} = R_{EX_{yy'}^-} \cdot R_{T_{yy'}} \cdot R_{EX_{yy'}^+}. \quad (2.66)$$

where the transfer matrix through each emittance exchanger is equal to:

$$R_{EX_{yy'}} = R_{dogleg_{yy'}} \cdot R_{Drift}(S_2) \cdot R_{dogleg_{yy'}}. \quad (2.67)$$

The transfer matrix for the drift in  $(y, y')$  phase space is simply:

$$R_{Drift}(L) = \begin{pmatrix} 1 & L \\ 0 & 1 \end{pmatrix}. \quad (2.68)$$

The transfer matrix for  $(y, y')$  phase space through each dogleg is invariant of its direction up or down and equal to:

$$R_{dogleg_{yy'}} = \begin{pmatrix} R_{33} & (-1 + R_{33}^2)/R_{43} \\ R_{43} & R_{33} \end{pmatrix}, \quad (2.69)$$

where

$$R_{33} = 1 + \tan \theta \left( -2\theta + \frac{S_1}{D} \tan \theta (-1 + \theta \tan \theta) \right) \quad , \quad (2.70)$$

$$R_{43} = \frac{\sin \theta \tan \theta (-2D + S_1 \tan \theta^2)}{D^2} \quad . \quad (2.71)$$

The transfer matrix for  $(y, y')$  phase space through the telescope  $T$  is equal to:

$$R_{T_{yy'}} = \begin{pmatrix} -1 & -L_{T_y} \\ 0 & -1 \end{pmatrix} \quad , \quad (2.72)$$

where the effective length along the  $y$ -direction in the telescope can be found as:

$$L_{T_y} = \frac{1}{3} L_{eff} \left( 2 - \frac{(1+m)^2}{(1+m^2)q} \right) \quad . \quad (2.73)$$

Finally, one can find the transfer matrix for  $(y, y')$  dynamics using equation (2.66) and its components listed above. The expressions are quite long so we omit it here. The resulting scheme is  $\sim 30$  m long along the  $z$ -axis in the laboratory frame for a realistic set of parameters. In the next section, we present numerical studies of the double emittance exchanger (DEEX) BC utilizing eigen-emittance analysis described in Section 2.2 and show that the CSR effects strongly compromise its applicability in FEL driven accelerators with extreme beam parameters, such as required for MARIE XFEL.

## 2.4 Double EEX bunch compressor: simulation studies.

### 2.4.1 Linear effects

The beam-optics parameters for DEEX BC (Table 2.1) were selected according to realistic electro-magnetic fields in bends and transverse deflecting cavities, as well as drift lengths to deliver an exact exchange and compression factor ( $m = 25$ ), as it is described by matrix formalism in the previous section in the linear regime. They were chosen for given electron beam parameters at 1 GeV beam energy for MaRIE XFEL (Table 2.2). Simulation studies were performed using the ELEGANT tracking code by Michael Borland [37] which we introduced in Sec. 1.2. Simulation results of this design for the case of linear dynamics are presented in Fig. 2.4. It is clear that under the linear single-particle dynamics, the

Table 2.1: Parameters of the components of DEEX BC for the initial design and two optimized designs optimized for MaRIE beam parameters I and II listed in Table 2.2.

Element/Design	Initial	Design I	Design II	Units
<b>EEX up (A)</b>				
Bend angle A	2.5	2.60	2.24	deg
Bend radius A	1.14	0.50	1.20	m
Drift S1 A	4.8	10.20	12.72	m
Drift S2 A	1.6	0.91	0.72	m
Cavity strength A	4.71	2.15	2.00	m <sup>-1</sup>
<b>EEX down (B)</b>				
Bend angle B	2.5	3.38	2.84	deg
Bend radius B	1.14	1.20	0.82	m
Drift S1 B	4.8	7.00	4.98	m
Drift S2 B	1.6	4.52	3.01	m
Cavity strength B	4.71	2.38	4.00	m <sup>-1</sup>

emittance exchange between the horizontal and longitudinal degrees of freedom is perfect in this design (Fig. 2.4 (a)). The appropriate compression ratio  $m = 25$  is reached. Fig. 2.4 (b)

Table 2.2: Desirable (I) and acceptable (II) beam parameters for MaRIE XFEL at the entrance of the second BC at 1 GeV.

<b>Electron beam</b>	Set I	Set II	Units
Normalized emittance	0.1	0.19	$\mu\text{m}$
Energy spread (rms)	25	70	keV
Bunch duration (rms)	90	90	$\mu\text{m}$
Energy chirp (rms)	0	0	keV
Beam energy	1	1	GeV
Bunch charge	100	100	pC
Required compression	25	25	

demonstrates that the invariants of the linear dynamics, eigen emittances, remain unchanged along the beam line as expected.

### 2.4.2 Real dynamics: nonlinear and CSR effects

First, we evaluate nonlinear effects on the single-particle dynamics by setting the tracking order to the second order in drifts (DRIF in ELEGANT) and the third order in bends (CSBEND in ELEGANT), while the TDC and telescope are simulated as linear matrices for simplicity. As we discussed in Sec. 1.2, similar tracking physics-wise can be realized by using CSR routines<sup>29</sup>, CSR BEND and CSR DRIFT, if one keeps the CSR-effects turned off by setting up the bunch charge to  $q = 0$  pC. Both approaches delivered the same result as expected. The nonlinear dynamics practically does not affect two eigen emittances,  $\lambda_1$  and  $\lambda_3$ , related to the initial/final rms emittances,  $\epsilon_y$  and  $\epsilon_z$  respectively, while  $\lambda_2$  related to initial/final  $\epsilon_x$  experiences a non-negligible grow (Fig. 2.5 (a)). In principal, nonlinear effects can be completely or partially mitigated by adjusting the parameters of the elements

---

<sup>29</sup>Using these routines typically take a longer calculation time of a single run, and this is not a proper way to do simulations if one performs a scan or an optimization of the single-particle dynamics. However, it might be convenient to use these routines in some cases since the CSR effects can be turned off in all elements at the same time.

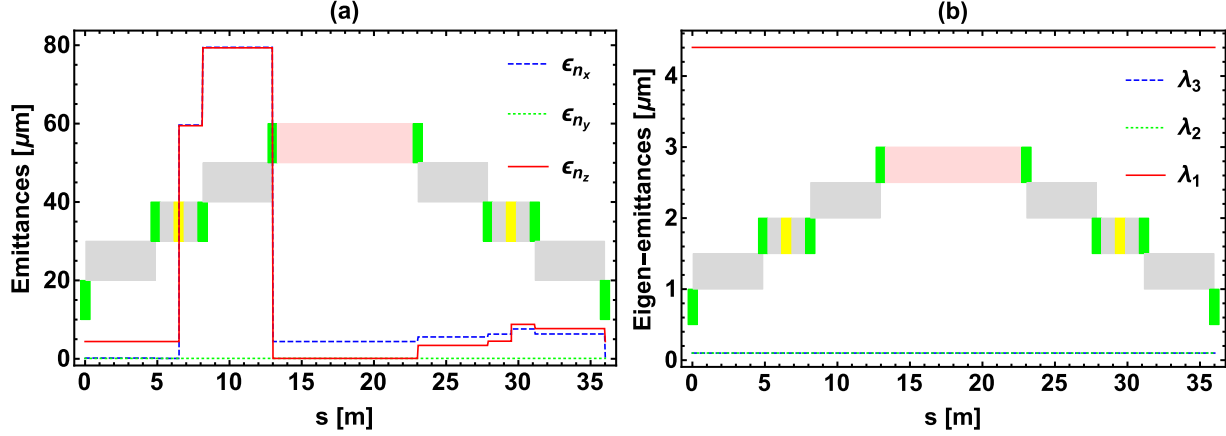


Figure 2.4: Normalized rms emittance (a) and normalized eigen-emittance (b) evolution from the distance along the path in the DEEX BC beamline. The elements are represented by the color scheme as follows: green is for the bending magnets, yellow is for the TDCs, gray is for the drifts and pink is for the telescope. The TDCs and dipole magnet lengths are enlarged on the scheme to be visualized better.

present in the scheme. This is because the beam sizes along the beamline can be optimized in order to nonlinear effects imposed in the different elements along the beamline would compensate each other. Alternative solution, increasing the complexity of the scheme, is to incorporate the high order elements: sextupoles, octupoles, etc. [98]. Before performing optimization of the scheme one needs to ensure that nonlinear effects is the dominating factor enlarging emittances in comparison to other collective effects, such as the CSR effects here in particular.

Once we turn on the CSR effects in bends and drifts by setting up the bunch charge to the operational 100 pC, eigen emittances start growing dramatically throughout the beamline (Fig. 2.5 (b)). Comparing Fig. 2.5 (a) and (b), it is clear that CSR effects strongly dominates over nonlinear effects for this design. Table 2.3 summarizes the parameters of the beam on the entrance and the exit of the DEEX BC. The determinant of the 6-dimensional  $\Sigma$ -matrix  $\det(\Sigma)$  of the electron beam, characterizing the phase space volume, is equal to the square of the product of all eigen emittances. It grows  $\sim 5208$  times, which means the product of

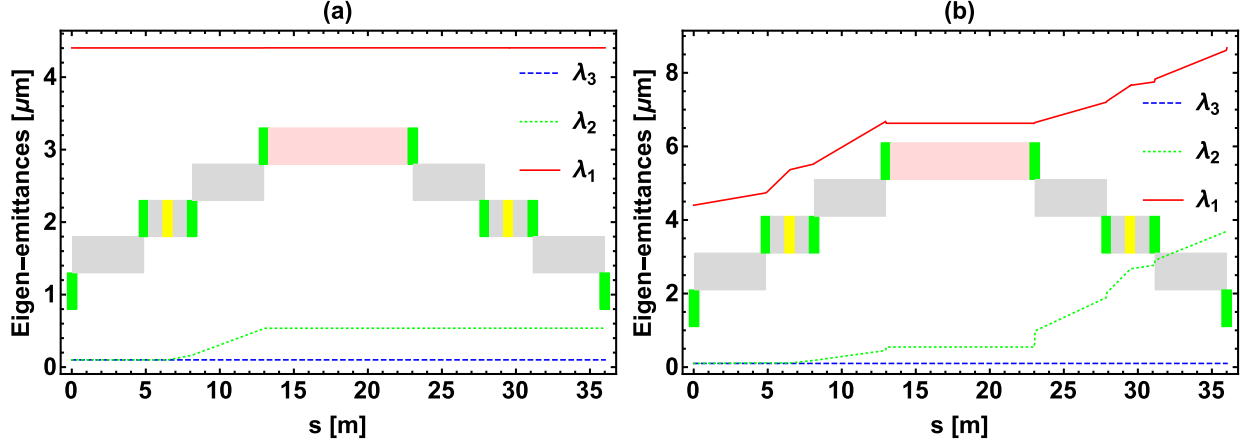


Figure 2.5: Evolution of eigen emittances evolution from the distance along the beam-path in the DEEX BC: (a) nonlinear dynamics without CSR effects and (b) nonlinear dynamics with CSR effects ( $q = 100$  pC). The elements of the beamline are represented by the color scheme as follows: green is for the bending magnets, yellow is for the TDCs, gray is for the drifts and pink is for the telescope. The TDCs and dipole magnet lengths are enlarged on the scheme to be better visualized.

eigen emittances grows roughly 72 times. The normalized transverse emittance  $\epsilon_{n_x}$  grows  $\sim 53$  times and normalized longitudinal emittance  $\epsilon_{n_z}$  grows  $\sim 1.8$  times, which makes the beam on the output of this compressor completely inappropriate to use for MaRIE XFEL. The product of all normalized emittances then grows approximately 95 times. Further, we find that the ratio between the final (at the exit of the scheme) multiplying emittance product (MEP) and the final product of eigen-emittance is  $\sim 1.4$ . This means that there are some residual correlations between transverse and longitudinal phase spaces imposed by the nonlinear and collective effects<sup>30</sup>, which can be compensated by tuning parameters of the scheme<sup>31</sup>. However, it is obvious that the growth of the eigen emittances due to collective effects much more significant than the remaining correlations between the transverse and longitudinal phase spaces. Therefore, its optimization should be prioritized. The CSR effects

<sup>30</sup>Indeed, the linear dynamics demonstrated an ideal exchange as reported in Fig. 2.4

<sup>31</sup>This can be done via two different approaches. First method is to keep the linear exchange exact by matching the cavity strength  $k$  while changing parameters of the EEX beam elements. This allows to significantly vary parameters of the scheme. Second approach is to slightly change all parameters of the scheme.

in this DEEX BC strongly disrupt the phase space. Interestingly, the final compression factor is still close to the designed value of  $m = 25$  and is not affected by CSR (Fig. 2.6). Nevertheless, significant modifications of the design are required to mitigate the impact of the collective effects on the degradation of the transverse phase space. The goal of such an optimization is to minimize eigen emittances at the exit of the bunch compressor.

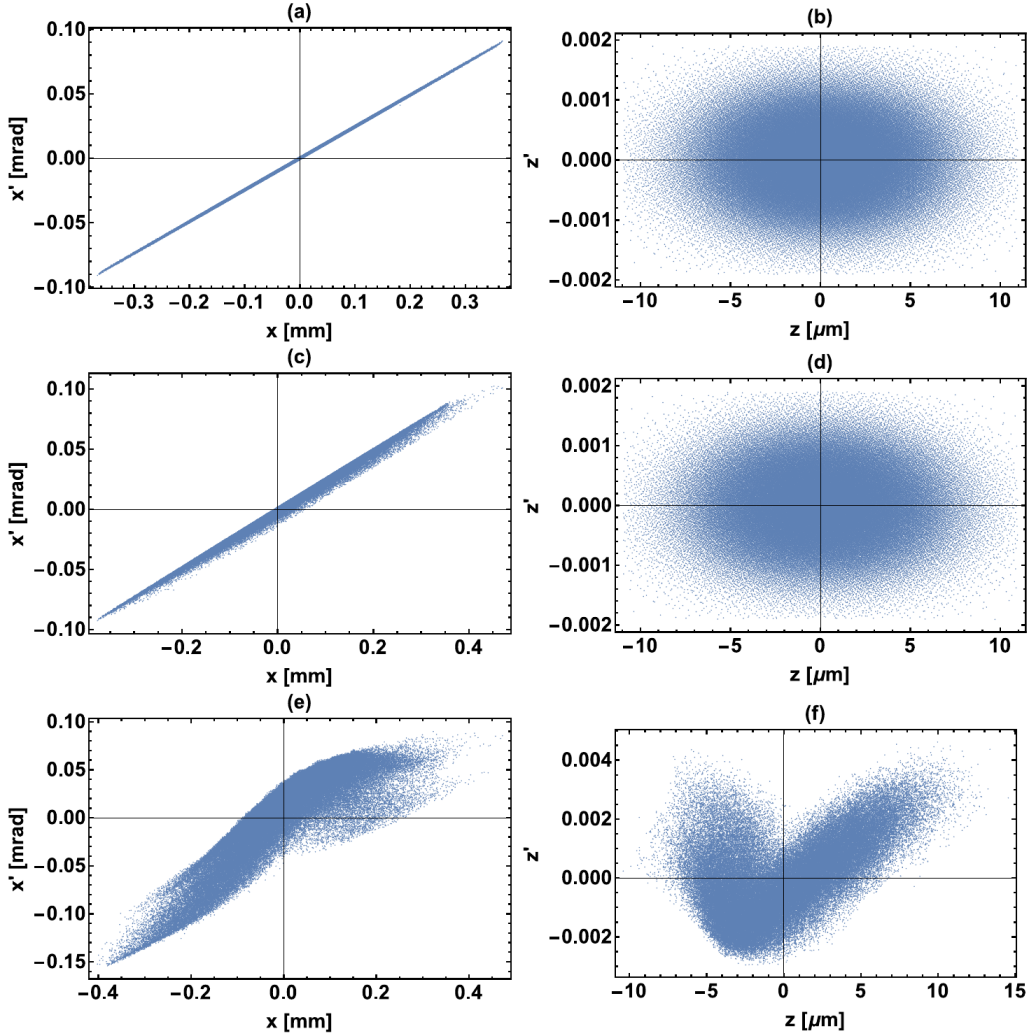


Figure 2.6: Transverse (left) and longitudinal (right) phase spaces for the linear (a-b) and nonlinear (c-d) single-particle dynamics, and the nonlinear dynamics with the CSR effects for  $q = 100$  pC (e-f) at the exit of DEEX BC.

Table 2.3: Initial and final beam parameters (rms) in the DEEX bunch compressor in different approximations of the particle dynamics: linear single particle dynamics (LSP), non-linear single-particle dynamics (NSP) and multi-particle dynamics including CSR effects for 100 pC bunch charge (MP).

<b>Electron beam</b>	Initial	Final			Units
<b>Parameters / regime</b>		LSP	NSP	MP	
Normalized emittance $\epsilon_{n_x}$	0.1	0.1	0.54	5.29	$\mu\text{m}$
Normalized emittance $\epsilon_{n_y}$	0.1	0.1	0.1	0.1	$\mu\text{m}$
Normalized emittance $\epsilon_{n_z}$	4.4	4.4	4.4	7.97	$\mu\text{m}$
Normalized eigen-emittance $\lambda_1$	4.4	4.4	4.4	8.7	$\mu\text{m}$
Normalized eigen-emittance $\lambda_2$	0.1	0.1	0.54	3.66	$\mu\text{m}$
Normalized eigen-emittance $\lambda_3$	0.1	0.1	0.1	0.1	$\mu\text{m}$
Bunch size $\sigma_x$	71.5	119.4	121.9	122.2	$\mu\text{m}$
Bunch size $\sigma_y$	122.5	117.5	117.4	117.4	$\mu\text{m}$
Bunch length $\sigma_z$	90	3.6	3.6	3.64	$\mu\text{m}$
Twiss parameter $\beta_x$	100	278.8	54.1	5.51	m
Twiss parameter $\alpha_x$	0	-68.5	-13.1	-1.86	
Twiss parameter $\beta_y$	293.5	269.8	269.8	269.8	m
Twiss parameter $\alpha_y$	0	-7.85	-7.85	-7.85	
Energy spread $\sigma_{\delta\gamma}$	25	625	625.1	1297.3	keV
Linear energy slope $\langle zz' \rangle / \sigma_z^2$	0	-0.04	-0.018	-180.3	$\text{m}^{-1}$
Beam energy $E$	1	1	1	1	GeV
Final compression $m = \sigma_{z_i} / \sigma_{z_f}$	-	25	25	24.7	

Beamlines designed for manipulation of the beam phase space, including conventional bunch compressors, and especially advanced schemes, such as DEEX, have a large number of beam optics elements each of which is usually characterized by multiple parameters. While working fine in the linear regime, all of these schemes requires multi-dimensional (over all set of parameters) optimization in the case of real dynamics accounting for the nonlinear and collective effects. This optimization is aimed to minimize emittance growth and phase-space distortions. Since even individual simulation runs of a whole bunch compressor beamline accounting for nonlinear and collective effects can take quite noticeable time, a fast adaptive multi-dimensional optimization algorithm is required. Thus, we implemented the optimiza-

tion algorithm known in the community as Extremum Seeking [99–102]. We introduce the working principles of the algorithm in the next section.

## 2.5 Extremum seeking

The Extremum Seeking (ES) optimization algorithm is designed for an  $n$ -dimensional dynamic system of the form:

$$\frac{d\mathbf{x}}{dt} = \mathbf{f}(\mathbf{x}, \mathbf{p}, t) \quad , \quad (2.74)$$

where  $\mathbf{f}$  is an unknown function,  $\mathbf{x} = (x_1, \dots, x_n)$  are physical parameters such as beam properties throughout an accelerator (beam sizes, energy spread, emittances, etc.), and  $\mathbf{p}(t) = (p_1(t), p_2(t), \dots, p_m(t))$  are tunable parameters which influence  $\mathbf{x}$  such as a length of a magnet or a free space propagation section, electromagnetic field amplitudes and phases, and others. ES can be used to minimize (maximize<sup>32</sup>) an analytically unknown, time-varying, user-defined “cost function,”  $C(\mathbf{x}, \mathbf{p}, t)$ . Minimization of this function corresponds to optimization of certain system properties of interest, such as a beam loss or a measure of how much beam phase space deviates from a desired distribution in a particular location along the beamline. Moreover ES is capable to deal with a possibly noise corrupted measurement of  $C(\mathbf{x}, \mathbf{p}, t)$  of the form:

$$\hat{C}(\mathbf{x}, \mathbf{p}, t) = C(\mathbf{x}, \mathbf{p}, t) + \underbrace{\nu(t)}_{\text{noise}} \quad , \quad (2.75)$$

---

<sup>32</sup>In general ES is designed to find an extremum, therefore got named as Extremum Seeking by its authors.

which is a useful feature if one needs to optimize a complex experimental system, or if computational errors are unavoidable during simulation studies. In order to minimize the analytically unknown  $C$ , the ES dynamics are given by:

$$\frac{dp_j}{dt} = \sqrt{\alpha\omega_j} \cos(\omega_j t + k\hat{C}) \quad , \quad (2.76)$$

where  $\alpha$ ,  $k$ ,  $\omega_j$  are ES parameters meaning of which will be explained further. If frequencies of ES oscillations  $\omega_j = \omega r_j$  where  $r_j$  are different numbers such that  $r_j \neq r_i$  for  $i \neq j$ , then in the limit as  $\omega \rightarrow \infty$ , the  $m$ -dimensional dynamics equation (2.76) is approximated by the average dynamics in the vector form:

$$\frac{d\mathbf{p}}{dt} = -\frac{k\alpha}{2} \nabla_{\mathbf{p}} C \quad , \quad (2.77)$$

which is simply a gradient descent of the actual, unknown function  $C$  with respect to  $\mathbf{p}$  [100, 101]. In equation (2.76) the term  $\alpha$  controls the size of the dither amplitude of each parameter and can be increased to escape local minima or/and to speed up convergence towards the minimum. The term  $k > 0$  serves as a feedback gain which also speeds up convergence. For the average dynamics approximation equation (2.77) to hold,  $\omega$  must be very large relative to the natural time variation of the system and may have to be increased as the values of  $k$  or  $\alpha$  are increased.

The  $\cos(\cdot)$  terms in equation (2.76) may be replaced by  $\sin(\cdot)$  functions, or the two can be mixed together. Convergence of the scheme requires that the perturbing functions are orthogonal in  $L^2[0, T]$ , which means that the inner products of any two functions uniformly converge to zero:

$$\lim_{\omega \rightarrow \infty} \int_0^T \cos(\omega r_i t) \cos(\omega r_j t) dt = 0 \quad .$$

For complex physical systems, such as particle accelerators, the values of the parameters  $\mathbf{p}$  may vary over several orders of magnitude and may have various bounds which should not be violated. Therefore it can be useful to normalize all parameters within a given range such as  $\mathbf{p}_{\text{nrm}} \in [-1, 1]$ . Normalization is performed by first defining upper and lower bounds on all parameters:

$$\mathbf{p}_{\text{max}} = (p_{1,\text{max}}, \dots, p_{m,\text{max}}) \quad , \quad (2.78)$$

$$\mathbf{p}_{\text{min}} = (p_{1,\text{min}}, \dots, p_{m,\text{min}}) \quad . \quad (2.79)$$

We then define

$$\Delta \mathbf{p}_+ = \frac{\mathbf{p}_{\text{max}} + \mathbf{p}_{\text{min}}}{2}, \quad \Delta \mathbf{p}_- = \frac{\mathbf{p}_{\text{max}} - \mathbf{p}_{\text{min}}}{2} \quad , \quad (2.80)$$

and normalize all parameters via

$$\mathbf{p} \longrightarrow \frac{\mathbf{p} - \Delta \mathbf{p}_+}{\Delta \mathbf{p}_-} = \mathbf{p}_{\text{nrm}} \in [-1, 1], \quad (2.81)$$

and un-normalize normalized values back to their physical ranges via

$$\mathbf{p}_{\text{nrm}} \longrightarrow \mathbf{p}_{\text{nrm}} \Delta \mathbf{p}_- + \Delta \mathbf{p}_+ = \mathbf{p} \in [\mathbf{p}_{\text{min}}, \mathbf{p}_{\text{max}}] \quad . \quad (2.82)$$

The iterative ES procedure assuming that all parameters are normalized is executed as follows. First, one has to choose physics-based estimates for initial parameter values,  $\mathbf{p}(1)$ . Second, a simulation or an experiment run with parameter settings  $\mathbf{p}(1)$  is performed and the desired measurement of the analytically unknown cost function is executed:

$$\hat{C}(1) = C(\mathbf{x}(\mathbf{p}(1)), \mathbf{p}(1)) + \nu(1) \quad . \quad (2.83)$$

After that one needs to calculate new normalized parameter values  $\mathbf{p}(2)$  according to:

$$p_j(2) = p_j(1) + \Delta \sqrt{\alpha_j \omega_j} \cos \left( \omega_j \Delta + k \hat{C}(1) \right) \quad , \quad (2.84)$$

and force normalized parameters values to remain within the bounds  $[-1, 1]$  via the simple check:

$$|p_j(2)| > 1 \implies p_{,j}(2) = \frac{\text{sign}(p_j(2))}{|p_j(2)|} \quad . \quad (2.85)$$

The procedure is continued iteratively with updates at step  $n$  of the form:

$$p_{\text{nrn},j}(n+1) = p_{\text{nrn},j}(n) + \Delta \sqrt{\alpha_j \omega_j} \cos \left( \omega_j n \Delta + k \hat{C}(n) \right) \quad , \quad (2.86)$$

which, for  $\Delta \ll \frac{1}{\max \omega_j} \ll 1$  is a finite difference approximation of the dynamics in equation (2.76) and results in minimization of  $C$ . This feedback scheme has several useful features. First, the average gradient descent in equation (2.77) takes place relative to the actual, unknown function  $C$ , despite being based only on its noise-corrupted measurement  $\hat{C}$ . Unlike standard gradient-descent approaches however, convergence time does not grow exponentially with the number of parameters and can handle noisy, time-varying multi-dimensional systems. Finally, despite operating on an analytically unknown dynamic system and minimizing an analytically unknown function,  $\hat{C}$ , this feedback has analytically known bounds on parameter variation and update rates, because the unknown function enters the parameter dynamics as the argument of a known, bounded function:

$$\begin{aligned} |p_j(n+1) - p_j(n)| &= \left| \Delta \sqrt{\alpha_j \omega_j} \cos \left( \omega_j \Delta n + k \hat{C}(n) \right) \right| \\ &\leq \left| \Delta \sqrt{\alpha_j \omega_j} \right| \quad , \end{aligned} \quad (2.87)$$

which makes this method safe and useful for in-hardware and in-software implementations. In particular, this algorithm is a very promising feature to be added in any beam tracking code. We discuss how to simultaneously optimize beam and beam optics parameters in order to minimize impact of the nonlinear and CSR effects in DEEX using ES algorithm coupled with simulations in ELEGANT in the next section.

## 2.6 Minimizing emittance growth

### 2.6.1 Twiss parameters optimization

According to the theoretical calculations in [42], the CSR effects impact on the transverse emittance growth in the bending plane of a dipole magnet can be quantified as:

$$\Delta\epsilon_n = 0.38\alpha^2 \frac{I_p}{I_A} \ln\left(\frac{\rho_0}{a}\right) \frac{\sigma_r^2}{\sigma_z} \quad , \quad (2.88)$$

where  $I_p$  is the beam peak current,  $I_A$  is the Alfvén current,  $\sigma_r$  is the radial beam size in the approximation of a cylindrical beam,  $\sigma_z$  is the bunch length and  $\rho_0$  is the radius of the beam pipe. The emittance growth here is meant to be added in quadrature to the initial emittance:

$$\epsilon_{n_f}^2 = \epsilon_{n_i}^2 + \Delta\epsilon_n^2 \quad . \quad (2.89)$$

One can see that it quadratically depends on the beam peak current at the constant bunch charge  $\Delta\epsilon_n \sim I_p/\sigma_z \sim I_p^2$ , so the effect becomes larger for shorter bunches. Moreover, quadratic scaling of the emittance growth from the transverse beam size and the bend angle suggests minimizing these parameters for suppressing the CSR effects. Therefore, the rule-of-thumb strategy for minimizing the emittance growth due to CSR effects in a DEEX-

based BC is to maintain as small as possible transverse sizes and as large as possible bunch length through the beamline and use the smaller angle bending magnets. The last results in increasing the overall compressor length and requires stronger TDCs ( $\kappa = -1/\eta \sim \theta^{-1}$ ). A more accurate strategy requires a careful analysis of the beam dynamics through the DEEX BC accounting for all the correlations in the phase space imposed in the upstream elements of the beamline.

Since transverse  $(x, x')$  and longitudinal dynamics  $(z, z')$  are highly coupled while a beam propagates through a DEEX BC, we expect to find a strong dependence of the CSR effects from the actual transverse phase space on the entrance of the beamline. It is defined by the initial Twiss parameters of the beam and can be adjusted at the entrance and the exit of the compressor if necessary by adding linear transverse optics elements: quads and drifts. Since the initial beam size  $\sigma_z$  is independent from the input Twiss parameters, and the longitudinal beam size after the first EEX strongly depends on them, we also analyze the longitudinal compression factor after the first EEX:  $m_1 = (\sigma_z)_i/(\sigma_z)_{EEX1}$  to find a rule-of-thumb for designing the DEEX BC.

Comparison of figures 2.7 (a) and 2.7 (b) indicates that the maximum degradation of the phase space (quantified by  $\det(\Sigma)$ ) occurs when the current after the first EEX is maximized (that is for the large value of the parameter  $m_1$ ). On the first look, this contradicts to the  $\sigma_z$  scaling presented in equation (2.88). Although it might be a coincidental occasion, we speculate that this may have some reasonable physical explanation. Figure 2.5 demonstrates that the major growth of eigen-emittance  $\lambda_2$  corresponding to the transverse emittance  $\epsilon_{n_x}$  on the entrance/exit of the beamline happens in the second EEX. This is predominantly because the initial longitudinal emittance is roughly 40 times bigger than the initial transverse emittance, and on the entrance of the second EEX module they are swapped. Similarly, the bunch length at the exit of the compressor roughly corresponds to its transverse bunch size at the entrance and what is more important at the exit of the beamline. The transverse

bunch size is suggested to be minimized according to equation (2.88). Since the beam phase space is highly-coupled through the DEEX BC it is hard to theoretically estimate the optimal transverse-longitudinal bunch profile along the beamline. Nevertheless, figure 2.7 (b) showcases the ability of tuning the longitudinal-transverse bunch sizes through the beamline and, in particular, allows to adjust the fraction of compression after the first EEX<sup>33</sup> using the initial Twiss parameters ( $\alpha_x$  and  $\beta_x$ ) associated with the horizontal degree of freedom.

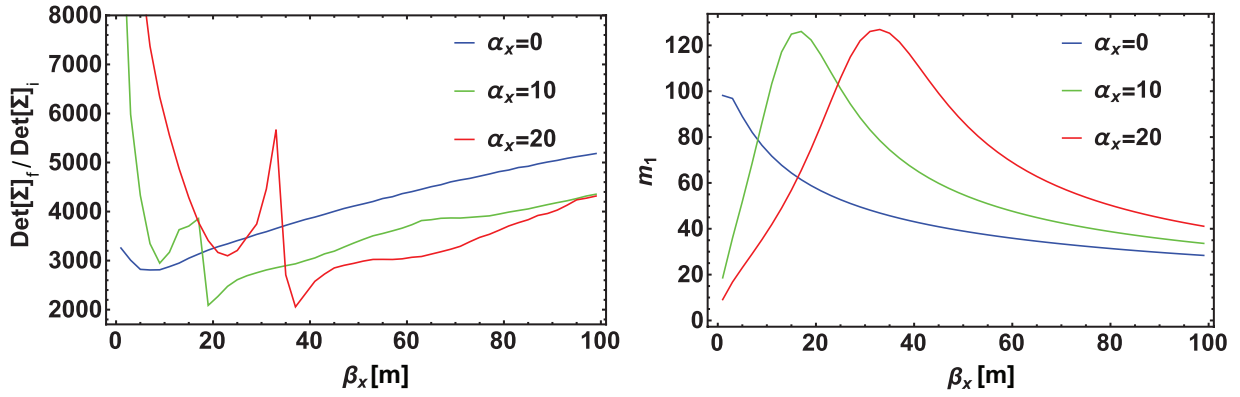


Figure 2.7: Dependence of the  $\Sigma$ -matrix determinant fold-increase (left) and the compression factor of the beam length after the 1st EEX (right) from the Twiss parameters.

### 2.6.2 Optimization of beamline elements: unsymmetrical DEEX

On the next step, we test the ES optimization algorithm in 2D space of the Twiss parameters versus a simple 2-dimensional scan search with a goal to find the actual minimum of the 6D phase space volume characterized by  $\det(\Sigma)$  at the end of the beamline. After a total of  $40 \times 20 = 800$  steps, describing the 2D grid of 40 points along  $\beta_x$  and 20 points along  $\alpha_x$ , we find that the minimum of  $\det(\Sigma)_f / \det(\Sigma)_i$  is reached at  $\beta_x \approx 33$  m and  $\alpha_x \approx 18$  resulting in  $\epsilon_{x_f} / \epsilon_{x_i} \approx 37.3$ . We find then the similar quantities for the optimal Twiss

<sup>33</sup>Note that the final compression factor  $m$  is independent of the Twiss parameters in the approximation of the linear single-particle dynamics.

parameters:  $\beta_x \approx 30.3$  m and  $\alpha_x \approx 16.3$ , resulting in the transverse emittance fold increase  $\epsilon_{x_f}/\epsilon_{x_i} \approx 38$  for 800 ES optimization steps. While the brutal force search is yet achievable in 2D space of parameters<sup>34</sup>, it requires tremendous amount of steps  $n$  for higher dimensional space of parameters, scaling as:  $n = k^m$ , where  $k$  is the average number of points along each direction, and  $m$  is the number of parameters.

The ideal scenario for linear beam optics is to ensure the real dynamics of the system, accounting for all nonlinear and collective effects, stays as close as possible to the linear dynamics<sup>35</sup>. Therefore, we use invariants of the linear dynamics, eigen emittances, or to be more specific, its square product  $\det(\Sigma)$  in most cases, as the cost function in the ES optimization, while varying parameters of the beamline and the Twiss parameters simultaneously. As we discussed in Section 2.5, this concept generally fits for any optimization problem, where there are a lot of tunable parameters but the specific model of the system is not known. Here we also demonstrate that this strategy might be useful when the beamline is known (DEEX), but the optimal configuration of the beam parameters along the beamline as well as the proper settings of the beamline elements (a bend angle, a free space propagation length, a cavity strength, etc.) are hard to predict analytically. In our particular case of DEEX BC, there are multiple beam elements in which CSR strongly affects beam dynamics. These effects strongly depend on the beam parameters in each element as well as on the element settings themselves. The beam parameters in the downstream elements are highly coupled to the beam dynamics in the upstream elements. Moreover, keeping the smallest possible eigen emittances in each element of the scheme does not necessary lead to the minimum eigen emittances at the exit of the beamline due to the potential emittance

---

<sup>34</sup>Each ELEGANT run pushing 100000 particles through all CSR drifts and CSR bends of the DEEX BC takes several minutes on the average performance computer, data analysis after each run and updating input files for the tracking code takes only few seconds.

<sup>35</sup>There are conceptually different accelerators: for example Integrable Optics Test Accelerator (IOTA) at Fermi National Accelerator Laboratory [103], which relies on integrable nonlinear optics for optimal beam dynamics.

compensation, which we will demonstrate in Section 2.6.4. Hence, optimizing eigen emittances after each element of the beamline is not necessary the most effective strategy. It is quite obvious that the actual beam parameters in each CSR producing element of a DEEX BC strongly depend not only on the beam parameters at the entrance of the compressor, but also on the parameters of the prior beam elements. While the final beam parameters at the exit of the DEEX BC are fixed, there is, in principal, an infinite amount of combinations for an exchange to be exact in each EEX module and deliver the compressed beam at the end in the approximation of the linear dynamics. All of these combinations potentially lead to a different output, when the realistic beam dynamics is considered. In this context, the optimization search is dedicated to find such an optimum.

One can independently vary a bend angle, a bend radius, and two drifts, while properly adjusting the cavity parameter  $\kappa = -1/\eta$  in order to maintain the exact exchange (see Section 2.3 for details) in each EEX modules composing the DEEX BC. Initially, first and second EEX were proposed to be identical. However, there is no limitation for them to be different, if the telescope parameters are properly adjusted. Indeed, initial transverse  $(x, x')$  and longitudinal  $(z, z')$  phase spaces have a quite different size and shape. the beam shape is completely changed after the phase spaces have been exchanged in the first EEX (ideally tuned for that input beam configuration) and compressed in transverse direction in the telescope. Therefore, a perfectly tuned second EEX is required. We add four more parameters of the beam optics in each EEX module in addition to two the Twiss parameters. This results in the overall ten parameters which have to be optimized. A “brute force” scan would have to be performed over a 10-dimension space of parameters which is impossible to accomplish in reasonable time ( $\sim 10^{10}$  steps for ten points in each direction). Therefore, we further use ES algorithm introduced in Sec. 2.5 for optimization. As mentioned above, this algorithm is capable to perform a fast multidimensional extremum search by oscillating all parameters independently at the same time. Figure 2.8 depicts the optimal configuration

of the Twiss parameters and the beam optics elements found after 800 steps. Right away, it delivers  $\epsilon_{n_x}$  fold increase of  $\sim 12$ , while  $\det(\Sigma)$  demonstrates  $\sim 230$ -fold increase. This is significantly improved result compared to the DEEX discussed above with symmetrical configuration and the optimal Twiss parameters. Pushing ES optimization further by adjusting its gain and amplitude (see section 2.5 for more details), we reach roughly 158-fold increase of  $\det(\Sigma)$  and  $(\epsilon_{n_x})_f/(\epsilon_{n_x})_i \approx 10$  for the desired state-of-the-art beam parameters for MaRIE XFEL which are listed as set I in Table 2.2. Output phases spaces for the case of real dynamics are getting much closer to the linear dynamics case than in the unoptimized design but are still highly distorted by the CSR effects (2.9). The only down-side of the derived unsymmetrical design is that the final compression factor got slightly reduced to  $m \approx 20$ . Table 2.4 summarizes the initial and final parameters of the beam for the initial symmetrical DEEX, for the symmetrical DEEX with the optimized Twiss parameters only and for the unsymmetrical DEEX found by ES optimization. It clearly demonstrates that significant minimization of enlargement of eigen emittances and emittances can be reached by tuning the Twiss parameters of the beam and parameters of the beamline elements at the same time. The quantitative analysis of emittances and the shape of the output phase space suggest that the further optimization of the BC is required so that it can be used in MaRIE XFEL accelerator.

### 2.6.3 Dependence of the phase space degradation from the input beam parameters

CSR in general dominates in enlarging emittances over nonlinear dynamics effects in this scheme. At this point, the only mechanism to optimize this particular DEEX design<sup>36</sup> for

---

<sup>36</sup>Adding new elements in the beamline including multipoles of the higher orders: sextupoles, octupoles, etc. is considered here as the modification of the design.

Table 2.4: Initial (i) and final (f) beam parameters (rms) in the DEEX bunch compressor for the unoptimized symmetrical design (SD), the symmetrical design with the optimized Twiss parameters (OSD) and the optimized unsymmetrical design (OUD). The simulations are performed for the multi-particle dynamics accounting for the CSR effects at 100 pC bunch charge.

Design	SD		OSD		OUD		Units
Electron beam parameters	i	f	i	f	i	f	
Normalized emittance $\epsilon_{n_x}$	0.1	5.29	0.1	3.79	0.1	1.0	$\mu\text{m}$
Normalized emittance $\epsilon_{n_y}$	0.1	0.1	0.1	0.1	0.1	0.1	$\mu\text{m}$
Normalized emittance $\epsilon_{n_z}$	4.4	7.97	4.4	8.5	4.4	8.98	$\mu\text{m}$
Normalized eigen-emittance $\lambda_1$	4.4	8.7	4.4	7.5	4.4	8.86	$\mu\text{m}$
Normalized eigen-emittance $\lambda_2$	0.1	3.66	0.1	2.66	0.1	0.63	$\mu\text{m}$
Normalized eigen-emittance $\lambda_3$	0.1	0.1	0.1	0.1	0.1	0.1	$\mu\text{m}$
Bunch size $\sigma_x$	71.5	122.2	41.1	82.9	54.8	25.5	$\mu\text{m}$
Bunch size $\sigma_y$	122.5	117.4	122.5	117.4	122.5	83.2	$\mu\text{m}$
Bunch length $\sigma_z$	90	3.64	90	3.61	90	4.49	$\mu\text{m}$
Twiss parameter $\beta_x$	100	5.51	33	3.55	58.8	1.27	m
Twiss parameter $\alpha_x$	0	-1.86	18	-2.56	16.08	-0.62	
Twiss parameter $\beta_y$	293.5	269.8	293.5	269.8	293.5	135.4	m
Twiss parameter $\alpha_y$	0	-7.85	0	-7.85	0	-8.72	
Energy spread $\sigma_{\delta\gamma}$	25	1297.3	25	1375.64	25	1185.8	keV
Linear energy slope $\langle zz' \rangle / \sigma_z^2$	0	-180.3	0	-183.8	0	-134.4	$\text{m}^{-1}$
Beam energy $E$	1	1	1	1	1	1	GeV
Final compression $m = \sigma_{z_i} / \sigma_{z_f}$	-	24.7	-	24.95	-	20.0	

these beam parameters is to add freedom on the initial longitudinal phase space which is left beyond the scope of this dissertation<sup>37</sup>. It is generally known that the fold emittance enlargement due to CSR effects will be less critical for “hotter” beams, e.g. if the initial transverse and longitudinal emittances are larger. This raises an interesting question: would the optimized design of unsymmetrical DEEX (Design I in Table 2.1) effectively work for the different set of initial beam parameters. Indeed, the optimum transverse-longitudinal profile

<sup>37</sup>Indeed, chirping or dechirping the beam before DEEX BC and removing the related energy slew after it may reduce CSR effects. Moreover, relatively small chirps do not seem to result in amplifying LSC-induced microbunch instabilities. While imposing and removing a correlated energy spread adds to the complexity of the DEEX and makes the overall BC scheme quite sophisticated, it might be an important “knob” for optimizing transverse-longitudinal beam profile along the beamline to minimize emittance enlargement.

(and generally speaking the 6-dimensional phase distribution) strongly depends on the input beam parameters. This suggests that the optimum beamline is required for each set of the initial beam parameters. We further investigate this question by simulating the dynamics of the beam with more relaxed initial parameters<sup>38</sup> (Set II in Table 2.2) through the previously optimized beamline (Design I) and by performing the additional ES optimization resulting in the new optimized beamline (Design II).

We start from Design I optimized for the previous beam parameters (Set I in Table 2.2) and test it with new beam parameters (Set II in Table 2.2). We find  $\epsilon_{n_x}$  fold increase is much lower than before and roughly 4.42, while its longitudinal counterpart is approximately 1.2. As mentioned above, since the input beam parameters are changed, there is no guarantee that this design delivers the optimum beam optics for new beam parameters. We perform another ES optimization<sup>39</sup> and find a new design (Design II in Table 2.1) with only 3.4-fold increase of the transverse emittance in the bending plane. It is clear that the real dynamics is much closer to the linear dynamics for the new set of the initial beam parameters which represent “hotter” beam. Moreover, the distortion of the phase space from the CSR effects is now comparable with the distortion due to the nonlinear effects in the approximation of the single-particle dynamics as can be seen in Figure 2.10. The actual parameters of the beamline elements for both DEEX designs are listed in Table 2.1 for comparison.

Further, we investigate how the transverse emittance enlargement scales from the compression factor  $m$  for both designs. During the scan, we adjust the initial longitudinal beam size  $\sigma'_z = \sigma_z \cdot m/25$  and energy spread  $\Delta E' = \Delta E \cdot 25/m$ , such that the resulting longitudinal emittance remains constant to the initial distribution used for the value of  $m = 25$  (see Fig. 2.11 (left)). We observe that both designs are perfectly tuned for the required compression ratio: the minimum of the final emittance  $\epsilon_{n_x}$  is reached at  $m = 25$ , while larger emittances

---

<sup>38</sup>Those are still considered acceptable for limited MaRIE XFEL applications.

<sup>39</sup>We started the ES search from the initial unoptimized symmetrical design.

are obtained at different compression factors. An individual optimization of DEEX BC for LCLS-II beam parameters for each compression ratio, discussed in Section 2.7, suggests that higher compression ratios typically result in more significant emittance degradation predominantly because of the final bunch length critical for the CSR effects in the last bending magnet. It is well-known that CSR effects cryptically depends on the bunch charge [42, 81]. In particular, the emittance enlargement in equation (2.88) scales linearly on the bunch charge. Figure 2.11 (right) demonstrates dependence of the CSR effects from the bunch charge for DEEX Design I and Design II for two sets of the beam parameters (Set I and Set II). The points  $q = 0$  pC represent the fold increase of emittance in DEEX in the approximation of the single-particle nonlinear dynamics. We find that the CSR effects in the optimized DEEX (Design II) got much smaller for more relaxed beam parameters (Set II) for the bunch charge less than 20 pC. This observation suggests that the unsymmetrical DEEX BC can successfully work for low charge bunches.

Ideally, a proper DEEX BC beamline should be found for each set of beam parameters. Design I and II have been optimized for the particular beam parameters:  $\epsilon_{n_x, n_y} = 0.10 \mu\text{m}$ ,  $\Delta E = 25$  keV, and  $\epsilon_{n_x, n_y} = 0.19 \mu\text{m}$ ,  $\Delta E = 70$  keV respectively. We use these optimized designs with different initial transverse emittances and energy spreads to understand scaling of the CSR effects in the context of the optimized beam optics. Figure 2.12 confirms that each of them delivers a minimum of the emittance degradation at the specific point for which it was optimized. As expected, the CSR effects are more critical at smaller initial beam emittances and become comparable with nonlinear effects for emittance values in excess of  $0.5 \mu\text{m}$ . Finally, we analyze how the CSR effects for these two optimized designs depend on the beam energy (Fig. 2.13). Indeed, the DEEX BC does not require having a chirper and dechirper and can be located at any position along the accelerator beamline. ES optimization of the DEEX BC beamline at energies of 250 MeV and 2 GeV does not reveal an improvement in mitigating CSR effects in comparison with results at 1 GeV. This is in a

good agreement with equation (2.88) stating the absence of the emittance enlargement due to CSR from the beam energy.

#### 2.6.4 CSR effects compensation in the low charge regime

Designing and building of the MaRIE facility is a tremendous ongoing project. Meanwhile, there is an interest in building a scaled version of a MaRIE-like photo-cathode delivering smaller charge of only 20 – 30 pC to an accelerator beamline for testing novel ideas at LANL<sup>40</sup>. As previously demonstrated in Fig. 2.11 (b) the CSR effects should become smaller for lower bunch charge. In this section, we discuss ES optimization of DEEX for the relaxed beam parameters (Set II) with the exception of the bunch charge which is reduced from 100 pC to 20 pC. This effort leads to Design III of DEEX. The parameters of the beam elements associated to Design III are listed in Table 2.5, and the optimal input Twiss parameters are  $\beta_x = 19$  m and  $\alpha_x = 6.1$ . This configuration leads to quite acceptable final emittances:  $\epsilon_{n_x}$  with a fraction growth of 35% compared to its initial values while  $\epsilon_{n_y}$  and  $\epsilon_{n_z}$  experience less than 1% enlargement.

The low-charge regime reveals several interesting features justifying the general optimization strategy. First, it is worthwhile to notice that nonlinear dynamics with turned off CSR effects results in actually bigger  $\epsilon_{n_x}$  growth of 70%. Final phase spaces for the cases of linear and nonlinear single-particle dynamics and the multi-particle dynamics accounting for CSR effects ( $q = 20$  pC) are presented in Fig. 2.14 and also confirm the previous statement. This fact should not be surprising, because the beam optics and beam parameters were optimized with ES for the real dynamics at  $q = 20$  pC. One can consider this effect from the different perspective. Indeed, the nonlinear effects in this optimized design are partially compensated

---

<sup>40</sup>Private communications with Nathan Moody.

Table 2.5: Parameters of the elements of DEEX BCs: initial unoptimized design, design II optimized for beam parameters of Set II listed in Table 2.2, design III optimized for the same beam parameters with an exception of the reduced bunch charge of  $q = 20$  pC.

Design	Initial	Design II	Design III	Units
Twiss parameters				
$\beta_x$	100.0	56.6	19	m
$\alpha_x$	0.0	18.6	6.1	
EEX up (A)				
Bend angle A	2.5	2.24	1.86	deg
Bend radius A	1.14	1.20	1.59	m
Drift S1 A	4.8	12.72	17.54	m
Drift S2 A	1.6	0.72	1.29	m
Cavity strength A	4.71	2.00	1.74	m <sup>-1</sup>
EEX down (B)				
Bend angle B	2.5	2.84	0.52	deg
Bend radius B	1.14	0.82	2.7	m
Drift S1 B	4.8	4.98	4.99	m
Drift S2 B	1.6	3.01	0.27	m
Cavity strength B	4.71	4.00	21.9	m <sup>-1</sup>

by the CSR effects resulting in the overall lower eigen emittances at the exit of the beamline. Second important observation is that the CSR and nonlinear effects imposed in the first EEX are partially compensated in the second EEX, as clearly seen from the eigen-emittance evolution through the DEEX beamline (Fig. 2.15). Table 2.6 compares beam parameters at the entrance of the beamline, at the exit of the first EEX module and at the exit of the DEEX BC. The eigen-emittance compensation most likely happens due to compensation of the nonlinear rather than CSR effects. Indeed, the compensation of eigen emittances did not appear in the high-charge (100 pC) regime, where CSR effects enlarge the transverse emittance much more than the nonlinear effects.

Figure 2.16 demonstrates the beam profiles  $\sigma_x$ ,  $\sigma_y$  and  $\sigma_z$  along the optimized beamline. The enlarged  $\sigma_x \approx 3$  mm after the first EEX module (and within the nearby region) might compromise a beam capability to fit in the regular-size beam pipe. This issue can be miti-

Table 2.6: Initial (I), after the first EEX module (M) and final (F) beam parameters (rms) in the DEEX bunch compressor for the optimized unsymmetrical design. The simulations are performed for the multi-particle dynamics accounting for CSR effects for 20 pC bunch charge.

Beam parameters	I	M	F	Units
Normalized emittance $\epsilon_{n_x}$	0.19	12.37	0.26	$\mu\text{m}$
Normalized emittance $\epsilon_{n_y}$	0.19	0.19	0.19	$\mu\text{m}$
Normalized emittance $\epsilon_{n_z}$	12.3	0.29	12.5	$\mu\text{m}$
Normalized eigen-emittance $\lambda_1$	12.3	12.4	12.5	$\mu\text{m}$
Normalized eigen-emittance $\lambda_2$	0.19	0.29	0.24	$\mu\text{m}$
Normalized eigen-emittance $\lambda_3$	0.19	0.19	0.19	$\mu\text{m}$
Bunch size $\sigma_x$	43.0	2983.5	100.6	$\mu\text{m}$
Bunch size $\sigma_y$	168.8	42.1	108.0	$\mu\text{m}$
Bunch length $\sigma_z$	90	0.86	3.60	$\mu\text{m}$
Twiss parameter $\beta_x$	19	1407.8	76.8	m
Twiss parameter $\alpha_x$	6.1	-74.3	-12.2	
Twiss parameter $\beta_y$	293.5	18.29	120.321	m
Twiss parameter $\alpha_y$	0	-2.76	-6.33	
Energy spread $\sigma_{\delta\gamma}$	70	366.57	1770.5	keV
Linear energy slope $\langle zz' \rangle / \sigma_z^2$	0	376.79	-30.6	$\text{m}^{-1}$
Beam energy $E$	1	1	1	GeV
Compression $m = \sigma_{z_i} / \sigma_{z_{m,f}}$	-	105	25	

gated by inserting several focusing lenses in the beamline. The alternative solution realized within the scope of beam elements already present in the DEEX BC can be found with additional ES optimization. One can set up a virtual border for the transverse beam profile along the beamline, which can be realized as an extra term added to the cost function.

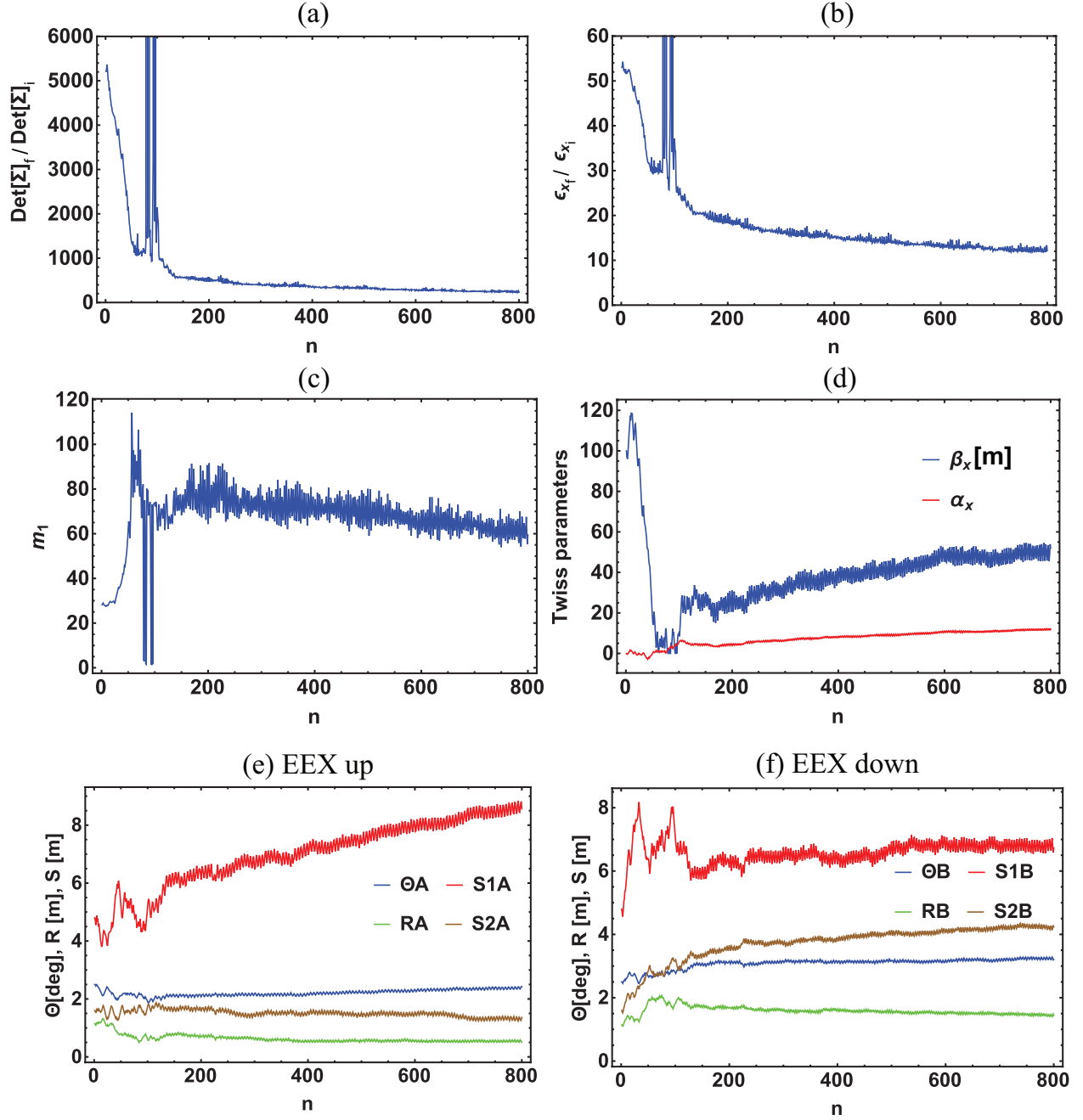


Figure 2.8: Evolution of the ES optimization from the iteration number  $n$  over 800 steps: (a) cost =  $\det(\Sigma)_f / \det(\Sigma)_i$ ; (b)  $(\epsilon_{n_x})_f / (\epsilon_{n_x})_i$ ; (c) the compression ratio after EEX up; (d) the Twiss parameters; (e) parameters of EEX up; (f) parameters of EEX down.

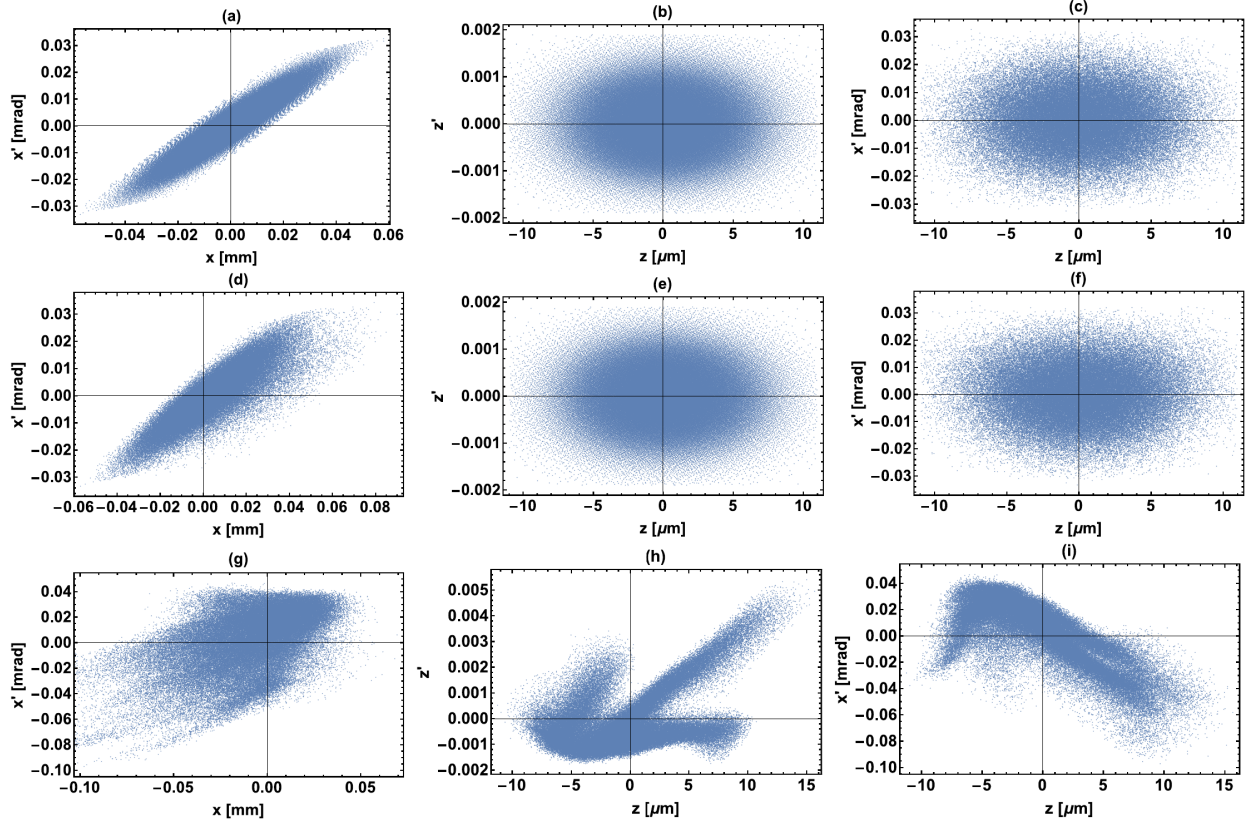


Figure 2.9: Transverse, longitudinal and  $(z, x')$  phase spaces (from left to right) for the linear (a-c) and nonlinear (d-f) single particle dynamics, and for the nonlinear dynamics with the CSR effects for  $q = 100$  pC on the exit of the optimized DEEX BC (Design I, set I). Real dynamics results in approximately 10-fold increase of  $\epsilon_{n_x}$  and 2-fold increase of  $\epsilon_{n_z}$ .

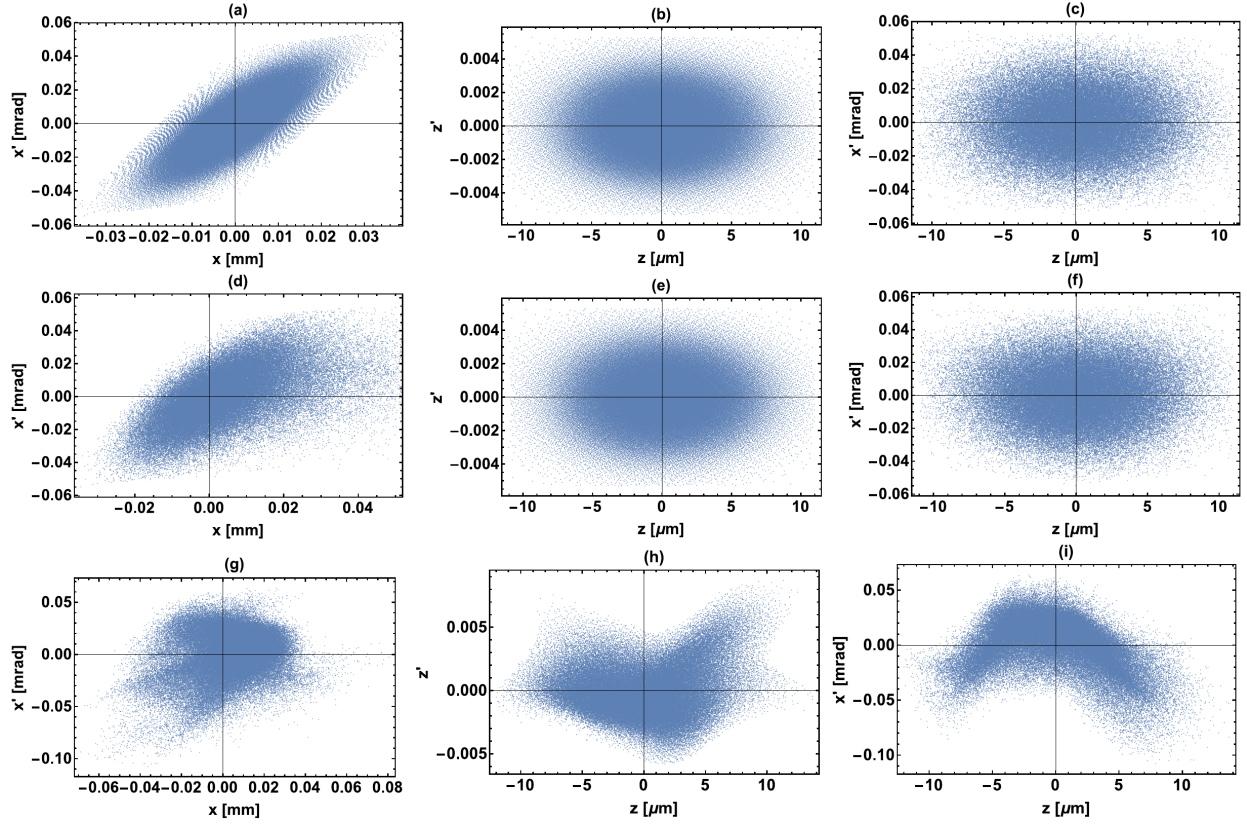


Figure 2.10: Transverse, longitudinal and  $(z, x')$  phase spaces (from left to right) for the different cases of beam dynamics at the end of the optimized DEEX BC (Design II, set II): (a-c) the linear single-particle dynamics; (d-f) the nonlinear single-particle dynamics (1.89-fold increase of  $\epsilon_{n_x}$ ,  $\epsilon_{n_z}$  does not change); (g-i) the multi-particle dynamics with the CSR effects for  $q = 100$  pC (3.44-fold increase of  $\epsilon_{n_x}$ , 1.16-fold increase of  $\epsilon_{n_z}$ ).

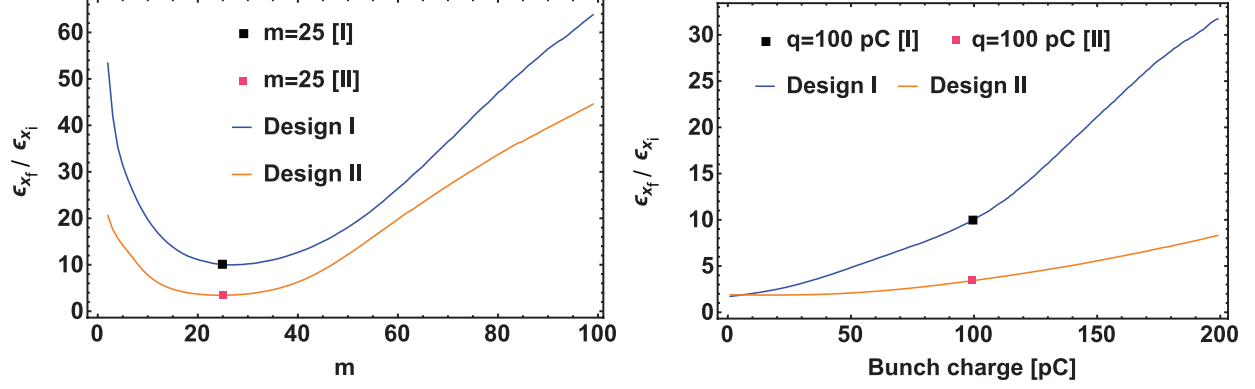


Figure 2.11: Left: dependence of the emittance fold increase from the compression factor  $m$  for Designs I and Design II of DEEX BC. Initial longitudinal parameters of the beam are adjusted to achieve the same beam size at the end of the compressor as expected for  $m = 25$ :  $\sigma'_z = \sigma_z \cdot m/25$  and  $\Delta E' = \Delta E \cdot 25/m$ . Right: dependence of the emittance fold increase in DEEX BC (Design I and II) from the bunch charge  $q$ . Points are marking the beam parameters for which each design was optimized.

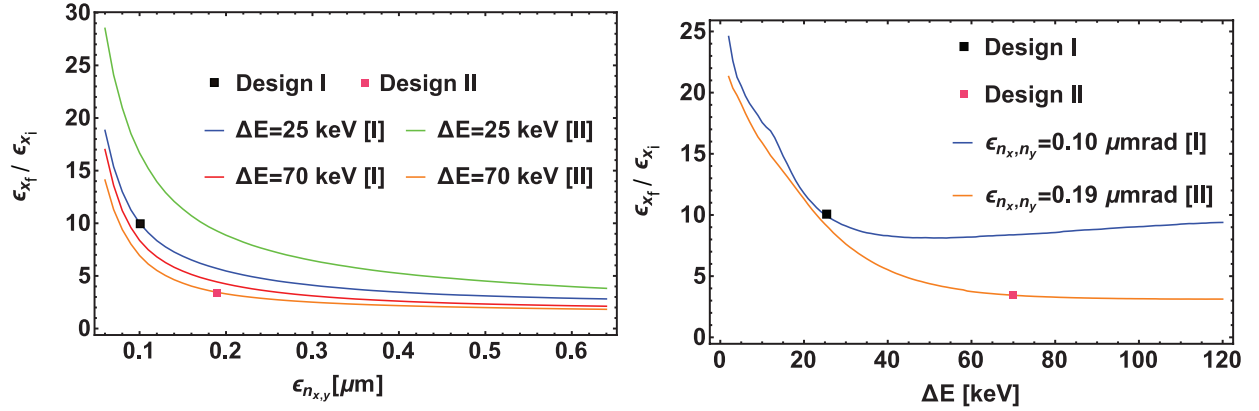


Figure 2.12: Dependence of the fold emittance increase from the initial transverse normalized emittances at different initial energy spreads for Design I and II (left). Dependence of the fold emittance increase from the initial energy spread for Design I and II (right). Points are marking the beam parameters for which each design was optimized.

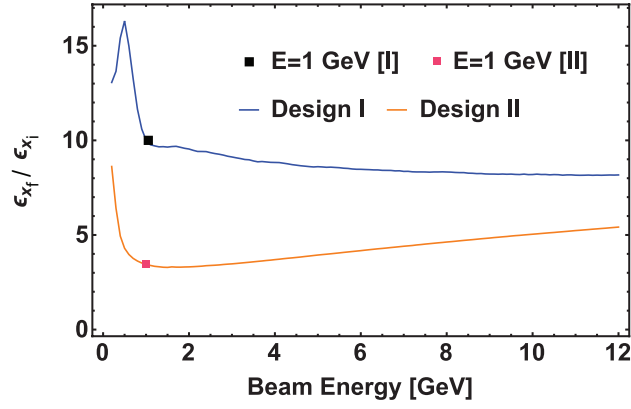


Figure 2.13: Dependence of the fold emittance increase from the beam energy for Design I:  $\epsilon_{n_x, n_y} = 0.10 \mu\text{m}$ ,  $\Delta E = 25 \text{ keV}$ ; and Design II:  $\epsilon_{n_x, n_y} = 0.19 \mu\text{m}$ ,  $\Delta E = 70 \text{ keV}$ . Points are marking the beam parameters for which each design was optimized.

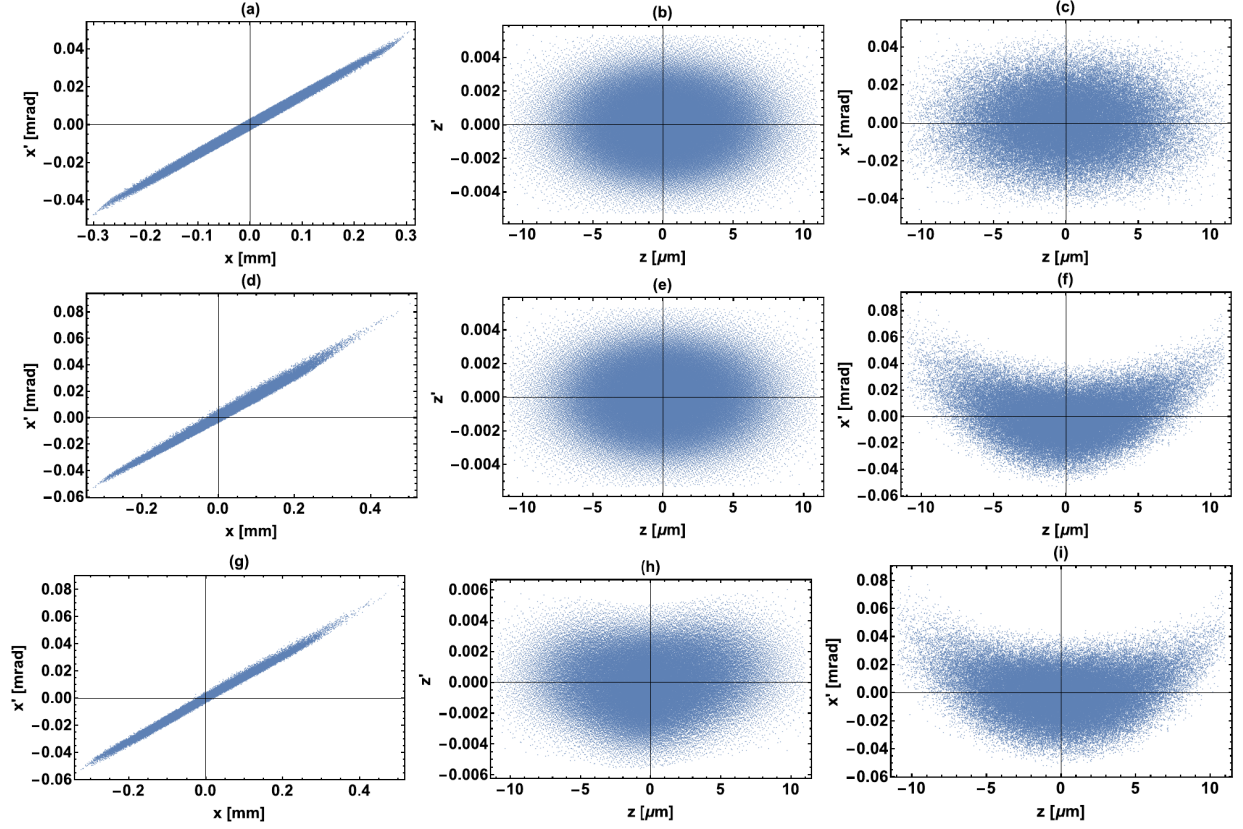


Figure 2.14: Transverse, longitudinal and  $(z, x')$  phase spaces at the exit of the optimized DEEX (Design III, set III) from left to right: (a-c) the linear single-particle dynamics; (d-f) the nonlinear single-particle dynamics resulting in 1.7-fold increase of  $\epsilon_{n_x}$ , 1.01-fold increase of  $\epsilon_{n_z}$ ; (g-i) the nonlinear dynamics with CSR for  $q = 20$  pC resulting in 1.35-fold increase of  $\epsilon_{n_x}$ , 1.01-fold increase of  $\epsilon_{n_z}$  (bottom). Real dynamics with the CSR effects, for which this design was optimized, results in better transverse beam quality than nonlinear dynamics without CSR.

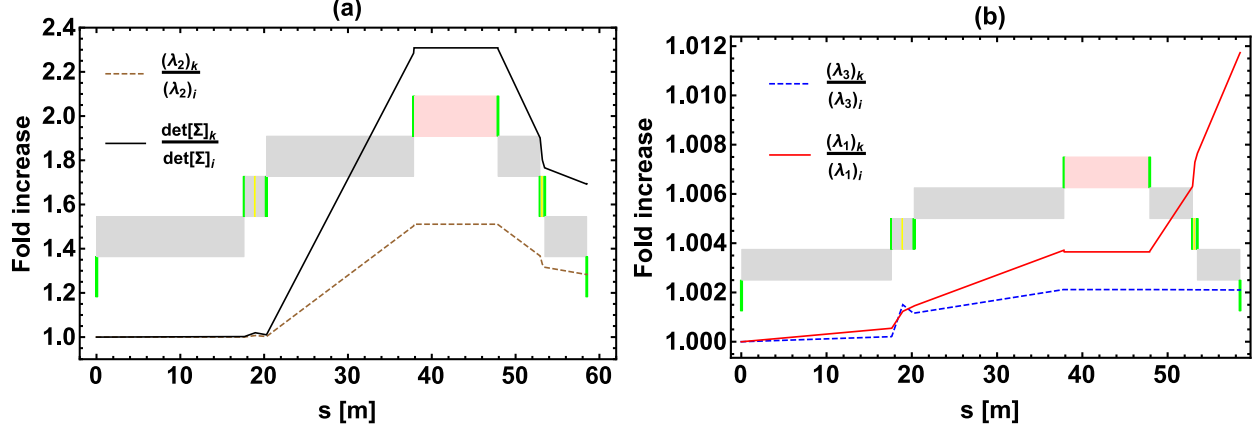


Figure 2.15: Evolution of the fold increase of eigen emittances after each beam element ( $k$ ) from the distance along the beamline in the optimized DEEX BC design III: (a)  $\det(\Sigma)$  and eigen-emittance  $\lambda_2$ , corresponding to  $\epsilon_x$  on the entrance/exit of the beamline; (b) eigen-emittance  $\lambda_3$ , corresponding to  $\epsilon_z$ , and eigen-emittance  $\lambda_1$ , corresponding to  $\epsilon_y$ . The elements of the beamline are represented by the color scheme as follows: green is for the bending magnets, yellow is for the TDCs, gray is for the drifts and pink is for the telescope. The TDCs and dipole magnet lengths are enlarged on the scheme to be better visualized.

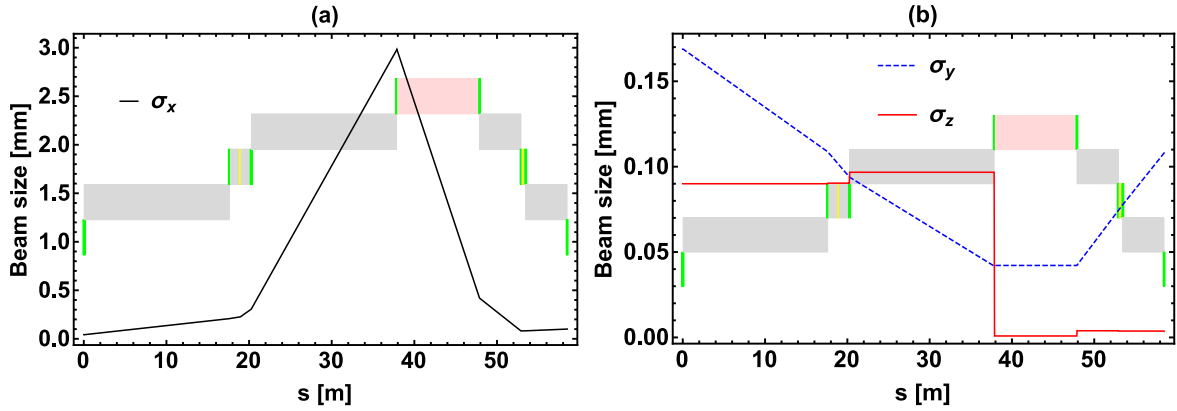


Figure 2.16: RMS beam sizes evolution through optimized DEEX BC: (a)  $\sigma_x$ ; (b)  $\sigma_y$  and  $\sigma_z$ .

## 2.7 2EEX BC optimum designs for another FELs

In this section, we present DEEX BC designs as an alternative solution to the chicane-based BCs at different FEL facilities: existing European XFEL and planning to be built LCLS-II at SLAC. As previously, beamline elements were optimized with ES algorithm. Beam parameters and beam-optics parameters are respectively summarized in Table 2.7 and Table 2.8. For both facilities, we assume no initial/residual energy chirp. We also define the initial longitudinal beam parameters from the required bunch duration and energy spread at the entrance of an undulator, while we keep the designed compression ratio as for MaRIE  $m = 25$ . European XFEL is driven by the beam with a large bunch charge  $q = 1$  nC and large

Table 2.7: European XFEL and LCLS-II beam parameters on the entrance of the bunch compressor used in our simulations [80]. Listed twiss parameters are found during optimization.

Electron beam	Eur. XFEL	LCLS-II	
Normalized emittance	1.4	0.45	$\mu\text{m}$
Energy spread (rms)	100	20	keV
Bunch duration (rms)	600	210	$\mu\text{m}$
Linear energy slope (rms)	0	0	$\text{m}^{-1}$
Beam energy	2	1.6	GeV
Bunch charge	1000	100	pC
Required compression	25	25	
Twiss parameter $\beta_x$	17.0	33.0	m
Twiss parameter $\alpha_x$	5.0	4.8	

emittances  $\epsilon_{n_x, n_y} = 1.4 \mu\text{m}$ . The optimized 2EEX BC results in roughly 3.7-fold increase of emittance  $\epsilon_{n_x}$ . The longitudinal emittance at the exit of the scheme is only 3% more than its initial value, while emittance  $\epsilon_{n_y}$  does not change as expected for the uncoupled ( $y, y'$ ) dynamics. In contrast, LCLS-II is expected to be driven by the beam with  $q = 100$  pC bunch charge, same as for MaRIE XFEL, and emittances  $\epsilon_{n_x, n_y} = 0.45 \mu\text{m}$ , which are larger than those for MaRIE XFEL. The optimized 2EEX BC at  $m = 25$  compression ratio results

in 1.8-fold increase of emittance  $\epsilon_{n_x}$ . The longitudinal emittance at the exit of the scheme is 12.5% larger than its initial value, while emittance  $\epsilon_{n_z}$  does not change.

Table 2.8: Parameters of the optimized 2EEX BCs for European XFEL and LCLS-II for the input beam parameters listed in Table 2.7.

Design	Eur. XFEL	LCLS-II	
<b>EEX up (A)</b>			
Bend angle A	3.38	2.17	deg
Bend radius A	0.57	1.46	m
Drift S1 A	17.53	17.04	m
Drift S2 A	0.44	1.08	m
Cavity strength A	0.96	1.54	m <sup>-1</sup>
<b>EEX down (B)</b>			
Bend angle B	0.53	0.36	deg
Bend radius B	2.77	2.25	m
Drift S1 B	6.24	4.82	m
Drift S2 B	0.02	0.02	m
Cavity strength B	17.34	32.95	m <sup>-1</sup>

The enlargement of the transverse emittance for LCLS-II beam parameters is quite moderate (much less than one for European XFEL) in the DEEX BC. Next, we optimize the parameters of the beam elements for different compression ratios starting from  $m = 17$  planned in the baseline design of LCLS-II. We use the initial beam parameters listed in Table 2.7 (for LCLS-II) with exceptions on the longitudinal beam size  $\sigma_z = 153 \mu\text{m}$  and energy spread  $\sigma'_{\delta\gamma} = 18.38 \text{ keV}$ . The Fig. 2.17 demonstrates the linear dependence of the fold emittance increase from the compression ratio  $m$ . In particular, larger compression in DEEX results in larger transverse emittance growth and smaller longitudinal emittance growth. The parameters of the beam elements and the final emittances for the different compression ratios are listed in Table 2.9. A reasonable emittance enlargement of 30% for  $m = 7$  justifies the applicability of DEEX BC as a second bunch compressor (or as its part) for LCLS-II.

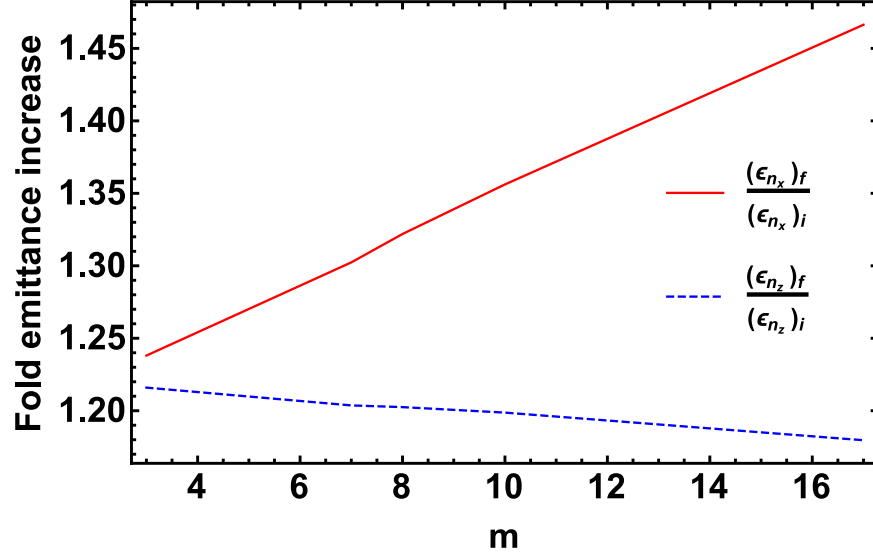


Figure 2.17: The ratio of final and initial emittances for transverse and longitudinal phase spaces from the compression ratio  $m$ . The beamline and the Twiss parameters are individually optimized for each compression ratio and summarized in Table 2.9, while other input beam parameters remain invariant.

Table 2.9: Parameters of the DEEX beamline for LCLS-II and fold increase of emittances for different compression ratios.

Compression $m$	17	10	8	7	3	Units
<b>Fold emittance increase</b>						
$(\epsilon_{n_x})_f / (\epsilon_{n_x})_i$	1.47	1.36	1.32	1.30	1.24	
$(\epsilon_{n_z})_f / (\epsilon_{n_z})_i$	1.180	1.199	1.202	1.204	1.216	
<b>Input Twiss parameters</b>						
$\beta_x$	11.5	12.6	14.8	14.9	18.1	m
$\alpha_x$	4.2	3.4	3.4	3.2	3.0	
<b>EEX up (A)</b>						
Bend angle A	2.31	2.17	2.34	2.40	2.60	deg
Bend radius A	0.5	0.5	0.5	0.5	0.51	m
Drift S1 A	19.74	19.60	19.67	19.65	19.44	m
Drift S2 A	0.95	1.33	1.53	1.348	1.53	m
Cavity strength A	1.25	1.25	1.24	1.21	1.1	$\text{m}^{-1}$
<b>EEX down (B)</b>						
Bend angle B	0.63	0.97	1.09	1.12	1.78	deg
Bend radius B	3.90	3.93	3.19	2.75	2.03	m
Drift S1 B	9.78	10.42	10.89	11.59	12.31	m
Drift S2 B	0.017	0.017	0.017	0.017	0.017	m
Cavity strength B	9.29	5.62	4.81	4.40	2.6	$\text{m}^{-1}$

## 2.8 Alternative emittance exchanger (AEEX) design with two bending magnets

Bending magnets are major elements imposing CSR effects in chicane-based and EEX-based bunch compressors<sup>41</sup>. Motivated by an idea to suppress the number of bending magnets in an EEX-based BC, we constructed an alternative configuration of the emittance exchanger<sup>42</sup>. The exact EEX is realized by two transverse deflecting cavities<sup>43</sup> separated by consequently lined up elements: a regular drift, a dogleg with a negative drift (a single triplet) between its bends, and another triplet (Fig. 2.18 (a)). This configuration is inspired by the permutation of matrices of the beam line modules of the standard EEX configuration, consisting of two doglegs and one deflecting cavity as discussed previously. The appearance of negative drifts is caused by necessity to satisfy the exact exchange conditions. The matrix of this EEX in 4D  $(x, x', z, z')$  phase space<sup>44</sup> can be found as multiplication of its structural components using Equations (2.4, 2.43, 2.44):

$$R_{AEEX} = R_{TDC}(k_2) \cdot R_{Drift}(L_2) \cdot R_{Dogleg}(L_{eff}, \eta, \psi) \cdot R_{Drift}(L_1) \cdot R_{TDC}(k_1) \quad , \quad (2.90)$$

---

<sup>41</sup>They can be further enhanced in consequent drifts.

<sup>42</sup>A similar EEX design was independently reported in [104], while an idea of reducing the number of bends in DEEX was also proposed in [105].

<sup>43</sup>A thin cavity approximation is assumed.

<sup>44</sup>The  $(y, y')$  dynamics is uncoupled as typically for an emittance exchanger and the related transfer matrices can be found as a product of its structural components similarly how it was shown for the standard EEX scheme.

so we obtain:

$$R_{AEEX} = \begin{pmatrix} 1 + k_1\eta & L_1 + L_2 + L_{eff} & k_1(L_1 + L_2 + L_{eff}) & \eta \\ k_1k_2\psi & 1 + k_2\eta & k_1 + k_2 + k_1k_2\eta & k_2\psi \\ k_1\psi & \eta & 1 + k_1\eta & \psi \\ k_1 + k_2 + k_1k_2\eta & k_1(L_1 + L_2 + L_{eff}) & k_1k_2(L_1 + L_2 + L_{eff}) & 1 + k_2\eta \end{pmatrix}. \quad (2.91)$$

If one chooses the beam elements parameters to satisfy the following equations:

$$k_1 = k_2 = -1/\eta \quad , \quad (2.92)$$

$$L_2 = -L_1 - L_{eff} \quad , \quad (2.93)$$

$$\psi = 0 \quad , \quad (2.94)$$

then this combination of elements will deliver the exact emittance exchange:

$$R_{AEEX} = \begin{pmatrix} 0 & 0 & 0 & \eta \\ 0 & 0 & -1/\eta & 0 \\ 0 & \eta & 0 & 0 \\ -1/\eta & 0 & 0 & 0 \end{pmatrix}. \quad (2.95)$$

Any orientation of the dogleg (up or down) can satisfy the first condition since the cavity strength can be of any sign. The condition in Equation (2.93) can be satisfied by using one negative drift such that  $L_2 < 0$  and  $L_1 > 0$ ,  $L_{eff} > 0$  or two negative drifts to make the design symmetrical element vice<sup>45</sup>:  $L_2 = L_1 = -0.5L_{eff} < 0$ . The negative drift can be realized using two triplets as discussed in Equation (2.60). Alternatively one can use a single

---

<sup>45</sup>The condition on the equality of two negative drifts is optional and introduced for simplicity.

triplet described in Eq. (2.59) to reduce the amount of focusing elements by swapping the sign of the last TDC on the opposite which results in the updated condition:  $k_2 = 1/\eta$ .

Dispersion  $\eta$  in the matrix of a conventional dogleg (with a regular free space propagation sections in between of two bending magnets) can be positive or negative depending on the direction of the shift defined by the angle of the first bending magnet, while  $L_{eff}$  and  $\psi$  are strictly positive for reasonable bend lengths and angles. For quantitative discussion, we consider here the same dogleg as we used in the traditional EEX scheme, with edge angles  $\alpha_1 = 0$  and  $\alpha_1 = \theta$  for the first magnet and  $\alpha_1 = \theta$  and  $\alpha_2 = 0$  for the second magnet<sup>46</sup>. We write down the dogleg parameters:

$$\eta = -\sec \theta (2D + L + L \sec \theta) \tan \frac{\theta}{2} \quad , \quad (2.96)$$

$$L_{eff} = \sec \theta (2D + L \sec \theta) \quad , \quad (2.97)$$

$$\psi = 2D(\sec \theta - \theta \csc \theta) + L \tan^2 \theta; \quad , \quad (2.98)$$

where  $D$  and  $\theta$  are dipole magnet length and angle, and  $L$  is the drift length in between of two bending magnets. If  $-\pi/2 < \theta < \pi/2$ , which is legitimate for the regular bending magnet, we find that  $\sec \theta > 0$  and  $L_{eff} > 0$  if  $L > 0$ . Similarly,  $\sec \theta - \theta \csc \theta = \sec \theta + \theta/\sin \theta > 0$  resulting in  $\psi > 0$  for  $L > 0$ . Since  $L_{eff}$  can be compensated by the negative drift  $L_2$  if necessary, we request  $L < 0$  such that  $\psi$  in Equation (2.98) satisfies the condition in

---

<sup>46</sup>Similarly the dogleg with symmetrical edge angles can be discussed using Equations (2.9-2.11).

Equation (2.94). We find then the final conditions on the matrix elements of the alternative emittance exchanger:

$$L = -\frac{2d(\sec \theta - \theta \csc \theta)}{\tan^2 \theta} \quad , \quad (2.99)$$

$$\eta = -2d \csc \theta (-1 + \theta \csc \theta) \quad , \quad (2.100)$$

$$L_{eff} = -d \csc^3 \theta (\sin(2\theta) - 2\theta) \quad , \quad (2.101)$$

which can be satisfied if the positive drift is substituted with a negative drift in a dogleg in between of two bending magnets.

The number of bending magnets (active sources of CSR) is reduced from four to two in each EEX. Interestingly, when two emittance exchangers are combined together to form a bunch compressor, the overall scheme reminds a chicane with additional deflecting cavities inserted before and after each dogleg<sup>47</sup> as demonstrated in Fig. 2.18 (b). Unfortunately, this

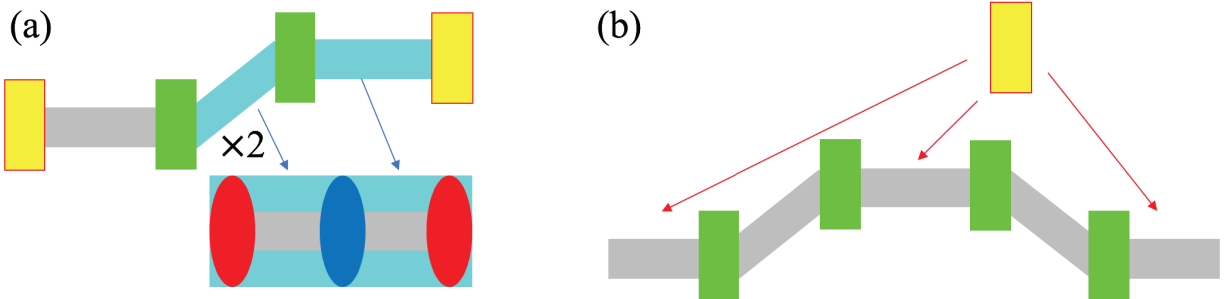


Figure 2.18: (a) Emittance Exchanger configuration with reduced number of bending magnets. (b) A bunch compressor, combined from two alternative EEX configurations, has a similar topology as a chicane with inserted transverse deflecting cavities. Yellow symbols represent TDCs, green rectangles represent dipole magnets, and blue and red ovals represent focusing and defocussing quadrupoles in respect to  $(x, x')$  phase space. The negative drift sections are highlighted blue, while the regular drift sections are gray.

sophisticated EEX topology “suffers” from the CSR effects even more than the standard EEX

<sup>47</sup>Another exception is that some positive drifts are substituted by the negative drifts.

scheme. In particular, it results in 60-fold increase of  $\epsilon_{n_x}$  at the exit of DEEX BC combined from AEEX modules. This and a double-chicane BC prove wrong the typical misconception that reducing the actual number of bending magnets leads to minimization of CSR effects in the overall scheme. While the proposed scheme does not work for these particular beam parameters as a module of the bunch compressor, it might be useful for different phase space manipulations of the beam. For example, this can be convenient for the longitudinal beam shaping required in dielectric wakefield accelerators. This beam shaping can be realized by a beam propagation through a transverse mask followed by an EEX [106]. As a result transverse shaping can be transferred to the longitudinal phase space.

## 2.9 Summary

We demonstrated a new type of a bunch compressor, the unsymmetrical double emittance exchanger. Each emittance exchanger is tuned to match with parameters of the propagating beam. While there is a general understanding of the strong CSR dependence from the instant beam parameters in each component of the scheme, as well as from the parameters of the beam elements, the optimum beamline design for the DEEX topology is practically unpredictable. This is due to two main factors: (a) the dynamics is highly coupled in 4-dimensional phase space; (b) the minimum of emittance (eigen emittance) degradation imposed by the CSR effects is not necessary reached when the CSR effects are minimized in each component of the beamline. The later statement is valid if the mutual compensation of the nonlinear or/and collective effects happens along the different elements of the beamline. This concept became clear when DEEX BC scheme was optimized in the low charge regime as discussed in Section 2.6.4. The unsymmetrical design of DEEX was found by the model independent Extremum Seeking optimization effectively working in a highly-dimensional space of

parameters. The invariants of linear dynamics, eigen emittances, were used to quantitatively characterize real dynamics along the BC beamline. Increase in the determinant of the 6-dimensional  $\Sigma$ -matrix was used as a cost function for the optimization. Such technique is fast and universal for the optimization of any complicated beamline relying on the linear beam dynamics<sup>48</sup>. The CSR effects for the state-of-the-art MaRIE parameters (ultra-low emittances and energy spread at relatively high bunch charge) still remain critical for the effective X-ray lasing even after the significant improvement of the scheme performance with described method. The methods and results are summarized in Ref. [107].

An alternative scheme of the emittance exchanger was demonstrated. This scheme has two bending magnets instead of four, which results in less active CSR-imposing elements than in the original EEX scheme. However, the detailed simulation studies for the MaRIE beam parameters showed that this scheme suffers from the CSR effects even more than the standard EEX configuration and is not capable to improve performance of DEEX BC. Finally, EEX-based bunch compressor, due to its flexibility, might be still convenient for the 6D electron beam shaping in order to increase FEL performance, similarly to the concept discussed in Chapter 4 for an ICS source.

---

<sup>48</sup>Tuning beam elements of the higher order, i.e. sextupoles, octupoles, etc. to compensate nonlinearities of the single-particle dynamics or collective effects can be also realized with the proposed method.

# CHAPTER 3

## CHIRPER AND DECHIRPER DESIGN BASED ON TRANSVERSE DEFLECTING CAVITIES

In this chapter, we discuss the beam optics required for imposing and removing the correlated energy spread along the bunch, or, using the terminology popular in the accelerator community: chirping and dechirping the beam. Such a configuration of the longitudinal phase space of the electron beam is required in the chicane-based bunch compressors as explained in Chapter 2. First, we overview the conventional technique for chirping and dechirping the beam using an off-crest acceleration. After that, we introduce the novel solution of how to impose the positive chirp on the beam using a series of transverse deflecting cavities separated by drifts, and describe it in the linear regime using the matrix formalism. Then, we present two designs of the TDC-based chirper at 250 MeV and 1 GeV for the MaRIE XFEL linac, aimed to impose a large correlated energy spread on the beam before the chicane of the second bunch compressor. Both designs are constructed to fit in respectively two and four cryomodules in the frame of the existing superconducting linac outline [80] with a minimal of modifications required. Simulation and optimization studies of the non-linear and longitudinal space charge effects are accomplished using the beam tracking code ELEGANT [37] and the derived results are presented. In the second part of the Chapter, we describe how the scheme can be modified with quadrupole magnets to impose a negative chirp on the beam (or remove the present chirp, *i.e.* dechirp the beam). In particular, we design two beamline schemes at 250 MeV for the MaRIE injector test stand to impose a negative chirp and at 1 GeV for the MaRIE linac to remove a positive chirp from the beam

after the chicane of the second bunch compressor. We also present the optimization results of both schemes accomplished with tuning of the input Twiss parameters, nonlinear optics and adjusting the voltage in the last deflecting cavity. The work described in this chapter is summarized in Ref. [108].

### 3.1 Standard Chirper configurations

A beam with nonzero correlated energy spread is required in front of a chicane. In particular, more energetic electrons should be located in front of the beam, and less energetic electrons in the tail of the beam. Following the methods explained in Chapter 2, we describe this action using the matrix formalism for the 4D phase space  $(x, x', z, z')$ . An ideal beam chirp is described via the following matrix:

$$R_{Chirp} = \begin{pmatrix} 1 & L & 0 & 0 \\ 0 & 1 & 0 & 0 \\ 0 & 0 & 1 & 0 \\ 0 & 0 & R_{65} & 1 \end{pmatrix}, \quad (3.1)$$

where  $R_{65} < 0$ , resulting in  $z'_f = z'_i + R_{65}z_i$ . It practically means that the electrons in the tail of the beam become more energetic, while electrons in the front of the beam become less energetic. The chirp action is linearly proportional to the electron coordinate, and there is no effect on the average energy of the beam. The same matrix is valid for dechirping the beam if  $R_{65} > 0$ , and describes exactly the opposite action. Meanwhile, transverse motion in  $(y, y')$  phase space is uncoupled in the approximation of the linear single-particle dynamics and

can be simply characterized by a free space propagation<sup>1</sup>. Typically, imposing an energy chirp on the beam is realized via an off-crest acceleration. The RF acceleration relies on the synchronization of the electron beam and the electromagnetic wave at the moment of interaction and can be simply described by the action of the Lorentz force on the electron beam:

$$F_L = eE = eE_0 \cos \phi \quad , \quad (3.2)$$

where  $e < 0$  is the electron charge,  $E_0$  is the amplitude of the RF field<sup>2</sup> and  $\phi$  is the relative phase between the RF and each electron in the beam. Next, we write down the Newton equation:

$$\frac{d(\gamma_e \beta m_e c)}{ds/c} = -eE_0 \cos \phi \quad , \quad (3.3)$$

where  $s$  is the coordinate along the beam-path and  $\beta(s) \approx 1$  and does not change significantly along the beamline in comparison with changes in  $\gamma$  during the acceleration. Both of those are valid approximations for the highly relativistic beam. Furthermore, we assume that the phase between the RF field and the test electron<sup>3</sup>  $\phi_0$  also does not change upon the acceleration<sup>4</sup> and that the initial energy spread is small ( $\delta\gamma \ll \gamma$ ). Given that the relative phase between an electron in the bunch  $\delta\phi = \omega\delta t \ll 2\pi$ , one can rewrite down the previous equation as the following<sup>5</sup>:

$$m_e c^2 \frac{d(\gamma + \delta\gamma)}{ds} = -eE_0 \left( \cos \phi_0 - \sin \phi_0 \omega \delta t - \frac{\cos \phi_0}{2} (\omega \delta t)^2 + \dots \right) \quad , \quad (3.4)$$

---

<sup>1</sup>Transverse motion in  $(x, x')$  phase space is also uncoupled from the longitudinal phase space in the regular chirper schemes. However, we use the 4-dimensional formalism here, since we describe a novel method of chirping involving this coupling later.

<sup>2</sup>Here, we assume the field is constant across and along the bunch for simplicity, which is valid in the first order approximation.

<sup>3</sup>As described in Chapter 1, the test electron characterizes the average motion of the electron beam.

<sup>4</sup>In other words, the proper synchronism is maintained

<sup>5</sup>For example,  $\sigma_t = 300$  fs for the bunch in between two bunch compressors at 250 MeV and 1 GeV and  $\omega = 3.9$  GHz for the MaRIE linac, which results in  $\omega\sigma_t \sim 10^{-3}$ .

From this expression, one can obtain for the zeroth order:

$$\gamma(s) = -\frac{eE_0}{m_e c^2} \cos \phi_0 s + \gamma(0) \quad . \quad (3.5)$$

This equation describes the principle of the linear acceleration, and suggests  $\phi_0 = 0$  for the maximum acceleration gradient. The imposed energy change can be found in the first order as following:

$$\delta\gamma(s) = \frac{eE_0(\omega/c) \sin \phi_0}{m_e c^2} s c \delta t + \delta\gamma(0) \quad . \quad (3.6)$$

Notice that at  $\phi_0 = 0$ , the accelerator cavity does not affect the beam in the first order. Therefore, imposing the linear energy slew is impossible at the maximum of the acceleration gradient. We then rewrite Equation (3.6) using the coordinates of the longitudinal phase space  $z$  and  $z'$ :

$$z'(s) = -\frac{eE_0(\omega/c) \sin \phi_0}{\gamma(s) m_e c^2} s z(0) + z'(0) \quad , \quad (3.7)$$

and immediately find the expression for  $R_{65}$  matrix element:

$$R_{65}(s) = -\frac{eE_0(\omega/c) \sin \phi_0}{\gamma(s) m_e c^2} s \quad . \quad (3.8)$$

It is obvious that one should pick the RF phase to chirp the beam such that  $\sin \phi_0 > 0$  and  $\cos \phi_0 > 0$  for the beam to be accelerated, resulting in  $0 < \phi_0 < \pi/2$ . Typically, the off-crest acceleration for imposing significant energy slews has the RF phase  $\sim \pi/4$ . For example, it is  $43^\circ$  for the LCLS linac between the first BC at 250 MeV and the second BC at 4.54 GeV, and results in the loss of 1.575 GeV of the beam energy [109]. One can impose the negative chirp on the beam using the same principles by choosing  $-\pi/2 < \phi_0 < 0$ , which results in  $R_{65} > 0$ .

### 3.2 Chirper design using transverse deflecting cavities

Imposing an energy chirp during the off-crest acceleration with the non-zero  $R_{65}$  is realized via a single beam element<sup>6</sup>, called the accelerating cavity, and does not involve any correlations between transverse and longitudinal phase spaces. In contrast, a beamline with nonzero  $R_{56}$  is realized via a chicane, combined from several beam elements, and relies on the correlations between  $xx'$  transverse and longitudinal phase spaces imposed in doglegs, or to be more precise, in bends. Perhaps, the “natural” single element imposing  $R_{56}$  is a free space propagation, where more energetic electrons enlarge their coordinate along the beam because they travel faster. The correct drift matrix in 6-dimensional phase space  $(x, x', y, y', z, z')$  can be written as:

$$R_{Drift} = \begin{pmatrix} 1 & L & 0 & 0 & 0 & 0 \\ 0 & 1 & 0 & 0 & 0 & 0 \\ 0 & 0 & 1 & L & 0 & 0 \\ 0 & 0 & 0 & 1 & 0 & 0 \\ 0 & 0 & 0 & 0 & 1 & \frac{L}{\gamma^2} \\ 0 & 0 & 0 & 0 & 0 & 1 \end{pmatrix}, \quad (3.9)$$

However, this would require a very long drift to impose a significant impact on the longitudinal bunch size for the relativistic beam, since  $R_{56} \ll L$  and the normalized energy spread  $z'$  is typically very small in the FEL driven linacs. As previously discussed, the solution for a large  $R_{56}$  is realized by involving a mixing between transverse and longitudinal phase spaces. We turned our attention to the scheme of an emittance exchanger looking for a similar solution for a new beamline with large  $R_{56}$ . In this scheme, two doglegs are mirror

---

<sup>6</sup>In general, it is typically done via a sequence of accelerating cavities, but all of them are similar in their action on the beam. Thus, we refer to all of them collectively as a single element.

matched<sup>7</sup> with one deflecting cavity to complete an emittance exchanger<sup>8</sup>. By looking at the matrices of a dogleg and a transverse deflecting cavity (in the thin approximation):

$$R_{Dogleg} = \begin{pmatrix} 1 & L & 0 & \eta \\ 0 & 1 & 0 & 0 \\ 0 & \eta & 1 & \xi \\ 0 & 0 & 0 & 1 \end{pmatrix}, \quad R_{TDC}(\kappa) = \begin{pmatrix} 1 & 0 & 0 & 0 \\ 0 & 1 & \kappa & 0 \\ 0 & 0 & 1 & 0 \\ \kappa & 0 & 0 & 1 \end{pmatrix}, \quad (3.10)$$

it is clear that  $z'$  acts on  $x$  and  $x'$  acts on  $z$  via the dispersion matrix element  $\eta$  in the dogleg, while the direction of the action is switched in the TDC and defined by the matrix element  $\kappa$ . These arguments made us look towards the TDC-based chirper beamline with a non-zero  $R_{65}$  which would be an analog of a chicane<sup>9</sup> with a non-zero  $R_{56}$ .

There is no action of the electromagnetic field on the center of the beam in a cavity with a single  $TM_{110}$  deflecting mode, because the field is zero on the  $z$ -axis at  $0^\circ$  RF phase. However, the transverse magnetic field depends on the coordinate along the bunch imposing deflection of the beam in respect to its longitudinal coordinate:  $(x')_f = (x')_i + \kappa z$ . In addition, the longitudinal electric field linearly varies across the beam (in the  $x$ -direction), resulting in an accelerating gradient along the  $x$ -axis. The matrix of the cavity accounting for its thickness and summarizing these actions can be written as following:

$$R_{TDC}(\kappa, L_c) = \begin{pmatrix} 1 & L_c & \frac{\kappa L_c}{2} & 0 \\ 0 & 1 & \kappa & 0 \\ 0 & 0 & 1 & 0 \\ \kappa & \frac{\kappa L_c}{2} & \frac{\kappa^2 L_c}{6} & 1 \end{pmatrix}, \quad (3.11)$$

---

<sup>7</sup>The transposed matrix of a dogleg (only  $\kappa$  is non zero) becomes a TDC matrix.

<sup>8</sup>As it was shown in the alternative EEX, a single dogleg can be matched with two transverse deflecting cavities.

<sup>9</sup>Interestingly, the sign of the matrix element  $R_{56}$  in a chicane can be flipped by inserting several quadrupole magnets between the dipole magnets. A similar approach will be described in Sec. 3.7.

where  $L_c$  [m] is the cavity length and  $\kappa$  [m<sup>-1</sup>] is the normalized deflection potential also referred as the geometric strength:

$$\kappa = eV_{\perp}/(mc^2\gamma a) \quad , \quad (3.12)$$

where  $V_{\perp}$  is the effective deflecting voltage,  $a$  is the characteristic cavity size (on the order of the RF wavelength), and  $\gamma$  is the mean bunch energy. For example,  $\kappa=0.21$  cm<sup>-1</sup> for the X-band LOLA cavity at SLAC [110]. Combining three deflecting cavities separated by drifts with a length  $D$  as shown in Fig. 3.1, and requesting the conditions  $\kappa_1 = \kappa_3 = \kappa$  and  $\kappa_2 = -2\kappa$ , we find the final TDC based chirper matrix ( $R_{TC}$ ) as a product of its elements<sup>10</sup>:

$$R_{TC} = R_{TDC}(\kappa, L_c)R_{Drift}(D)R_{TDC}(-2\kappa, 2L_c)R_{Drift}(D)R_{TDC}(\kappa, L_c) \quad . \quad (3.13)$$

This results in the final matrix of the TDC-based chirper:

$$R_{TC} = \begin{pmatrix} 1 & 2D + 4L_c & 0 & 0 \\ 0 & 1 & 0 & 0 \\ 0 & 0 & 1 & 0 \\ 0 & 0 & -\frac{2}{3}\kappa^2(3D + 2L_c) & 1 \end{pmatrix} . \quad (3.14)$$

The subplots in Figure 3.1 illustrate the physics behind this scheme. While even the TDC itself imposes the  $(x, z)$  correlations  $\sim \kappa L_c$ , it relies on significant length of the cavity. In contrast, the  $(x', z)$  correlations imposed in the first deflecting cavity can be transferred to the  $(x, z)$  correlations in the upstream drift overall resulting in  $\Delta x_z = (d + L_c/2)\kappa z$ . The drift can be chosen to be much longer than the cavity length. At this point, before entering the third TDC, the beam becomes slightly dechirped:  $\Delta z'_z = -L_c\kappa^2 z$ , but more

---

<sup>10</sup>All the cavities are chosen to be of the same RF amplitudes for simplicity. As soon as the conditions on  $\kappa$  are satisfied, the cavity lengths can be varied.

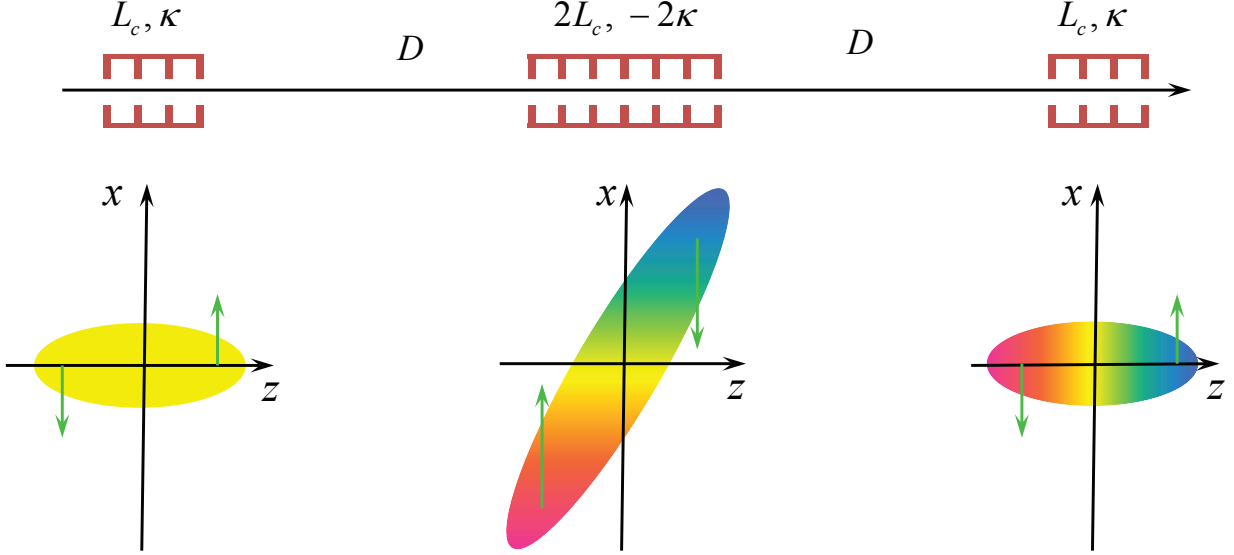


Figure 3.1: The schematics of the TDC-based chirper beamline (above) consisting of three TDCs for imposing longitudinal energy chirp in relativistic bunches. Subplots below show the  $(x, z)$  bunch distribution inside each TDC. Green arrows in these plots show  $z$ -dependent deflection provided by each cavity and color shows the particle energy at the corresponding location: the red color corresponds to the highest energy and the blue color to the lowest energy in the bunch.

importantly, it has a large transverse size and strong  $(x, z)$  correlations. Predominantly because of this, the additional energy spread imposed across the bunch ( $R_{61} \neq 0$ ) in the middle cavity results in the large energy chirp. The following drift and the last deflecting cavity remove the residual correlations between the transverse and longitudinal phase spaces with the chirped beam at the end of the scheme<sup>11</sup>.

The TDC-based chirper works by different principles in comparison to an off-crest acceleration which was discussed previously. It is important to evaluate whether the novel method is more effective than its commonly used counterpart. The element  $R_{65} = -\frac{2}{3}\kappa^2(3D + 2L_c) \approx -\kappa^2 D$  in the approximation of  $D \gg L_c$ . In comparison,  $R_{65} = -\kappa$  for the off-crest acceleration in the cavity of the same strength. A 1 m drift length in the TDC chirper results in  $\kappa D \gg 1$  for the typical cavity strength of  $\kappa \sim 0.05 - 1 \text{ cm}^{-1}$  meaning that the new scheme

<sup>11</sup>The last elements have almost no affect on the imposed chirp: it is reduced on the negligible quantity of  $L_c \kappa^2(z)/6$ .

is beneficial. The drift sections in conventional accelerators are relatively cheap<sup>12</sup> and, while the new method would be more expensive, is still cheaper than the cost of the accelerating structures and the power required to drive them in the superconducting accelerators. Even if the drift sections can be very long virtually, the maximum chirp is still limited. Indeed, the major chirp is imposed in the middle cavity and relies on the presence of  $(x, z)$  correlations and enlarging of the transverse size of the beam in  $x$ -direction occurring in the upstream section of the scheme, which scales as  $\sigma_x \sim \kappa D \sigma_z$ . We can rewrite the matrix element using this approximation:  $R_{65} \approx -\sigma_x / \sigma_z \kappa$ . The overall transverse size in each cavity should be less than the characteristic scale of the RF field (a few mm to few cm) as defined by its wavelength, otherwise the nonlinear effects associated with inhomogeneity of the electromagnetic fields become significant and have to be accounted for. Hence, the proposed scheme performs roughly  $\sigma_x / \sigma_z \sim 10 - 100$  times better than the off-crest acceleration, depending on the longitudinal beam size, and is especially beneficial for short bunch sizes, such as those found in FEL-driven linacs after the final bunch compressor. Finally, the initial transverse size and divergence do not have any impact on the performance of the scheme in the linear regime. Therefore, the Twiss parameters of the beam can be varied to optimize the transverse beam size along the beamline in order to minimize higher order effects as we will demonstrate in Section 3.5.1 of this chapter.

---

<sup>12</sup>The facility construction and maintenance costs around empty vacuum tubes are not negligible. Perhaps the actual space for the linac can be quite limited due to the natural conditions of the landscape. A good practical example of this is the MaRIE linac at LANL. It is planned to be built near the existing Proton radiography facility at the LANSCE Mesa, where the place is physically limited by the neighboring canyon. In general, the benefit of avoiding the off-crest acceleration can eventually gain in reducing the overall linac length in comparison to the conventional schemes.

### 3.3 Design optimization for the MaRIE linac

The proposed scheme is strongly beneficial for normal-conducting accelerators, where free space propagation is realized as empty tubes with high vacuum. For the superconducting accelerator case, such as for the planned to-be-built LCLS-2 [57] or MaRIE XFEL [58], the drift lengths between the TDC cavities come at the cost of the cryogenic module. In this section, we discuss the outline of the proposed scheme within the frame of the MaRIE cryomodules for which we provide numerical studies and optimization of nonlinear effects up to the third order. The conceptual MaRIE design requires imposing a large ( $\pm 5$  MeV) correlated energy spread between chicanes of the two bunch compressors located at 250 MeV and 1 GeV [80]. The related chirp roughly delivers an optimum trade-off between the slice energy spread growth caused by the LSC-induced microbunch instabilities during the low gradient off-crest acceleration<sup>13</sup> and the emittance growth in the chicane due to CSR effects<sup>14</sup>. The MaRIE linac is planned to be built using superconducting cavities placed in a series of 12.4-m-long cryomodules [58, 80]. The novel TDC-based chirper scheme has been proposed already, but only after the conceptual MaRIE outline had been approved. Keeping that in mind, we designed it so it can effectively fit within the exact number of cryomodules to simplify the replacement. The layout of the proposed TDC-based chirper assumes using two cryomodules for the chirper at 250 MeV beam energy and four cryomodules at 1 GeV beam energy (Fig. 3.2). The parameters of the beam elements and the beam for these schemes are listed in Table 3.1. The optimum ratio between the cavity length and the drifts are chosen to maximize the efficiency of the proposed scheme while accounting for both, the outline of the cryomodules and the cost efficiency. Lastly, the cost of the RF was compared with the

---

<sup>13</sup>Due to the close energy of the two bunch compressors, the off-crest acceleration has to happen at the large phase resulting in roughly two times smaller accelerating gradient.

<sup>14</sup>see Chapter 2 for more details.

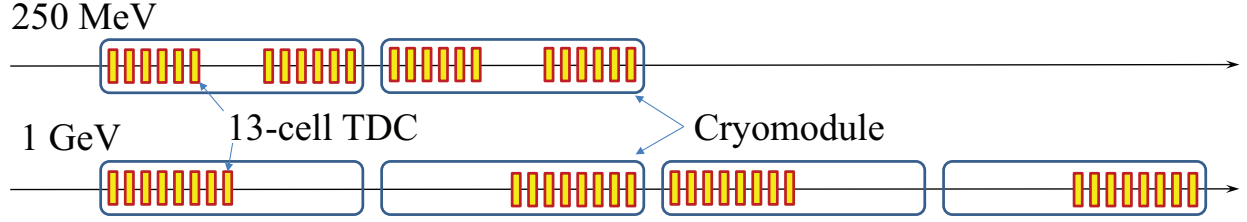


Figure 3.2: The layout of TDCs inside the cryomodules for the MaRIE linac. The design shows the TDC-based chirper consisting of twenty four total 13-cell cavities within two cryomodules at 250 MeV (above) and at 1 GeV with thirty two total 13-cell cavities within four cryomodules (below). The cryomodule contours are represented by blue ovals, each 13-cell TDC is represented by a yellow rectangle, and the black arrows point along the direction of the beam propagation.

cost of vacuum drift tubes within the cryogenic environment, specifically accounting for the cost of the tunnel, the structure, and the cryomodules.

Table 3.1: Parameters of the TDC-based chirper for MaRIE x-ray FEL

<b>Electron beam</b>			
Beam energy $E = \gamma mc^2$	250	1000	MeV
Bunch charge $q$	100	100	pC
Bunch length $\sigma_z$	90	90	$\mu\text{m}$
Normalized transverse emittances $\epsilon_{n_{x,y}}$	0.1	0.1	$\mu\text{m}$
Normalized longitudinal emittance $\epsilon_{n_z}$	5.72	5.72	$\mu\text{m}$
Uncorrelated energy spread $\gamma mc^2 \sigma_{z'_u}$	32.5	32.5	keV
Correlated energy spread (imposed) $\gamma mc^2 R_{65} \sigma_z$	6.7	8.1	MeV
<b>Beamline components</b>			
Total number of cryomodules	2	4	
Total number of 13-cell cavities	24	32	
Cavity frequency	3.9	3.9	GHz
Effective RF length in each cavity	0.5	0.5	m
Deflecting voltage in each cavity	2.5	2.5	MeV
Number of 13-cell cavities per TDC	6	8	
Drift length $D$	3.39	6.58	m
TDC length $L_c$	4.28	5.72	m
TDC strength $\kappa$	4.9	1.63	$\text{m}^{-1}$
$R_{65}$	300	90	$\text{m}^{-1}$

### 3.4 Transverse deflecting cavity models in ELEGANT

Transverse deflecting cavities in the beamline of the double emittance exchanger BC were simulated by the first-order transfer matrices in the thin-lens approximation for simplicity (Chapter 2). By contrast, each TDC was simulated by available in ELEGANT element RFDF here to uncover potentially important effects of the nonlinear single-particle dynamics coming from the large total energy spread originated by the gigantic imposed chirp. The transverse magnetic field in the RFDF element is similar<sup>15</sup> to the form written in Equation (2.48):

$$B_y = B_0 \cos(\omega t) \quad , \quad (3.15)$$

<sup>15</sup>The phase offset of  $\pi/2$  ( $90^\circ$ ) has to be chosen in each RFDF element to provide zero deflection of the particles in the center of the bunch ( $z = 0$ ).

The longitudinal electric field is similar to the form written in Equation (2.45):

$$E_z = B_0 \omega x \sin(\omega t) \quad . \quad (3.16)$$

The action of the Lorentz force on the particle momenta<sup>16</sup> is calculated using these fields [38]:

$$\Delta p_x = e B_0 \Delta L \cos(\omega t) \quad , \quad (3.17)$$

$$\Delta p_y = 0 \quad , \quad (3.18)$$

$$\Delta p_z = \frac{e B_0 \omega x \Delta L}{c} \sin(\omega t) \quad , \quad (3.19)$$

where  $\Delta L$  is the length of the slice passing through and  $\Delta p_i$  describes the changes of the variable  $p_i$  after propagation through this interval. The transverse deflection in RFDF element is constant as a function of transverse coordinates and is specified by the deflection voltage:

$$V = B_0 c \Delta L \quad . \quad (3.20)$$

Such configuration of the electromagnetic fields suggests that in the beam coordinates  $(\mathbf{r}, \mathbf{p})$  the effects of the second, third and higher orders associated with the relative phase of the particle along the bunch in respect to the RF field can appear according to the following equations:

$$\Delta p_x = e B_0 \Delta L \left( -(\omega t) + \frac{(\omega t)^3}{6} + \dots \right) \quad , \quad (3.21)$$

$$\Delta p_y = 0 \quad , \quad (3.22)$$

$$\Delta p_z = \frac{e B_0 \omega x \Delta L}{c} \left( 1 - \frac{(\omega t)^2}{2} + \dots \right) \quad . \quad (3.23)$$

---

<sup>16</sup>Units of  $mc$  used in reference [38], which is why the expressions there are different from here.

In the ultrarelativistic regime, where all the particles have the similar energy  $\gamma$  and fly with approximately the same speed  $\beta_z c$ , the time interval then can be written in terms of a coordinate along the bunch and momenta:

$$t = \frac{z}{\beta_z c} = \frac{z\gamma}{p_z/m} = \frac{z\sqrt{1 + (p_z^2 + p_x^2 + p_y^2)/(mc)^2}}{p_z/m} = \frac{z}{c} \sqrt{1 + \frac{(mc)^2}{p_z^2} + \frac{p_x^2}{p_z^2} + \frac{p_y^2}{p_z^2}}. \quad (3.24)$$

Next, we assume that the reference particle has only the longitudinal component of the momentum vector  $p_0 \gg 1$ , and that the momentum components of each particle in the bunch are  $p_z \sim p_x \sim p_y \ll p_0$ . Then, one can obtain the following result using the Taylor expansion series:

$$t \approx \frac{z}{c} \sqrt{1 + \frac{(mc)^2}{p_0^2}} \left( 1 + \frac{\frac{p_z}{p_0} \left(\frac{mc}{p_0}\right)^2}{1 + \frac{(mc)^2}{p_0^2}} - \frac{3 \left(\frac{p_z}{p_0}\right)^2 \left(\frac{mc}{p_0}\right)^2}{2 \left(1 + \frac{(mc)^2}{p_0^2}\right)^2} - \frac{\left(\frac{p_x}{p_0}\right)^2}{1 + \frac{(mc)^2}{p_0^2}} - \frac{\left(\frac{p_y}{p_0}\right)^2}{1 + \frac{(mc)^2}{p_0^2}} + \dots \right). \quad (3.25)$$

The expressions in Equations (3.15-3.16) can be rewritten for the proper coordinate system  $(x, x', y, y', z, z')$  chosen for the convenience of the beam propagation description through the beamline. First, the expression in Eq. (3.24) can be rewritten in terms of the Lorentz factor  $\gamma$  and the normalized velocity components  $\beta_x \approx x'$  and  $\beta_y \approx y'$  since  $\beta_z \sim 1$ :

$$t = \frac{z}{\beta_z c} = \frac{z/c}{\sqrt{\beta^2 - \beta_x^2 - \beta_y^2}} = \frac{z/c}{\sqrt{1 - 1/\gamma^2 - \beta_x^2 - \beta_y^2}}. \quad (3.26)$$

Assuming that the reference particle has  $\beta_x = \beta_y = 0$  and  $\gamma = \gamma_0$ , we can find the relative shift in time of a particle in the bunch using the Taylor expansion series:

$$t \approx \frac{z/c}{\sqrt{1 - 1/\gamma_0^2}} \left( 1 - \frac{\Delta\gamma/\gamma_0^3}{1 - \gamma_0^2} + \frac{3\Delta\gamma^2/\gamma_0^4}{2(1 - \gamma_0^2)^2} + \frac{\beta_x^2/2}{1 - 1/\gamma_0^2} + \frac{\beta_y^2/2}{1 - 1/\gamma_0^2} + \dots \right), \quad (3.27)$$

which is similar to the expression in Eq. (3.25). Second, one has to express the left parts of Eqs. (3.15-3.16) in these coordinates using the linear differentiation rule in respect to the slice  $\Delta L$ :

$$\frac{\Delta p_x}{mc} = \Delta(\gamma\beta_x) = \beta_x\Delta\gamma + \gamma\Delta\beta_x = \beta_x\Delta(\gamma_0 + \delta\gamma) + (\gamma_0 + \delta\gamma)\Delta\beta_x, \quad (3.28)$$

$$\frac{\Delta p_z}{mc} = \Delta(\gamma\beta_z) = \beta_z\Delta\gamma + \gamma\Delta\beta_z = \beta_z\Delta\gamma + \gamma\Delta\sqrt{1 - \frac{1}{(\gamma_0 + \delta\gamma)^2} - \beta_x^2 - \beta_y^2} = \dots, \quad (3.29)$$

where the second legs in both equations assume that  $\langle\beta_x\rangle = \langle\beta_y\rangle = 0$  and  $\beta_x$  and  $\beta_y$  then describe then the relative normalized velocities (slopes) of a particle in the bunch, while the normalized energy spread is  $z' = \delta\gamma/\gamma_0$ .

In spite of the description, the RFDF routine in ELEGANT, even with the approximation of uniform electromagnetic fields, accounts for nonlinear effects which can be significant upon reaching a large normalized energy spread  $z'$ , slopes  $x'$  and  $y'$ , etc. This approximation, however, has to be properly checked against the real TDC structure (or upon designing one) containing a mixture of TM- and TE-like modes, which can be done in the electromagnetic simulation software, for example in CST MICROWAVE STUDIO [111], or experimentally. The electromagnetic field map then can be transferred to ELEGANT for the accurate simulations of the TDC-based chirper beamline with the actual TDCs structures. Apart from the RFDF element, an alternative routine, RFTM110, is available in ELEGANT. This routine uses the field for a pure TM110 mode in the approximation of cylindrical symmetry [38]. However, the deflecting mode is a hybrid of TE and TM modes in a real deflecting cavity with entrance and exit tubes and the deflection has no dependence on the radial coordinate. Therefore, using the RFDF element instead of the element TM110 is more convenient for practical applications which is also recommended by the authors of ELEGANT [38].

### 3.5 Nonlinear effects and its optimization for 250 MeV Chirper

First, we report on the emittance enlargement while imposing a chirp in the scheme at 250 MeV, where we account for the high order effects of the single-particle dynamics in drifts and transverse deflecting cavities. Figure 3.3 demonstrates the evolution of the transverse (a) and longitudinal (b) emittances and eigen emittances (c) and (d) along the beamline. The transverse and longitudinal emittances significantly grow during the propagation, since the motions in the transverse  $(x, x')$  and longitudinal  $(z, z')$  phase spaces are highly coupled. The transverse emittance  $\epsilon_{n_x}$  at the end of the beamline is  $0.39 \mu\text{m}$  which is roughly four times bigger than its initial value of  $0.1 \mu\text{m}$ . The eigen emittance  $\lambda_2$  related to the transverse phase space  $(x, x')$  predominantly grows in the third deflecting cavity and comes back close to its original value in the last cavity resulting in only 5% enlargement. Such a big difference between  $\epsilon_{n_x}$  and  $\lambda_2$  suggests the presence of the strong residual correlations between transverse and longitudinal phase spaces. The longitudinal emittance as well as its associated eigen emittance  $\lambda_1$  at the end of the beamline are respectively  $31.8 \mu\text{m}$  and  $31.9 \mu\text{m}$ , which means they increased significantly in comparison to their initial values of  $5.72 \mu\text{m}$ . The transverse dynamics in  $(y, y')$  phase space is uncoupled and results in no visible change in related normal and eigen emittances in comparison to their initial values of  $0.1 \mu\text{m}$ . Degradation of the transverse emittance  $\epsilon_{n_x}$  is caused by the remaining correlations between transverse and longitudinal phase spaces at the exit of the beamline as clearly visualized in Fig. 3.4. In particular, the slope  $x'$  linearly depends on both the distance along the bunch and the energy spread, which are related through the large chirp imposed on the beam. In addition, the transverse coordinate  $x$  quadratically depends on the longitudinal parameters of the beam. Quadratic correlations are caused by the large energy spread associated with the imposed chirp. Indeed, the total energy spread reaches a value of approximately 7 MeV in

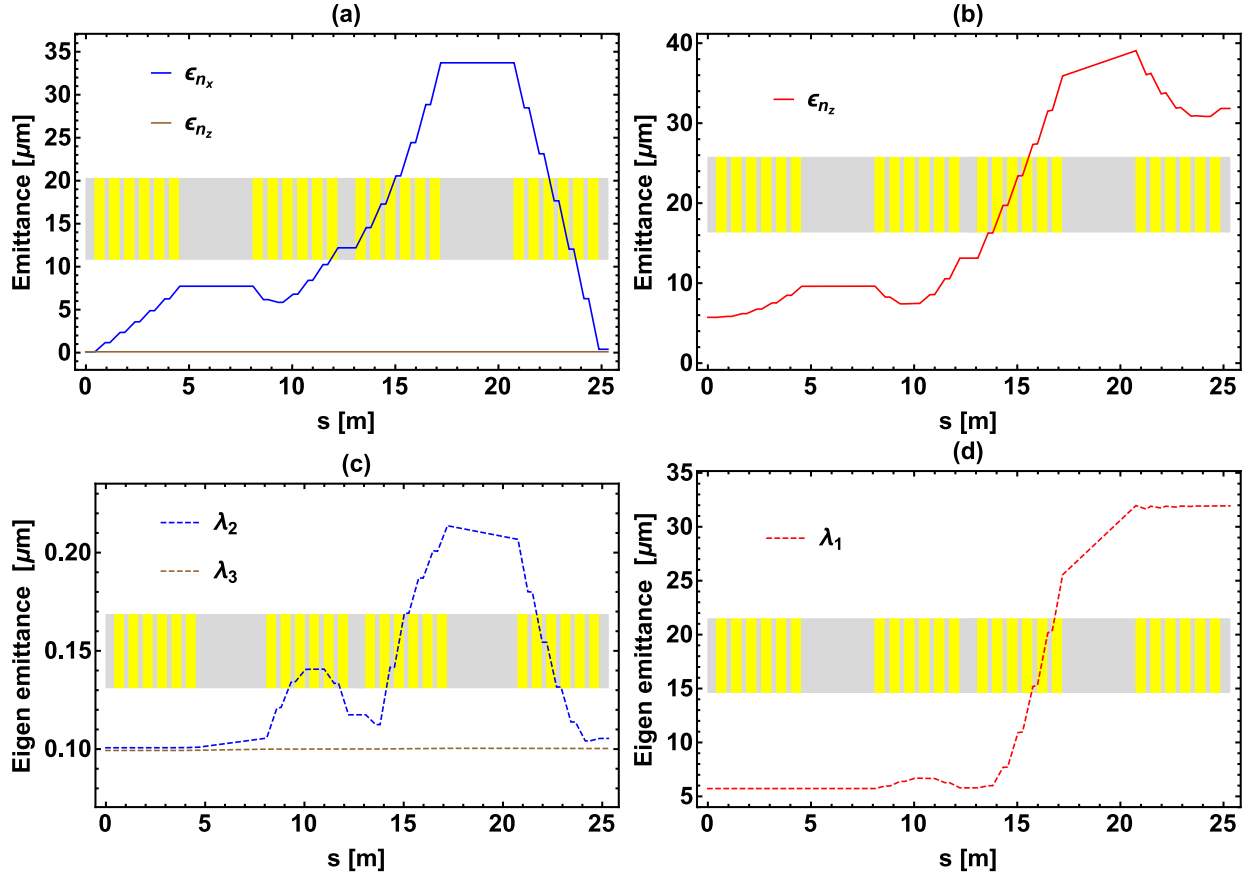


Figure 3.3: Transverse and longitudinal emittances and eigen emittances along the beamline for the input Twiss parameters  $\beta_x = \beta_y = 5$  m and  $\alpha_x = \alpha_y = 0$ . Each 13-cell cavity is marked as a yellow rectangle representing its actual geometric length and position within the beamline. The ordinate  $s = 0$  m corresponds to the entrance of the beamline.

the end of the third TDC and only slightly changes in the rest of the beamline (Fig. 3.5 (c)). This value is comparable to the total beam energy of 250 MeV and results in the normalized energy spread of  $\delta\gamma/\gamma \sim 0.028$ . This value should be much smaller than 1 to hold the matrix formalism of the linear dynamics legitimate and requires accounting for higher order dynamics in the opposite case. In particular, quadratic correlations most likely caused by the nonzero  $T_{ij6}$  terms related to the nonlinear effects in TDCs. The nonlinear effects are still negligible in the first cavity due to a relatively small total energy spread. The energy chirp becomes larger in the second cavity, and consequently the nonlinear effects, predominantly

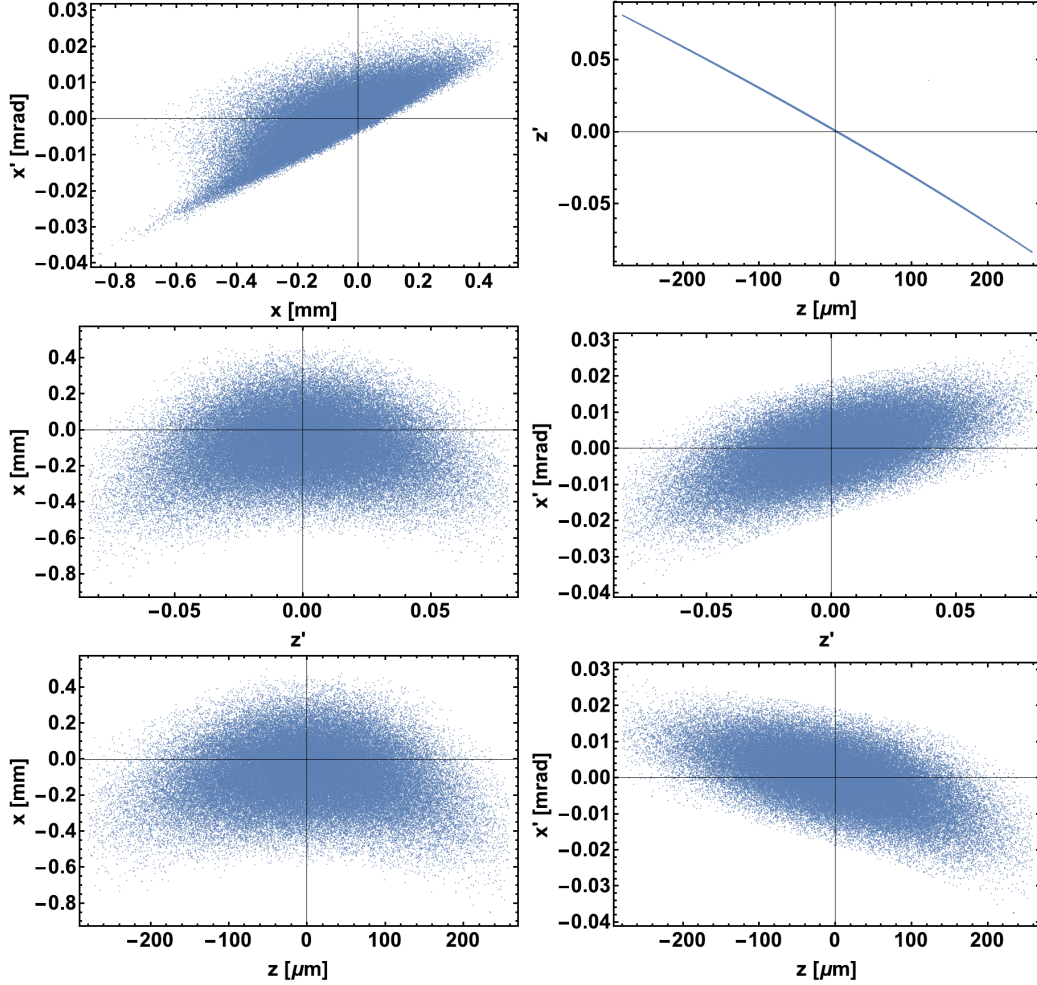


Figure 3.4: Phase spaces at the exit of the TDC-based chirper at 250 MeV for nonlinear single-particle dynamics  $\beta_x = \beta_y = 5$  m and  $\alpha_x = \alpha_y = 0$ .

due to the  $T_{256}$  matrix element (see Equations 3.21 and 3.27 for details), result in correlations between  $x'$  and  $(z')^2$ ,  $x^2$ , and  $z^2$ , while every pair of coordinates from the trio  $x$ ,  $z$ , and  $z'$  are linearly correlated with each other. In the downstream drifts and cavities, the  $T_{256}$  term results in transferring of the quadratic correlations to the  $x$  coordinate due to the growing energy chirp and the linear correlations in  $(x, x')$  phase space. This eventually results in the domination of the  $T_{166}$  matrix element for the overall beamline, which explains

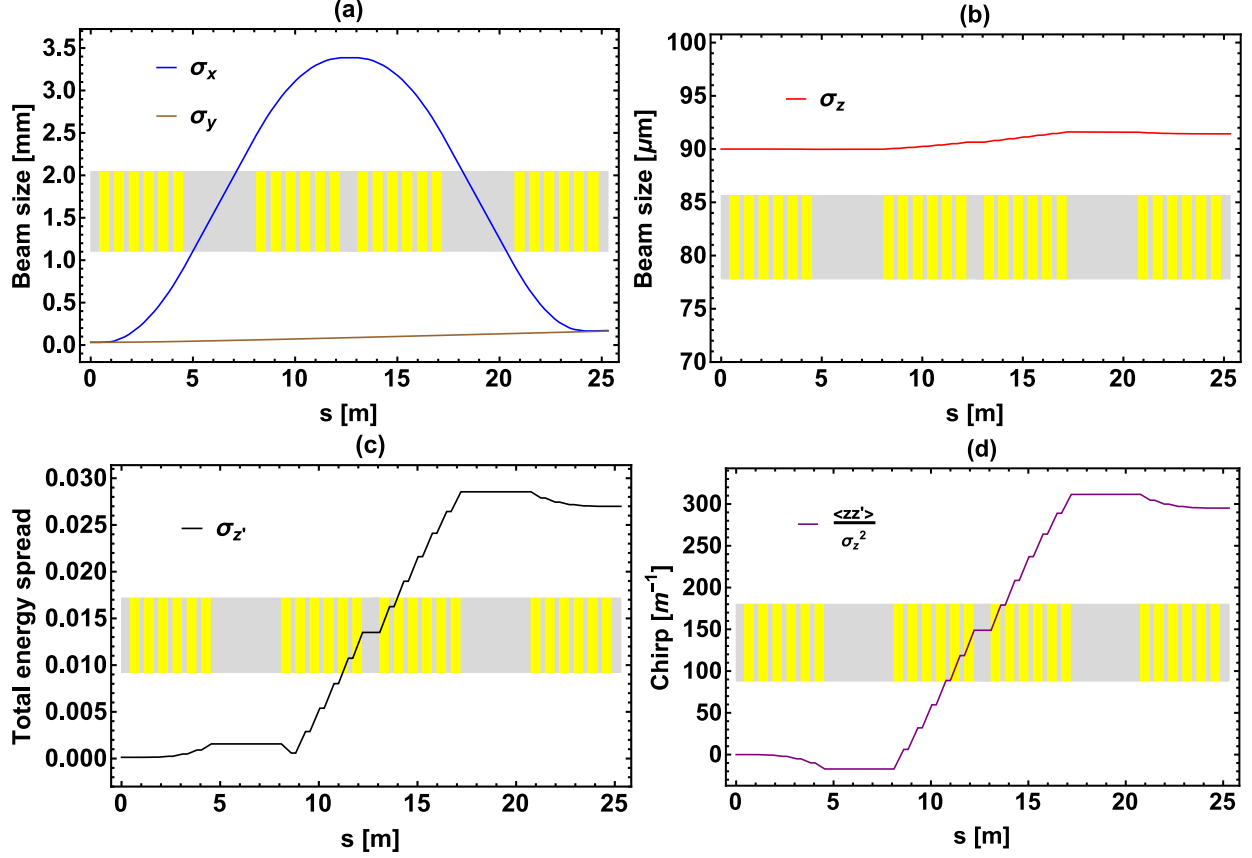


Figure 3.5: Beam parameters at a distance  $s$  along the beamline in TDC-based chirper at 250 MeV ( $\beta_{x,y} = 5$  m and  $\alpha_{x,y} = 0$ ): (a)  $\sigma_x$  and  $\sigma_y$ ; (b)  $\sigma_z$ ; (c) the total energy spread; (d) the chirp. The ordinate  $s = 0$  m corresponds to the entrance of the beamline.

the final correlations between  $x$  and  $(z')^2$ , while quadratic correlations between  $x$  and  $(z)^2$  immediately follow due to the linear energy chirp imposed on the beam.

### 3.5.1 Optimization of the Twiss parameters

At least the largest of two effects, quadratic or linear correlations between the coordinates of the longitudinal phase space and respectively  $x$  and  $x'$  coordinates, can be optimized by choosing the appropriate set of the input Twiss parameters. Indeed, optimizing  $\sigma_x$  and  $\sigma_{x'}$  along the beamline can reduce the correlations between the transverse and longitudinal phase

spaces at the exit of the beamline and consequently reduce the transverse emittance growth. As clearly demonstrated in Fig. 3.5, the transverse beam size in the middle of the scheme:

$$\sigma_{x_m} = \sqrt{\sigma_x^2 - 2(D + 2L_c)\langle xx' \rangle + (D + 2L_c)^2\sigma_{x'}^2 + \kappa^2(D + 2L_c)^2\sigma_z^2} \quad , \quad (3.30)$$

where  $\sigma_x$ ,  $\sigma_{x'}$ ,  $\sigma_z$  and  $\langle xx' \rangle$  are the beam parameters on the entrance of the beamline, is much bigger than at the entrance and the exit of the scheme. This is due to the size being predominantly defined by the longitudinal beam parameters, since the longitudinal emittance is much large than  $\epsilon_{n_x}$ . Using Eq. (3.30), one can find (accounting for the values of the parameters listed in Table 3.1):

$$\sigma_{x_m} \approx \kappa(D + 2L_c)\sigma_z \quad , \quad (3.31)$$

Hence,  $\sigma_x$  and  $\sigma_{x'}$  can be significantly controlled by the Twiss parameters only close to the entrance and the exit of the beamline. Figure 3.6 presents the dependence of the final transverse (a) and longitudinal (c) emittances and relates them to eigen emittances (b, d) from the input Beta-function ( $\beta_x$ ) at  $\alpha_x = 0$ . The minimum of  $\epsilon_{n_x} \approx 0.27 \mu\text{m}$  is reached at  $\beta_x \approx 25 \text{ m}$ . The longitudinal emittance and associated eigen emittance  $\lambda_1$  observe insignificant changes. Next, we demonstrate that imposing the initial linear correlations on  $(x, x')$  phase space by adjusting  $\alpha_x$  can reduce the transverse emittance even further. Figure 3.7 depicts that the minimum of the transverse emittance  $\epsilon_{n_x} \approx 0.20 \mu\text{m}$  is reached at  $\beta_x = 59 \text{ m}$  and  $\alpha_x = 2.1$ . Figure 3.8 demonstrates how the parameters of the beam change along the beamline for the optimal Twiss parameters  $\beta_x = 59 \text{ m}$  and  $\alpha_x = 2.1$ . The input Twiss parameters  $\beta_y$  and  $\alpha_y$  were adjusted accordingly so one can see how transverse parameters in  $(x, x')$  phase space would change if TDCs are turned off ( $V = 0$  and consequently  $\kappa = 0$ )

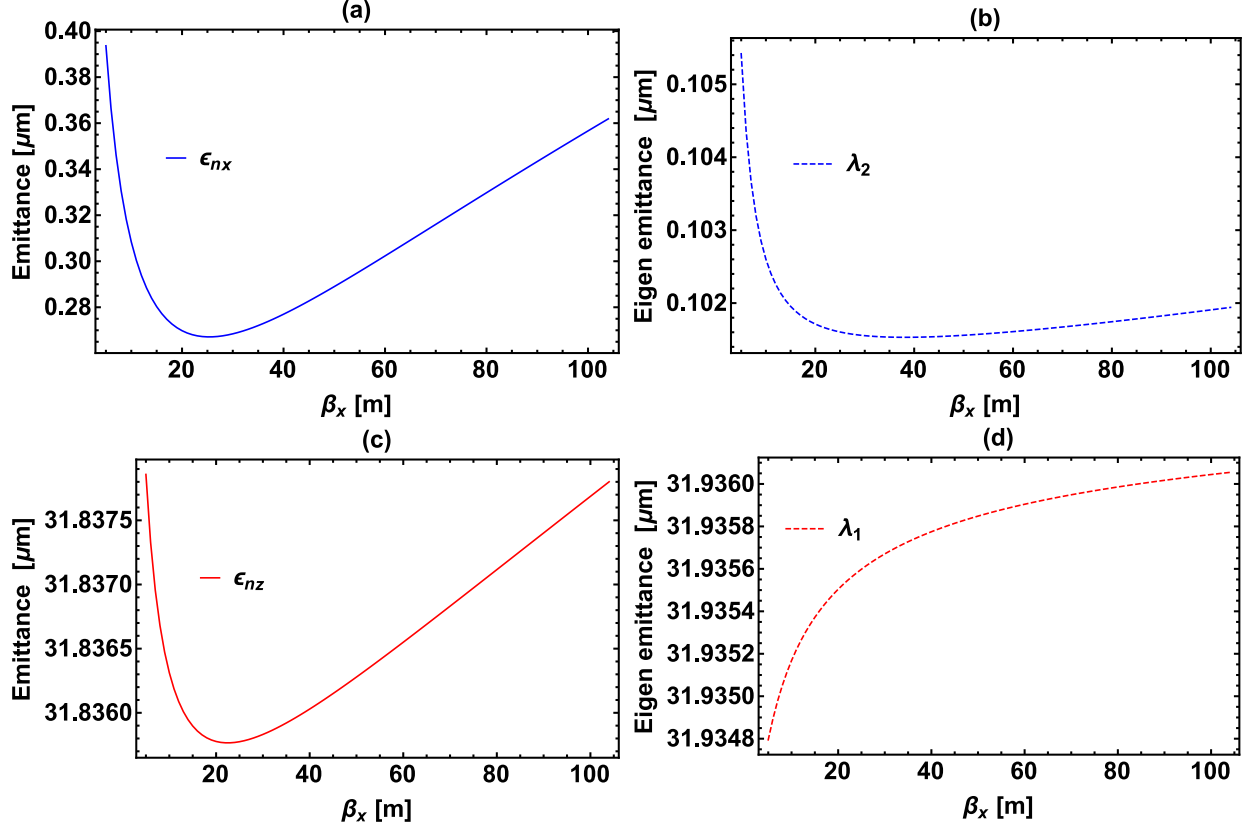


Figure 3.6: Transverse and longitudinal emittances and eigen emittances from the input beta-function  $\beta_x$  at  $\beta_y = 5$  m and  $\alpha_x = \alpha_y = 0$ .

resulting in the absence of the transverse-longitudinal coupling and in a zero chirp<sup>17</sup>. Figure 3.9 demonstrates how normal and eigen emittances transition along the beamline for the optimized transverse beam profile. Comparing these results with Fig. 3.3, we can conclude that the longitudinal parameters of the beam remain unchanged, while the transverse beam size  $\sigma_y$  ( $\sigma_x$  if the cavities are turned off) reaches its minimum approximately in the middle of the last TDC. This beam profile results in compensation of the second order correlations in the final TDC, which were imposed in upstream elements of the beamline. As a result, it reduces the degradation of the transverse emittance. The output beam phase spaces are

<sup>17</sup>Changing  $\beta_y$  and  $\alpha_y$  demonstrated no visible impact on the transverse ( $x, x'$ ) and longitudinal dynamics, as was theoretically predicted due to the fact that  $(y, y')$  dynamics is uncoupled.

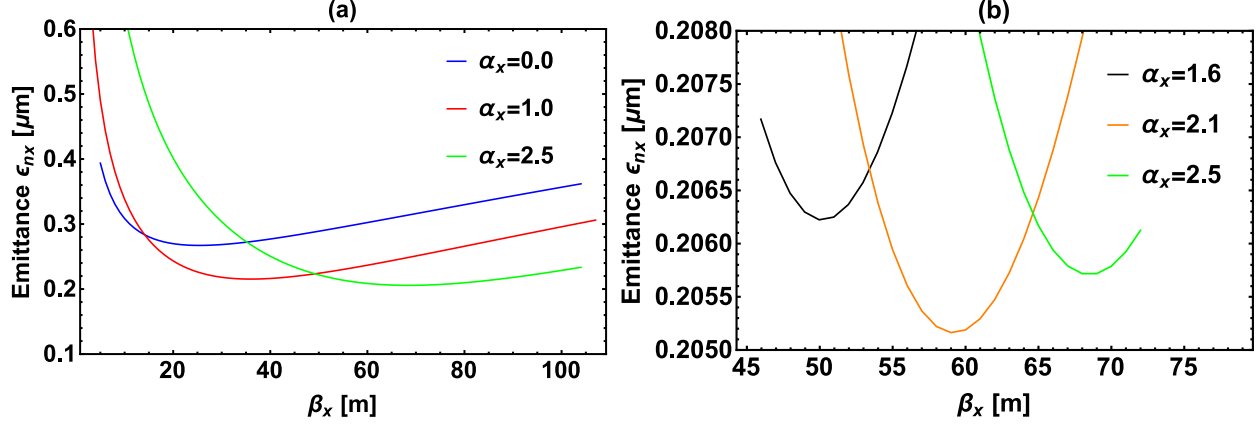


Figure 3.7: Transverse and longitudinal emittances and eigen emittances from the Beta-function  $\beta_x$  for different  $\alpha_x$  ( $\beta_y = 5$  m and  $\alpha_y = 0$ ).

presented in Fig. 3.10. Noticeable improvements in  $(x, x')$  phase space in comparison to the unoptimized case (Fig. 3.4) are demonstrated.

### 3.5.2 Suppressing linear correlations

Next, we report on how emittance degradation depends on the final imposed chirp in the scheme with optimized Twiss parameters. The imposed chirp is varied by changing the deflecting voltage simultaneously in each cavity, while another parameters of the scheme remain invariant. Figure 3.11 (a) demonstrates that imposing a 5 MeV chirp will result in approximately 40% enlargement of the transverse emittance  $\epsilon_{nx}$ , suggesting that the scheme requires further optimization. The presence of residual linear correlations in  $(x', z)$  and  $(x', x')$  phase spaces (Fig. 3.10) suggests that the effective cavity strength  $\kappa$  in the approximation of the nonlinear single-particle dynamics varies between the different cavities along the beamline which means that it depends on the beam parameters which vary along the beamline. However, the beam size, the total energy spread and other parameters reported in Figures 3.5 and 3.8 should not affect the linear dynamics according to the presented for-

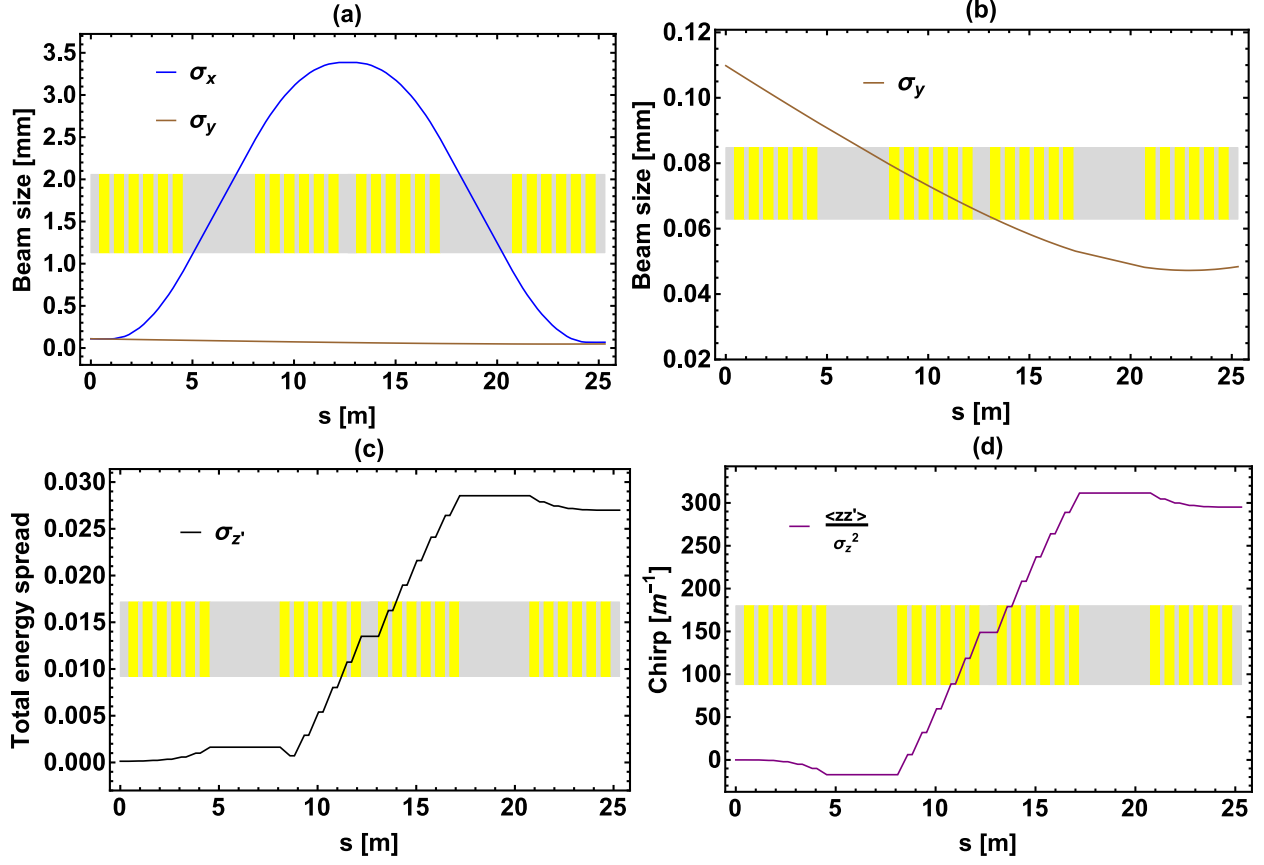


Figure 3.8: Beam parameters at a distance  $s$  along the beamline in TDC-based chirper at 250 MeV with the optimized Twiss parameters  $\beta_x = \beta_y = 59$  m and  $\alpha_x = \alpha_y = 2.1$ : (a)  $\sigma_x$  and  $\sigma_y$  together; (b)  $\sigma_y$  on the different scale; (c) the total energy spread; (d) the energy chirp. The longitudinal beam profile remains identical to the previous case and is not shown.

malism. Interestingly, the nonlinear effects result not only in the degradation of the phase space shape (Fig. 3.4 and 3.10) but also change the average beam parameters. For instance, the final average position of the beam for the nonlinear single-particle dynamics is shifted relative to the central axis of the beamline for both sets of input Twiss parameters as can be noticed in Figures 3.4 and 3.10. Moreover, the normalized beam energy  $\gamma_f = 489.124$  at the end of the beamline is slightly smaller than its initial value  $\gamma_i = 489.225$ . These values<sup>18</sup> at the entrance of second, third and fourth cavities are respectively  $\gamma_2 = 489.221$ ,  $\gamma_3 = 489.268$

<sup>18</sup>These values are presented for the scheme with the optimized Twiss parameters, while they are almost identical for the scheme with initial Twiss parameters  $\beta_x = 5$  and  $\alpha_x = 0$ .

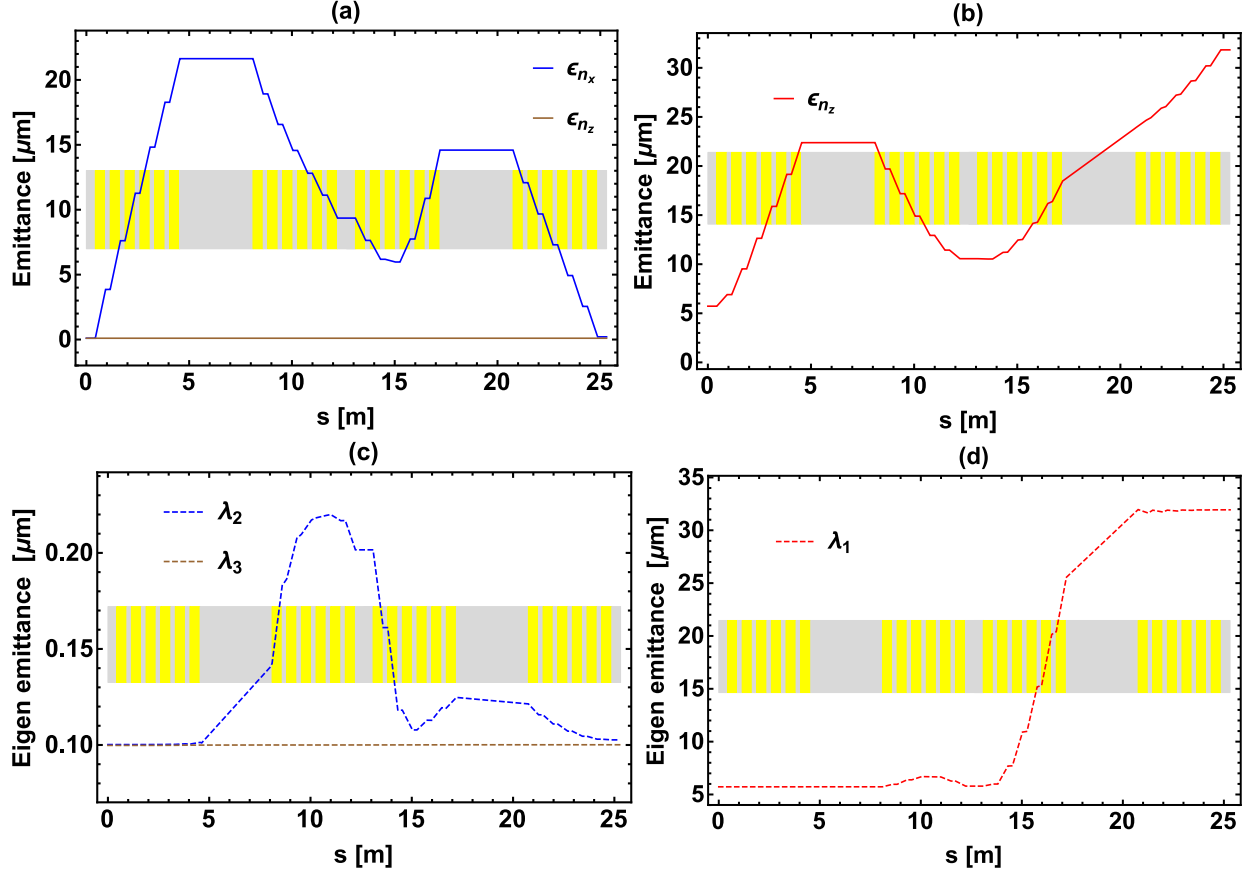


Figure 3.9: Transverse and longitudinal emittances and eigen emittances along the beamline for the optimum input Twiss parameters  $\beta_x = \beta_y = 59$  m and  $\alpha_x = \alpha_y = 2.1$ .

and  $\gamma_3 = 489.327$ . Variations in the average bunch energy along the beamline, initially caused by the nonlinear effects, result in changing of the effective cavity strength in different cavities which explains the presence of the residual linear correlations between transverse and longitudinal phase spaces. Such correlations can be removed by slightly adjusting the voltage in the last cavity, while all other parameters of the beamline are kept unchanged. Shifting the voltage in the last cavity from 2.5 MV to 2.5265 MV ( $\Delta V = +26.5$  kV) results in the final  $\epsilon_{n_x}$  of  $0.144 \mu\text{m}$  for the maximum imposed correlated energy spread of 6.74 MeV, using input Twiss parameters  $\beta_x = 59$  m and  $\alpha_x = 2.1$ . In this case, the final chirp is practically unchanged (less than 0.12% reduction). Interestingly, Figure 3.12 demonstrates

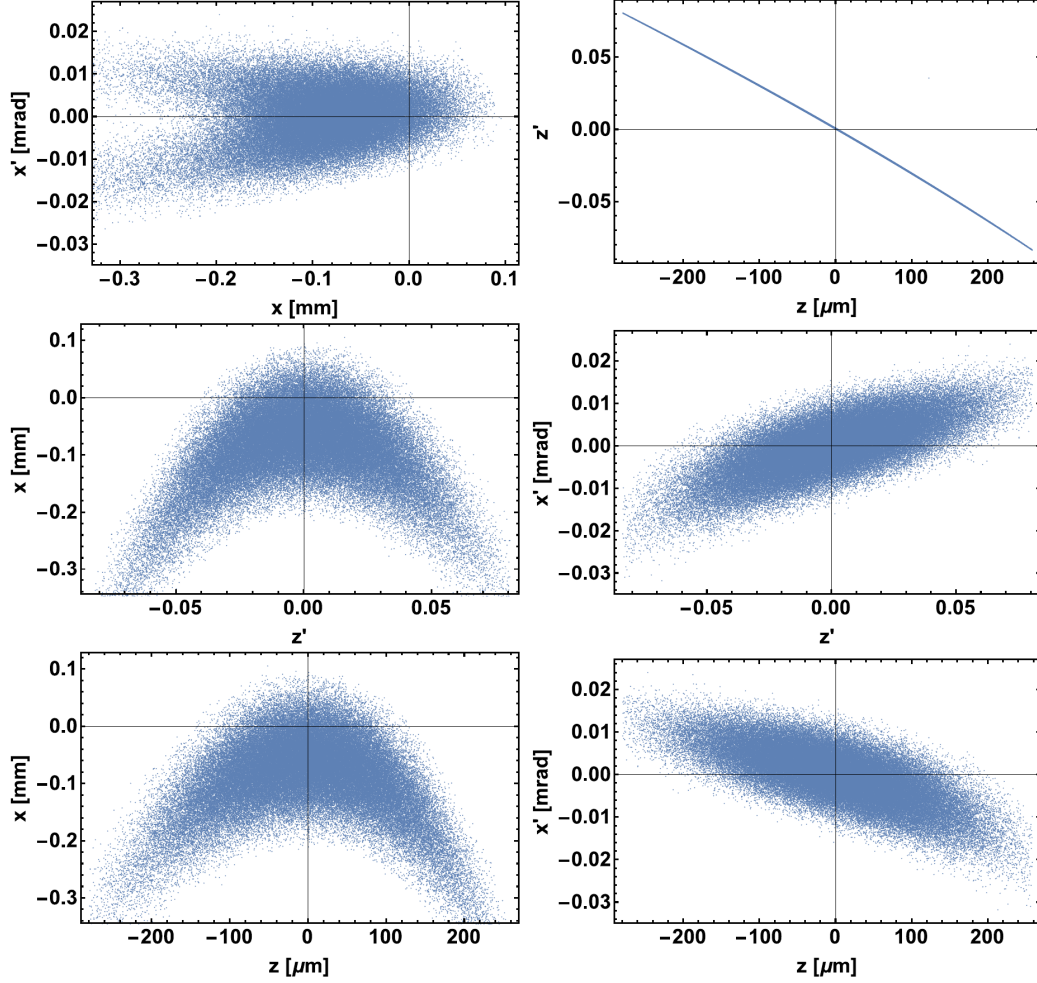


Figure 3.10: Phase spaces at the exit of the TDC-based chirper at 250 MeV for the nonlinear single-particle dynamics for the optimal Twiss parameters  $\beta_{x,y} = 59$  m and  $\alpha_{x,y} = 2.1$ .

that the minimum of the transverse emittance  $\epsilon_{n_x}$  is reached at the same voltage at which the longitudinal normal and eigen emittances become identical, confirming suppression of the linear correlations between the transverse and longitudinal phase spaces (Fig. 3.13).

The twiss parameters can be further optimized to minimize the emittance degradation due to the quadratic correlations only, since the linear correlations  $(x', z)$  and  $(x', z')$  are completely suppressed. The new optimal set  $\beta_x = 150$  m and  $\alpha_x = -1.3$  result in the transverse emittance enlargement of only 5% for the maximum applied chirp of  $300 \text{ m}^{-1}$ . The

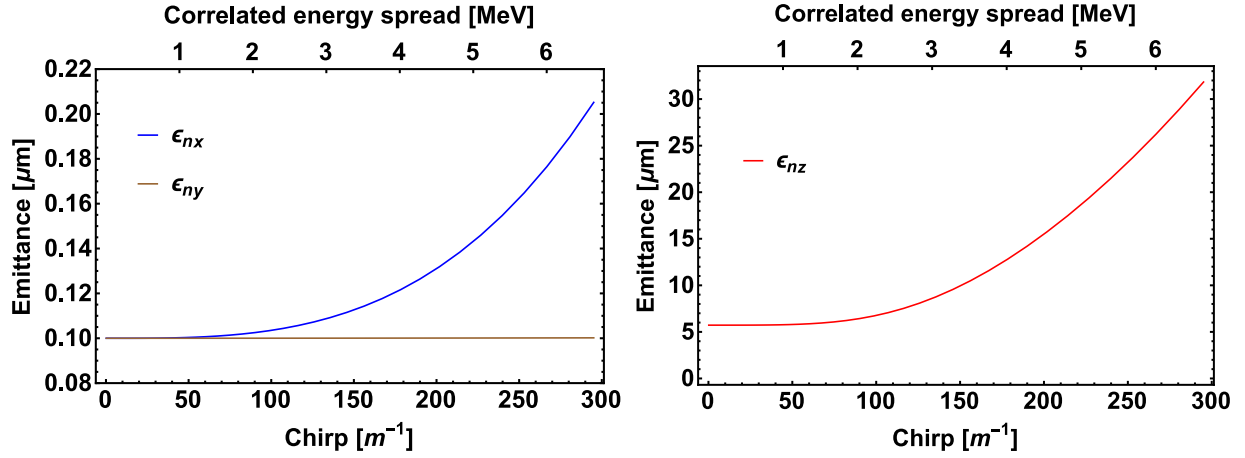


Figure 3.11: Normalized emittances at the exit of the TDC-based chirper at 250 MeV with the optimized Twiss parameters in respect to the applied chirp at the end of the beamline. The upper horizontal axes relate the imposed chirp to the final correlated energy spread of the beam.

longitudinal emittance and related eigen emittance  $\lambda_2$  are still much larger 31.86  $\mu\text{m}$  than their initial value of 5.72  $\mu\text{m}$ . The corresponding phase spaces at the exit of the beamline are presented in Fig. 3.14. The transverse phase space is practically degradation-free, while only minimal residual correlations between transverse and longitudinal phase spaces are present. The slight bend in the longitudinal phase space explains the enlargement of the longitudinal emittance. The evolution of the normal and eigen emittances for this beamline is presented in Figure 3.15.

The last cavity voltage should be adjusted proportionally to its initial value (voltage in other cavities) when defining the imposed chirp. For example, if one needs a smaller chirp corresponding to a voltage of 2 MV instead of the maximum applied chirp at 2.5 MV, the optimal voltage in the last cavity is smaller, *i.e.*  $\Delta V = 13$  kV. This is because the nonlinear effects shift the average beam energy less with a smaller total normalized energy spread. For  $V = 1.5$  MV it is correspondingly  $\Delta V = 5.25$  kV and for  $V = 1.0$  MV we find  $\Delta V = 1.6$  kV. These points follow the approximate relation:  $\Delta V [\text{kV}] = 1.696 \cdot V^3 [\text{MV}]$ , which defines the proper rule for adjustment of the voltage in the last cavity in order to

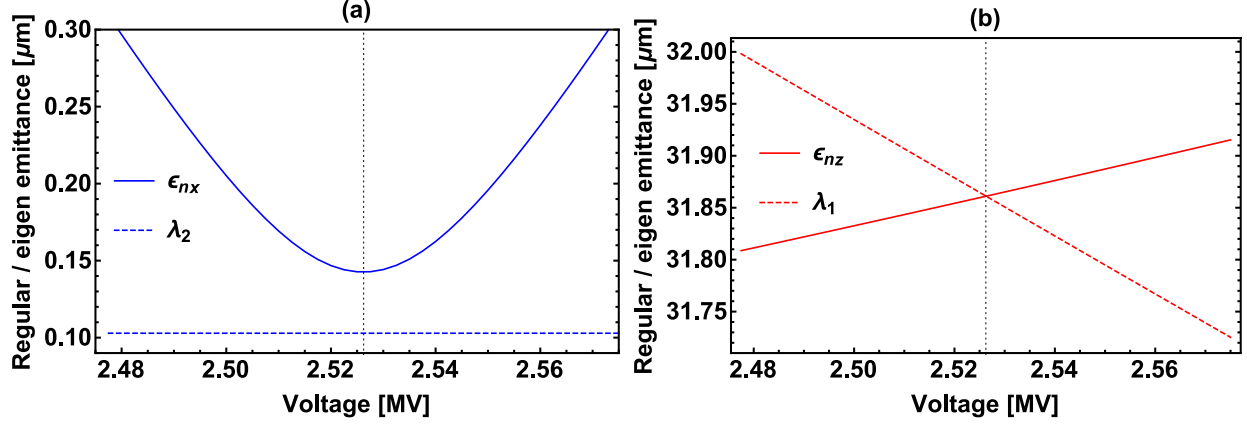


Figure 3.12: Transverse and longitudinal emittances and eigen emittances from the voltage in the last TDC at the Twiss parameters values of  $\beta_{x,y} = 59$  m and  $\alpha_{x,y} = 2.1$ . The dotted vertical line demonstrates the optimal voltage when the minimum of the transverse emittance is reached, which happens when the longitudinal regular and eigen emittances match.

suppress the residual linear correlations between transverse and longitudinal phase spaces at the exit of the beamline. This numerically derived dependence can be explained as follows. The total energy spread is predominantly defined by the imposed chirp which quadratically scales from the normalized deflection potential  $\kappa$  according to Eq. (3.14) and the transverse cavity voltage  $V$  according to Eq. (3.12). Relative adjustment of the deflecting voltage in the last cavity then scales as  $\frac{\Delta V}{V} \sim V^2 \sim \frac{\Delta \gamma}{\gamma}$ . Therefore, the average shift of the bunch energy is most likely due to the dominating second order effect defined by the matrix element  $T_{256}$ , while the longitudinal bunch size remains approximately invariant along the beamline.

### 3.5.3 Longitudinal space charge effects

In the next stage we investigate the impact of the LSC forces during propagation through the beamline. Vacuum drifts were simulated using ELEGANT subroutine, LSCDRIFT, which assumes no beam pipe and ignores transverse fields as discussed in Section 1.2. Simulations of the beam with 100 pC bunch charge, required for MaRIE, did not show any significant

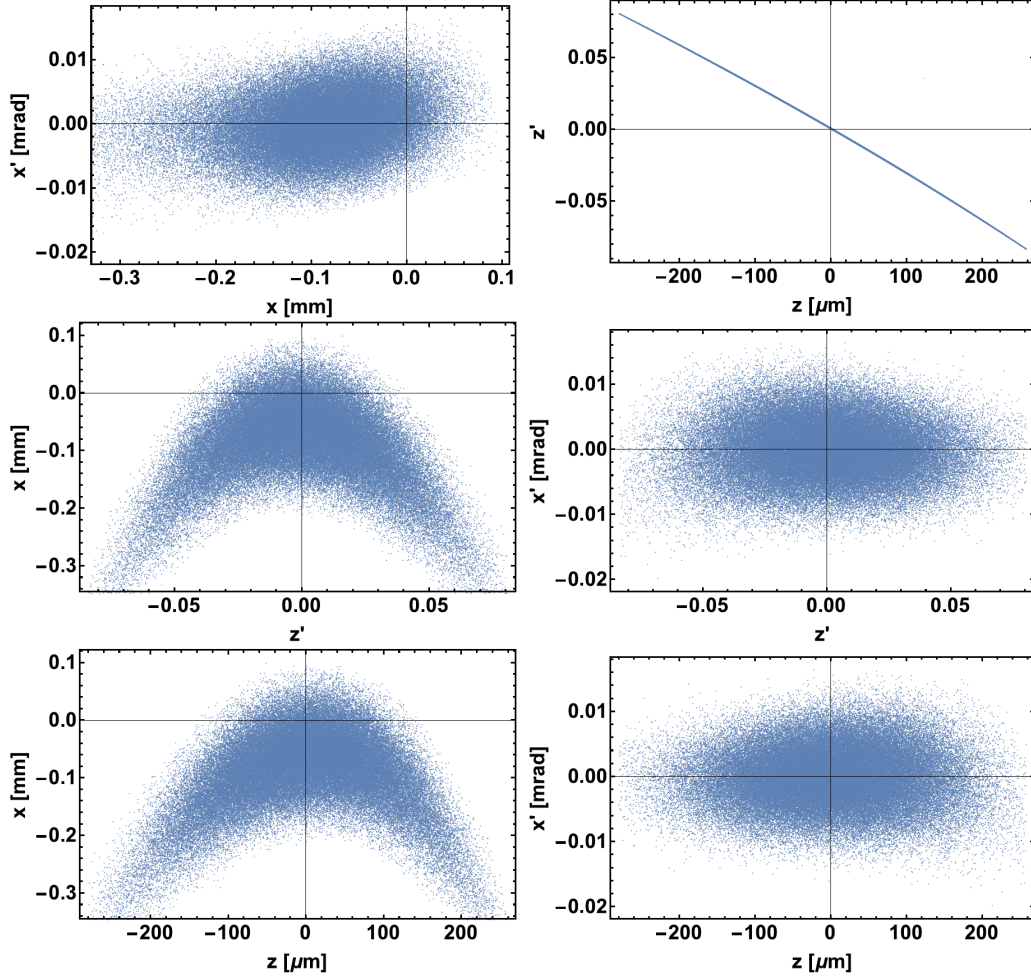


Figure 3.13: Phase spaces at the exit of the TDC-based chirper at 250 MeV for non-linear single-particle dynamics at  $\beta_{x,y} = 59$  m and  $\alpha_{x,y} = 2.1$  with the tuned voltage ( $\Delta V = +26.5$  kV) in the last TDC.

difference in the final transverse emittance (Table 3.2) or the shape of the transverse phase space ( $x, x'$ ). Moreover, the longitudinal phase space experiences unnoticeable changes at this charge, which only become visible at 10 nC bunch charge in the form of the energy spread wake along the bunch as demonstrated in Fig. 3.16. While the transverse space charge effects can also become important for the 10 nC bunch charge, we omit it in our simulations. This is because we predominantly discuss the TDC-based chirper beamline for 100 pC MaRIE

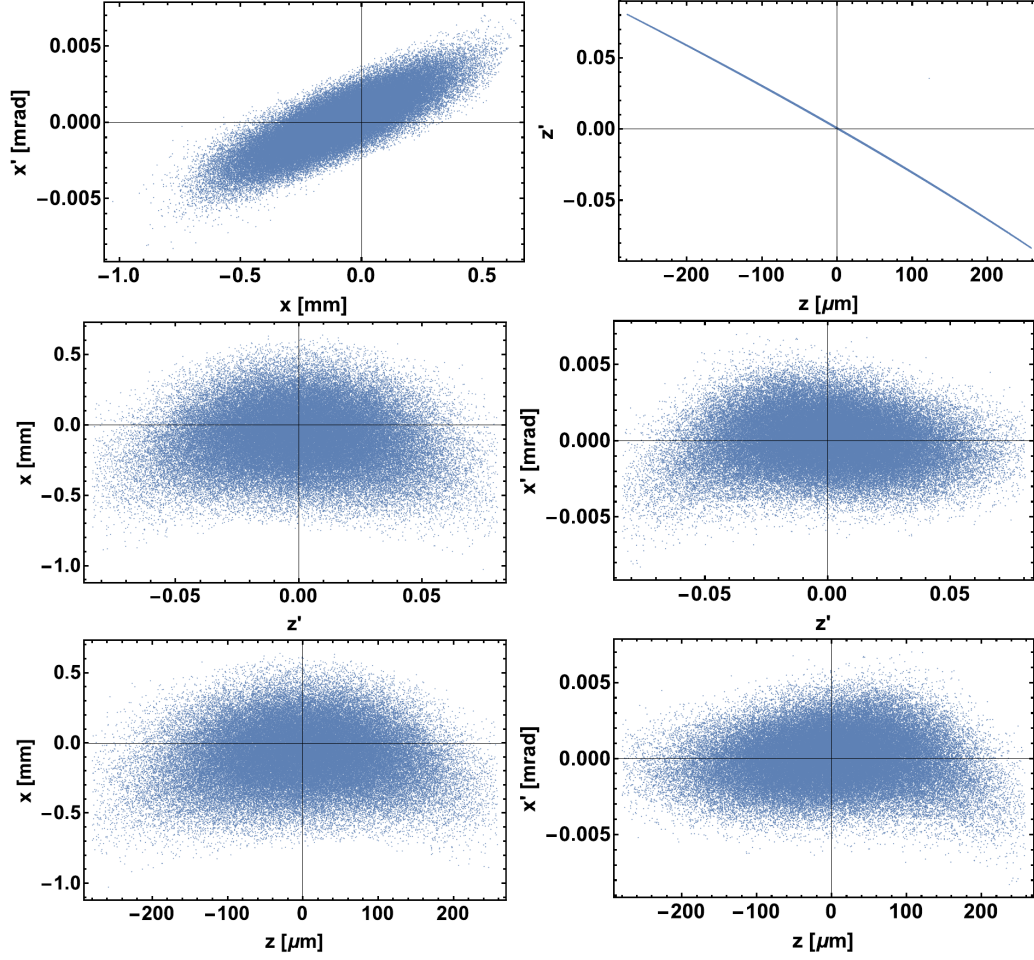


Figure 3.14: Phase spaces at the exit of the TDC-based chirper at 250 MeV for nonlinear single-particle dynamics with tuned voltage ( $\Delta V = +26.5$  kV) in the last TDC for the new optimal set of the input Twiss parameters  $\beta_{x,y} = 150$  m and  $\alpha_{x,y} = -1.3$ .

bunch charge, where TSC effects are expected to be insignificant (see Section 1.2 for more details).

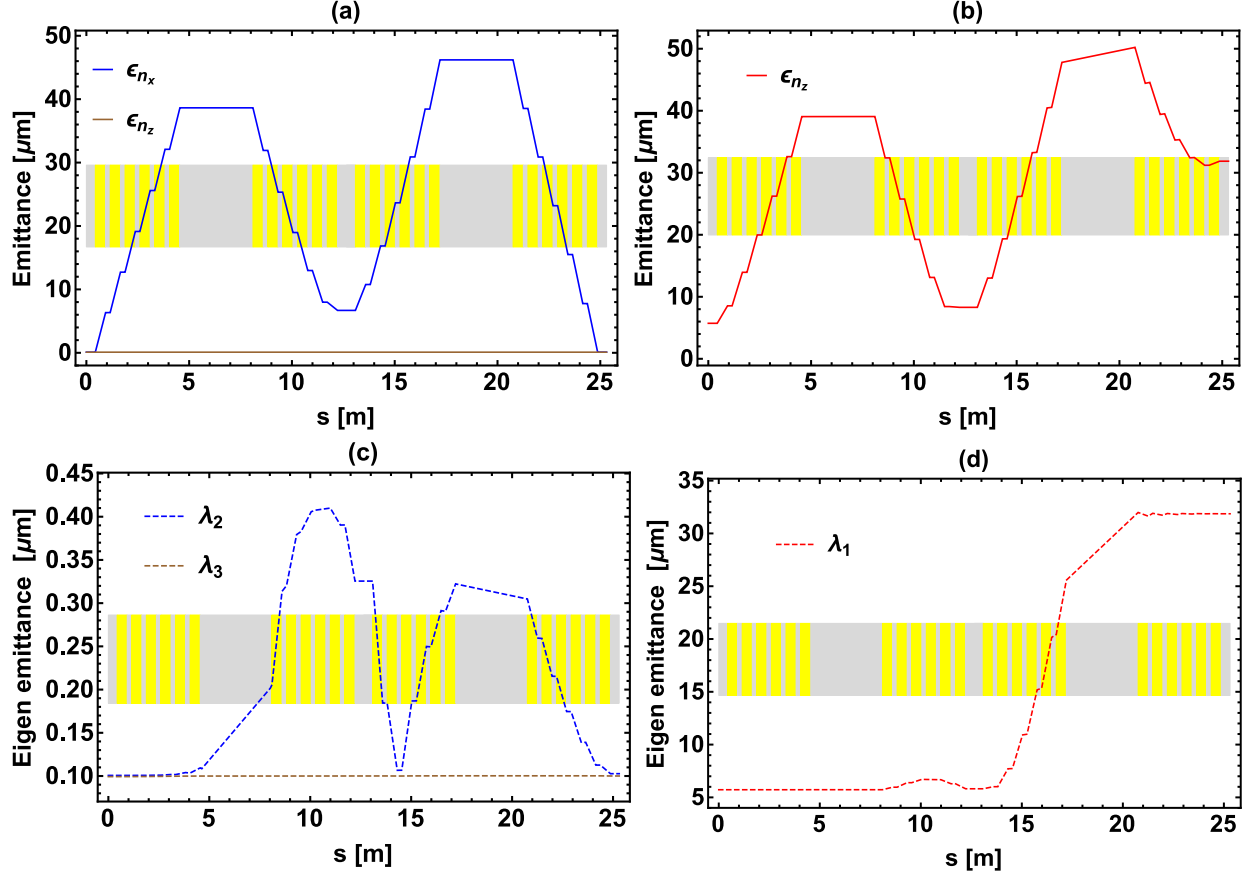


Figure 3.15: Transverse and longitudinal emittances and eigen emittances along the beamline with the adjusted voltage in the last TDC at the new optimal Twiss parameters  $\beta_{x,y} = 150$  m and  $\alpha_{x,y} = -1.3$ .

### 3.5.4 Nonlinear optics for correction of the longitudinal emittance

The degradation of the transverse emittance  $\epsilon_{n_x}$  due to nonlinear effects was minimized by suppressing residual transverse-longitudinal correlations and by adjusting the input Twiss parameters reaching an acceptable emittance enlargement of 5% while imposing 6.7 MeV correlated energy spread on the beam. The longitudinal emittance matched with its related eigen emittance  $\lambda_1$  after tuning the voltage in the last cavity. Later, both quantities were

Table 3.2: Emittance degradation in the 250 MeV chirper accounting for the LSC effects for different bunch charges.

	In	Out			
<b>Bunch charge</b> $q$ [nC]		0	0.1	10	20
<b>Emittance</b> $\epsilon_{n_x}$ [ $\mu\text{m}$ ]	0.1	0.105	0.105	0.112	0.125
<b>Emittance</b> $\epsilon_{n_z}$ [ $\mu\text{m}$ ]	5.72	31.86	31.84	84.17	159.7

practically unaffected by adjustment of the Twiss parameters. The final  $\lambda_1 = 31.86 \mu\text{m}$  is roughly 5.5 times bigger than its initial value. According to Figure 3.15, it starts growing in the second TDC but comes back close to its initial value. It significantly grows in the third TDC and its subsequent drift, and then remains unchanged in the last cavity. Figure 3.17 demonstrates strong quadratic correlations between  $x'$  and  $z'$  in the middle of the beamline. Since  $z'$  is linearly correlated with  $z$  and  $x$ , similar quadratic correlations are present in  $(x, x')$  and  $(z, x')$  phase spaces (Fig. 3.17). These correlations in  $(x, x')$  phase space can be suppressed by a sextupole<sup>19</sup> (non zero  $T_{211}$ ), which would automatically correct the rest of the quadratic nonlinearities in other phase spaces due to the present linear correlations (Fig. 3.18). Using a sextupole<sup>20</sup> with  $k = 4.5 \text{ m}^{-3}$  will instantaneously decrease the transverse eigen emittance  $\lambda_2$  (close to its minimum value) and increase the longitudinal eigen emittance (Fig. 3.19 (a), (b)). The last value will be increased even more in upstream cavity than without a sextupole. This suggest that the sextupole strength should be adjusted to compensate for the enlargement of the eigen emittance  $\lambda_1$  in upstream cavity (third TDC). The same approach can be repeated by using an additional sextupole between third and last cavity to minimize  $\lambda_1$  and  $\epsilon_{n_z}$  at the exit of the beamline. One might also add an additional sextupole between first and second TDCs in order to minimize  $\lambda_1$  at the exit of second cav-

<sup>19</sup>A sextupole is a nonlinear element in which the effective focal length is linearly changed across the radius. Thus, it can be used directly for imposing/removing quadratic correlations in the transverse phase space.

<sup>20</sup>The length of all sextupoles was chosen to be 0.1 m for simplicity and can be enlarged if required geometric strengths are too extreme. Each sextupole was simulated in ELEGANT as the SEXT element implemented as a matrix to the 3rd order [38].

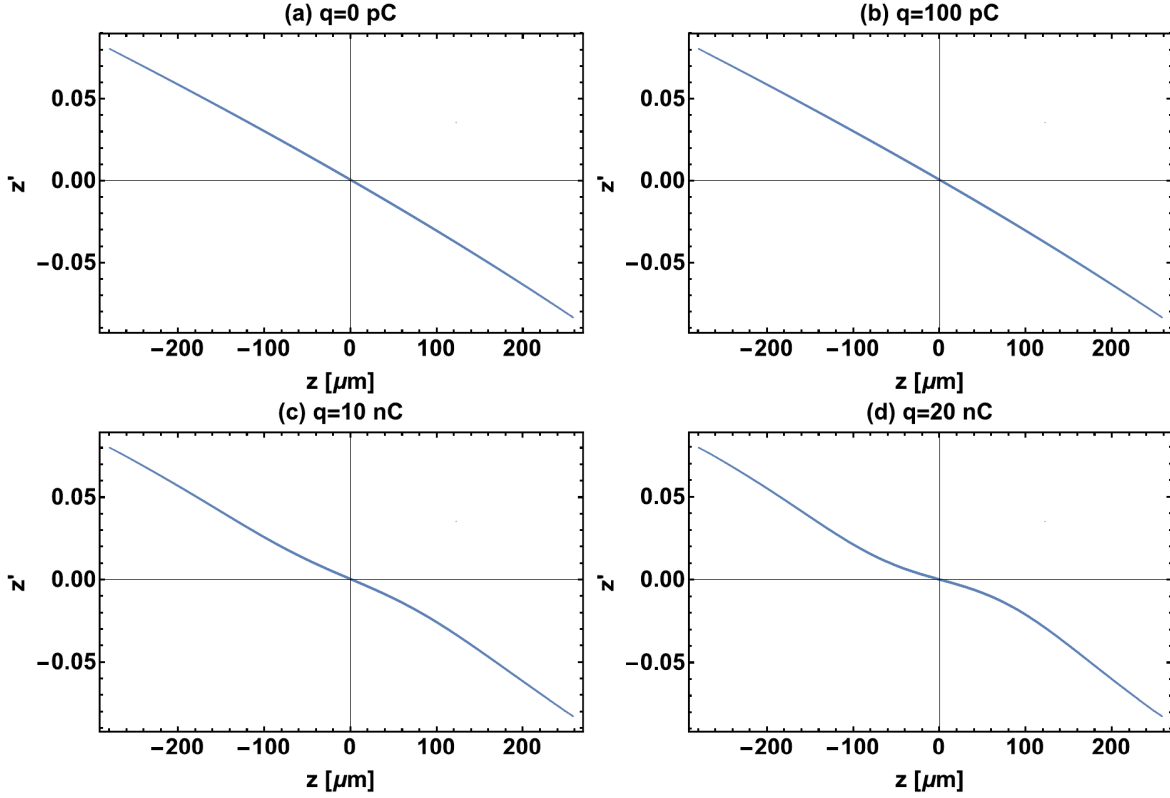


Figure 3.16: LSC effects on the final longitudinal phase space in the TDC-based chirper at 250 MeV for different bunch charges: (a) 0 pC; (b) 100 pC; (c) 10 nC and (d) 20 nC.

ity. The combination of three sextupoles,  $k_1 = 5.6 \text{ m}^{-3}$ ,  $k_2 = -21.5 \text{ m}^{-3}$ ,  $k_3 = -22 \text{ m}^{-3}$ , results in a final longitudinal emittance of  $6.07 \text{ } \mu\text{m}$ , which is only 6% bigger than its initial value (Fig. 3.19 (c), (d)). The main problem of this approach is that inserting sextupoles unavoidably change the transverse eigen emittance  $\lambda_2$  profile. This results in destroying the almost ideal compensation of  $\lambda_2$  along the beamline demonstrated in Fig. 3.15 and the final eigen emittance becomes approximately 15 times bigger than its initial value. This problem can be partially mitigated by readjusting the input Twiss parameters, which has almost no effect on the longitudinal emittance as was noted earlier<sup>21</sup>. The minimum of the transverse emittance  $\epsilon_{n_x} = 0.174$  is reached at  $\beta_x = 589 \text{ m}$  and  $\alpha_x = 35$  and is 74% bigger than its

<sup>21</sup>This is most likely because the longitudinal emittance is much bigger than its transverse counterpart.

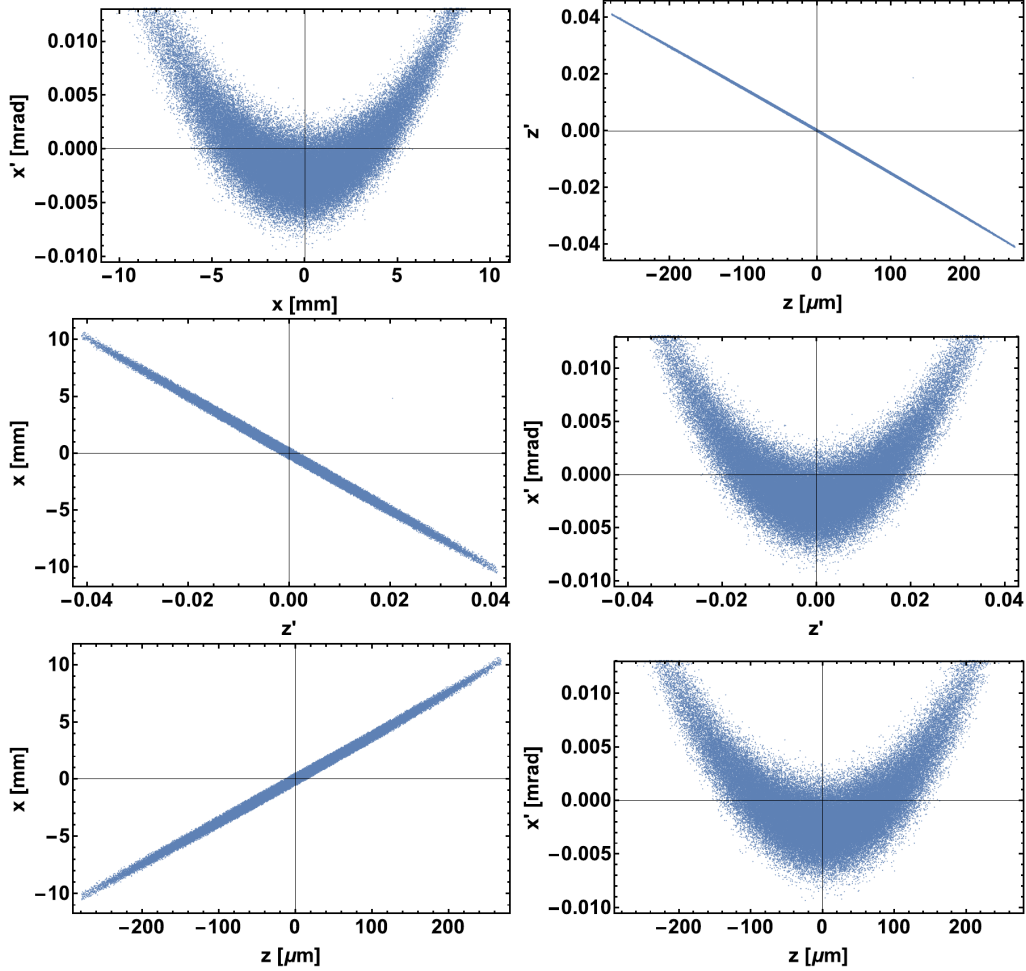


Figure 3.17: Phase spaces in the middle of the TDC-based chirper at 250 MeV with tuned voltage in the last TDC and Twiss parameters:  $\beta_x = \beta_y = 150$  m and  $\alpha_x = \alpha_y = -1.3$ .

initial value while the longitudinal eigen emittance is unchanged relative to the previous case (Fig. 3.19 (e, f)). This suggest that minimizing the longitudinal eigen emittance along the beamline is not necessarily the most effective strategy for simultaneous compensation of both transverse and longitudinal emittances and their related eigen emittances. The optimal strategy is most likely adjusting the sextupoles in such a way that  $\lambda_2$  remains as small as possible at the exit of the beamline while the final  $\lambda_1$  is minimized after each iteration. However, even this method does not guarantee that degradation of both emittances can

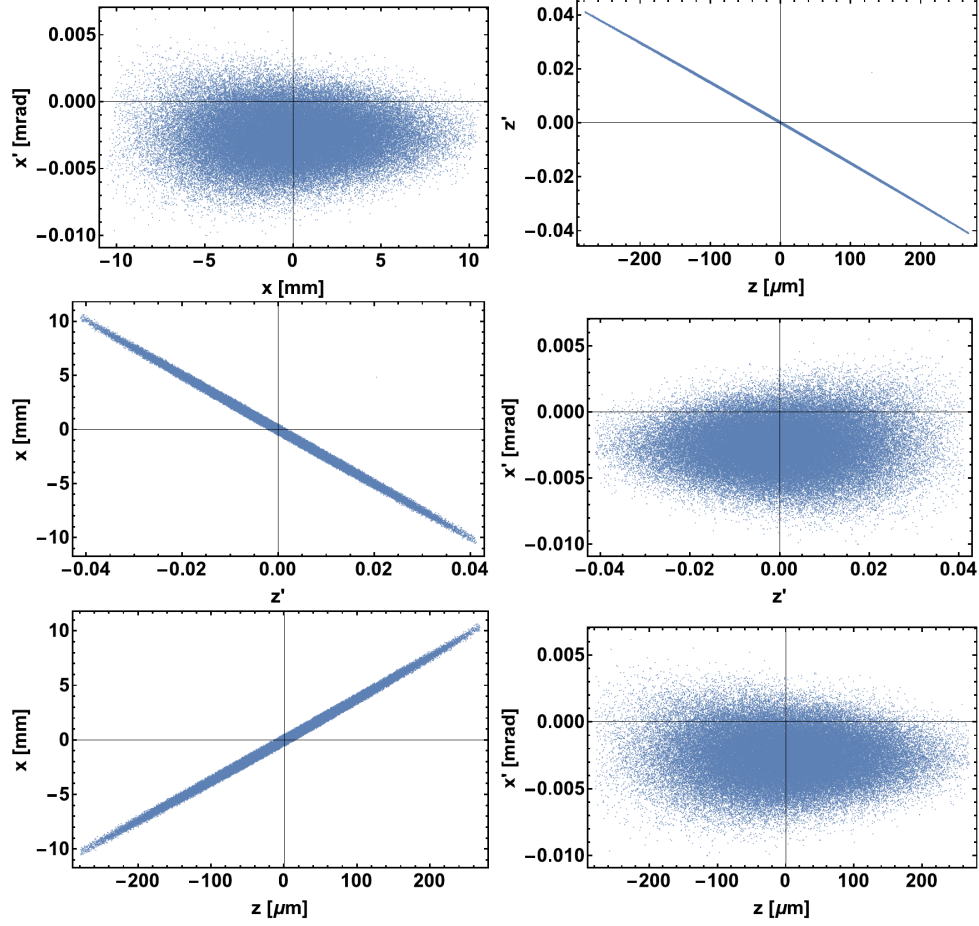


Figure 3.18: Phase spaces in the middle of the TDC-based chirper at 250 MeV after the sextupole with  $k_1 = 4.5 \text{ m}^{-3}$ . The voltage in the last TDC is up-shifted and the input Twiss parameters are  $\beta_x = \beta_y = 150 \text{ m}$  and  $\alpha_x = \alpha_y = -1.3$ .

be completely suppressed, as we will demonstrate in the next section regarding a 1 GeV TDC-based chirper.

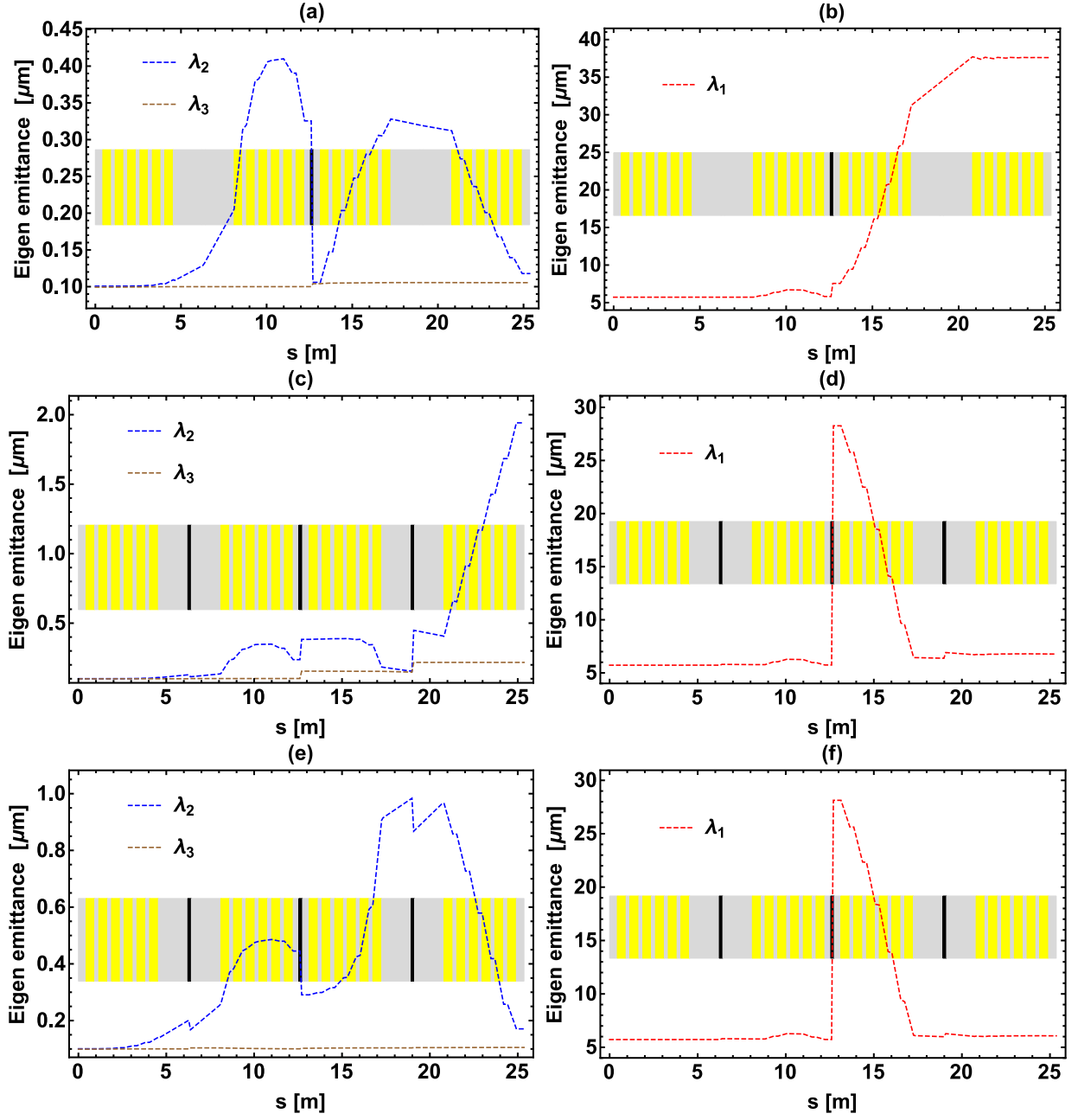


Figure 3.19: Transverse and longitudinal eigen emittances along the beamline: (a,b) one sextupole  $k_1 = 4.5 \text{ m}^{-3}$  adjusted to suppress quadratic correlations in  $(z', x')$ ,  $(x, x')$  and  $(z, x')$  phase spaces in the middle of the beamline; (b,c) three sextupoles  $k_1 = 5.6 \text{ m}^{-3}$ ,  $k_2 = -21.5 \text{ m}^{-3}$  and  $k_3 = -22 \text{ m}^{-3}$  adjusted to minimize the longitudinal eigen emittance with the previously optimized Twiss parameters  $\beta_{x,y} = 150 \text{ m}$  and  $\alpha_{x,y} = -1.3$ ; (e,f) the same sextupole configuration with re-optimized Twiss parameters  $\beta_{x,y} = 589 \text{ m}$  and  $\alpha_{x,y} = 35$ . The black lines mark the actual positions of the sextupoles within the beamline.

### 3.6 Chirper at 1 GeV beam energy

After demonstration of the TDC-based chirper scheme at 250 MeV beam energy fitting within two cryomodules, we turn our attention to the chirper design at 1 GeV using similar deflecting cavities. Imposing the same correlated energy spread on the beam at four times higher energy (1 GeV vs. 250 MeV) will result in approximately four times smaller total normalized energy spread<sup>22</sup>. As a result, nonlinear effects associated with large normalized energy spread should become much smaller, and possibly would not require any compensation/optimization of the transverse emittance degradation. Moreover, demonstrating a good performance of the scheme at larger energy (1 GeV) will allow the choice of whether it is convenient to impose the chirp at lower beam energy (250 MeV) and further accelerate the beam or, conversely, impose the chirp on the previously accelerated beam right before the chicane. This is in regards to the minimization of the LSC-induced microbunch instabilities in the bunch compressor combined from such a chirper and a chicane<sup>23</sup>. We consider this discussion beyond the scope of this work since it requires further detailed theoretical and simulation studies. In comparison with the 250 MeV design, the TDC-based chirper at 1 GeV is twice as long and fits in four cryomodules instead of two (Fig. 3.2). In addition, this scheme requires more RF power which results in longer sections of the deflecting cavities with the same deflecting voltage as was chosen for the 250 MeV design (See Table 3.1 for more details).

The observed enlargement of transverse emittances in the 1 GeV chirper scheme is very small. For example, for the imposed correlated energy spread of 8 MeV and the input Twiss

---

<sup>22</sup>Indeed, the total energy spread is dominated by the correlated energy spread which is still much larger than the uncorrelated energy spread

<sup>23</sup>The most convenient TDC based chirper location can be, in principle, at any point along the accelerator beamline between 250 MeV or 1 GeV. These borders are defined by the current locations of two chicanes of the first and second BCs according to the conceptual MaRIE beamline design [58]

parameters  $\beta_x = 175$  m and  $\alpha_x = 0.3$ , the scheme demonstrates less than 2% enlargement of  $\epsilon_{n_x}$ , while the changes are completely negligible for  $\epsilon_{n_y}$  ( $< 0.02\%$ ). The performed simulations account for the longitudinal space charge effects in drifts for a 100 pC bunch charge, which does not impose any visible effects on the beam dynamics at this charge and will therefore be neglected in further simulations of this section. The dependences of the final emittances from the applied chirp, which can be controlled by adjusting the voltage in all deflecting cavities simultaneously, are plotted in Fig. 3.20. It is clear that only the longitudinal emittance experiences significant degradation, resulting in a roughly 2.25-fold increase of  $\epsilon_{n_z}$  for the imposed correlated energy spread of 8 MeV and approximately 25% enlargement of  $\epsilon_{n_z}$  for the correlated energy spread of 5 MeV.

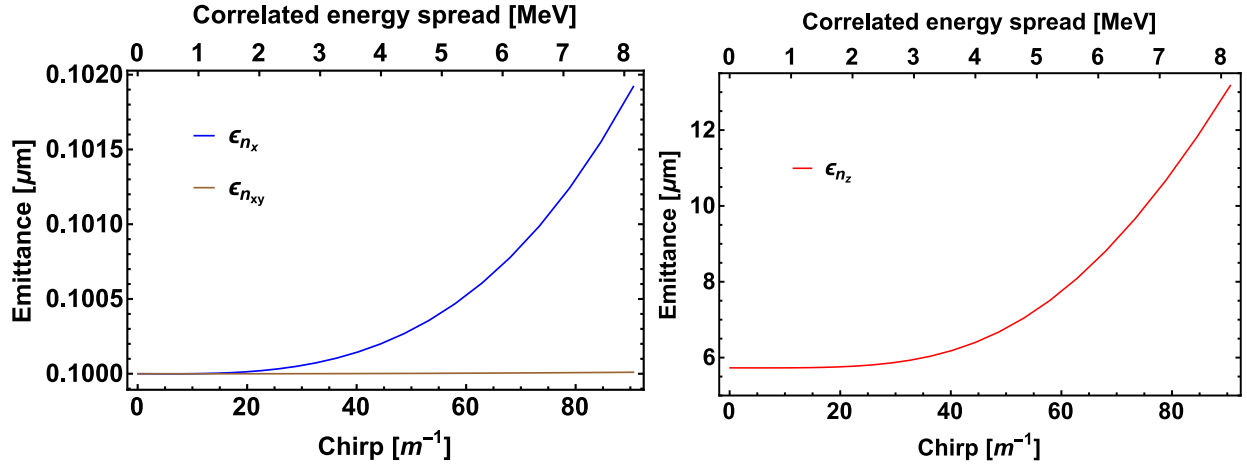


Figure 3.20: Normalized emittances at the exit of the TDC-based chirper at 1 GeV in respect to the applied chirp. The upper horizontal axes relate the imposed chirp to the final correlated energy spread of the beam.

We analyze the degradation of the longitudinal emittance by tracking change in the emittances and their related eigen emittances along the beamline (Fig. 3.21). The evolution of the beam parameters along the beamline is presented in Fig. 3.22. The dependences are similar to the 250 MeV chirper, with the exception that the longitudinal beam size remains completely invariant along the beamline. The phase spaces on the exit of the beamline are

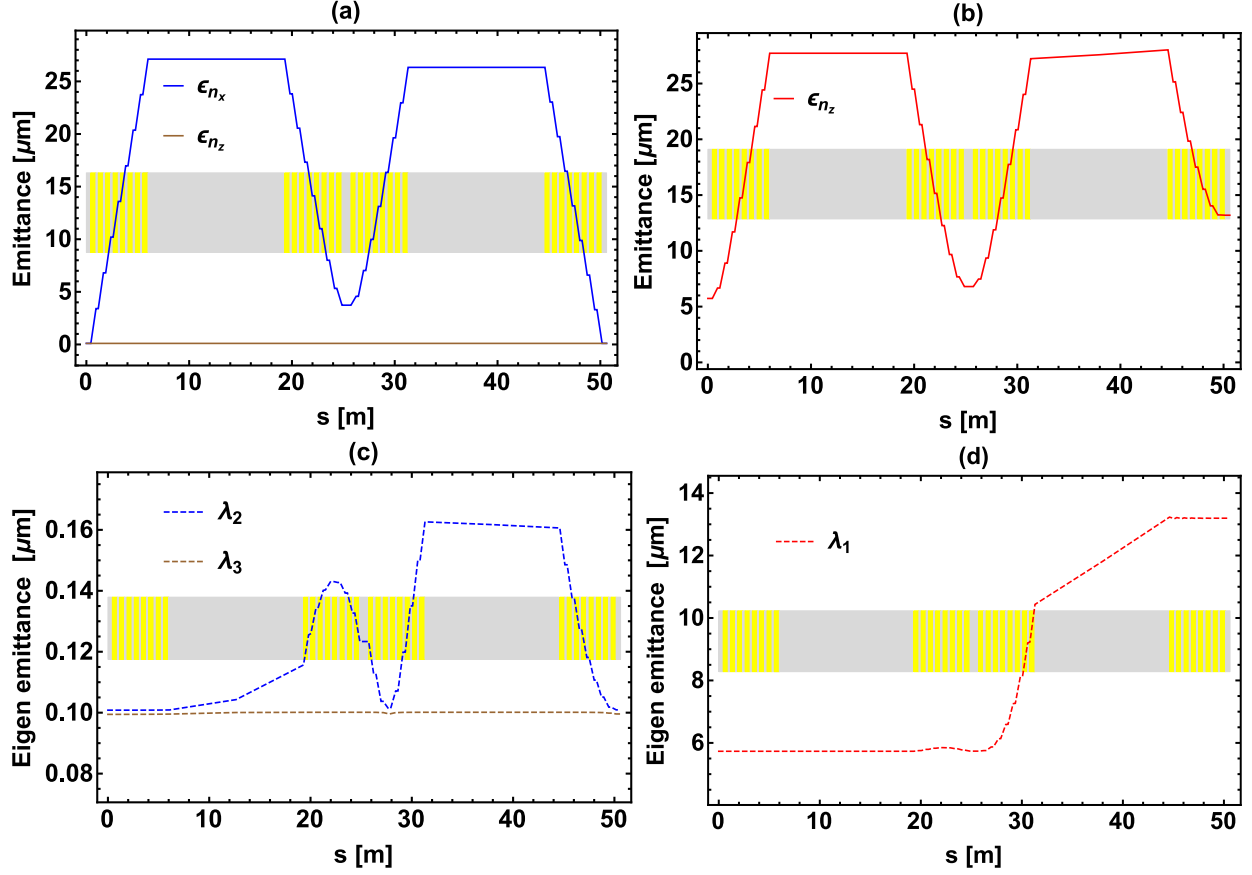


Figure 3.21: Transverse and longitudinal emittances and eigen emittances along the beamline of the TDC-based chirper at 1 GeV for the input Twiss parameters  $\beta_x = \beta_y = 175$  m and  $\alpha_x = \alpha_y = 0.3$ .

demonstrated in Figure 3.23. The slight bend in the longitudinal phase space explains the enlargement of the longitudinal emittance.

The imposed chirp at 1 GeV energy results in a larger normalized energy spread and smaller longitudinal emittance degradation, which is almost negligible for the transverse phase space but still significant for the longitudinal phase space, especially for a large chirp. Next, we demonstrate that the longitudinal emittance degradation can be minimized with sextupoles, at the price of a relatively small enlargement of the transverse emittances. We add three sextupoles to compensate for the eigen emittance  $\lambda_1$  associated to the longitudinal phase space. In particular, we insert one sextupole in between of each two TDCs as was

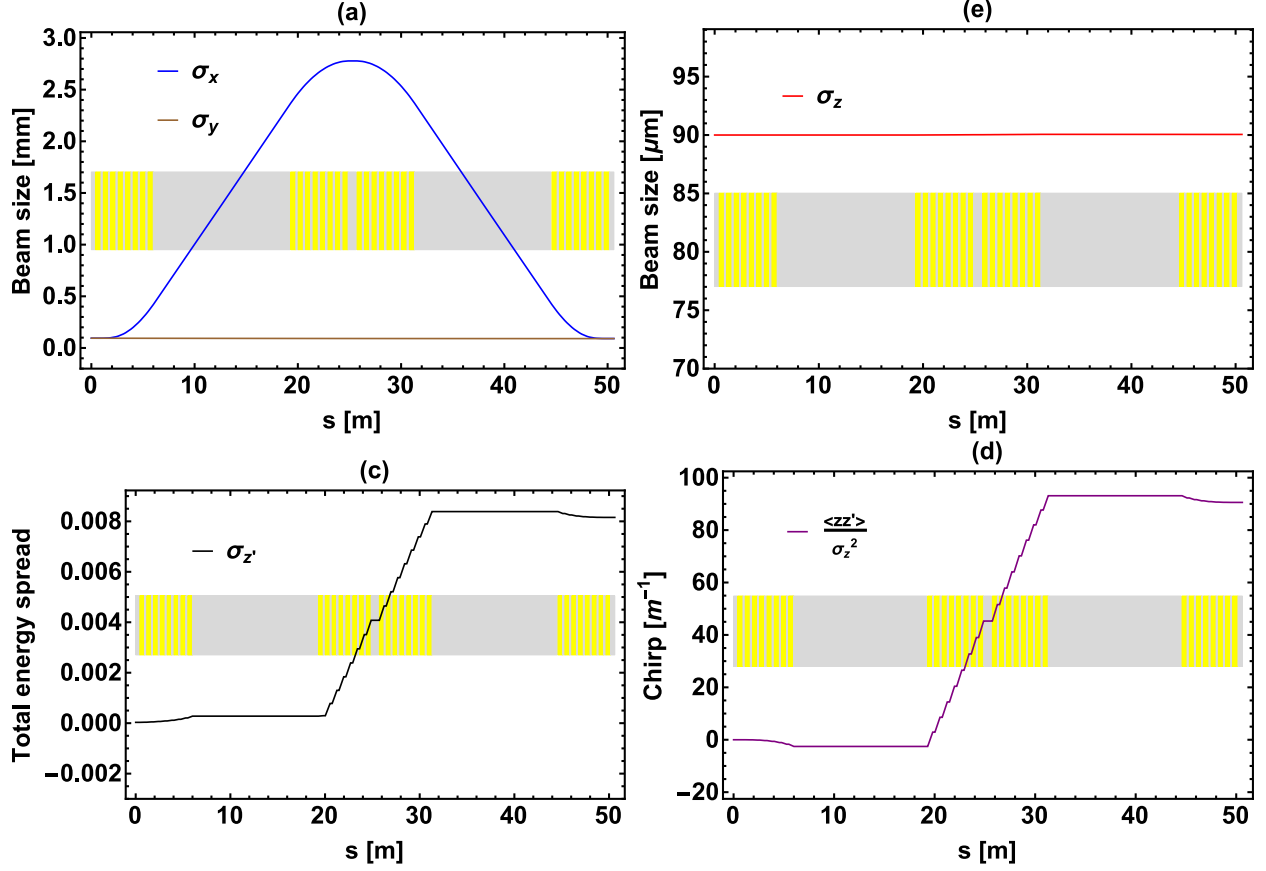


Figure 3.22: Beam parameters at a distance  $s$  along the beamline for the optimized Twiss parameters  $\beta_x = \beta_y = 175$  m and  $\alpha_x = \alpha_y = 0.3$ : (a)  $\sigma_x$  and  $\sigma_y$ ; (b)  $\sigma_z$ ; (c) the total energy spread; (d) the energy chirp. The ordinate  $s = 0$  m corresponds to the entrance of the beamline.

previously accomplished for 250 MeV scheme. Similarly, we tune the first sextupole to minimize  $\lambda_1$  at the end of the second cavity. This step and the sextupole ( $k_1 = 0.2 \text{ m}^{-3}$ ) itself can be omitted, since  $\lambda_1$  is very close to its initial value. We then adjust the second sextupole to minimize “longitudinal” eigen emittance in the end of the third cavity. Then, we adjust the third sextupole to optimize  $\lambda_1$  on the exit of the beamline. The geometric strengths of the three sextupoles are correspondingly  $k_1 = 0 \text{ m}^{-3}$ ,  $k_2 = -2.5 \text{ m}^{-3}$  and  $k_3 = -12 \text{ m}^{-3}$ . On the final step we slightly adjust the input Twiss parameters in order to compensate for the transverse emittance degradation. These actions result in  $\epsilon_{n_x} = \lambda_2 = 0.11 \text{ } \mu\text{m}$  and

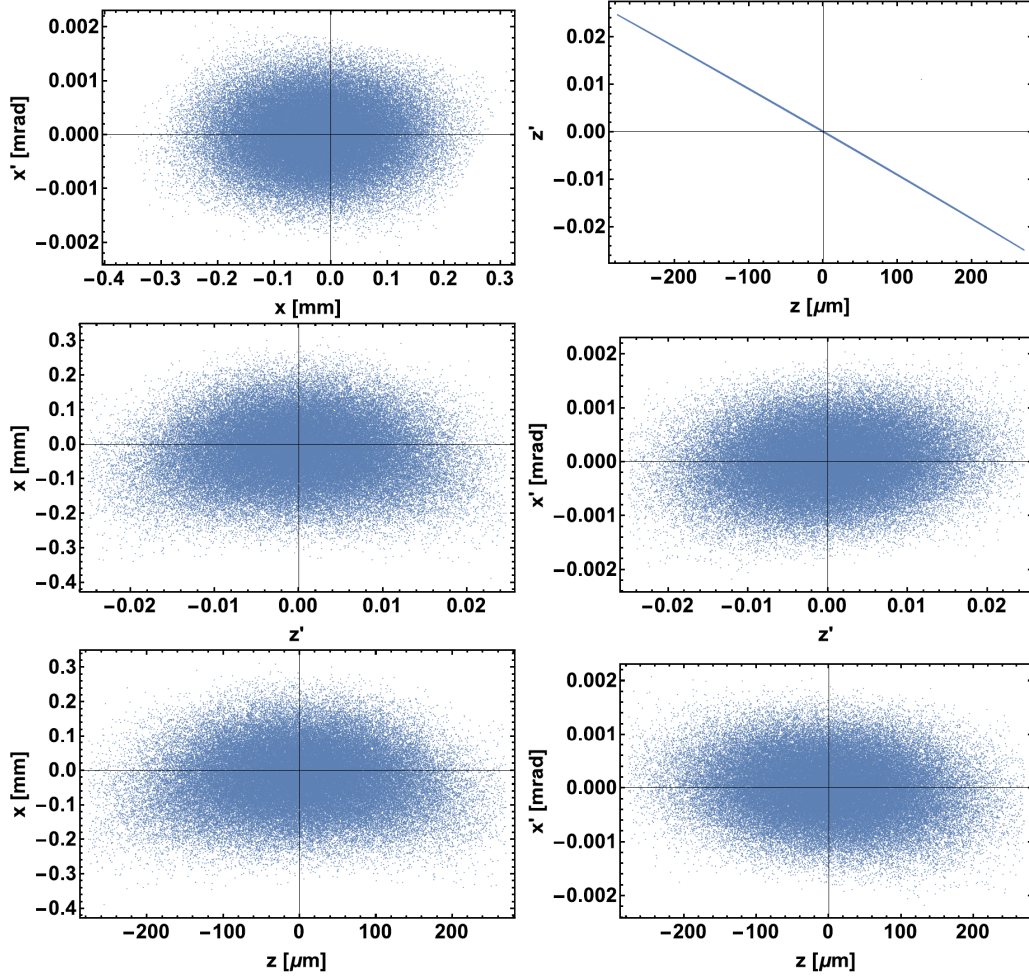


Figure 3.23: Phase spaces at the exit of the TDC-based chirper at 1 GeV with the nonlinear dynamics accounting for the LSC at  $q=100$  pC,  $\beta_x = \beta_y = 175$  m and  $\alpha_x = \alpha_y = 0.3$ .

$\epsilon_{n_z} = \lambda_1 = 5.75 \mu\text{m}$ , while their initial values were respectively  $0.10 \mu\text{m}$  and  $5.72 \mu\text{m}$ . Thus, the enlargement of the the transverse emittance  $\epsilon_{n_x}$  is 10%, while the enlargement of the longitudinal emittance is approximately 0.5%. The evolution of the normalized emittances and eigen emittances along the beamline, presented in Fig. 3.24, demonstrates that both emittances,  $\epsilon_{n_x}$  and  $\epsilon_{n_y}$ , and their related eigen emittances,  $\lambda_2$  and  $\lambda_1$ , come close to their initial values. The evolution of the beam parameters along the scheme is presented in Fig. 3.25. As is clearly seen in Figure 3.26, there are some remaining correlations between

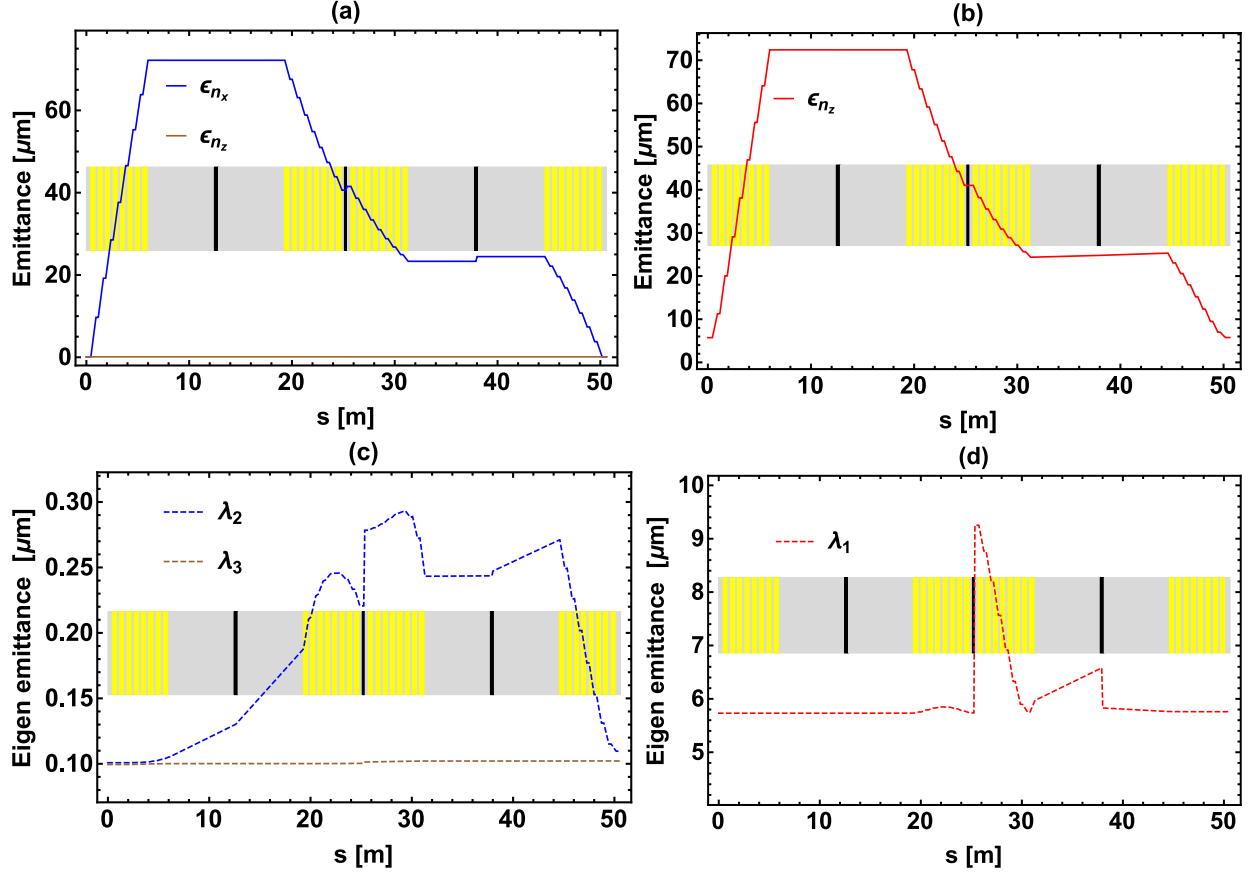


Figure 3.24: Transverse and longitudinal emittances and eigen emittances along the beamline of the TDC-based chirper at 1 GeV with sextupoles ( $k_1 = 0 \text{ m}^{-3}$ ,  $k_2 = -2.5 \text{ m}^{-3}$ ,  $k_3 = -12 \text{ m}^{-3}$ ) tuned to preserve the longitudinal phase space. Twiss parameters are  $\beta_x = \beta_y = 1472.5 \text{ m}$  and  $\alpha_x = \alpha_y = 40$ .

transverse and longitudinal phase spaces at the exit of the beamline. This explains the small degradation of the transverse emittance  $\epsilon_{n_x}$  and its related eigen emittance  $\lambda_2$ .

Adjusting two sextupoles (the second and the third, while the first one is turned off) in such a way that  $\lambda_2$  remains the same at the exit of the beamline (close to its initial value) and  $\lambda_1$  get reduced on each step results in geometric strength values of the sextupoles of  $k_1 = 0 \text{ m}^{-3}$ ,  $k_2 = -4.5 \text{ m}^{-3}$ , and  $k_3 = 18 \text{ m}^{-3}$ . The following optimization of the input Twiss parameters suggests to choose  $\beta_x = \beta_y = 100 \text{ m}$  and  $\alpha_x = \alpha_y = 0.6$ . These actions result in similar enlargements of the transverse emittance: 7% vs. 10% previously, while

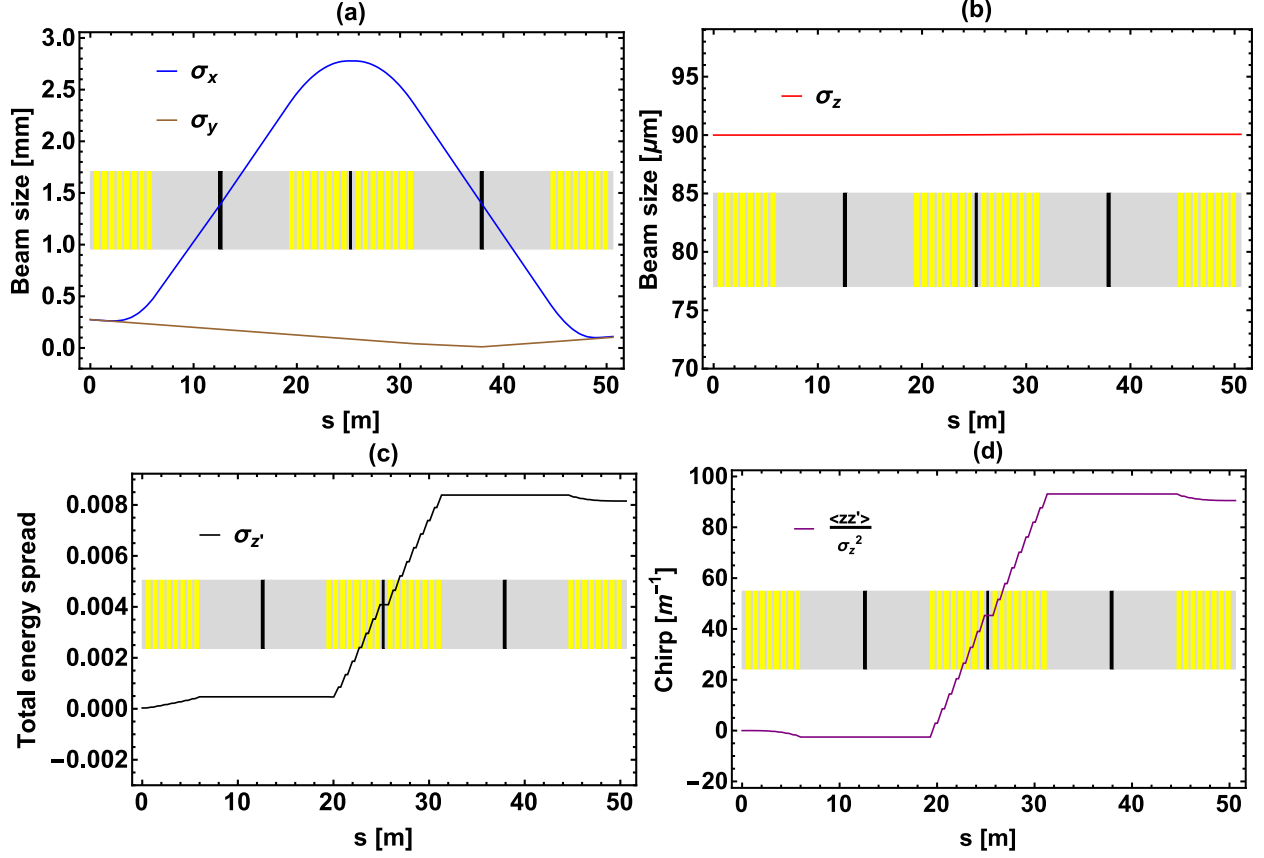


Figure 3.25: Beam parameters: (a)  $\sigma_x$  and  $\sigma_y$ ; (b)  $\sigma_z$ ; (c) the total energy spread; (d) the energy chirp, at a distance  $s$  along the beamline of the TDC-based chirper at 1 GeV with sextupoles  $k_1 = 0 \text{ m}^{-3}$ ,  $k_2 = -2.5 \text{ m}^{-3}$ , and  $k_3 = -12 \text{ m}^{-3}$  tuned to preserve the quality of the longitudinal phase space. The Twiss parameters are  $\beta_x = \beta_y = 1472.5 \text{ m}$  and  $\alpha_x = \alpha_y = 40$ .

the longitudinal emittance enlargement is approximately 39%, which is significantly greater than before. This strategy allows us to choose an acceptable level of the transverse emittance enlargement and minimizing the longitudinal emittance until this boundary limit is reached. The simultaneous optimization of the transverse and longitudinal emittances is a complex problem which most likely can be accomplished as a multi-dimensional optimization over the 2-dimensional space of the input Twiss parameters and an additional 3(5)-dimensional space of parameters of three sextupoles<sup>24</sup>. This problem can be most likely solved by the

<sup>24</sup>An additional two sextupoles can be added. Moreover, adding several octupoles might be useful as well.

Extremum Seeking algorithm introduced in the previous Chapter (see Section 2.5 for details), however we leave this approach beyond the scope of this dissertation.

Summarizing Sections 3.5-3.6, we presented two efficient TDC-based chirper designs at 250 MeV and 1 GeV beam energy. The first design imposes a large total energy spread on the beam, which results in the degradation of both transverse and longitudinal phase space due to strong nonlinear effects. This can be compensated by suppressing linear correlations by tuning the voltage in the last TDC and by adjustment of the input Twiss parameters. The enlargement of the longitudinal phase space can be compensated using sextupoles, which, however, unavoidably leads to the degradation of the transverse phase space demonstrating the emittance enlargement of 74%. By contrast, the scheme at 1 GeV beam energy imposes approximately the same correlated energy spread but less normalized energy spread, which results in smaller nonlinear effects. In particular, the transverse emittance degradation is practically negligible, and the longitudinal emittance enlargement is much smaller. Moreover, it can be completely compensated for with the incorporation of sextupoles, at the cost of a small transverse emittance degradation ( $\sim 10\%$ ). Despite the obvious benefits of the chirping beamline at 1 GeV, the main disadvantage that it is roughly four times longer, and requires larger-length deflecting cavities, and consequently more RF power to drive them. Finally, the flexibility of the TDC-based chirper to be realized at different beam energies and its good performance proves the feasibility of the proposed scheme. This also suggests that such a beamline can be applied for practically all existing and planned to be built accelerators where it is required to impose a large correlated energy spread on the beam instead of the conventional off-crest acceleration, which is comparatively useful in terms of RF power consumption and ultimately taxpayer money.

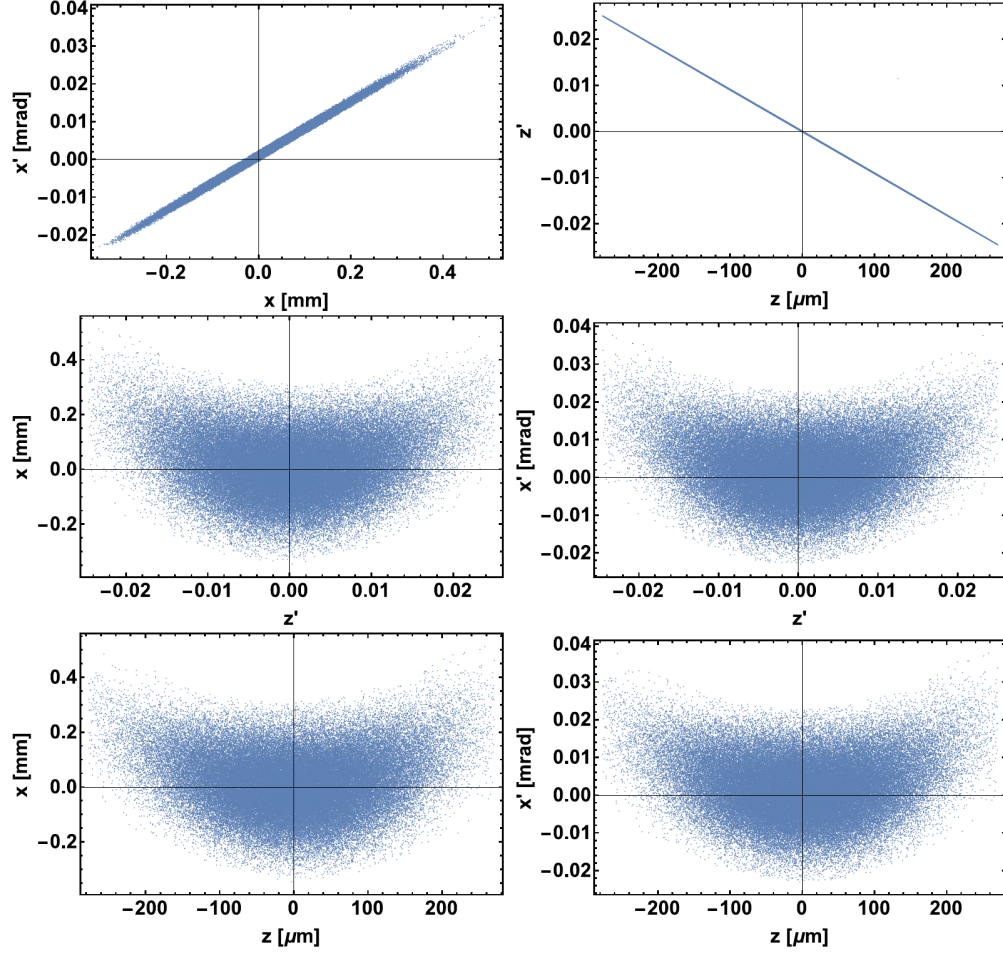


Figure 3.26: Phase spaces at the exit of the TDC-based chirper at 1 GeV with sextupoles tuned to preserve the longitudinal phase space. The simulations use nonlinear dynamics accounting for the LSC at  $q=100$  pC and input Twiss parameters  $\beta_x = \beta_y = 1472.5$  m and  $\alpha_x = \alpha_y = 40$ .

## 3.7 Dechirper design using transverse deflecting cavities

### 3.7.1 Linear design

A dechirper, which is an element of a beamline imposing a negative chirp on the beam (or removing the previously imposed chirp), is represented by the matrix in Eq. (3.1) with  $R_{65} > 0$ . The TDC-based chirper scheme described by the matrix in Eq. (3.14) has  $R_{65} = -\frac{2}{3}\kappa^2(3D + 2L_c)$ , which quadratically depends on the cavity strength, thus it cannot be switched simply by changing the voltage on it to the opposite sign. Rather, it linearly depends on the drift size between the cavities, and hence the sign can be flipped by substituting regular drifts with negative drifts. The matrix of the overall scheme suggests that if  $|D| > \frac{2}{3}L_c$  and  $D < 0$ , the  $R_{65}$  matrix element will become positive. In practice, the gaps between the cavities will add up to the cavity length and have to be accounted for. As we discussed in Chapter 2, a negative drift can be constructed as a combination of focusing and defocussing quadrupole magnets separated by drifts<sup>25</sup>. Therefore, the earlier proposed scheme of the TDC-based chirper can be modified to the TDC-based dechirper by simply inserting several quadrupole magnets in the drift section. The concept of the transverse-longitudinal mixing is conserved and the energy chirp is still mostly imposed in the middle cavity, with the only exception being sign. Such a scheme can significantly reduce the length of the beamline in comparison to the currently required off-crest acceleration. This would also allow placement of the bunch compressor and following TDC-based dechirper at the highest beam energy<sup>26</sup> right in front of an undulator (if it is convenient). In the next section we discuss the design

---

<sup>25</sup>We refer to Section 2.3 for details and formulas.

<sup>26</sup>In principal, it can be placed at any appropriate location along the accelerator.

of the prototype which we are planing to construct and test at the MaRIE injector test stand at LANL.

### 3.7.2 Dechirper design for the MaRIE Injector test stand

The design described in this section was designed to be tested at MITS at a 250 MeV beam energy as a proof of work of the TDC-based dechirper concept [112]. The dechirper fits inside a single standard International Linear Collider (ILC) cryomodule [113]. The superconducting magnets with reasonable peak gradient are inserted in the scheme to provide negative drifting as shown in Fig. 3.27. The beam parameters and the parameters of the

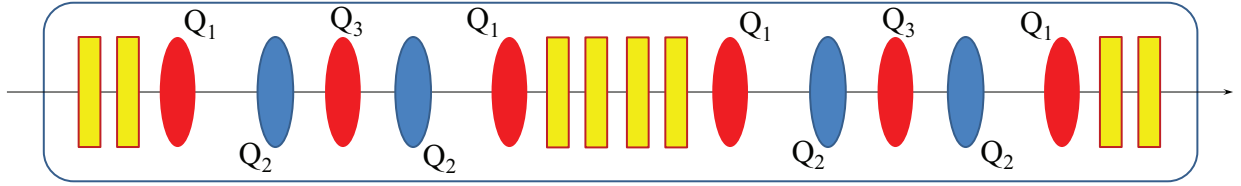


Figure 3.27: The layout of TDC-based dechirper inside the cryomodule for MITS. Each 13-cell cavity is represented by a yellow rectangle with a red border, while the focusing and defocussing quadrupoles in respect to the  $(x, x')$  phase space are represented respectively by the blue and red ovals. The large blue rectangular contour with smoothed corners represents the cryomodule boundary.

beam elements are listed in Table 3.3. Since the beam in the injector test stand is designed to have a negligible correlated energy spread, beam simulations of the scheme were performed in the approximation of the input beam with a zero chirp. This results in a negative energy chirp imposed on the beam. The LSC effects are almost negligible at the designed bunch charge of 100 pC. The longitudinal emittance on the exit of the beamline is  $6.02 \mu\text{m}$  for a 0 pC bunch charge and  $6.08 \mu\text{m}$  for a 100 pC bunch, while its value on the entrance of the

Table 3.3: Parameters of the TDC-based dechirper beamline for MITS

<b>Electron beam</b>		
Beam energy	250	MeV
Bunch charge	100	pC
Bunch length (rms)	90	$\mu\text{m}$
Uncorrelated energy spread (rms)	32.5	keV
Transverse normalized emittances $\epsilon_{n_{x,y}}$	0.1	$\mu\text{m}$
Longitudinal normalized emittance $\epsilon_{n_z}$	5.72	$\mu\text{m}$
<b>Beamline components</b>		
Total number of cryomodules	1	
Total number of 13-cell cavities	8	
Total number of quads	10	
Cavity frequency	3.9	GHz
Effective RF length/cavity	0.5	m
Deflecting voltage/cavity	2.5	MeV
TDC length $L_c$	0.66	m
Effective RF length	0.5	m
TDC strength $\kappa$	26.8	$\text{m}^{-1}$
Quadrupole length $L_q$	5	cm
Quadrupole 1 geometric strength	23.8	$\text{m}^{-2}$
Quadrupole 2 geometric strength	-28.4	$\text{m}^{-2}$
Quadrupole 3 geometric strength	65.3	$\text{m}^{-2}$
Minimum correlated energy spread, $\gamma mc^2 R_{65} \sigma_z$	-600	KeV

beamline is  $5.72 \mu\text{m}$ . A small longitudinal<sup>27</sup> energy spread wake along the bunch appears on the exit of the beamline for the bunch charge of 1 nC (Figure 3.28). The longitudinal wake becomes larger and dominates the shape of the longitudinal phase space of the beam for 10 nC bunch charge. Further, we present the simulations results for nonlinear particle dynamics accounting for the LSC effects at a 100 pC bunch charge. The observed final transverse emittances  $\epsilon_{n_{x,y}}$  were found to be respectively 16.45% and 16.44% larger than the input emittance ( $\epsilon_{n_{x,y}} = 0.1 \mu\text{m}$ ) for the applied negative correlated energy spread of -600 keV<sup>28</sup>

<sup>27</sup>Transverse space charge effects might be also critical for 1 nC and higher bunch charges and have to be accounted for in simulations if one is interested in applying the scheme to a beam with such a large bunch charge.

<sup>28</sup>This is the minimum possible value achieved in this scheme for the maximum voltage of 2.5 MV in all 13-cell cavities

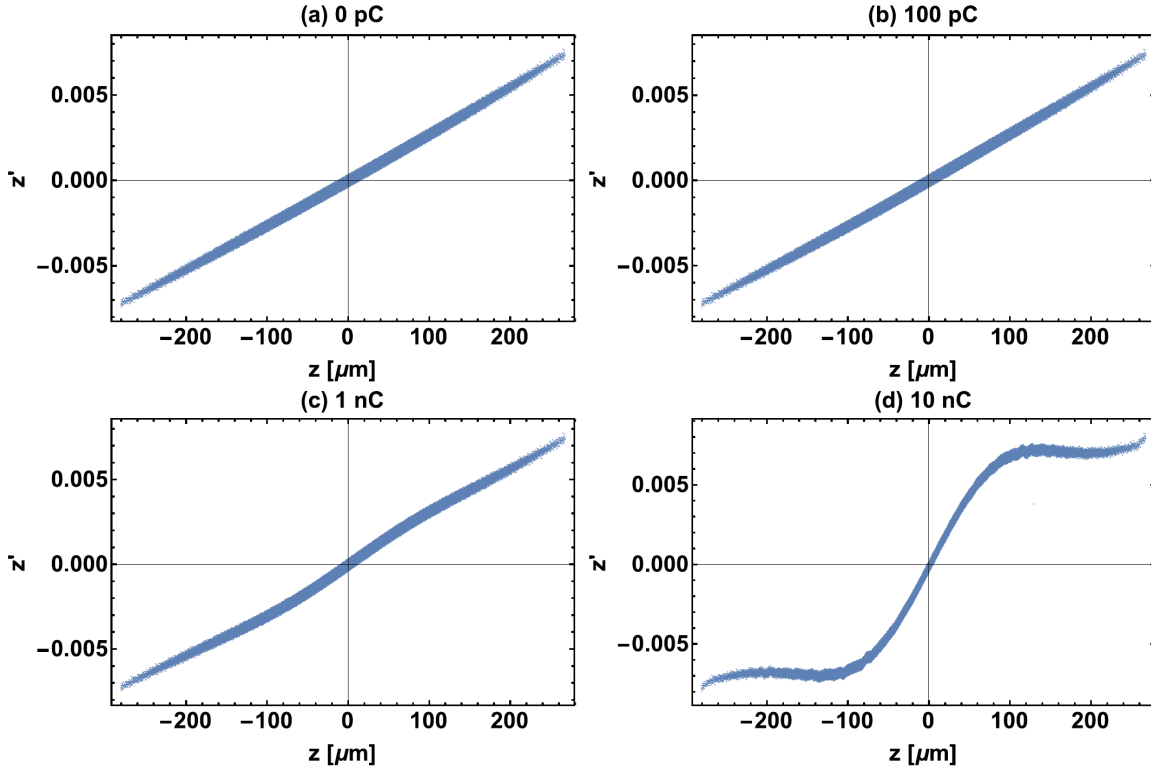


Figure 3.28: Longitudinal phase spaces on the exit of the TDC-based dechirper for MITS for the nonlinear particle dynamics accounting for the LSC effects for different bunch charges: (a) 0 pC; (b) 100 pC; (c) 1 nC; (d) 10 nC. The beam has zero chirp on the entrance of the beamline, and gains a negative chirp in the dechirper.

and the input Twiss parameters  $\beta_{x,y} = 4.16$  m and  $\alpha_{x,y} = -1$ . The beam dynamics becomes effectively coupled<sup>29</sup> between two transverse phase spaces due to quadrupoles which focus the beam in one direction ( $x$ ) and defocus it in another direction ( $y$ ). The nonlinear effects in the quadrupole magnets results in enlarging of the eigen emittances  $\lambda_2$  and  $\lambda_3$  (corresponding to transverse emittances) along the beamline as demonstrated in Fig. 3.29. Interestingly, these eigen emittances become the same value in the second-to-last quadrupole. Thus,  $\lambda_2$  becomes

<sup>29</sup>There is no actual coupling between the coordinates of  $(x, x')$  and  $(y, y')$  phase spaces in the approximation of the linear dynamics. However, a small coupling can be present through the second and higher orders:  $x(y^2)$ ,  $x(y'^2)$ , etc.

associated with  $\epsilon_{n_y}$  and  $\lambda_3$  is associated with  $\epsilon_{n_z}$  at the end of the beamline<sup>30</sup>. Figure 3.30

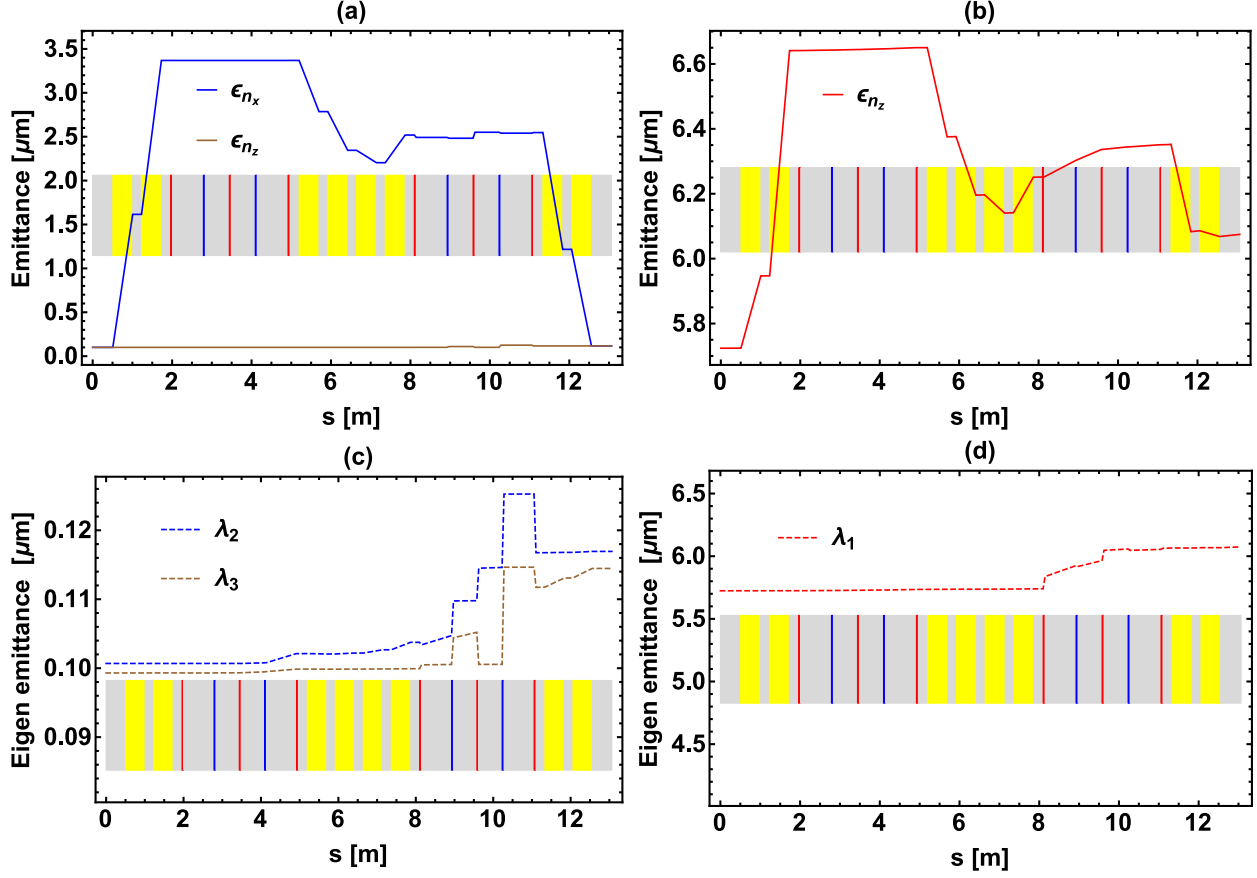


Figure 3.29: Evolution of the normalized emittances (a,b) and related to them eigen emittances (c,d) at a distance  $s$  along the beamline of the TDC-based dechirper at 250 MeV. The ordinate  $s = 0$  m corresponds to the entrance of the beamline. The Twiss parameters are  $\beta_{x,y} = 4.16$  m and  $\alpha_{x,y} = -1$ .

represents the evolution of the beam parameters along the beamline. There are some remaining quadratic correlations between the coordinates of the transverse and longitudinal phase spaces at the exit of the beamline as demonstrated in Figure 3.31. These correlations explain the degradation of the transverse emittance. Both can be reduced by adjusting the input Twiss parameters of the beam. In contrast to the chirper beamline, the adjustment of the Twiss parameters  $\beta_x$  and  $\alpha_x$  should be done separately from their counterparts cor-

<sup>30</sup>This is because eigen emittances are typically ordered according to their magnitudes, chosen to be from the largest to smallest in the scope of this dissertation.

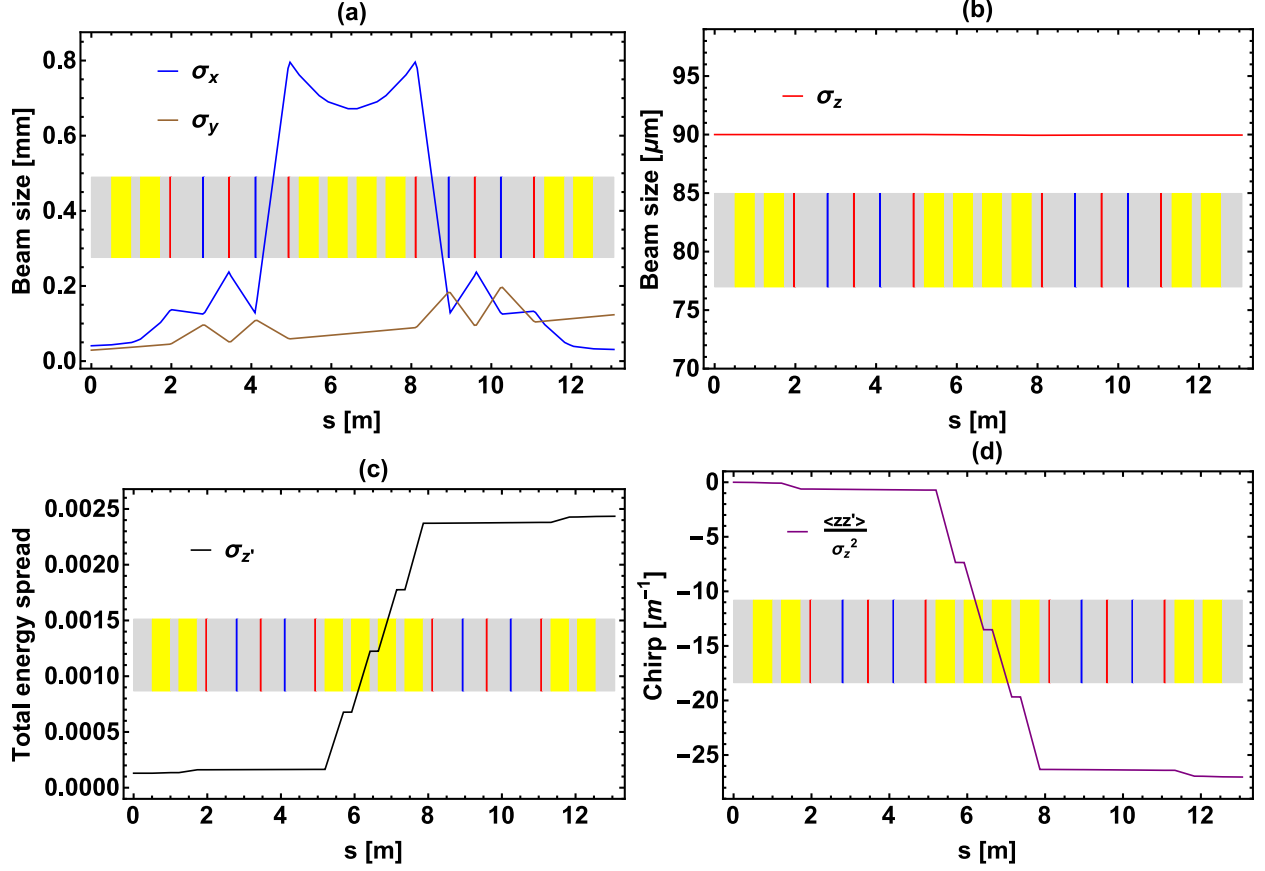


Figure 3.30: Beam parameters: (a)  $\sigma_x$  and  $\sigma_y$ ; (b)  $\sigma_z$ ; (c) the total energy spread; (d) the energy chirp, at a distance  $s$  along the beamline of the TDC-based dechirper at 250 MeV. The ordinate  $s = 0$  m corresponds to the entrance of the beamline. The input Twiss parameters are  $\beta_{x,y} = 4.2$  m and  $\alpha_{x,y} = -1$ .

responding to  $(y, y')$  phase space for the dechirper beamline. This is because the nonlinear dynamics in two transverse phase spaces are effectively coupled in the quadrupoles magnets as mentioned above. The optimization results in final transverse emittances  $\epsilon_{n_x} = 0.1029 \mu\text{m}$  and  $\epsilon_{n_y} = 0.1003 \mu\text{m}$ , and a final longitudinal emittance  $\epsilon_{n_z} = 6.08 \mu\text{m}$  for the optimal values of the input Twiss parameters  $\beta_x = 28.8$  m  $\beta_y = 9.8$  m,  $\alpha_x = -7$ , and  $\alpha_y = 1$ . The evolution of the normalized emittances and their related eigen emittances along the beamline with these optimal values are presented in Fig. 3.32. Respectively, Figure 3.33 demonstrates the evolution of the beam parameters along the beamline. In particular, the transverse bunch

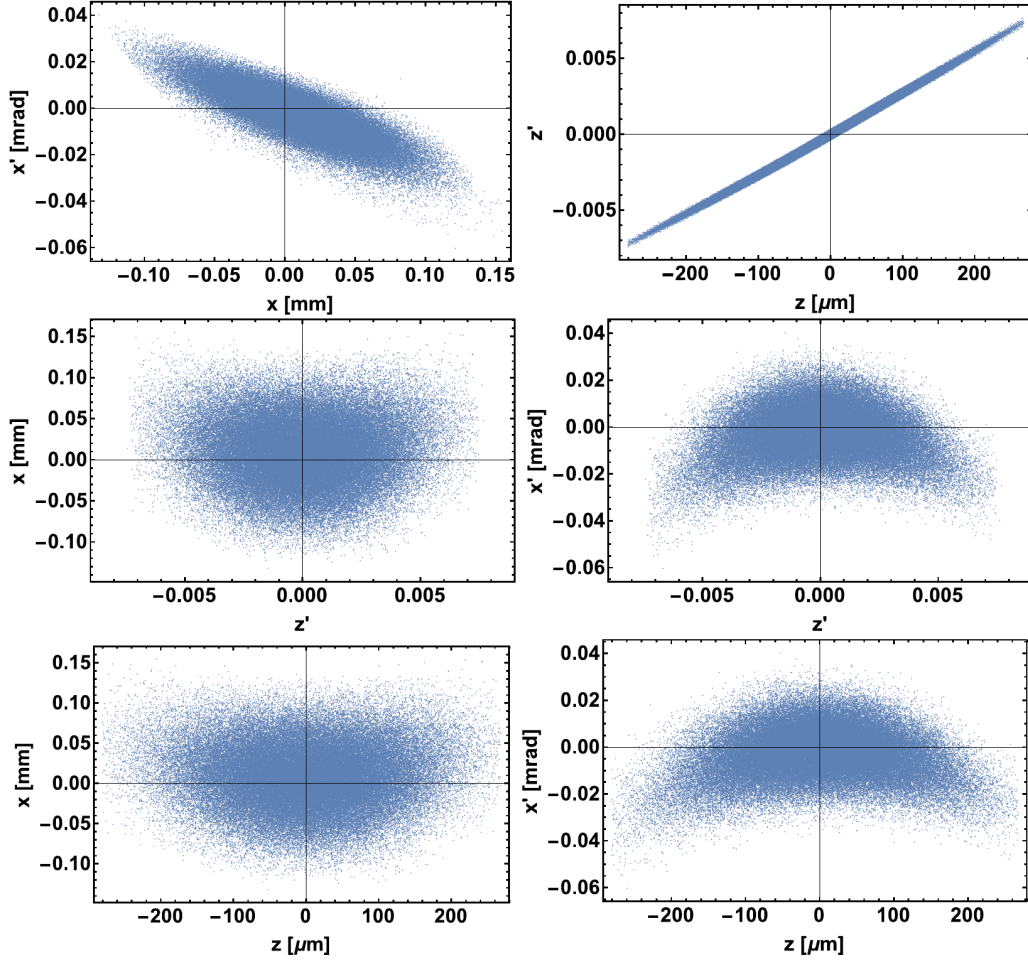


Figure 3.31: Phase spaces at the exit of the TDC-based dechirper for MITS. Simulations account for nonlinear dynamics with LSC-effects at a 100 pC bunch charge. The beam has zero chirp on the entrance of the beamline.

size  $\sigma_x$  becomes smaller at the end of the beamline, the transverse bunch size  $\sigma_y$  is symmetrical along the beamline, while the total energy spread and the chirp remain identical to the previous case, as expected. The quadratic correlations between the coordinates of the transverse and longitudinal phase spaces on the exit of the beamline become smaller as demonstrated in Figure 3.34 in comparison to the previous case (Fig. 3.31). Despite their presence, we do not find a critical necessity of including nonlinear beam optics for practical applications of the scheme. This is because the degradation of the transverse emittances due

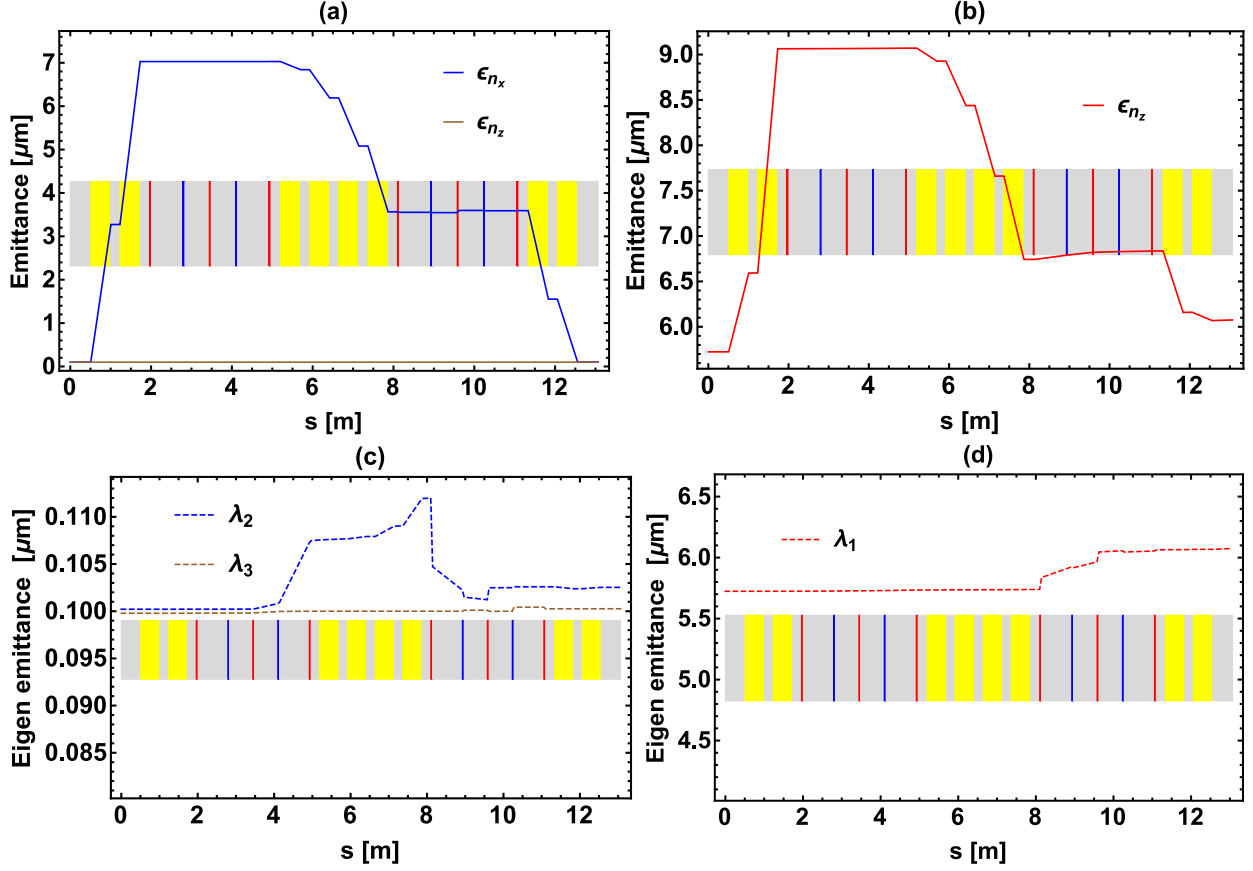


Figure 3.32: Evolution of the normalized emittances (a,b) and related to them eigen emittances (c,d) at a distance  $s$  along the beamline of the TDC-based dechirper at 250 MeV for the optimal Twiss parameters  $\beta_x = 28.8$  m,  $\beta_y = 9.8$  m,  $\alpha_x = -7$ , and  $\alpha_y = 1$ .

to nonlinear effects is almost completely compensated for by adjustment of the Twiss parameters. However, a compensation of the chromatic aberrations with nonlinear optics can still be tested in the scheme at MITS by adjusting the input Twiss parameters from their optimal value<sup>31</sup> and compensating for the appearing nonlinear effects<sup>32</sup> with sextupoles, octupoles, etc.

<sup>31</sup>This adjustment should be made to the point where the enlargement of emittances is detectable with available diagnostics.

<sup>32</sup>Additional nonlinear effects can appear from the real configuration of the electromagnetic fields in transverse deflecting cavities.

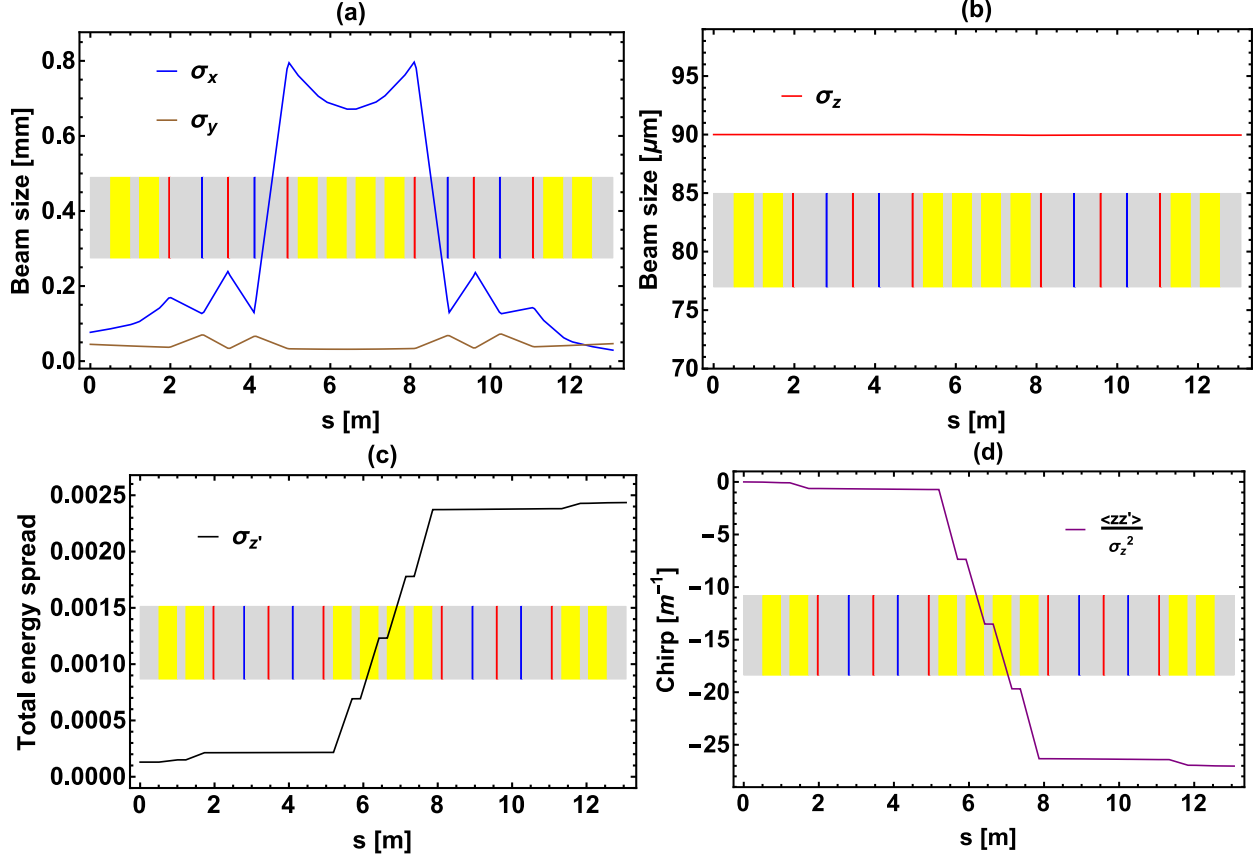


Figure 3.33: Beam parameters: (a)  $\sigma_x$  and  $\sigma_y$ ; (b)  $\sigma_z$ ; (c) the total energy spread; (d) the energy chirp, at a distance  $s$  along the beamline of the TDC-based dechirper at 250 MeV. The ordinate  $s = 0$  m corresponds to the entrance of the beamline. The Twiss parameters are  $\beta_x = 28.8$  m  $\beta_y = 9.8$  m,  $\alpha_x = -7$ , and  $\alpha_y = 1$ .

### 3.7.3 Dechirper design for the MaRIE linac at 1 GeV

Now that a concept for the TDC-based dechirper for MITS has been demonstrated, we turn our attention to the design of the dechirper for the MaRIE linac in this section. The overall design fits in six cryomodules and is demonstrated in Fig. 3.35. The parameters of the beamline elements are listed in Table 3.4. Identical negative drifts are implemented in second and fourth cryomodules. Each of them is constructed from five quadrupole magnets separated by drifts. The beam parameters are also listed in Table 3.4 and account for the

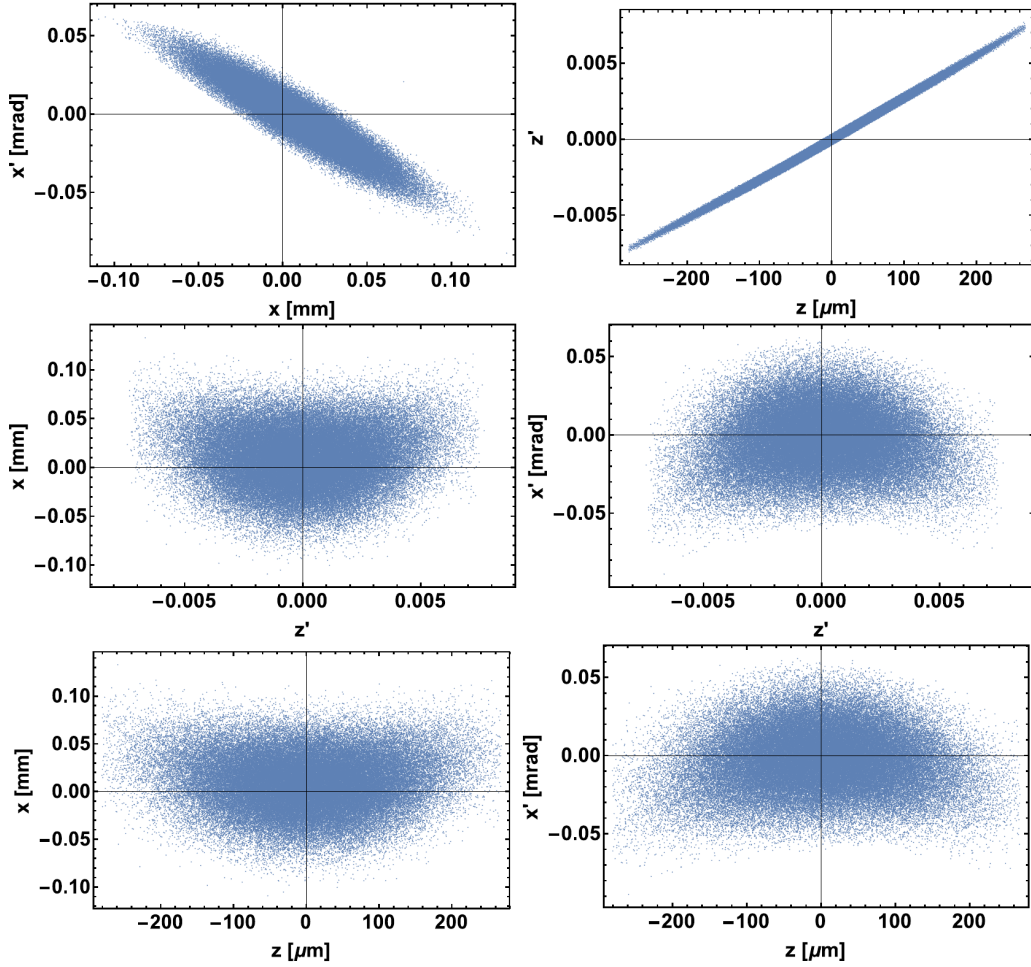


Figure 3.34: Phase spaces at the exit of the TDC-based dechirper with optimized input Twiss parameters for MITS.

compression in the preceding chicane ( $m \approx 23.1$ ) resulting in 750 keV rms energy spread at 1 GeV beam energy and  $3.9 \mu\text{m}$  rms longitudinal bunch length. The longitudinal space charge effects are expected to be more significant in this scheme because of the very short bunch. In addition, a chirp (up to 5.2 MeV) was applied to the beam at the entrance of the scheme to simulate the beam coming out of the chicane. Moreover, this chirp was varied in respect to the strength of the TDC-based dechirper beamline. The strength was changed by

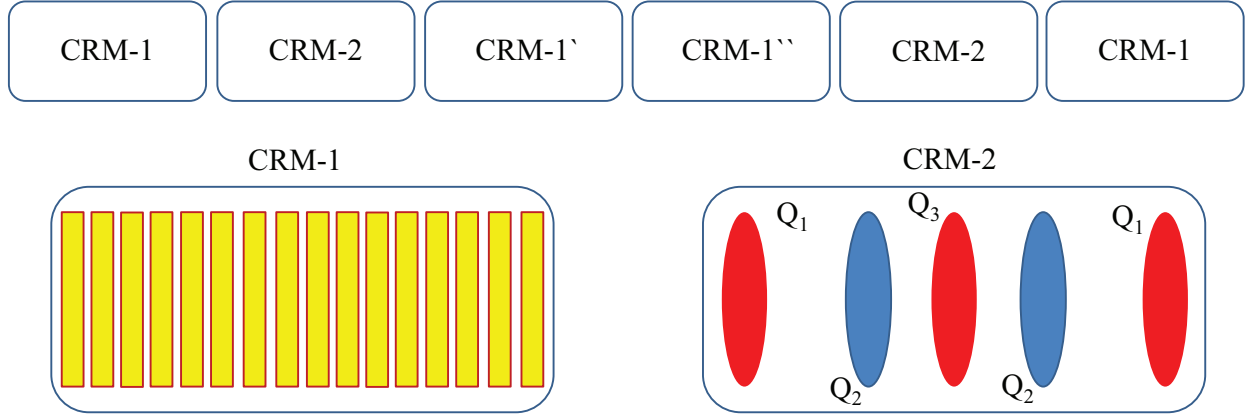


Figure 3.35: The layout of TDC-based dechirper at 1 GeV fitting inside of six cryomodules for MaRIE. The cryomodules one, two, three and six contain a single TDC beamline each. The TDCs are combined from sixteen 13-cell cavities. Each 13-cell cavity is represented by a yellow rectangle with a red border. The TDCs are shifted towards each other in cryomodules three (CRM-1') and four (CRM-1'') to keep the same gap between 13-cell cavities. The cryomodules two and five contain the negative drift beamlines combined from focusing (blue) and defocussing (red) quadrupoles in respect to the  $(x, x')$  phase space.

adjusting the voltage in deflecting cavities (all at the same time) for the sake of the simulation studies of the performance of the scheme and the degradation of the beam quality.

Optimization of the Twiss parameters, directed to minimize transverse final emittances, resulted in  $\epsilon_{n_x} = 0.126 \mu\text{m}$ ,  $\epsilon_{n_y} = 0.103 \mu\text{m}$  and  $\epsilon_{n_z} = 7.24 \mu\text{m}$  for input values of  $\beta_x = 95 \text{ m}$ ,  $\beta_y = 56 \text{ m}$ ,  $\alpha_x = -3.1$ , and  $\alpha_y = 2.0$  while accounting for the LSC effects for a 100 pC bunch charge. In the approximation of the nonlinear single-particle dynamics (0 pC bunch charge) transverse emittances remain almost the same:  $\epsilon_{n_x} = 0.127 \mu\text{m}$ ,  $\epsilon_{n_y} = 0.101 \mu\text{m}$ , while the longitudinal emittance becomes less,  $\epsilon_{n_z} = 6.54 \mu\text{m}$ . This fact validates that the LSC effects have to be accounted for during the optimization of this scheme. The longitudinal phase space at the exit of the dechirper beamline accounting for the LSC effects for different bunch charges are demonstrated in Fig 3.36. The second order nonlinearities define the shape of the longitudinal phase space at a 0 pC bunch charge, while the major part of the initial chirp was removed. The shape of the phase space starts changing at 40 pC ( $\epsilon_{n_z} = 6.59 \mu\text{m}$ ).

Table 3.4: Parameters of the TDC-based dechirper beamline at 1 GeV for MaRIE

<b>Electron beam</b>		
Beam energy	1	GeV
Bunch charge	100	pC
Bunch length (rms)	3.9	$\mu\text{m}$
Uncorrelated energy spread (rms)	750.0	keV
Transverse normalized emittances $\epsilon_{n_{x,y}}$	0.1	$\mu\text{m}$
Longitudinal normalized emittance $\epsilon_{n_z}$	5.72	$\mu\text{m}$
<b>Beamline components</b>		
Total number of cryomodules	6	
Number of 13-cell cavities per TDC	16	
Total number of 13-cell cavities	64	
Total number of quads	10	
Cavity frequency	3.9	GHz
Effective RF length per cavity	0.5	m
Deflecting voltage per cavity	2.5	MeV
TDC length $L_c$	0.66	m
Effective RF length	0.5	m
TDC strength $\kappa$	26.8	$\text{m}^{-1}$
Quadrupole length $L_q$	5	cm
Quadrupole 1 geometric strength	2.2	$\text{m}^{-2}$
Quadrupole 2 geometric strength	-5.0	$\text{m}^{-2}$
Quadrupole 3 geometric strength	16.5	$\text{m}^{-2}$
Sextupole geometric strength (optional element)	35.5	$\text{m}^{-3}$
Maximum removed correlated energy spread, $\gamma mc^2 R_{65} \sigma_z$	5.2	MeV

The changes become clearly visible at 100 pC (the bunch charge of the MaRIE beam). Finally, the longitudinal wake dominates the shape of the beam in  $(z, z')$  phase space at a 1 nC bunch charge resulting in the strongly enlarged longitudinal emittance  $\epsilon_{n_z} = 35.4 \mu\text{m}$  at the exit of the beamline. Further, we analyze the degradation of the transverse and longitudinal emittances and their related eigen emittances along the beamline (Fig. 3.37). Eigen emittances,  $\lambda_1$  and  $\lambda_2$  increased in the final quadrupole of the first negative drift section. The related to  $(x, x')$  phase space  $\lambda_2$  descends back in upstream elements of the beamline, demonstrating the concept of self-compensation of the nonlinear effects in the scheme. In contrast, the “longitudinal” eigen emittance  $\lambda_1$  experiences further enlargement

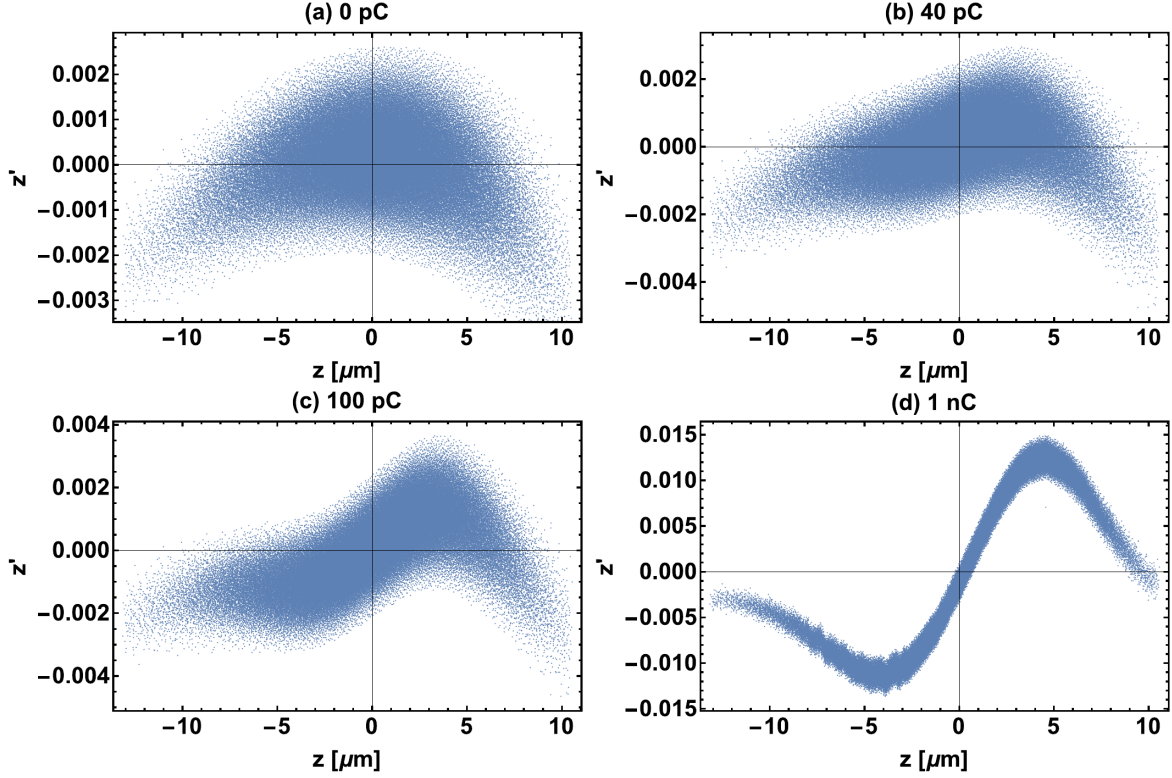


Figure 3.36: Longitudinal phase spaces at the exit of the TDC-based dechirper at 1 GeV for MaRIE for the nonlinear dynamics accounting for the LSC effects for different bunch charges: (a) 0 pC; (b) 40 pC; (c) 100 pC; (d) 1 nC. The beam has a chirp at the entrance of the beamline, which is removed in the dechirper.

predominantly due to strong LSC effects. Figure 3.38 demonstrates the evolution of the beam parameters along the beamline. In particular, transverse bunch sizes  $\sigma_{x,y}$  become larger at the end of the beamline, while the bunch length  $\sigma_z$  slightly decreased. The total energy spread and the chirp experience major changes in the middle TDCs as expected. The latter appears to be negative at the end of the beamline due to the energy-spread wake along the bunch as a result of the LSC effects.

Adding a sextupole ( $k_1 = 35.5 \text{ m}^{-3}$ ) in the middle of the scheme between third and fourth cryomodules can significantly minimize the degradation of the longitudinal emittance resulting in  $\epsilon_{nz} = 5.88 \text{ } \mu\text{m}$  at the exit of the beamline. It also slightly improves the quality

of the beam in  $(x, x')$  phase space resulting in  $\epsilon_{n_x} = 0.122 \mu\text{m}$ . However, both results are provided in the approximation of the nonlinear single-particle dynamics ( $q = 0 \text{ pC}$ ). Indeed, the LSC effects for a 100 pC bunch immediately reduce those improvements resulting in the final transverse and longitudinal emittances:  $\epsilon_{n_x} = 0.124 \mu\text{m}$  and  $\epsilon_{n_z} = 6.92 \mu\text{m}$ . The evolution of eigen emittances for 0 pC and 100 pC bunch charges are compared in Fig. 3.39. The subplots (b) and (d) of this figure clearly demonstrate that, in the absence of the LSC effects, eigen emittance  $\lambda_1$ , corresponding to the longitudinal dynamics, remains almost unchanged after it was compensated by the sextupole in the middle of the scheme. The sextupole position is marked with a black line in the scheme. Eigen emittances  $\lambda_2$  and  $\lambda_3$  associated with the transverse dynamics are slightly affected by the LSC effects, and only in the second negative drift section (Fig. 3.39 (a) and (c)). The phase spaces at the exit of the beamline are demonstrated in Fig. 3.40 for the nonlinear single-particle dynamics and for the nonlinear dynamics with LSC effects for a 100 pC bunch charge in Fig. 3.41 for comparison. Further optimization, aimed to compensate for the impact of the LSC effects on the longitudinal dynamics by inserting additional sextupoles along the beamline, did not bring about any significant improvement in minimization of the longitudinal emittance.

The initial chirp value of 5.2 MeV was selected so that it can be exactly compensated for by the TDC-based dechirper with 2.5 MV voltage in each cavity in the approximation of the linear single-particle dynamics. Next, we investigate how the residual chirp depends on the input chirp for the nonlinear single-particle dynamics and additionally accounting for the LSC effects, while the input chirp was matched by adjusting voltages in the TDCs in the approximation of the linear single-particle dynamics (Fig. 3.42). Subplot (a) clarifies that nonlinear effects result in a very small effective reduction of the scheme performance, since the beam still has a slight positive chirp at the exit of the beamline. In contrast, subplot (b) demonstrates that the LSC effects result in the presence of a negative chirp which can be compensated for by slightly reducing voltages in all cavities at the same time for the

given initial chirp. The dependences of the final longitudinal and transverse emittances from the initial chirp are demonstrated in Fig. 3.43 in the approximation of the nonlinear single-particle dynamics on the left and for the nonlinear dynamics accounting for the LSC effects ( $q = 100$  pC) on the right. Finally, we turn our attention to the small residual linear correlations between the coordinates of the transverse ( $x, x'$ ) and longitudinal phase spaces which can be adjusted by tuning the voltage in the last TDC, similar to what was accomplished for the 250 MeV chirper scheme. We emphasize that this adjustment is opposite to the previous case. Indeed, the voltage in the last cavity must be reduced as demonstrated in Fig. 3.44 (a-d). The voltages needed to reach the minimum of the transverse emittance are identical for both cases as clearly seen in the subplots (a) and (c), but should be slightly different in order to match the values of the longitudinal emittance and its associated eigen emittance as demonstrated in the subplots (b) and (d).

### 3.7.4 Summary

In this chapter we demonstrated the novel scheme (the TDC-based chirper) for imposing a linear energy chirp on an electron bunch using a combination of transverse deflecting cavities separated by drifts. Then, we modified the scheme with quadrupole magnets (the TDC-based dechirper) to impose a negative chirp (for MITS) or remove a positive chirp from the bunch (for MaRIE at 1 GeV). In particular, two chirper designs, located at 250 MeV and 1 GeV beam energy, were constructed to impose the correlated energy spread on the beam before the chicane of the second MaRIE bunch compressor. Both schemes effectively work while preserving the beam quality and causing insignificant emittance growth in transverse directions. Compensation of the higher-order effects was required in the scheme at 250 MeV because of the large total energy spread. This was successfully accomplished by two methods:

adjusting the voltage in the last TDC and tuning of the input Twiss parameters. The former was aimed to suppress residual linear correlations between the coordinates of the transverse  $(x, x')$  and longitudinal phase spaces. The latter was dedicated to find the appropriate transverse beam profile along the beamline so that the nonlinear effects in different elements would cancel each other and minimize the final transverse emittances. The minimization of the longitudinal emittance degradation in this scheme was accomplished by inserting nonlinear beam optics elements (sextupoles), and was done at the cost of sacrificing the transverse beam quality and significant enlargement of the corresponding emittance  $\epsilon_{n_x}$ . By contrast, this approach allowed compensation of the transverse and longitudinal emittances at the same time in the chirper beamline at 1 GeV beam energy. This is because the total energy spread at 1 GeV is approximately four times smaller for the same imposed correlated energy spread (the absolute value in MeV) than at 250 MeV resulting in less impact of the nonlinear effects. The better quality of the beam achieved in the chirper at 1 GeV requires a longer length of RF structures, and the total length of the scheme is doubled.

In addition, two designs of the dechirper beamline were presented at 250 MeV and 1 GeV beam energy for respectively the MaRIE injector test stand and the MaRIE linac. The first beamline was designed to prove the concept on the small scale at MITS, while the second beamline was developed for the actual MaRIE parameters and upon success can be integrated in the linac beamline to substitute the off-crest acceleration after the chicane of the second bunch compressor. The simulation studies of the dechirper at 250 MeV demonstrated that the Twiss parameters corresponding to  $(x, x')$  and  $(y, y')$  phase spaces should be tuned independently since the beam dynamics are effectively coupled through the quadrupole magnets. Suppression of the emittance degradation (caused by the nonlinear effects) was accomplished by adjusting the input Twiss parameters and did not require any nonlinear optics in the scheme. By contrast, the enlargement of emittances due to the second order effects were still significant at the optimal Twiss parameters in the dechirper at 1 GeV in

the approximation of the single-particle dynamics. Moreover, the LSC effects additionally caused a degradation of the beam quality in the longitudinal phase space. Their impact becomes significant already at a 100 pC bunch charge because of the short bunch length of  $3.9 \mu\text{m}$  which is roughly 23 times smaller than in the previous schemes. The degradation of emittances due to the nonlinear effects in the scheme were minimized by adding a sextupole in the middle of the scheme. These improvements are significant in the approximation of the single-particle dynamics. However, they are practically “washed out” by the LSC effects.

Both schemes, the TDC-based chirper and the TDC-based dechirper, have similar operating principles, where an energy chirp is imposed/removed predominantly in the middle TDC, while the rest of the beamline elements are used to provide with the necessary correlations between the beam parameters before the middle TDC and remove them after it. The nonlinear effects, caused by the enlarged total energy spread due to the large imposed chirp in both schemes, can be optimized by varying the input Twiss parameters of the beam and by implementing nonlinear optics if required. Moreover, the residual linear correlations between the coordinates of the transverse and longitudinal phase spaces might be present if a very large chirp is imposed. This happens because the nonlinear effects shift the average energy of the beam along the beamline, which makes otherwise identical TDCs have different effective geometric strengths. This issue can be mitigated by slightly adjusting the voltage in the last cavity for both schemes. Finally, based on the demonstrated results, we emphasize that the proposed schemes are universal and can be realized for imposing/removing chirp at different beam energies along the accelerator beamline, which allows more freedom on the actual location of the chicane-based bunch compressor. Moreover, using the proposed method instead of the conventional off-crest acceleration might reduce the cost of the actual accelerator beamline upon reaching an optimal balance between the length of the drift sections and the length of the RF structures.

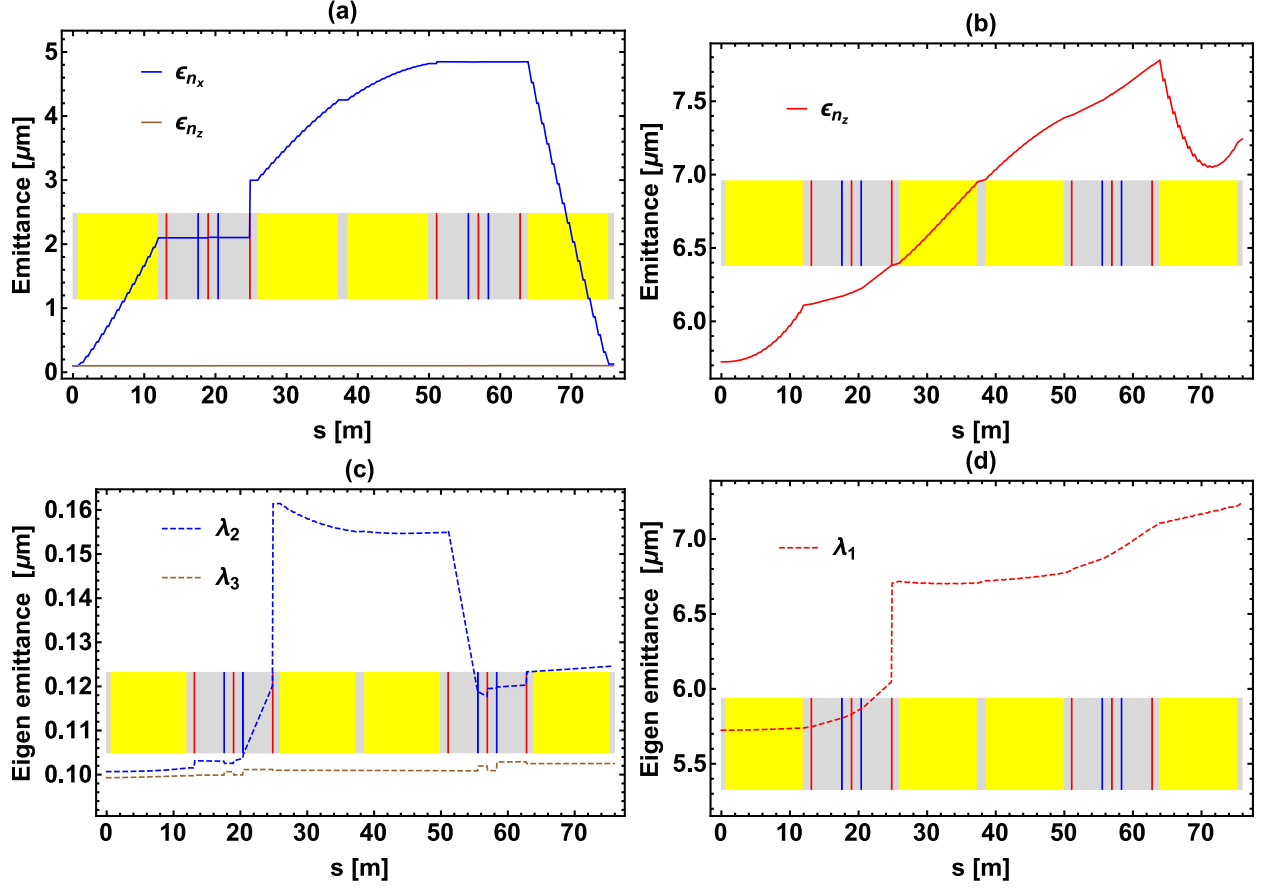


Figure 3.37: Evolution of the normalized emittances (a,b) and related to them eigen emittances (c,d) at a distance  $s$  along the beamline of the TDC-based dechirper at 1 GeV for the optimal Twiss parameters  $\beta_x = 95$  m,  $\beta_y = 56$  m,  $\alpha_x = -3.1$ , and  $\alpha_y = 2$ . Each TDC, comprised of sixteen 13-cell cavities, is represented by a yellow rectangle, while focusing and defocussing quadrupoles in respect to  $(x, x')$  phase space are marked by blue and red lines respectively. The ordinate  $s = 0$  m corresponds to the entrance of the beamline.

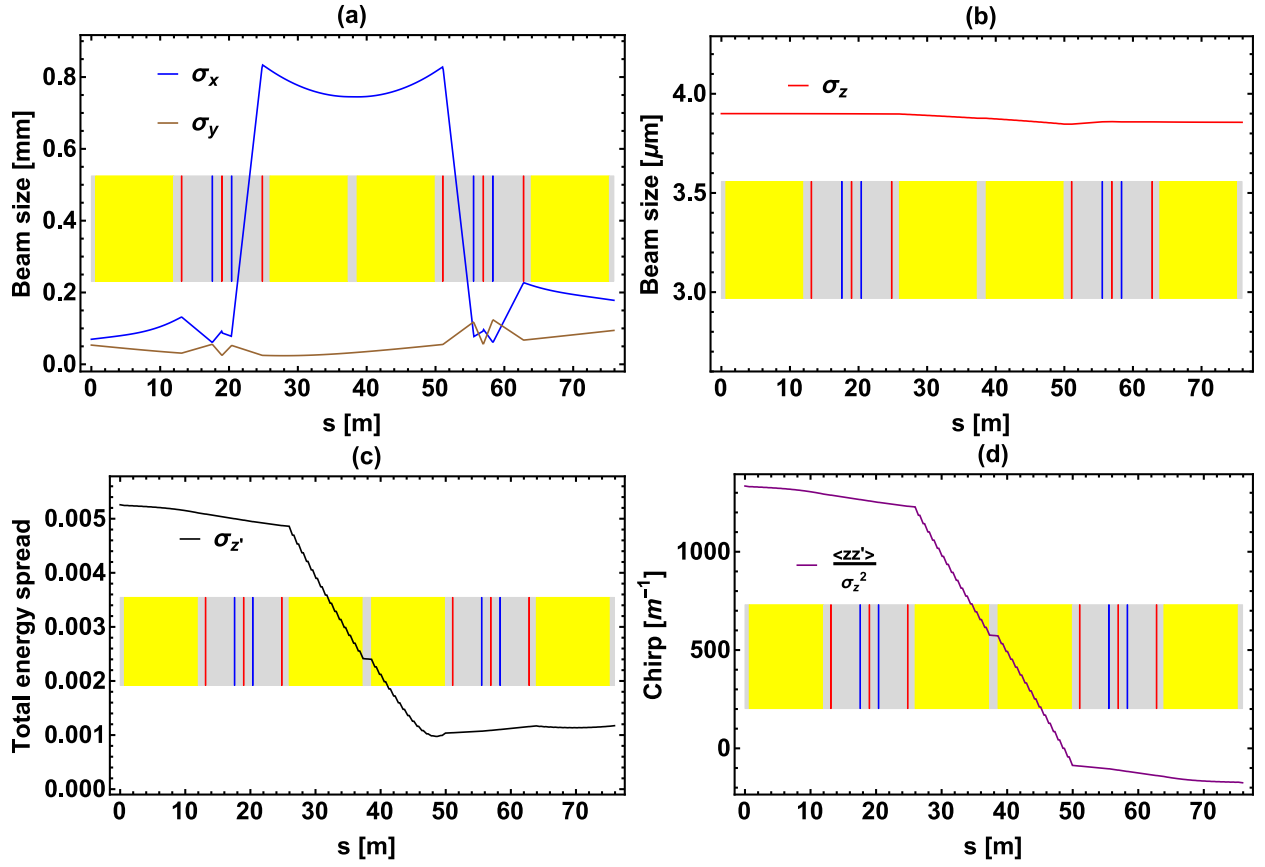


Figure 3.38: Beam parameters: (a)  $\sigma_x$  and  $\sigma_y$ ; (b)  $\sigma_z$ ; (c) the total energy spread; (d) the energy chirp, at a distance  $s$  along the beamline of the TDC-based dechirper at 1 GeV. Twiss parameters are  $\beta_x = 95$  m,  $\beta_y = 56$  m,  $\alpha_x = -3.1$ , and  $\alpha_y = 2.0$ .

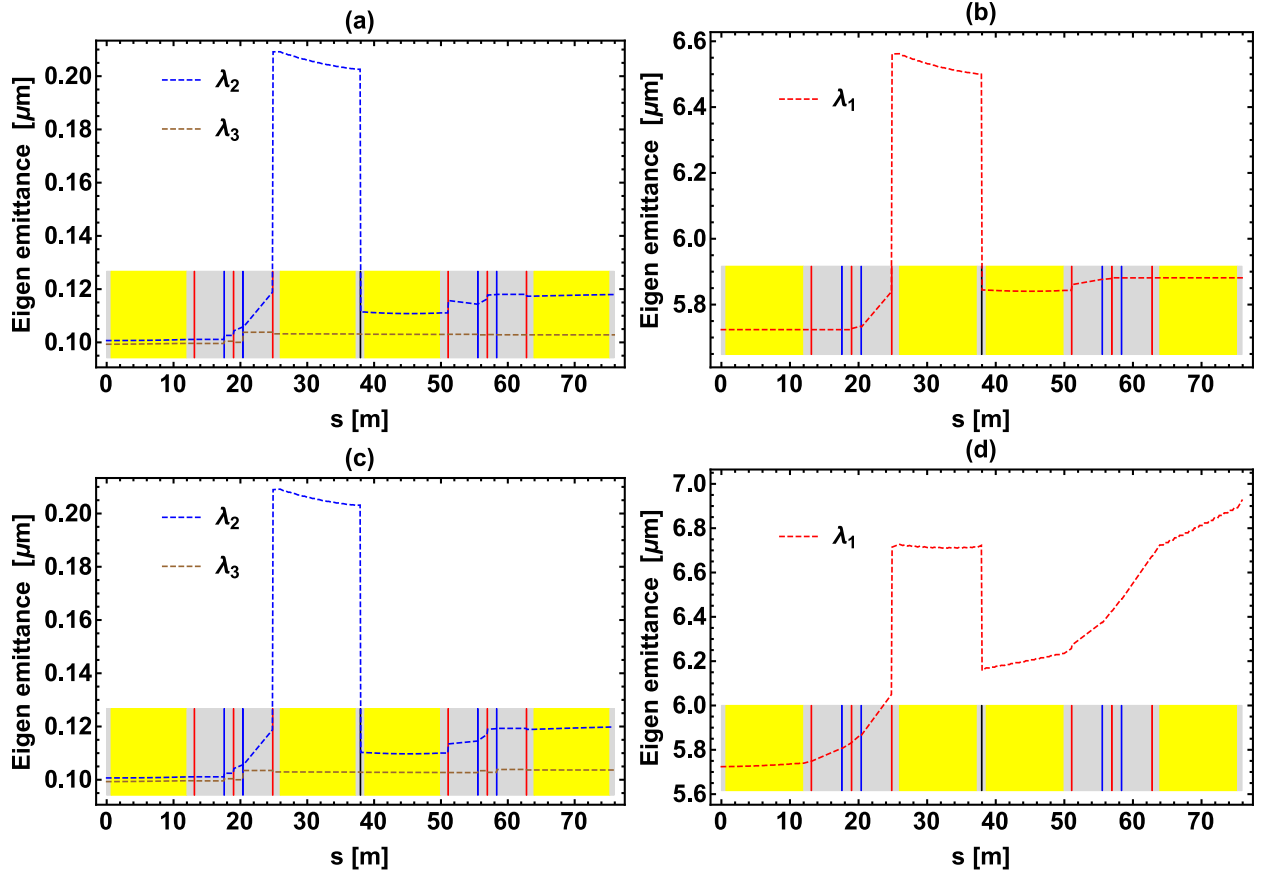


Figure 3.39: Evolution of eigen emittances at a distance  $s$  along the beamline with a sextupole ( $k_1 = 35.5 \text{ m}^{-3}$ ) added in the middle of the scheme (marked by a black line) for the different bunch charges: (a,b) 0 pC; (c,d) 100 pC. The optimal Twiss parameters for this configuration of the scheme are  $\beta_x = 70.0 \text{ m}$ ,  $\beta_y = 62.1 \text{ m}$ ,  $\alpha_x = -3.7$ , and  $\alpha_y = 1.6$ .

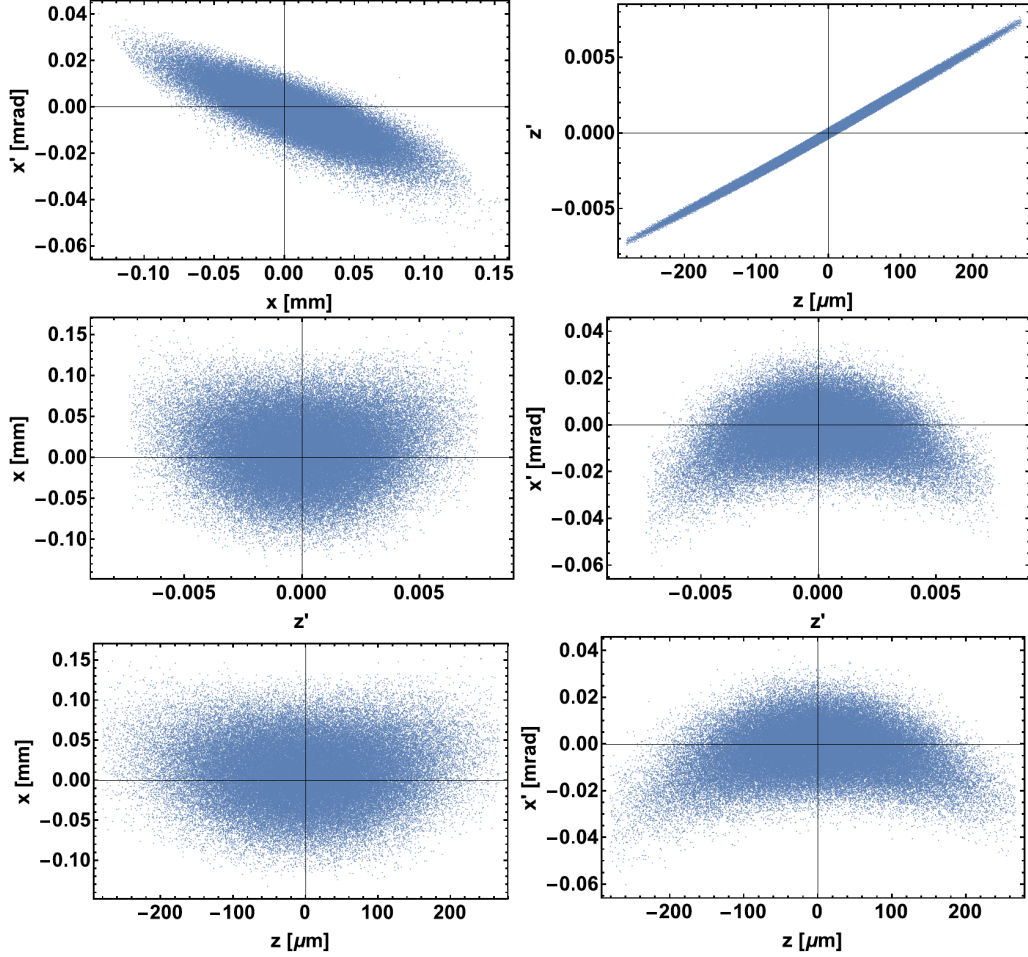


Figure 3.40: Phase spaces at the exit of the TDC-based dechirper at 1 GeV with the sextupole  $k_1 = 35.5 \text{ m}^{-3}$  in the middle of the scheme and the optimized input Twiss parameters  $\beta_x = 70.0 \text{ m}$ ,  $\beta_y = 62.1 \text{ m}$ ,  $\alpha_x = -3.7$ , and  $\alpha_y = 1.6$  in the approximation of the nonlinear single-particle dynamics.

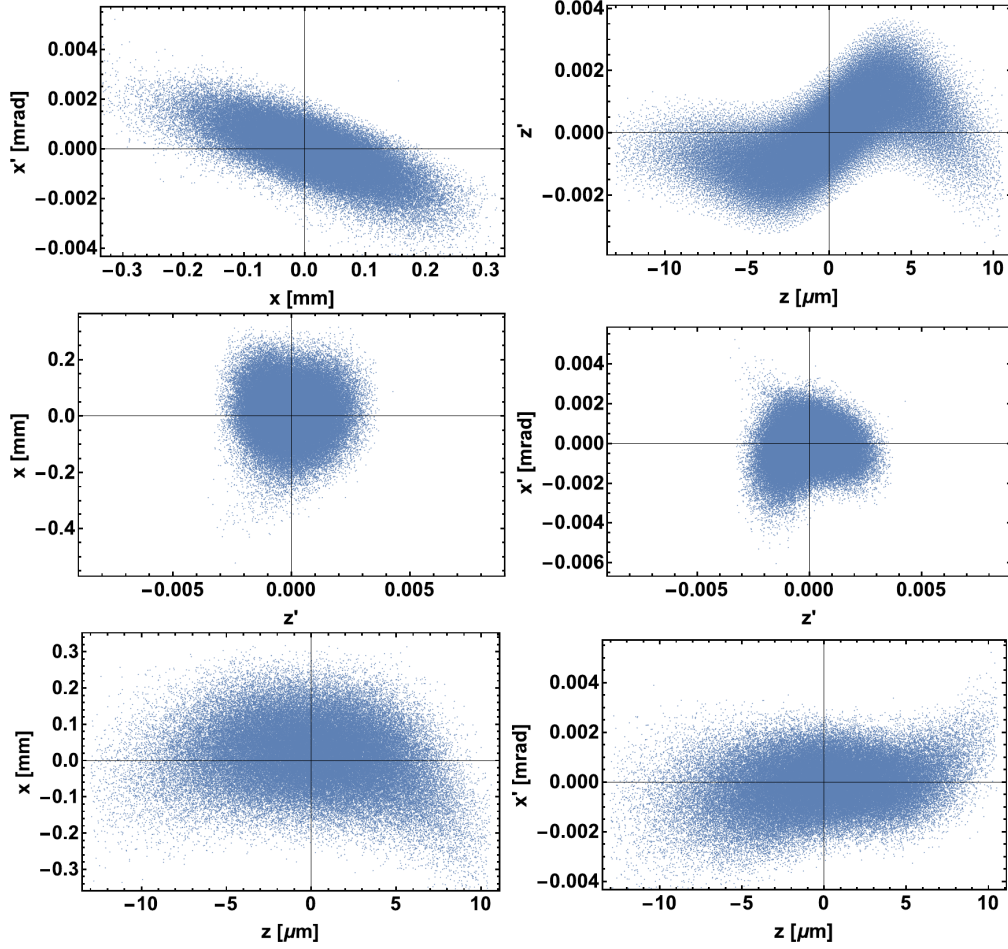


Figure 3.41: Phase spaces at the exit of the TDC-based dechirper at 1 GeV with the sextupole ( $k_1 = 35.5 \text{ m}^{-3}$ ) in the middle of the scheme with the optimized input Twiss parameters  $\beta_x = 70.0 \text{ m}$ ,  $\beta_y = 62.1 \text{ m}$ ,  $\alpha_x = -3.7$ , and  $\alpha_y = 1.6$  in the approximation of the nonlinear dynamics with the LSC effects ( $q=100 \text{ pC}$ ).

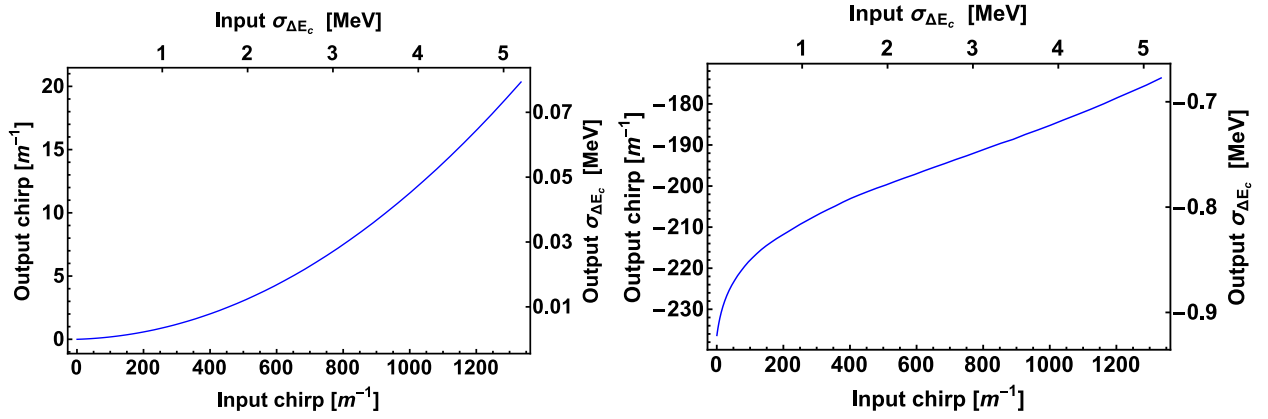


Figure 3.42: Dependence of the output energy spread of the beam from the input energy spread in the TDC-based dechirper at 1 GeV with the sextupole  $k_1 = 35.5 \text{ m}^{-3}$  in the middle of the scheme. The case without the LSC effects is presented on the left and the case accounting for the LSC effects ( $q=100 \text{ pC}$ ) is on the right. The upper horizontal axes relate the initial chirp to the initial correlated energy spread of the beam. The right vertical axes relate the final chirp to the final correlated energy spread.

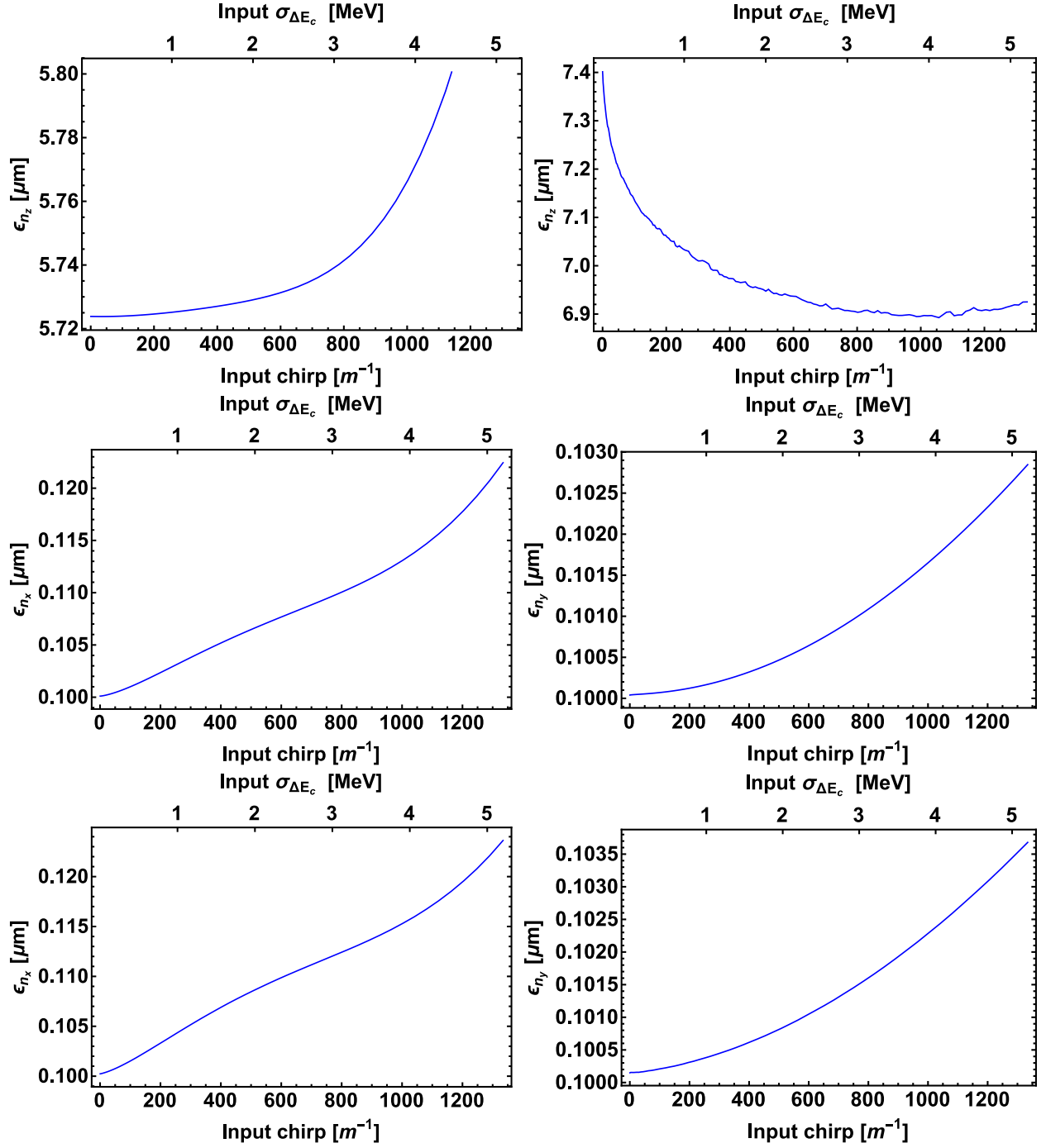


Figure 3.43: Dependence of the final emittances from the initial chirp in the TDC-based dechirper for the nonlinear single particle dynamics on the left and for the nonlinear dynamics with LSC effects ( $q = 100$  pC) on the right. The upper horizontal axes relate the initial chirp to the initial correlated energy spread of the beam. The voltage in all TDCs was adjusted to exactly compensate for the initial chirp in the approximation of the linear single-particle dynamics.

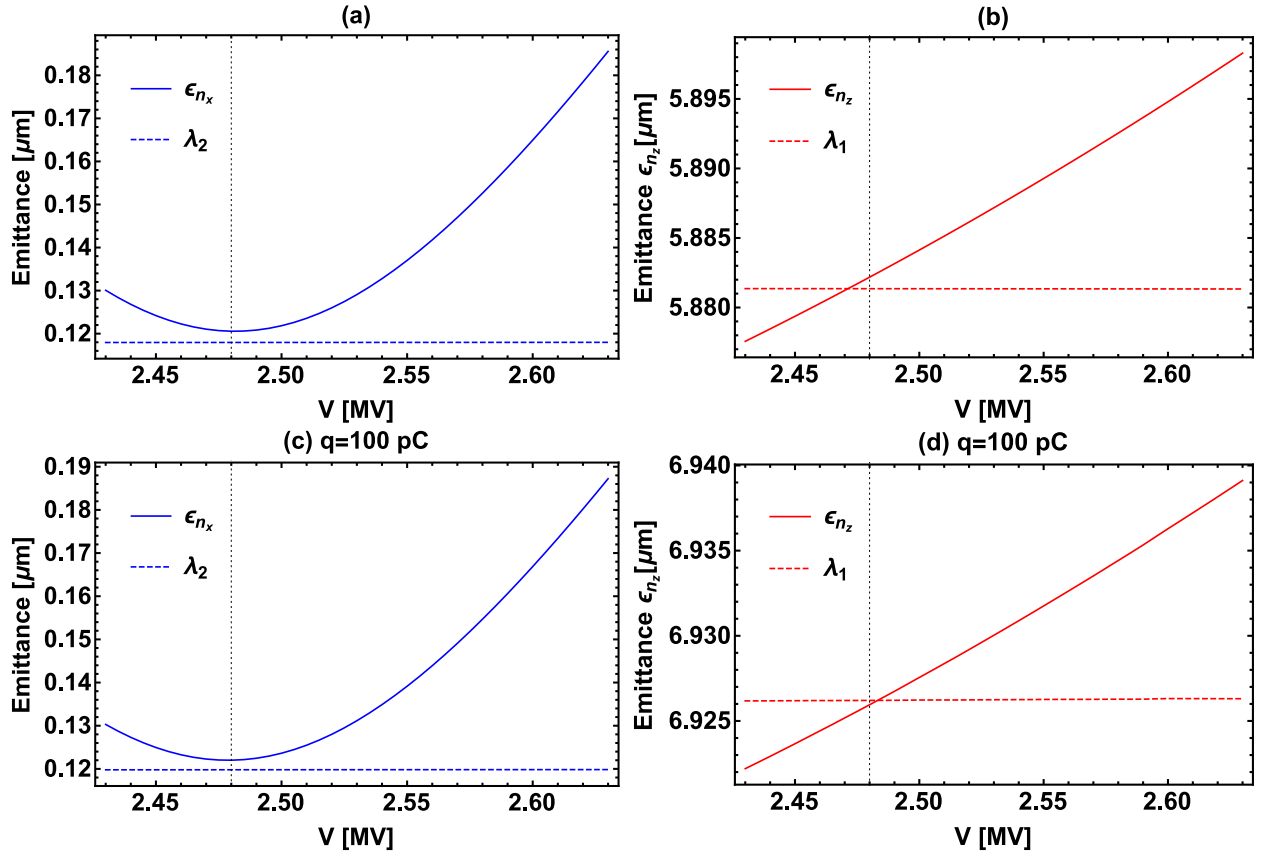


Figure 3.44: Dependence of the final emittances and their related eigen emittances from the voltage in the last TDC for the nonlinear single particle dynamics on the top and the for nonlinear dynamics with LSC effects ( $q = 100$  pC) on the bottom. The dotted vertical lines demonstrate the optimal voltage minimizing the transverse emittance for both cases.

## CHAPTER 4

### 6D PHOTON PHASE SPACE OF AN ICS SOURCE USING THE WIGNER FUNCTION APPROACH

The brightness of inverse Compton scattering (ICS) sources is limited by the electron beam quality since electrons traveling at different angles and/or having different energies, produce photons with different energies. Thus, the spectral brightness of the source is defined by the shape and size of 6D electron phase space, as well as parameters of the incoming laser pulse. The peak brightness of the ICS source can be maximized then if the electron phase space is transformed in a way so that all electrons scatter off the X-ray photons of same frequency in the same direction. However, the existing theoretical models of ICS are not able to quantitatively estimate this effect. Indeed, a typical approach simply assumes that the electron beam has no correlations in phase space. To cover this gap, we demonstrate how an ICS problem can be solved in 6D for an arbitrary-shaped electron beam using the Wigner function formalism. In this approach, a Wigner function characterizes the produced radiation in 6-dimensional phase space of corresponding photons. We discuss an optimal shape of the phase-space distribution of the electron beam maximizing the peak brightness of an ICS source. We also speculate how such an optimal distribution of the electron beam can be constructed from the initially uncorrelated beam using the available arsenal of the beam optics elements: bends, drifts, etc. Furthermore, we demonstrate that the derived result can be inverted. A 6-dimensional electron phase space in the Gaussian approximation can be analytically expressed as a function of a 6-dimensional photon distribution (also considered in a Gaussian form). This result opens up a unique path towards a complete non-

invasive 6-dimensional diagnostics of electron beams in accelerators. The 6D phase space of an electron beam can be reconstructed by analyzing the radiation naturally produced in bending magnets and undulators. Alternatively, it can be accomplished by shining the laser beam on the electron bunch in the accelerator (in order to initiate the ICS process) and by analyzing the produced radiation on the up-shifted frequency. The results of this chapter are summarized in [114].

## 4.1 The Wigner function formalism and brightness

A light source can be described by its brightness, the 4D photon distribution function, and a media where the emitted radiation propagates according to Kim [70–72]. Such a description is not complete because the 4D photon distribution function can also vary in the frequency- and time-domain. The formalism can be partially extended by introducing the spectral brightness, which is equal to the flux of photons per unit area per solid angle per unit bandwidth interval. This still does not cover the time dependence of the produced radiation. More important, the conventional definitions of brightness and spectral brightness do not account for possible correlations in the 6D photon phase space. For instance, the photon arrival time at the observer location or/and its frequency (energy) can be correlated to the direction from which it was emitted at the source. Going into more details, the additional correlations of those with the actual positions within the observer’s detector may exist<sup>1</sup>. Since X-ray light sources, such as an FEL or an ICS source, do not perform in a continuous mode, the brightness formalism should be further extended.

The complete description can be achieved by incorporating a canonically conjugated variables, frequency (or energy  $E = \hbar\omega$ ) of the photon and the time at which it was emitted

---

<sup>1</sup>Different photons arrive at the distinct locations within the observer’s detector (assumed to be of the finite size) since they were initially emitted in the various direction by the individual electrons.

at the source (or arrival time at the observer location), to the conventional 4D transverse phase space<sup>2</sup>. This results in the 6-dimensional photon phase space of the emitted (observed) radiation with all possible correlations between the coordinates which can only exist for FEL or ICS sources. Accordingly, the maximum of the distribution defines the peak brightness of the light source.

We introduce a 6D Wigner function (WF), an auto-correlation function of the electric field of a radiation, in order to characterize the distribution of the photons in phase space, based of the Quantum Mechanical Wigner function proposed by E. Wigner in 1932 [68]:

$$W_{6d}(\mathbf{r}, \mathbf{k}_w; t) = W_0 \cdot \int_{-\infty}^{\infty} E_{rad} \left( \mathbf{r} + \frac{\boldsymbol{\xi}}{2}; t \right) E_{rad}^* \left( \mathbf{r} - \frac{\boldsymbol{\xi}}{2}; t \right) e^{i\mathbf{k}_w \boldsymbol{\xi}} d^3 \boldsymbol{\xi} \quad . \quad (4.1)$$

The coefficient in front of the integral can be introduced as following:

$$W_0 = \frac{\epsilon_0}{\hbar \omega_0} \quad , \quad (4.2)$$

where  $\epsilon_0$  is the permittivity of vacuum,  $\hbar$  is the reduced Planck constant and  $\omega_0$  is the average frequency of radiation. Thus, the Wigner function in this configuration defines the number of emitted photons<sup>3</sup>. The 6-dimensional WF is the extension of its 4-dimensional counterpart introduced for describing the transverse brightness of a light source by Kim [70–72]. We emphasize that in the above definition  $t$  is the evolution variable, while  $z$ – coordinate and  $k_{wz}$ –component of a wave-vector are canonically conjugated variables of the longitudinal photon phase space. The alternative description relies on the variables  $t$  and  $\omega$ , while the coordinate along the direction towards observer becomes the evolution variable. The last choice of coordinates is similar to the description of an electron beam propagation in an

---

<sup>2</sup>The medias considered here do not change the frequency of photons upon their propagation.

<sup>3</sup>The energy density in 3D space is  $\sim \epsilon_0 E^2$ . Correspondingly, if one omits the average photon energy,  $\hbar \omega_0$ , in coefficient  $W_0$  the Wigner function will characterize the energy of radiation.

accelerator and, thus, can be convenient for an ICS problem. However, the first coordinate system provides with one evolution variable for all possible observer locations, and hence is more appropriate here.

There are multiple distinct electrons in the bunch interacting with the incoming electromagnetic field of a laser in an ICS source. Each of them starts oscillating in the laser field and emits synchrotron radiation. A direct way to find the Wigner function of the source is to calculate the total field emitted by all electrons in the bunch. This can be found as a superposition of the fields emitted by each individual electron. One can obtain then the WF for the total emitted field. This approach seems quite complicated due to the quadratic form of the WF. Unlike in FELs, in which electrons self-bunch at the wavelength of the produced radiation and emit coherently, electrons in an ICS source, are randomly distributed along the bunch and emit radiations with random phases, *e.g.* different electrons radiate incoherently<sup>4</sup>. Consequently, the total Wigner function (TWF) of the radiation emitted by the electron bunch can be found as the direct sum of the Wigner functions characterizing radiation emitted by each individual electron. We will further refer the WF of a radiation produced by an individual electron as the single-electron Wigner function (SWF).

## 4.2 Radiation emitted by a moving electron

Radiation produced by a charged particle moving along the trajectory  $\mathbf{r}(t')$  can be found in the far-field approximation [43, 71]:

$$\mathbf{E} = \frac{e}{c^2 R} \left[ \mathbf{n} \times \left[ \mathbf{n} \times \frac{d^2 \mathbf{r}[t'(t)]}{dt^2} \right] \right] , \quad (4.3)$$

---

<sup>4</sup>This is the main reason why the typical brightness of an ICS source is dramatically smaller than of an FEL.

where  $R$  is the distance to an observer from the origin of the lab frame,  $\mathbf{n} = \mathbf{R}/R$  is the unit vector pointing in the direction to the observer,  $e$  is the particle charge,  $c$  is the speed of light in vacuum,  $t'$  is the emitted (retarded) time, and  $t$  is the observer (advanced) time. The time variables  $t$  and  $t'$  are related through the geometric length between the points where the radiation was emitted and where it was detected as following:

$$t = t' + \frac{1}{c} \sqrt{(\mathbf{R} - \mathbf{r}(t'))^2} \quad . \quad (4.4)$$

Electron trajectory in the field of a plane electromagnetic wave can be found analytically in the approximation of a small wave amplitude:  $a_0 = \frac{eE_0}{mc\omega_{las}} \ll 1$ . Then, one can find the radiation emitted by a particle moving on the known trajectory using Eq. (4.3). Most of the ICS power is emitted along with the relativistic beam. The radiation is well-collimated and can be detected by an observer located in the far zone slightly off the  $z$ -axis ( $x/z \sim y/z \ll 1$ ) in the form of a spherical wave:

$$E_{rad} = \alpha_s E_0 e^{-i\mathbf{q}(\mathbf{k})\mathbf{r} + i\mathbf{q}(\mathbf{k})t} \quad , \quad (4.5)$$

where  $\mathbf{k}$  is the wave-vector of the incoming radiation and the counterpart of the emitted radiation is:

$$\mathbf{q}(\mathbf{k}) = q(\mathbf{k})\mathbf{n} = \frac{\mathbf{k} - \beta_0\mathbf{k}}{1 - \beta_0\mathbf{n}} \mathbf{n} \quad . \quad (4.6)$$

The introduced dimensionless coefficient is defined as following:

$$\alpha_s = \frac{1}{2\gamma_0^5} \frac{e^2}{Rmc^2} \quad , \quad (4.7)$$

and characterizes the ratio between the incoming and scattered radiation. Finding the radiation field allows to find the corresponding Wigner function from Eq. (4.1) as will be demonstrated in the next section.

### 4.3 The single-electron Wigner function: simple approximations

#### 4.3.1 The continuous plane wave approximation

There are different approaches how to find the single-electron Wigner function in the process of interaction with the incoming laser pulse. The simplest one is approximating the laser field as a continuous homogeneous plane wave ( $E_0 e^{i\omega_{las}(z/c+t)}$ ) for which the radiation emitted by a single electron was found in the previous section. Using the result of Eq. (4.5), one can immediately derive the SWF in Eq. (4.1):

$$\begin{aligned}
 W_{1e} &= W_0 \int_{-\infty}^{\infty} E_{rad}(\mathbf{r} + \frac{\boldsymbol{\xi}}{2}; t) E_{rad}^*(\mathbf{r} - \frac{\boldsymbol{\xi}}{2}; t) e^{i\mathbf{k}_w \boldsymbol{\xi}} d^3 \boldsymbol{\xi} \\
 &= W_0 (\alpha_s E_0)^2 \int_{-\infty}^{\infty} e^{-i\mathbf{q}(\mathbf{k})(\mathbf{r} + \frac{\boldsymbol{\xi}}{2}) + i\mathbf{q}(\mathbf{k})t} \left( e^{-i\mathbf{q}(\mathbf{k})(\mathbf{r} - \frac{\boldsymbol{\xi}}{2}) + i\mathbf{q}(\mathbf{k})t} \right)^* e^{i\mathbf{k}_w \boldsymbol{\xi}} d^3 \boldsymbol{\xi} \\
 &= W_0 (\alpha_s E_0)^2 \int_{-\infty}^{\infty} e^{i(\mathbf{k}_w - \mathbf{q}(\mathbf{k})) \boldsymbol{\xi}} d^3 \boldsymbol{\xi} \\
 &= W_0 (2\pi)^3 (\alpha_s E_0)^2 \delta(\mathbf{k}_w - \mathbf{q}(\mathbf{k})) \quad ,
 \end{aligned} \tag{4.8}$$

where  $W_1^c = (2\pi)^3 \alpha_s^2 E_0^2 W_0$ ,  $\mathbf{n} = \mathbf{r}/r$  is the unit vector pointing from the initial electron location to the observer location, and  $\mathbf{k}_w$  is the Wigner function wave-vector introduced in

Eq. (4.1). One can also rewrite the  $\delta$ -function of the vector argument in Eq. (4.8) as a multiplication product of the  $\delta$ -functions of each component of the vector<sup>5</sup>:

$$W_{1e} = W_1^c \delta\left(\frac{n_x}{n_z}k_{wz} - k_{wx}\right) \delta\left(\frac{n_y}{n_z}k_{wz} - k_{wy}\right) \delta\left(k_{wz} - n_z \frac{w_{rad}}{c}\right) , \quad (4.9)$$

This demonstrates the directional dependence of the Wigner function caused by the direct propagation of photons in a free space<sup>6</sup>. The derived SWF is time-independent which is straight-forward to understand. An electron would continuously emit photons during the interaction with a continuous plane-wave in the approximation that its energy does not dissipate<sup>7</sup> if  $a_0 \ll 1$ .

### 4.3.2 The time-limited plane wave approximation

The time-limited plane wave is more realistic approximation of the laser pulse better describing the ICS process. We consider a laser pulse with a large number of oscillations:  $T_p \gg \frac{2\pi}{\omega_{las}}$ . Under this assumption, the radiation is emitted within the pulse duration ( $T_p$ ). However, observer detects shorter radiation pulse  $T_{rad} = \frac{T_p}{2\gamma^2}$  at the up-shifted frequency. Considering a Gaussian profile of the laser pulse  $\sim e^{-\frac{(z/c+t)^2}{2T_p^2}}$ , one can find the radiation emitted by an individual electron:

$$E_{rad} = \alpha_s E_0 e^{-\frac{(r-ct)^2}{2\sigma_r^2}} e^{-i\mathbf{q}(\mathbf{k})\mathbf{r} + i\mathbf{q}(\mathbf{k})ct} , \quad (4.10)$$

---

<sup>5</sup>This result can be derived directly from the second from last line in Eq. (4.8) by using multiplicative identity property of the exponential function and integrating individually over each component  $\xi_i$  for  $i = x, y, z$ .

<sup>6</sup>The photon wave-vector at the observer location is aligned with the direction in which it was emitted in a free space. Adding X-ray optics can change the direction.

<sup>7</sup>This approximation is unrealistic, because eventually all electron energy will be emitted with radiation.

where the radiation vector is:

$$\mathbf{q}(-k_l \hat{\mathbf{z}}) = q(-k_l \hat{\mathbf{z}}) \mathbf{n} = \frac{1 + \beta_z}{1 - \beta_0 \mathbf{n}} k_l \mathbf{n} . \quad (4.11)$$

The space-time interval and the duration of the incoming/emitted radiation pulse are related according to the following expressions:

$$(z + ct)k_l = (r - ct)q(-k_l \hat{\mathbf{z}}) , \quad (4.12)$$

$$\frac{(z + ct)}{cT_p} = \frac{(r - ct)}{\sigma_r} , \quad (4.13)$$

$$\sigma_r = cT_p \frac{k_l}{q(-k_l \hat{\mathbf{z}})} . \quad (4.14)$$

One can immediately obtain the corresponding Wigner function in Eq. (4.1):

$$\begin{aligned} W_{1e} &= W_0 \int_{-\infty}^{\infty} E_{rad}(\mathbf{r} + \frac{\boldsymbol{\xi}}{2}; t) E_{rad}^*(\mathbf{r} - \frac{\boldsymbol{\xi}}{2}; t) e^{i\mathbf{k}_w \boldsymbol{\xi}} d^3 \boldsymbol{\xi} \\ &= W_0 (\alpha_s E_0)^2 e^{-\frac{(r-ct)^2}{\sigma_r^2}} \int_{-\infty}^{\infty} e^{-\frac{(\boldsymbol{\xi} \mathbf{n})^2}{4\sigma_r^2}} e^{-i\mathbf{q}(\mathbf{k})(\mathbf{r} + \frac{\boldsymbol{\xi}}{2}) + i\mathbf{q}(\mathbf{k})ct} \cdot \left( e^{-i\mathbf{q}(\mathbf{k})(\mathbf{r} - \frac{\boldsymbol{\xi}}{2}) + i\mathbf{q}(\mathbf{k})ct} \right)^* e^{i\mathbf{k}_w \boldsymbol{\xi}} d^3 \boldsymbol{\xi} \\ &= W_0 (\alpha_s E_0)^2 e^{-\frac{(r-ct)^2}{\sigma_r^2}} \int_{-\infty}^{\infty} e^{-\frac{(\boldsymbol{\xi} \mathbf{n})^2}{4\sigma_r^2}} e^{i(\mathbf{k}_w - \mathbf{q}(\mathbf{k})) \boldsymbol{\xi}} d^3 \boldsymbol{\xi} , \end{aligned} \quad (4.15)$$

Using the following approximation:

$$\boldsymbol{\xi} \cdot \mathbf{n} = \xi_x n_x + \xi_y n_y + \xi_z n_z \approx \xi_z n_z, \quad n_z \gg n_{x,y} , \quad (4.16)$$

one can evaluate the integral in Eq. (4.15):

$$\begin{aligned}
W_{1e} &= W_0(2\pi)^2(\alpha_s E_0)^2 \delta(k_{wx} - q(\mathbf{k})n_x) \delta(k_{wy} - q(\mathbf{k})n_y) e^{-\frac{(r-ct)^2}{\sigma_r^2}} \\
&\cdot \int_{-\infty}^{\infty} e^{-\frac{\xi_z^2 n_z^2}{4\sigma_r^2}} e^{i(k_{Wz} - q(\mathbf{k})n_z)\xi_z} d\xi_z = \\
&= W_0 8\pi^{5/2} (\alpha_s E_0)^2 \frac{\sigma_r}{n_z} \delta(k_{wx} - q(\mathbf{k})n_x) \delta(k_{wy} - q(\mathbf{k})n_y) e^{-\frac{(r-ct)^2}{\sigma_r^2}} e^{-\left(\frac{k_{Wz}}{n_z} - q(\mathbf{k})\right)^2 \sigma_r^2} .
\end{aligned} \tag{4.17}$$

where we arguments of the  $\delta$ -functions are different in comparison to Eq. (4.9). This, however is the result of the “poor” approximation in Eq. (4.17). Perhaps, the 3D integral in Eq. (4.15) can be evaluated analytically using a few permutations:

$$\begin{aligned}
W_{1e} &= W_0(\alpha_s E_0)^2 e^{-\frac{(r-ct)^2}{\sigma_r^2}} \\
&\cdot \int_{-\infty}^{\infty} \int_{-\infty}^{\infty} e^{i(k_{Wx} - q(\mathbf{k})n_x)\xi_x} e^{i(k_{Wy} - q(\mathbf{k})n_y)\xi_y} \left( \int_{-\infty}^{\infty} e^{-\frac{(\xi_z n_z + \xi_x n_x + \xi_y n_y)^2}{4\sigma_r^2}} e^{i(k_{Wz} - q(\mathbf{k})n_z)\xi_z} d\xi_z \right) d\xi_x d\xi_y \\
&= W_0 2\sqrt{\pi} (\alpha_s E_0)^2 \frac{\sigma_r}{n_z} e^{-\frac{(r-ct)^2}{\sigma_r^2}} e^{-\left(\frac{k_{Wz}}{n_z} - q(\mathbf{k})\right)^2 \sigma_r^2} \\
&\cdot \int_{-\infty}^{\infty} \int_{-\infty}^{\infty} e^{i(k_{Wx} - q(\mathbf{k})n_x)\xi_x} e^{i(k_{Wy} - q(\mathbf{k})n_y)\xi_y} e^{-i(k_{Wz} - q(\mathbf{k})n_z)\left(\frac{n_x}{n_z}\xi_x + \frac{n_y}{n_z}\xi_y\right)} d\xi_x d\xi_y \\
&= \frac{2\sqrt{\pi} W_0 \sigma_r \alpha_s^2 E_0^2}{n_z} e^{-\frac{(r-ct)^2}{\sigma_r^2}} e^{-\left(\frac{k_{Wz}}{n_z} - q(\mathbf{k})\right)^2 \sigma_r^2} \int_{-\infty}^{\infty} e^{i(k_{Wx} - k_{Wz} \frac{n_x}{n_z})\xi_x} d\xi_x \int_{-\infty}^{\infty} e^{i(k_{Wy} - k_{Wz} \frac{n_y}{n_z})\xi_y} d\xi_y \\
&= \frac{W_0 8\pi^{5/2} \sigma_r \alpha_s^2 E_0^2}{n_z} e^{-\frac{(r-ct)^2}{\sigma_r^2}} e^{-\left(\frac{k_{Wz}}{n_z} - q(\mathbf{k})\right)^2 \sigma_r^2} \delta\left(\frac{n_x}{n_z} k_{Wz} - k_{wx}\right) \delta\left(\frac{n_y}{n_z} k_{Wz} - k_{wy}\right) .
\end{aligned} \tag{4.18}$$

By introducing a coefficient  $W_1 = 8\pi^{5/2}(\alpha_s E_0)^2 \frac{\sigma_r}{n_z} W_0$  we can rewrite the result in terms of the incoming pulse duration  $T_p$  as following:

$$W_{1e} = W_1 \delta\left(\frac{n_x}{n_z} k_{Wz} - k_{wx}\right) \delta\left(\frac{n_y}{n_z} k_{Wz} - k_{wy}\right) e^{\frac{-(r-ct)^2}{c^2 T_{rad}^2}} e^{-\left(\frac{k_{Wz}}{n_z} c - w_{rad}\right)^2 T_{rad}^2} . \tag{4.19}$$

The derived Wigner function is time-limited as expected. Furthermore, it has a finite bandwidth  $\sim 1/T_{rad}$ . The arguments of the  $\delta$ -functions are exactly matching with those derived

in the continuous plane-wave approximation in Eq. (4.9). We check the accuracy of the latest derivations by considering the infinite pulse duration:  $T_{rad} \rightarrow \infty$ . It is convenient to use the following definition of the Dirac  $\delta$ -function:

$$\delta(x) = \lim_{\delta_x \rightarrow 0} \left\{ \frac{1}{\sqrt{\pi}\delta_x} e^{-\left(\frac{x}{\delta_x}\right)^2} \right\} . \quad (4.20)$$

One can immediately find for the interval corresponding to the frequency of the produced radiation:

$$\lim_{T_{rad} \rightarrow \infty} \left\{ e^{-\left(\frac{k w_z}{n_z} c - w_{rad}\right)^2 T_{rad}^2} \right\} = \sqrt{\pi} \frac{n_z}{c T_{rad}} \delta \left( k w_z - n_z \frac{w_{rad}}{c} \right) , \quad (4.21)$$

while the space-time Gaussian distribution becomes uniform:

$$\lim_{T_{rad} \rightarrow \infty} e^{\frac{-(r-ct)^2}{c^2 T_{rad}^2}} = 1 . \quad (4.22)$$

By combining the corresponding coefficients one can match the amplitudes of the Wigner function in Equations (4.9 and 4.19):

$$W'_1 = W_1 \cdot \sqrt{\pi} \frac{n_z}{c T_{rad}} = 8\pi^{5/2} \alpha_s^2 E_0^2 \frac{c T_{rad}}{n_z} W_0 \cdot \sqrt{\pi} \frac{n_z}{c T_{rad}} = (2\pi)^3 \alpha_s^2 E_0^2 W_0 = W_1^c , \quad (4.23)$$

validating the results of the time-limited approximation.

Ultra short laser pulses focused to very small sizes ( $\sim \lambda_{las}$ ) are often considered in ICS sources in order to reach large field intensities and high peak brightness of the emitted radiation. In this configuration, approximation of a homogeneous plane wave has to be validated for different pulse configurations. Adding space limitations on the plane wave in the transverse directions is a common approach aimed to resolve the issue. In this approximation the beam interacts with the incoming radiation only within the pulse area, where the approximation of the homogeneous (or time-limited) plane wave is considered. This model requires

validation for the case when the laser pulse is focused to a size comparable with the diffraction limit:  $\sigma_r \sim \lambda_{las}$ . In the next section, we evaluate the WF of a single electron interacting with a realistic laser pulse and explore different regimes of scattering corresponding to different ratios between the transverse and longitudinal pulse sizes. We find the regime in which the time-limited plane wave approximation discussed here becomes a valid approximation.

#### 4.4 The single-electron Wigner function: arbitrary laser pulse

An arbitrary laser pulse can be presented as a direct sum of plane waves (*e.g.* modes) propagating in different directions. This is valid due to the linear property of the Maxwell equations for the electromagnetic fields. In such a model the overall motion of a single electron can be considered as a virtual superposition of individual motions in which it independently interacts with each distinct mode of the laser pulse. During each interaction the electron emits slightly different photons on the up-shifted frequency. Such a radiation field has to be summed coherently to find the overall radiation emitted by the single particle. The corresponding single-electron Wigner function of the total field can be then immediately found using Eq. (4.1).

##### 4.4.1 Total emitted radiation as a superposition of single modes

Upcoming laser field can be presented as a continuous superposition of plane waves without any limitations:

$$E_{las}(\mathbf{r}; t) = \frac{\kappa}{(2\pi)^{3/2}} \int E_0(\mathbf{k}) e^{i\omega(\mathbf{k})t - i\mathbf{k}\mathbf{r}} d^3\mathbf{k} \quad , \quad (4.24)$$

where  $\omega(k) = \sqrt{\mathbf{k}^2}c = kc$  is the dispersion relation in vacuum, and  $\kappa$  is a coefficient introduced to preserve the dimension of the electric field for each individual mode, *e.g.*  $[E_{las}] = [E_0]$ . This coefficient can be found directly for a given laser profile using the corresponding Fourier transform equations<sup>8</sup>:

$$\begin{aligned} g(\mathbf{k}) &= \frac{1}{(2\pi)^{n/2}} \int f(\mathbf{r}) e^{i\mathbf{k}\mathbf{r}} d^n \mathbf{r} \quad , \\ f(\mathbf{r}) &= \frac{1}{(2\pi)^{n/2}} \int g(\mathbf{k}) e^{-i\mathbf{k}\mathbf{r}} d^n \mathbf{k} \quad . \end{aligned} \tag{4.25}$$

An electron interacts with a plane wave  $E_0(\mathbf{k})e^{i\omega(\mathbf{k})t-i\mathbf{k}\mathbf{r}}$  from Eq. (4.24) and emits radiation  $E_{rad}[E_0(\mathbf{k})]$  which can be evaluated using Eq. (4.5). One can immediately find the total field generated by the single electron as a continuous superposition of the individual modes:

$$E_{rad1e}(\mathbf{r}; t) = \frac{\kappa}{(2\pi)^{3/2}} \int E_{rad}[E_0(\mathbf{k}), \mathbf{r}, t] d^3 \mathbf{k} \quad . \tag{4.26}$$

---

<sup>8</sup>Note that functions  $g(\mathbf{k})$  and  $f(\mathbf{r})$  are of the different dimension in these equations.

### 4.4.2 The single-electron Wigner function

Using Equations (4.5-4.7 and 4.26) one can rewrite the corresponding Wigner function in Eq. (4.1) as a 9-dimensional integral:

$$\begin{aligned}
W_{6d} &= W_0 \int_{-\infty}^{\infty} E_{rad}(\mathbf{r} + \frac{\boldsymbol{\xi}}{2}; t) E_{rad}^*(\mathbf{r} - \frac{\boldsymbol{\xi}}{2}; t) e^{i\mathbf{k}_w \boldsymbol{\xi}} d^3 \boldsymbol{\xi} \\
&= W_0 \int_{-\infty}^{\infty} \frac{\kappa^2}{(2\pi)^3} \int E_{rad}[E_0(\mathbf{k}), \mathbf{r} + \frac{\boldsymbol{\xi}}{2}, t] d^3 \mathbf{k} \left( \int E_{rad}[E_0(\mathbf{k}'), \mathbf{r} - \frac{\boldsymbol{\xi}}{2}, t] d^3 \mathbf{k}' \right)^* e^{i\mathbf{k}_w \boldsymbol{\xi}} d^3 \boldsymbol{\xi} \\
&= W_1 \int_{-\infty}^{\infty} \int E_0(\mathbf{k}) e^{-i\mathbf{q}(\mathbf{k})(\mathbf{r} + \frac{\boldsymbol{\xi}}{2}) + i\mathbf{q}(\mathbf{k})ct} d^3 \mathbf{k} \left( \int E_0(\mathbf{k}') e^{-i\mathbf{q}(\mathbf{k}')(\mathbf{r} - \frac{\boldsymbol{\xi}}{2}) + i\mathbf{q}(\mathbf{k}')ct} d^3 \mathbf{k}' \right)^* e^{i\mathbf{k}_w \boldsymbol{\xi}} d^3 \boldsymbol{\xi} \\
&= W_1 \int \int E_0(\mathbf{k}) E_0(\mathbf{k}') e^{-i(\mathbf{q}(\mathbf{k}) - \mathbf{q}(\mathbf{k}'))(\mathbf{r} - ct)} \left( \int_{-\infty}^{\infty} e^{-i(\frac{\mathbf{q}(\mathbf{k}) + \mathbf{q}(\mathbf{k}')}{2} - \mathbf{k}_w) \boldsymbol{\xi}} d^3 \boldsymbol{\xi} \right) d^3 \mathbf{k} d^3 \mathbf{k}' ,
\end{aligned} \tag{4.27}$$

where  $W_1 = \frac{\kappa^2 \alpha_s^2}{(2\pi)^3} W_0$ . Integral over  $\boldsymbol{\xi}$  can be immediately evaluated resulting in:

$$W_{6d}(\mathbf{r}, \mathbf{k}_w) = W_2 \int \int E_0(\mathbf{k}) E_0(\mathbf{k}') e^{-i(\mathbf{q}(\mathbf{k}) - \mathbf{q}(\mathbf{k}'))(\mathbf{r} - ct)} \delta\left(\frac{\mathbf{q}(\mathbf{k}) + \mathbf{q}(\mathbf{k}')}{2} - \mathbf{k}_w\right) d^3 \mathbf{k} d^3 \mathbf{k}' . \tag{4.28}$$

where  $W_2 = W_0 \alpha_s^2 \kappa^2$ . This Wigner function represented in the 6-dimensional integral form characterizes the radiation emitted by a single electron during the interaction with an arbitrary laser pulse. The derived result is symmetric over  $\mathbf{k}$  and  $\mathbf{k}'$  which is due to the initial symmetry of the Wigner function in Eq. (4.1) in respect to the electric field and the complex conjugated counterpart. Similarly to Eq. (4.9), we present the  $\delta$ -function of a vector argument as a multiplication product of scalar components. While the argument of the  $\delta$ -function is a 3-dimensional vector, it depends on vectors  $\mathbf{k}$  and  $\mathbf{k}'$ , over which the

integral in Eq. (4.28) is evaluated, only as a scalar product (see Eq. (4.6) for details). For  $\mathbf{q}(\mathbf{k}) = q(\mathbf{k})\mathbf{n}$  the 3-dimensional  $\delta$ -function can be represented as following:

$$\delta\left(\frac{\mathbf{q}(\mathbf{k}) + \mathbf{q}(\mathbf{k}')}{2} - \mathbf{k}_w\right) = \delta\left(\frac{q(\mathbf{k}) + q(\mathbf{k}')}{2}n_z - k_{wz}\right) \delta\left(\frac{k_{wz}n_x - k_{wx}}{n_z}\right) \delta\left(\frac{k_{wz}n_y - k_{wy}}{n_z}\right), \quad (4.29)$$

where the sifting property of the delta-function  $f(x)\delta(x-a) = f(a)\delta(x-a)$  was used. The corresponding Wigner function in Eq. (4.28) becomes:

$$W_{6d}(\mathbf{r}, \mathbf{k}_w) = W_2 \delta\left(\frac{n_x}{n_z}k_{wz} - k_{wx}\right) \delta\left(\frac{n_y}{n_z}k_{wz} - k_{wy}\right) \cdot \int \int E_0(\mathbf{k}) E_0(\mathbf{k}') e^{-i(q(\mathbf{k}) - q(\mathbf{k}'))(r-ct)} \delta\left(\frac{q(\mathbf{k}) + q(\mathbf{k}')}{2}n_z - k_{wz}\right) d^3\mathbf{k} d^3\mathbf{k}' \quad (4.30)$$

One can notice the same directional dependence of the transverse component of the Wigner function in Eq. (4.30) with the results found for the continuous (4.9) and time-limited (4.19) plane wave approximations. As discussed in Sec. 4.3.1, a photon in a free space travels along a straight line. Thus, an observer will detect photons with wave-vector  $\mathbf{k}_w$  aligned with vector  $\mathbf{n}$  pointing from the electron position to the observer location. The electron interacting with distinct plane waves of the incoming laser field is considered to be in the same location in space<sup>9</sup>. Consequently, it generates unidirectional photons towards the observer, while the spectrum of the produced radiation and the time-of-arrival may change which is described by the integral part in Eq. (4.30) representing the longitudinal component of the Wigner

---

<sup>9</sup>We assume that the observer location also remains invariant.

function. Furthermore, this longitudinal component can be represented as a 1-dimensional Wigner function:

$$\begin{aligned}
W_z &= \int \int E_0(\mathbf{k}) E_0(\mathbf{k}') e^{-i(q(\mathbf{k}) - q(\mathbf{k}'))(r - ct)} \delta\left(\frac{q(\mathbf{k}) + q(\mathbf{k}')}{2} n_z - k_{wz}\right) d^3\mathbf{k} d^3\mathbf{k}' \\
&= \frac{2}{n_z} \int E_0(\mathbf{k}') e^{-2i\left(\frac{k_{wz}}{n_z} - q(\mathbf{k}')\right)(r - ct)} \left( \int E_0(\mathbf{k}) \delta\left(q(\mathbf{k}) + q(\mathbf{k}') - \frac{2k_{wz}}{n_z}\right) d^3\mathbf{k} \right) d^3\mathbf{k}' \quad (4.31) \\
&= \frac{2}{n_z} \int E_0(\mathbf{k}') e^{-2i\left(\frac{k_{wz}}{n_z} - q(\mathbf{k}')\right)(r - ct)} I_1(q_0(\mathbf{k}')) d^3\mathbf{k}' \quad ,
\end{aligned}$$

where new notations were introduced:

$$q_0(\mathbf{k}') = \frac{2k_{wz}}{n_z} - q(\mathbf{k}') \quad , \quad (4.32)$$

$$I_1(q_0) = \int E_0(\mathbf{k}) \delta(q(\mathbf{k}) - q_0) d^3\mathbf{k} \quad . \quad (4.33)$$

One may notice that the term accompanying the electric field in Eq. (4.31):

$$g = e^{-2i\left(\frac{k_{wz}}{n_z} - q(\mathbf{k}')\right)(r - ct)} I_1(q_0(\mathbf{k}')) = e^{-2i\left(q_0(\mathbf{k}') - \frac{k_{wz}}{n_z}\right)(r - ct)} I_1(q_0(\mathbf{k}')) = g(q_0(\mathbf{k}')) \quad , \quad (4.34)$$

is invariant on the 2D surface  $q_0(\mathbf{k}') = \text{const.}$  Using this observation, one can represent the longitudinal component as a Wigner function of  $I_1\left(\frac{k_{wz}}{n_z}\right)$ :

$$\begin{aligned}
W_z &= \frac{2}{n_z} \int E_0(\mathbf{k}') g(q_0(\mathbf{k}')) d^3 \mathbf{k}' \\
&= \frac{2}{n_z} \int E_0(\mathbf{k}') \left( \int_{-\infty}^{+\infty} g(q'_0) \delta(q'_0 - q_0(\mathbf{k}')) dq'_0 \right) d^3 \mathbf{k}' \\
&= \frac{2}{n_z} \int_{-\infty}^{+\infty} g(q'_0) \left( \int E_0(\mathbf{k}') \delta(q'_0 - q_0(\mathbf{k}')) d^3 \mathbf{k}' \right) dq'_0 \\
&= \frac{2}{n_z} \int_{-\infty}^{+\infty} g(q'_0) \left( \int E_0(\mathbf{k}') \delta\left(q(\mathbf{k}') - \frac{2k_{wz}}{n_z} + q'_0\right) d^3 \mathbf{k}' \right) dq'_0 \\
&= \frac{2}{n_z} \int_{-\infty}^{+\infty} g(q'_0) I_1\left(\frac{2k_{wz}}{n_z} - q'_0\right) dq'_0 \\
&= \frac{2}{n_z} \int_{-\infty}^{+\infty} e^{-2i\left(q'_0 - \frac{k_{wz}}{n_z}\right)(r-ct)} I_1(q'_0) I_1\left(\frac{2k_{wz}}{n_z} - q'_0\right) dq'_0 \\
&= \frac{2}{n_z} \int_{-\infty}^{+\infty} e^{-i2\psi'(r-ct)} I_1\left(\frac{k_{wz}}{n_z} + \psi'\right) I_1\left(\frac{k_{wz}}{n_z} - \psi'\right) d\psi' \\
&= \frac{1}{n_z} \int_{-\infty}^{+\infty} e^{-i\psi(r-ct)} I_1\left(\frac{k_{wz}}{n_z} + \frac{\psi}{2}\right) I_1\left(\frac{k_{wz}}{n_z} - \frac{\psi}{2}\right) d\psi \quad .
\end{aligned} \tag{4.35}$$

For the inverse Compton scattering radiation<sup>10</sup>  $q(\mathbf{k}) \geq 0$  according to Eq. (4.6). This suggests that  $q_0 \geq 0$  in Eq. (4.33), otherwise  $I_1 = 0$  (see Eq. (4.32) for details). Consequently, the integration over  $\psi$  from the infinite interval can be substituted by the integration over finite interval  $[\frac{-2k_{wz}}{n_z}; \frac{2k_{wz}}{n_z}]$ . It is convenient to move the  $\mathbf{k}$ -independent part of  $q(\mathbf{k}) = \frac{k - \beta \mathbf{k}}{1 - \beta \mathbf{n}}$  out of the integral:

$$I_1(q_0) = (1 - \beta \mathbf{n}) \int_{R_3} E_0(\mathbf{k}) \delta(k - \beta \mathbf{k} - k_0(q_0)) d^3 \mathbf{k} \quad , \tag{4.36}$$

---

<sup>10</sup>The formalism described in this section up to now was not limited to the ICS process, *i.e.* the Wigner function corresponding to dipole radiation of a charged particle in an external electric field can be calculated using Eq. (4.35), etc.

where  $k_0(q_0) = q_0(1 - \beta \mathbf{n})$ . According to the coarea formula from the geometric measure theory, the integral with a  $\delta$ -function over an  $n$ -dimensional volume can be found as an integral over the corresponding  $(n - 1)$ -dimensional surface:

$$\int f(\mathbf{r}^n) \delta(g(\mathbf{r}^n)) d^n \mathbf{r} = \int \frac{f(\mathbf{r}^n)}{|\nabla g(\mathbf{r}^n)|} d^{n-1} \sigma \quad , \quad (4.37)$$

where  $\forall \mathbf{r} \in \sigma : g(\mathbf{r}) = 0$ . Argument of the  $\delta$ -function in  $I_1$ :

$$k - \beta \mathbf{k} = k_0 \quad , \quad (4.38)$$

represents an elliptical surface<sup>11</sup> with an axis of symmetry along the vector of the normalized electron velocity  $\beta$ . It is convenient to align the  $z$ -axis of the spherical coordinates system with  $\beta$  and further simplify the equation of that elliptical surface:

$$k(1 - \beta \cos \theta) = k_0 \quad , \quad (4.39)$$

where one of the focuses is placed at the origin of the coordinate system. Summarizing this section, one would have to evaluate  $I_1$  as an integral of the specific laser profile  $E_0(\mathbf{k})$  over the ellipsoid surface in  $\mathbf{k}$ -space, then calculate the longitudinal component of the WF in Eq. (4.35) using derived function  $I_1$  and finally obtain the Wigner function in Eq. (4.30) representing the radiation generated by a single electron while interacting with an arbitrary laser pulse.

---

<sup>11</sup>Generally, the surface described by this equation can also represent the hyperboloid. Since  $\beta < 1$  for any electron it is strictly elliptical.

## 4.5 The Gaussian approximation of the laser pulse

In principal, one can numerically calculate the single-electron Wigner function for an arbitrary laser pulse using using Eq. (4.30). However, an analytical solution for the corresponding Wigner function is of the big interest since the final goal is to find the WF characterizing radiation from an arbitrary shaped in 6D electron bunch. The later is described in accelerators as a 6D Gaussian distribution characterized by the  $\Sigma$ -matrix, matrix of the second order momentums, as discussed in Chapter 1. Following this approach, we aim to find an analytical solution for the SWF for the incoming laser pulse in the Gaussian approximation at  $t = 0$ :

$$E_{las}(\mathbf{r}; 0) = E_0 e^{-\frac{x^2}{2\sigma_x^2} - \frac{y^2}{2\sigma_y^2} - \frac{z^2}{2\sigma_z^2}} e^{ik_{las}z} . \quad (4.40)$$

The expression for each mode (plane wave) of the laser pulse can be found using the Fourier transform in Eq. (4.25):

$$\begin{aligned} \kappa E_0(\mathbf{k}) &= \frac{1}{(2\pi)^{3/2}} \int E_0 e^{-\frac{x^2}{2\sigma_x^2} - \frac{y^2}{2\sigma_y^2} - \frac{z^2}{2\sigma_z^2}} e^{ik_{las}z} e^{i\mathbf{k}\mathbf{r}} d^3\mathbf{r} \\ &= E_0 \sigma_x \sigma_y \sigma_z e^{-\frac{k_x^2 \sigma_x^2}{2} - \frac{k_y^2 \sigma_y^2}{2} - \frac{(k_z + k_{las})^2 \sigma_z^2}{2}} \\ &= \kappa E_0 e^{-\frac{k_x^2 \sigma_x^2}{2} - \frac{k_y^2 \sigma_y^2}{2} - \frac{(k_z + k_{las})^2 \sigma_z^2}{2}} , \end{aligned} \quad (4.41)$$

where the amplitude of the electric field of each mode is:

$$E_0(\mathbf{k}) = E_0 e^{-\frac{k_x^2 \sigma_x^2}{2} - \frac{k_y^2 \sigma_y^2}{2} - \frac{(k_z + k_{las})^2 \sigma_z^2}{2}} , \quad (4.42)$$

and the introduced coefficient  $\kappa = \sigma_x \sigma_y \sigma_z$ . Next, we evaluate the integral part of the expression in Eq. (4.36):

$$I'_1(q_0) = \int E_0(\mathbf{k}) \delta(k - \beta \mathbf{k} - k_0(q_0)) d^3 \mathbf{k} \quad , \quad (4.43)$$

in different approximations. The integrand expression in Eq. (4.43) reaches the maximum on the elliptical surface in the point  $(k = -\frac{k_0}{1+\beta}, \theta = 0)$ . Integration over the elliptical surface can be substituted by integration over a plane<sup>12</sup> tangent to the surface in that point, if  $\sigma_{x,y} \rightarrow +\infty$ :

$$I'_1 = G^{-1} E_0 e^{-\left(\frac{k_0}{1+\beta_z} - k_{las}\right)^2 \frac{\sigma_z^2}{2}} \int_{R_2} e^{-\frac{k_x^2 \sigma_x^2}{2} - \frac{k_y^2 \sigma_y^2}{2}} dk_x dk_y = \frac{2\pi}{\sigma_x \sigma_y} G^{-1} E_0 e^{-\left(\frac{k_0}{1+\beta_z} - k_{las}\right)^2 \frac{\sigma_z^2}{2}} \quad , \quad (4.44)$$

where  $G = 1 + \beta_z$  and  $k_0 = q_0(1 - \beta \mathbf{n})$ . Respectively, the expression in Eq. (4.36) becomes:

$$I_1(q_0) = (1 - \beta \mathbf{n}) \frac{2\pi}{\sigma_x \sigma_y (1 + \beta_z)} E_0 e^{-\left(\frac{q_0(1 - \beta \mathbf{n})}{1 + \beta_z} - k_{las}\right)^2 \frac{\sigma_z^2}{2}} \quad , \quad (4.45)$$

and one can evaluate the longitudinal component of the Wigner function in Eq. (4.35):

$$\begin{aligned} W_z &= \frac{1}{n_z} \left( (1 - \beta \mathbf{n}) \frac{2\pi}{\sigma_x \sigma_y (1 + \beta_z)} E_0 \right)^2 \cdot \\ &\cdot \int_{-\infty}^{+\infty} e^{-i\xi(r-ct)} e^{-\left(\frac{\left(\frac{k_{wz}}{n_z} + \frac{\xi}{2}\right)(1 - \beta \mathbf{n})}{1 + \beta_z} - k_{las}\right)^2} e^{-\left(\frac{\left(\frac{k_{wz}}{n_z} - \frac{\xi}{2}\right)(1 - \beta \mathbf{n})}{1 + \beta_z} - k_{las}\right)^2} d\psi \\ &= \frac{1}{n_z} \left( (1 - \beta \mathbf{n}) \frac{2\pi}{\sigma_x \sigma_y (1 + \beta_z)} E_0 \right)^2 \frac{2\pi^{1/2} (1 + \beta_z)}{\sigma_z (1 - \beta \mathbf{n})} e^{-\frac{(r-ct)^2}{\left(\sigma_z \frac{1 - \beta \mathbf{n}}{1 + \beta_z}\right)^2}} e^{-\left(k_{las} \frac{1 + \beta_z}{1 - \beta \mathbf{n}} - \frac{k_{wz}}{n_z}\right)^2 \left(\sigma_z \frac{1 - \beta \mathbf{n}}{1 + \beta_z}\right)^2} \\ &= \frac{1}{n_z} (1 - \beta \mathbf{n}) \frac{8\pi^{5/2}}{(\sigma_x \sigma_y)^2 \sigma_z (1 + \beta_z)} E_0^2 e^{-\frac{(r-ct)^2}{\left(\sigma_z \frac{1 - \beta \mathbf{n}}{1 + \beta_z}\right)^2}} e^{-\left(k_{las} \frac{1 + \beta_z}{1 - \beta \mathbf{n}} - \frac{k_{wz}}{n_z}\right)^2 \left(\sigma_z \frac{1 - \beta \mathbf{n}}{1 + \beta_z}\right)^2} \quad . \end{aligned} \quad (4.46)$$

---

<sup>12</sup>Hint to match the coefficients with the result derived for the time-limited plane wave approximation in Eq. (4.19) is to correctly calculate the gradient in Eq. (4.37).

The overall single-electron Wigner function in Eq. (4.30) can be immediately found:

$$\begin{aligned}
W_{6d}(\mathbf{r}, \mathbf{k}_w) &= W_2 \delta \left( \frac{n_x}{n_z} k_{wz} - k_{wx} \right) \delta \left( \frac{n_y}{n_z} k_{wz} - k_{wy} \right) \cdot \\
&\cdot \frac{1}{n_z} (1 - \beta \mathbf{n}) \frac{8\pi^{5/2}}{(\sigma_x \sigma_y)^2 \sigma_z (1 + \beta_z)} E_0^2 e^{-\frac{(r-ct)^2}{\left(\sigma_z \frac{1-\beta \mathbf{n}}{1+\beta_z}\right)^2}} e^{-\left(k_{las} \frac{1+\beta_z}{1-\beta \mathbf{n}} - \frac{k_{wz}}{n_z}\right)^2 \left(\sigma_z \frac{1-\beta \mathbf{n}}{1+\beta_z}\right)^2} \\
&= \frac{W_0}{n_z} \left( \sigma_z \frac{1 - \beta \mathbf{n}}{1 + \beta_z} \right) 8\pi^{5/2} (\alpha_s E_0)^2 \cdot \\
&\cdot e^{-\frac{(r-ct)^2}{\left(\sigma_z \frac{1-\beta \mathbf{n}}{1+\beta_z}\right)^2}} e^{-\left(k_{las} \frac{1+\beta_z}{1-\beta \mathbf{n}} - \frac{k_{wz}}{n_z}\right)^2 \left(\sigma_z \frac{1-\beta \mathbf{n}}{1+\beta_z}\right)^2} \delta \left( \frac{n_x}{n_z} k_{wz} - k_{wx} \right) \delta \left( \frac{n_y}{n_z} k_{wz} - k_{wy} \right)
\end{aligned} \tag{4.47}$$

The derived result matches with one obtained for the time-limited plane wave approximation in Eq. (4.19) validating both, the advanced formalism of this section and a simple assumption of substituting the elliptical surface of integration with the plane<sup>13</sup>. We reported in [115] that the radiation spectrum represented by the longitudinal component of the Wigner function becomes blue-shifted if the incoming laser pulse is strongly focused:  $\sigma_{x,y} \sim \sigma_z$ . This result was derived by approximating the elliptical surface of integration  $g(\mathbf{k}) = k - \beta \mathbf{k} - k_0 = 0$  with the tangent parabolic surface with the same radius of curvature in the point  $(k = -\frac{k_0}{1+\beta}, \theta = 0)$ , where the integrand expression reaches its maximum on the surface. Such an assumption is more accurate than the previous one and legitimate if the integrand  $E_0(\mathbf{k})/|\nabla g|$  rapidly descends away from that point on both surfaces. However, this approximation is valid only if the integrand has a single maximum reached at that point. The detailed analysis showed that the single extremum on the surface exists only in the regions:  $\sigma_x < \frac{\sigma_z}{\sqrt{1+\beta}}$  or  $\sigma_x > \gamma \sigma_z$ .

Apparently<sup>14</sup>, the integral  $I'_1(q_0)$  in Eq. (4.43) can be analytically evaluated for the Gaussian laser profile without a surface simplification, perhaps, using its original  $\delta$ -function nota-

<sup>13</sup>Integral over  $\psi$  was evaluated over the infinite interval rather than  $\left[-\frac{2k_{wz}}{n_z}, \frac{2k_{wz}}{n_z}\right]$  because the elliptical surface was substituted with the plane.

<sup>14</sup>Another surfaces of integration was considered, *e.g.* a cylindrically symmetrical conical surface, etc.

tion. Several reasonable assumptions are required. We consider an electron bunch traveling along the  $z$ -axis, which means  $\beta_{x,y} \ll \beta_z$  for each individual electron. Since the effects of the electron velocity distribution<sup>15</sup> on the wave vector of the emitted radiation  $q(\mathbf{k})$  are much more significant in the denominator  $1 - \beta_i \mathbf{n}_i$  than in the numerator  $k - \beta_i \mathbf{k}$ , we approximate the last one as  $k - \beta_i \mathbf{k} \simeq k - \beta k_z$  where  $\beta = \beta \hat{\mathbf{z}}$  to simplify integration. Under the listed assumptions the integral in Eq. (4.43) can be analytically evaluated (in terms of the special functions) for the axially-symmetrical Gaussian laser pulse, *e.g.*  $\sigma_x = \sigma_y$ :

$$\begin{aligned}
I'_1(q_0) &= \int E_0 e^{-\frac{(k_x^2 + k_y^2)\sigma_x^2}{2} - \frac{(k_z + k_{las})^2\sigma_z^2}{2}} \delta(k - \beta k_z - k_0(q_0)) d^3\mathbf{k} \\
&= E_0 \int_0^{2\pi} \int_0^\pi \int_0^{+\infty} e^{-\frac{k^2\sigma_x^2\sin^2\theta}{2} - \frac{(k\cos\theta + k_{las})^2\sigma_z^2}{2}} \cdot \delta(k - \beta k\cos\theta - k_0) k^2 dk \sin\theta d\theta d\phi \\
&= \frac{2\pi E_0}{\beta} \int_\pi^0 \int_0^{+\infty} e^{-\frac{k^2\sin^2\theta\sigma_x^2}{2} - \frac{(k\cos\theta + k_{las})^2\sigma_z^2}{2}} \delta\left(\cos\theta - \frac{1 - k_0/k}{\beta}\right) k dk d\cos\theta \\
&= \frac{2\pi E_0}{\beta} \int_0^{+\infty} \int_{-1}^1 e^{-\frac{k^2(1-t^2)\sigma_x^2}{2} - \frac{(kt + k_{las})^2\sigma_z^2}{2}} \delta\left(t - \frac{1 - k_0/k}{\beta}\right) dt k dk \\
&\quad \left\{ \int_{x_1}^{x_2} \delta(x - a) f(x) = f(a), \forall a \in [x_1, x_2], \text{ otherwise } 0 \right\} \\
&\quad \left\{ \forall k_0 \geq 0, \frac{1 - k_0/k}{\beta} \in [-1; 1] \rightarrow k \in \left[\frac{k_0}{1 + \beta}; \frac{k_0}{1 - \beta}\right] \right\} \\
&= \frac{2\pi E_0}{\beta} \int_{\frac{k_0}{1 + \beta}}^{\frac{k_0}{1 - \beta}} e^{-\left(k^2 - \left(\frac{k - k_0}{\beta}\right)^2\right)\frac{\sigma_x^2}{2} - \left(\frac{k - k_0}{\beta} + k_{las}\right)^2\frac{\sigma_z^2}{2}} k dk \\
&= \frac{2\pi E_0}{\beta} \int_{k_1}^{k_2} e^{ak^2 + 2bk + c} k dk \quad ,
\end{aligned} \tag{4.48}$$

where the borders of integration are:

$$k_1 = \frac{k_0}{1 + \beta} \quad , \tag{4.49}$$

$$k_2 = \frac{k_0}{1 - \beta} \quad , \tag{4.50}$$

---

<sup>15</sup>Index  $i$  represents a specific electron in the bunch.

and the introduced coefficients of the integrand are defined as following:

$$a = \frac{\sigma_x^2(1 - \beta^2) - \sigma_z^2}{2\beta^2} , \quad (4.51)$$

$$b = \frac{k_0(\sigma_z^2 - \sigma_x^2)}{2\beta^2} - \frac{k_{las}\sigma_z^2}{2\beta} , \quad (4.52)$$

$$c = \frac{k_0\sigma_x^2}{2\beta^2} - \frac{\sigma_z^2(k_{las}\beta - k_0)^2}{2\beta^2} . \quad (4.53)$$

$$(4.54)$$

Depending on the sign of  $a$  the integral can be expressed in terms of the Gauss error functions:

Erf and Erfi. Thus, for the beam with  $\sigma_x > \gamma\sigma_z \rightarrow a > 0$  we find:

$$\begin{aligned} I_1'' &= \int_{k_1}^{k_2} e^{ak^2+2bk+c} k dk \\ &= \frac{e^{-\frac{b^2}{a}+c}}{2a^{3/2}} \left( \sqrt{a} \left( e^{\frac{(b+ak_2)^2}{a}} - e^{\frac{(b+ak_1)^2}{a}} \right) + \sqrt{\pi} \left( \operatorname{Erfi} \left( \frac{b+ak_1}{\sqrt{a}} \right) - \operatorname{Erfi} \left( \frac{b+ak_2}{\sqrt{a}} \right) \right) \right) . \end{aligned} \quad (4.55)$$

For the special case  $\sigma_x = \gamma\sigma_z$ , the answer can be found as a limit of the expression derived in Eq. (4.55) or by direct integration of the expression in Eq. (4.48) directly putting  $a = 0$ :

$$I_1'' = \left( \frac{-1 + 2bk_1}{4b^2} \right) e^{c+2bk_1} + \left( \frac{1 - 2bk_2}{4b^2} \right) e^{c+2bk_2} . \quad (4.56)$$

For  $\sigma_x < \gamma\sigma_z$  or  $a < 0$  the answer can be expressed in terms of Erf. By using the sifting property  $\text{Erfi}(ix) = i \text{Erf}(x)$  in Eq. (4.55), one can immediately find:

$$\begin{aligned}
 I_1'' &= \int_{k_1}^{k_2} e^{ak^2+2bk+c} k dk \\
 &= e^{-\frac{b^2}{a}+c} \left( \frac{\left( e^{\frac{(b+ak_2)^2}{a}} - e^{\frac{(b+ak_1)^2}{a}} \right)}{2a} + \frac{\sqrt{-ab}\sqrt{\pi}}{2a^2} \left( \text{Erf} \left( \frac{b+ak_1}{\sqrt{-a}} \right) - \text{Erf} \left( \frac{b+ak_2}{\sqrt{-a}} \right) \right) \right) .
 \end{aligned} \tag{4.57}$$

Using functions  $I_1(q_0)$  derived in Equations (4.55-4.57), one can find the corresponding longitudinal component of the Wigner function<sup>16</sup> by numerically integrating<sup>17</sup> the expression in Eq. (4.35). The obtained result strongly depends on the parameters of the laser pulse and can be classified into three separate regimes<sup>18</sup>.

For the weak focusing regime  $\sigma_x \geq \gamma\sigma_z$ , the numerically calculated Wigner function in the positive part of the spectrum ( $k_{w_z} > 0$ ) ideally matches with the Wigner function derived in the time-limited plane wave approximation as demonstrated in Fig. 4.1. It is convenient to work with dimensionless parameters. Parameters used in Fig. 4.1 and following figures in this section are normalized according to the equations:

$$W_n = \frac{W_z}{W_0 \alpha_s^2 E_0^2} , \tag{4.58}$$

$$r_n = (r - ct) k_{las} , \tag{4.59}$$

$$k_n = k_{w_z} / k_{las} , \tag{4.60}$$

$$\sigma_{x_n, z_n} = k_{las} \sigma_{x, z} . \tag{4.61}$$

---

<sup>16</sup>Further in this section we will simply refer this as a Wigner function, since the transverse behavior is straight-forward from the analytical expression of the corresponding part in Eq. (4.30).

<sup>17</sup>Several unsuccessful attempts to analytically evaluate the corresponding integral forced us to proceed with a numerical solution.

<sup>18</sup>Numerical integration is realized using Mathematica [31].

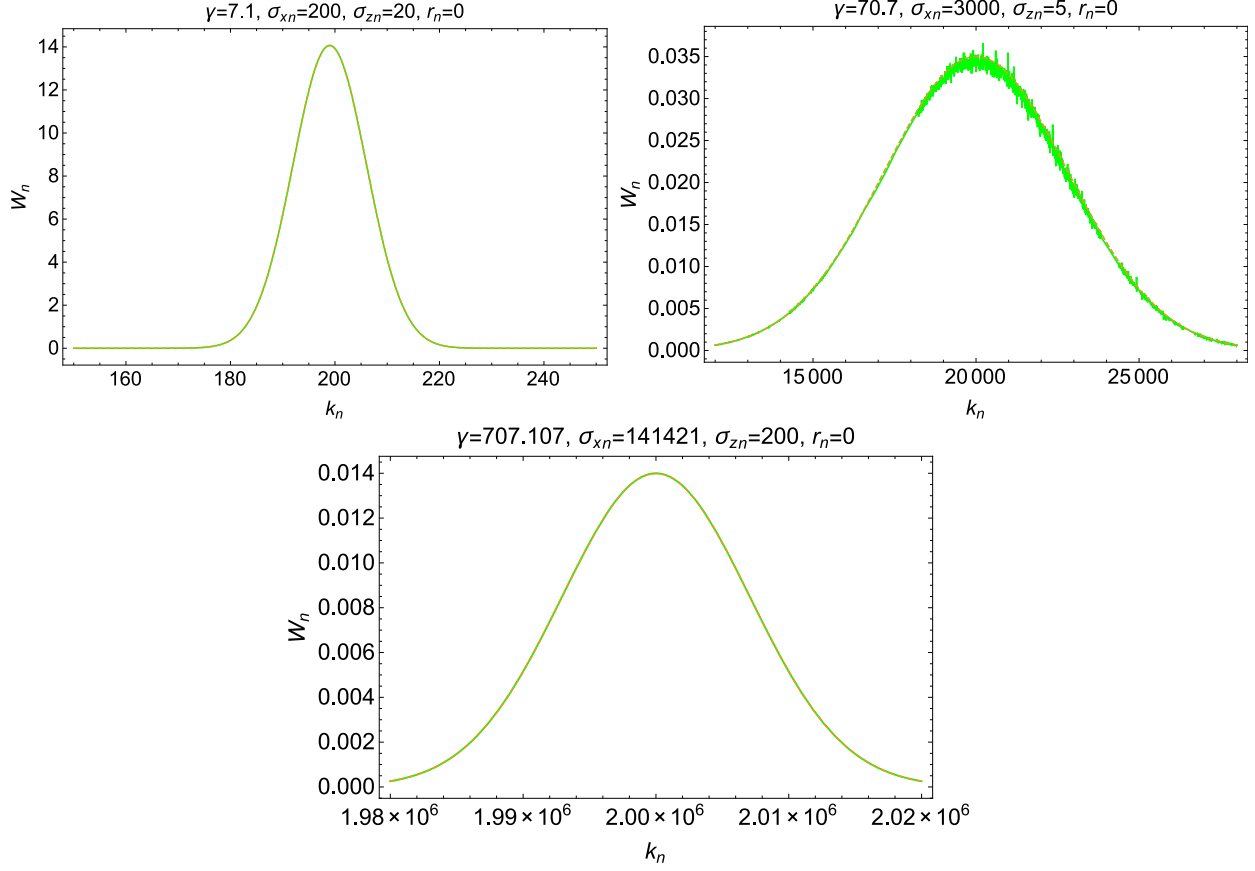


Figure 4.1: The numerically calculated Wigner function (solid-green) and its time-limited plane wave approximation (dashed-brown) at  $r_n = 0$ : for the weak focusing regime ( $\sigma_x > \gamma\sigma_z$ ) on the top and for the special case,  $\sigma_x = \gamma\sigma_z$ , on the bottom. The chosen values of the Lorentz factor ( $\gamma$ ) respectively correspond to the electron energies of 3.5 MeV, 35 MeV and 350 MeV.

Normalized sizes  $\sigma_{x_n}$  and  $\sigma_{z_n}$  represent a number of transverse and longitudinal oscillations in the incoming laser pulse. Interestingly, looking on the left part of the spectrum one can notice that the Wigner function becomes negative with an absolute minimum at  $k_n = -1$  or  $k_{w_z} = -k_{las}$  (Fig. 4.2). Such a behavior of the derived Wigner function mathematically demonstrates the “nature” of the ICS process during which the small part ( $\sim \alpha_s^2 \ll 1$ ) of photons of the laser pulse are scattered back on the up-shifted frequency by the electron. The frequency of the emitted radiation becomes larger for a faster traveling electron (Fig. 4.2). A negative part of the Wigner function is similar for different electron velocities  $\beta c$  due

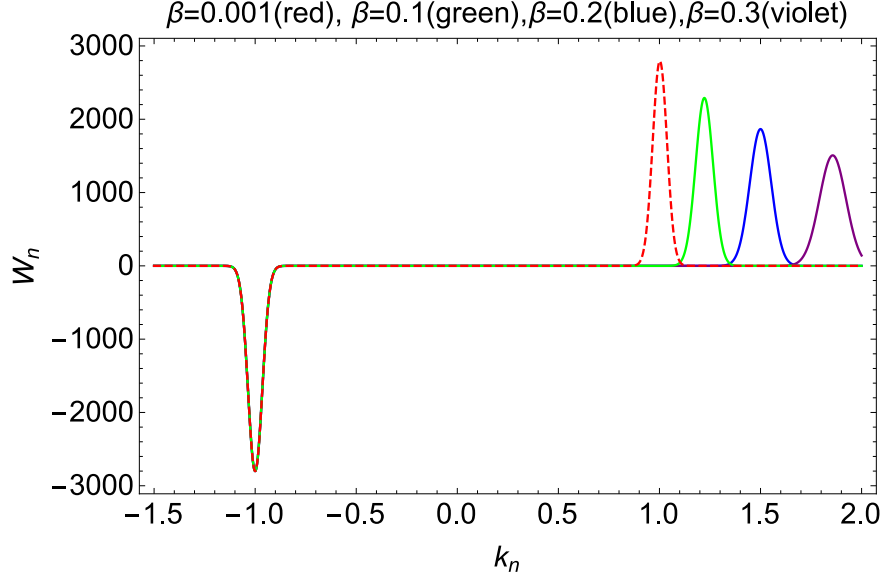


Figure 4.2: The numerically calculated Wigner function at  $r_n = 0$  in the weak focusing regime ( $\sigma_{x_n} = 200$  and  $\sigma_{x_z} = 20$ ) for different electron velocities  $\beta c$  represented by distinct colors.

to normalization<sup>19</sup> introduced in Eq. (4.58). The Wigner function characterizes photon distribution in 6-dimensional phase space. Yet, the negative behavior of the derived Wigner function should not be confusing. If one evaluates the Wigner function of total field, the superposition of radiation field and field of the laser, then the negative part of the Wigner function in the nearby region of  $k_{wz} \sim -k_{las}$  will sum with the positive Wigner function corresponding to the incoming laser pulse<sup>20</sup> resulting in the overall positive Wigner function  $\sim (1 - \alpha_s^2)$ . The absolute maximum of the negative and positive parts of the spectrum is reached at the same space-time interval quantity:  $r - ct = 0$ . This demonstrates the causality in respect to an observer. Indeed, the observer with an appropriate measurement device will detect the emitted radiation and the information about changes in the laser pulse at the same time. If one consider using the negative part of the Wigner function derived here to estimate the total loss of the incoming photons during scattering, he has to integrate

<sup>19</sup>The longitudinal part of the Wigner function depends on the electron energy through  $\alpha_s \sim 1/\gamma^5$ .

<sup>20</sup>The laser pulse travels in the opposite direction to the  $z$ -axis, which explains the negative sign of a  $k$ -vector.

the derived Wigner function for all possible observer locations within the solid angle  $\sim \frac{1}{\gamma^2}$  centered along the  $z$ -axis.

If laser pulse is focused tighter:  $\sigma_x < \sigma_z/\sqrt{1+\beta}$ , which we refer here as the extreme focusing regime, the radiation spectrum becomes “blue-shifted” in respect with the result predicted by the time-limited plane wave approximation (Fig. 4.3). Focusing the laser pulse more causes larger up-shift of the spectrum and eventually leads to the unsymmetrical shape of the Wigner function in  $k$ -space. This result might be of the special interest for those who consider running an ICS source in such a regime. Interestingly, Figure 4.3 justifies that the time-limited approximation is legitimate for the special case of the strongly focused laser pulse:  $\sigma_x = \sigma_z/\sqrt{1+\beta}$ .

In the regime of a moderately focused laser pulse,  $\sigma_z/\sqrt{1+\beta} < \sigma_x < \gamma\sigma_z$ , the numerically evaluated Wigner function demonstrates a “red shift” in respect with the result derived in the time-limited plane-wave approximation for the laser pulse (Fig. 4.4). We were not able to clarify where exactly in this regime the time-limited approximation stops working and how this point depends on the electron energy and parameters of the laser pulse. This is because the numerical routine realized in Mathematica has troubles evaluating the integral for the fast oscillating functions in the integrand when  $\sigma_x \sim \gamma\sigma_z$  or  $\sigma_z/\sqrt{1+\beta} < \sigma_x < \gamma\sigma_z$ . In particular, an estimated error exceeds the result. We are convinced, this is associated with a lack of proper treatment for integration of such a function. Analyzing behavior of the Wigner function and legitimacy of the time-limited plane-wave approximation in this regime requires further analytical and numerical investigation. At this point we can guarantee a proper work of the time-limited plane-wave approximation if  $\sigma_x \geq \gamma\sigma_z$  or  $\sigma_x = \sigma_z/\sqrt{1+\beta}$ . Assuming one of these conditions is satisfied, we use the analytical solution for the single-electron Wigner function in Eq. (4.19) in the next section in order to find the corresponding Wigner function of total radiation emitted by the electron bunch.

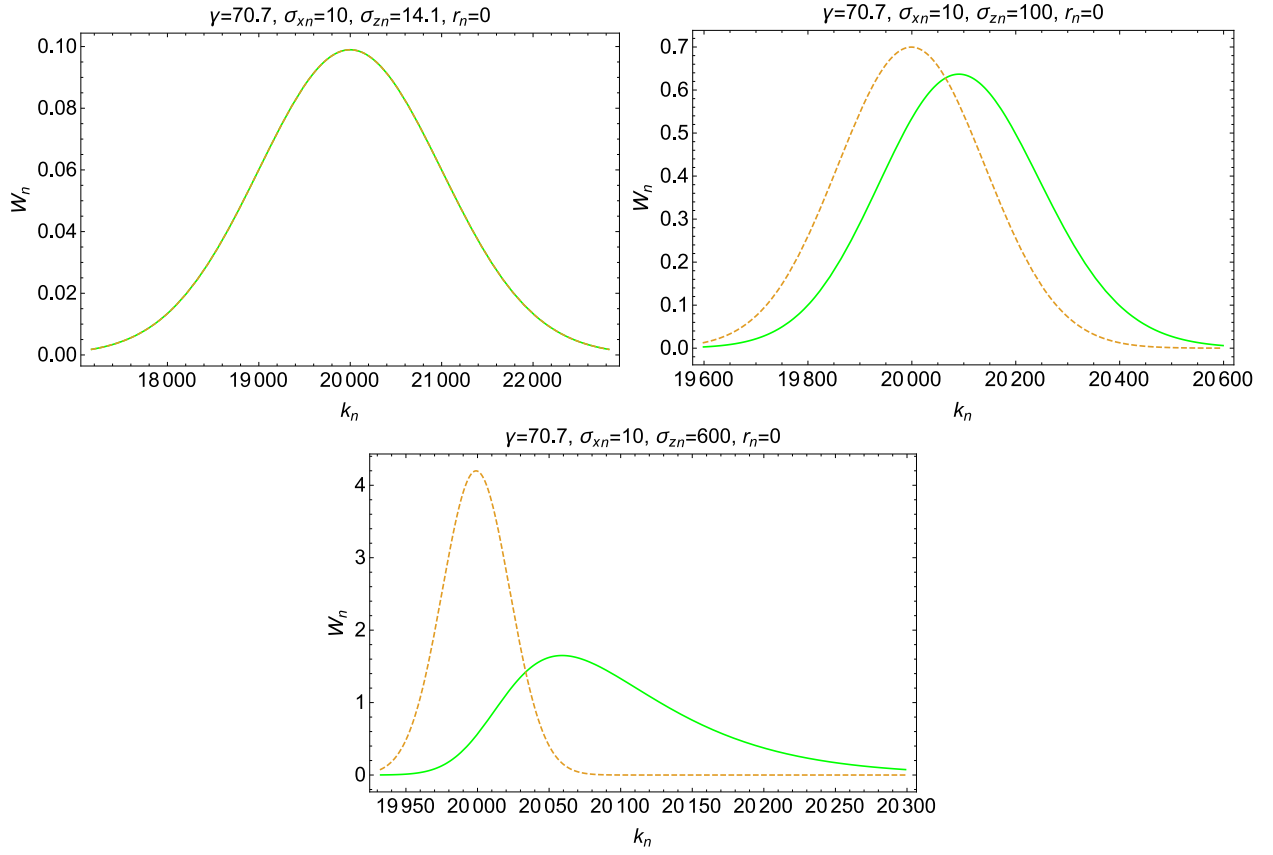


Figure 4.3: The numerically calculated Wigner function (solid-green) versus its time-limited plane-wave approximation (dashed-brown) in the extreme focusing regime for different parameters of the laser pulse.

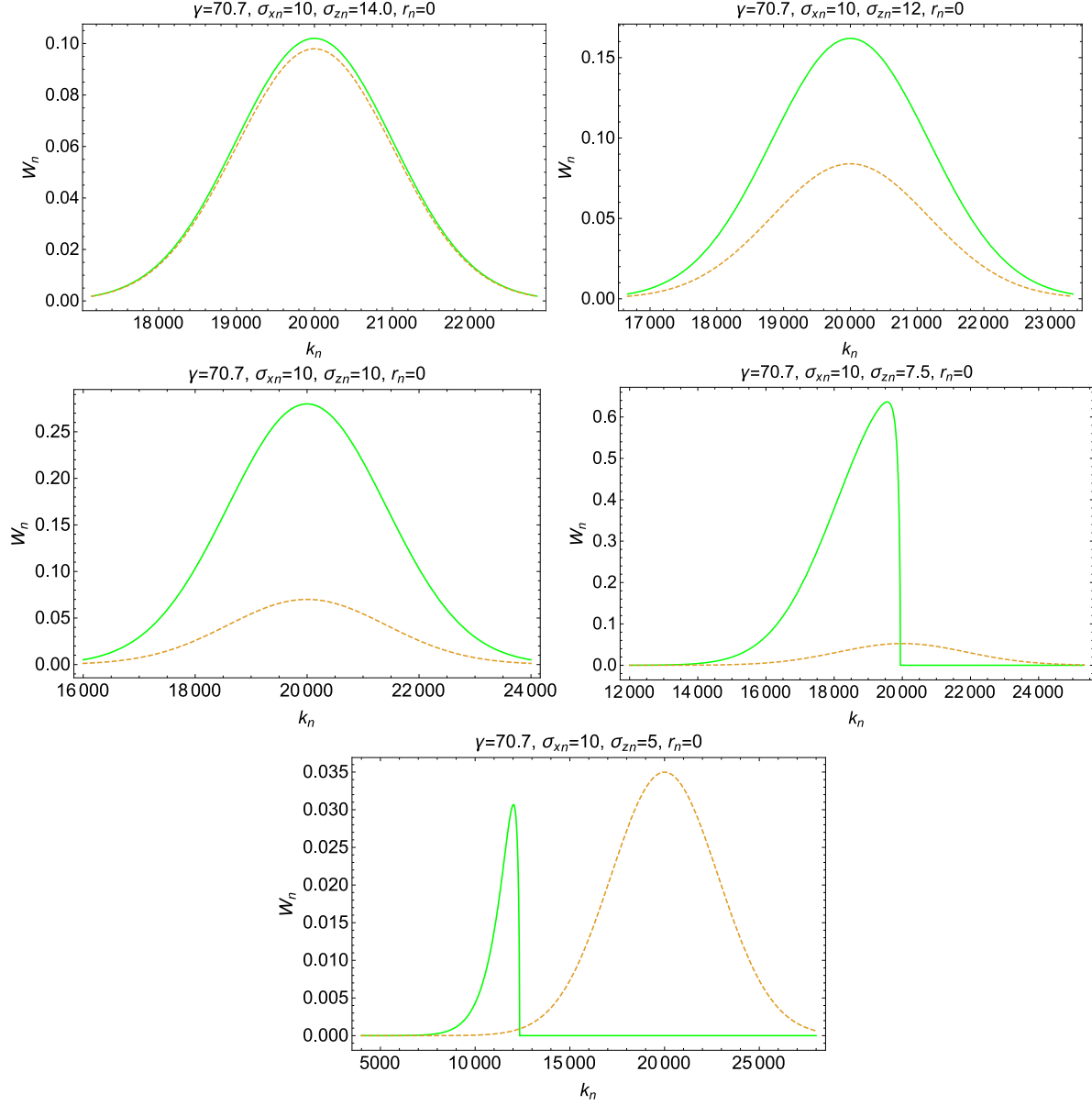


Figure 4.4: The numerically calculated normalized Wigner function (solid-green) versus its time-limited plane-wave approximation (dashed-brown) in the moderate focusing regime for different parameters of the laser pulse.

## 4.6 The Wigner function of radiation emitted by the electron bunch

The time-limited plane-wave approximation for the incoming laser pulse derived in Section 4.3.2 is legitimate if  $\sigma_x \geq \gamma\sigma_z$  as was justified in the previous section. The corresponding single-electron Wigner function in Eq. (4.19) can be rewritten as following:

$$W_{1e} = W_1 \cdot \delta\left(\frac{n_x}{n_z}k_{wz} - k_{wx}\right) \delta\left(\frac{n_y}{n_z}k_{wz} - k_{wy}\right) e^{-\left(\frac{r-ct}{\sigma_{rad}}\right)^2} e^{-\left(\frac{k_{wz}/n_z - k_{rad}}{\sigma_{k_{rad}}}\right)^2}, \quad (4.62)$$

where  $k_{rad} = \frac{k_{zlas}(1+\beta_z)}{1-\beta_n}$ ,  $\sigma_{rad} = \frac{\sigma_z(1-\beta_n)}{(1+\beta_z)}$ ,  $\sigma_{k_{rad}} = \frac{1}{\sigma_{rad}}$ , and  $W_1 = 8\pi^{5/2}\alpha_s^2 E_0^2 \frac{\sigma_{rad}}{n_z} W_0$ . First, we emphasize that  $\mathbf{n} = \frac{\mathbf{r}-\mathbf{r}_e}{|\mathbf{r}-\mathbf{r}_e|}$  and  $\beta = \frac{v_e}{c}$  depend on the initial electron coordinates ( $\mathbf{r}_e$ ) and velocities ( $\mathbf{v}_e$ ) in the moment of interaction with a laser pulse. Consequently, each electron in the bunch generates unique radiation characterized by the corresponding SWF. For the finite amount of randomly distributed electrons in the bunch the total Wigner function (TWF) can be found as a direct sum of SWFs from each electron. Since an electron bunch can be approximated with a continuous distribution function as discussed in Chapter 1, the TWF can be found in the form of the convolution theorem<sup>21</sup>.

*The convolution theorem.* Under an assumption that electrons in a bunch emit incoherent radiation, the total Wigner function of radiation generated by this electron bunch can be found as the convolution of the single-electron Wigner function with the distribution function in 6D phase space ( $f(\zeta_e)$ ):

$$W_{beam} = \int W_{1e}(\zeta_e, \zeta_{ph}) f(\zeta_e) d^6 \zeta_e, \quad (4.63)$$

---

<sup>21</sup>The theorem is presented here without proof.

where the electron distribution function is normalized according to:

$$\int f(\zeta_e) d^6 \zeta_e = 1 \quad . \quad (4.64)$$

Typical electron bunches in accelerators are much smaller than characteristic scales of electromagnetic fields. That allows using linear approximation of fields resulting in matrix formalism for electron dynamics in phase space, while the electron distribution function can be approximated as a 6D Gauss (see Chapter 1 for more details):

$$f(\zeta_e) = \sqrt{\pi}^{-6} \sqrt{\det[\Sigma^{-1}]} e^{-\zeta_e^T \Sigma^{-1} \zeta_e} \quad , \quad (4.65)$$

where  $\Sigma$ -matrix is a 6-dimensional matrix of second order momenta:  $\Sigma_{ij} = \langle \zeta_e^{(i)} \zeta_e^{(j)} \rangle$  in Eq. (1.42).

Fortunately, the expression in Eq. (4.62) can be presented in the similar matrix-form as of the electron distribution function. First, each delta-function must be expressed using its definition presented in Eq. (4.66). Second, 6-dimensional photon and electron coordinates are considered in respect with a corresponding reference particle, in such a way that reference photon is emitted by reference electron. Third, photon phase-space distribution is back-propagated in free space from the observer location to the source, *e.g.* the location of interaction of the electron bunch and the laser pulse. Finally, each bi-quadratic form of the obtained functions is represented as a matrix multiplication. The following procedure is described in great detail in the next subsection.

### 4.6.1 Representing single-electron Wigner function in 6D form

One can represent each  $\delta$ -function in Eq. (4.62) in the form of exponential function using Eq. (4.66):

$$\delta(x) = \lim_{\delta_x \rightarrow 0} \left\{ \frac{1}{\sqrt{\pi}\delta_x} e^{-\left(\frac{x}{\delta_x}\right)^2} \right\} . \quad (4.66)$$

This allows to find SWF in an exponential form:

$$W_{1e} = \frac{W_1}{\pi\delta_x\delta_y} e^{-\left(\frac{\frac{n_x}{n_z}kw_z - kw_x}{\delta_x}\right)^2} e^{-\left(\frac{\frac{n_y}{n_z}kw_z - kw_y}{\delta_y}\right)^2} e^{-\left(\frac{r-ct}{\sigma_{rad}}\right)^2} e^{-\left(\frac{kw_z/n_z - k_{rad}}{\sigma_{k_{rad}}}\right)^2} . \quad (4.67)$$

Different electrons emit distinct photons arriving at the observer location at particular time from the certain angle. Since time ( $t$ ) was chosen as an evolution variable for photon phase space, one has to consider a finite size of a detector at the observer location, *e.g.* photons emitted by different electrons arrive in distinct points:  $\mathbf{r} = \mathbf{r}_0 + \Delta\mathbf{r}$ . Reference electron located at the origin of the coordinate system at  $t = 0$  emits reference photon. Such a photon traveling with a speed of light arrives at the observer location ( $\mathbf{r}_0$ ) at  $t = \sqrt{x_0^2 + y_0^2 + z_0^2}/c$ . One can rewrite the space-time interval in the following form:

$$r - ct = \sqrt{(x_0 + \Delta x - x_e)^2 + (y_0 + \Delta y - y_e)^2 + (z_0 + \Delta z - z_e)^2} - c\sqrt{x_0^2 + y_0^2 + z_0^2} , \quad (4.68)$$

where  $\mathbf{r}_e$  defines the electron position at the moment of interaction with a laser pulse ( $t = 0$ ) in respect with the test electron and  $\Delta\mathbf{r}$  defines the photon location emitted by this electron in respect with the reference photon. By keeping only linear terms of the Taylor's series expansion, one can immediately find:

$$r - ct = n_{x_0}(\Delta x - x_e) + n_{y_0}(\Delta y - y_e) + n_{z_0}(\Delta z - z_e) , \quad (4.69)$$

where

$$n_{x_0} = \frac{x_0}{\sqrt{x_0^2 + y_0^2 + z_0^2}} \quad (4.70)$$

$$n_{y_0} = \frac{y_0}{\sqrt{x_0^2 + y_0^2 + z_0^2}} \quad (4.71)$$

$$n_{z_0} = \frac{z_0}{\sqrt{x_0^2 + y_0^2 + z_0^2}} \quad (4.72)$$

These results were derived in the approximation that coordinates of both phase spaces are of the same order, and  $|\mathbf{r}_e|, |\Delta \mathbf{r}| \ll z_0$ . The additional condition,  $|x_e|, |\Delta x| \ll |x_0|$ , must be satisfied if the observer is located off-axis ( $x_0 \neq 0$ ) resulting in that second-order terms are smaller than first order terms and can be neglected. Those are legitimate assumptions in the far-field approximation. For the  $k_x$ -component of SWF, we find:

$$\frac{n_x}{n_z} k_{w_z} - k_{w_x} = \frac{x_0 + \Delta x - x_e}{z_0 + \Delta z - z_e} (k_{w_{z_0}} + \Delta k_{w_z}) - (k_{w_{x_0}} + \Delta k_{w_x}) \quad , \quad (4.73)$$

where  $k_{w_{x_0}}$  and  $k_{w_{z_0}}$  are  $x$ - and  $z$ -component of the wave-vector of reference photon which related to components of  $\mathbf{n}$  according to:

$$\frac{k_{w_{x_0}}}{k_{w_{z_0}}} = \frac{n_{x_0}}{n_{z_0}} = \frac{x_0}{z_0} \quad . \quad (4.74)$$

After linearization one can find:

$$\frac{n_x}{n_z} k_{w_z} - k_{w_x} = \frac{k_{w_{z_0}}}{z_0} (\Delta x - x_e) - \frac{k_{w_{z_0}}}{z_0} \frac{x_0}{z_0} (\Delta z - z_e) - \Delta k_{w_x} + \frac{x_0}{z_0} \Delta k_{w_z} \quad , \quad (4.75)$$

which can be rewritten in a different form:

$$\frac{n_x}{n_z} k_{w_z} - k_{w_x} = \frac{k_{w_{z_0}}}{z_0} \left[ \left( \left( \Delta x - z_0 \frac{\Delta k_{w_x}}{k_{w_{z_0}}} \right) - x_e \right) - \frac{n_{x_0}}{n_{z_0}} \left( \left( \Delta z - z_0 \frac{\Delta k_{w_z}}{k_{w_{z_0}}} \right) - z_e \right) \right] \quad . \quad (4.76)$$

Similarly,  $k_y$ -component of SWF becomes:

$$\frac{n_y}{n_z} k_{w_z} - k_{w_y} = \frac{k_{w_{z_0}}}{z_0} \left[ \left( \left( \Delta y - z_0 \frac{\Delta k_{w_y}}{k_{w_{z_0}}} \right) - y_e \right) - \frac{n_{y_0}}{n_{z_0}} \left( \left( \Delta z - z_0 \frac{\Delta k_{w_z}}{k_{w_{z_0}}} \right) - z_e \right) \right] \quad (4.77)$$

The expression for  $k_z$ -component of SWF is more complicated:

$$\begin{aligned} k_{w_z}/n_z - k_{rad} &= \frac{k_{w_{z_0}}}{z_0 (1 - \mathbf{n}_0 \beta_0)} \cdot \\ &\cdot [(n_{x_0} - \beta_{x_0}) (\Delta x - x_e) + (n_{y_0} - \beta_{y_0}) (\Delta y - y_e) + \left( n_{z_0} - \beta_{z_0} - \frac{1 - \mathbf{n}_0 \beta_0}{n_{z_0}} \right) (\Delta z - z_e) \\ &- z_0 \left( \frac{n_{x_0}}{n_{z_0}} \Delta \beta_x + \frac{n_{y_0}}{n_{y_0}} \Delta \beta_y + \frac{n_{z_0}}{n_{z_0}} \Delta \beta_z \right)] + \frac{\Delta k_{w_z}}{n_{z_0}} \quad (4.78) \end{aligned}$$

Arguments of the exponential functions in Equations (4.69, 4.76-4.78) are of the same kind,  $\zeta_{ph} - \zeta_e$ . However some of the vector components are missing, for instance, terms  $\Delta k_{w_x}$  and  $\Delta k_{w_y}$  in (4.78). This is because these photon phase-space coordinates describe radiation at the observer location, rather than at the source. The causality suggests to look for an answer in the form of  $\zeta_{ph}^i - \zeta_e$ , where  $\zeta_{ph}^{(i)} = D^{-1} \zeta_{ph}^{(f)}$  is 6D vector of photon phase space at the source, and  $D^{-1}$  is the matrix of back-propagation in free space such that  $D^{-1}[z_0] = D[-z_0]$ . Absence of electron momentums in Equations (4.76 and 4.77) confirms this idea.

The symplectic matrix of photon propagation in free space can be reconstructed from the corresponding components of SWF<sup>22</sup>:

$$D[-z_0] = \begin{pmatrix} 1 & -(1 - n_{x_0}^2) z_0 & 0 & n_{x_0} n_{y_0} z_0 & 0 & n_{x_0} n_{z_0} z_0 \\ 0 & 1 & 0 & 0 & 0 & 0 \\ 0 & n_{x_0} n_{y_0} z_0 & 1 & -(1 - n_{y_0}^2) z_0 & 0 & n_{y_0} n_{z_0} z_0 \\ 0 & 0 & 0 & 1 & 0 & 0 \\ 0 & n_{x_0} n_{z_0} z_0 & 1 & n_{y_0} n_{z_0} z_0 & 1 & -(1 - n_{y_0}^2) z_0 \\ 0 & 0 & 0 & 0 & 0 & 1 \end{pmatrix} \quad (4.79)$$

The nonzero terms off the main-diagonal blocks appear due to the choice of the coordinate system and disappear, if an observer is located on the  $z$ -axis resulting in  $n_{x_0} = n_{y_0} = 0$ . The space-time interval in Eq. (4.69) is invariant under direct/inverse free-space propagation of any length:

$$\begin{aligned} n_{x_0} \Delta x' + n_{y_0} \Delta y' + n_{z_0} \Delta z' &= \\ &= n_{x_0} \left( \Delta x - (1 - n_{x_0}^2) z_0 \frac{\Delta k_{wx}}{k_{wz_0}} + n_{x_0} n_{y_0} z_0 \frac{\Delta k_{wy}}{k_{wz_0}} + n_{x_0} n_{z_0} z_0 \frac{\Delta k_{wz}}{k_{wz_0}} \right) + \\ &+ n_{y_0} \left( \Delta y + n_{x_0} n_{y_0} z_0 \frac{\Delta k_{wx}}{k_{wz_0}} - (1 - n_{y_0}^2) z_0 \frac{\Delta k_{wy}}{k_{wz_0}} + n_{y_0} n_{z_0} z_0 \frac{\Delta k_{wz}}{k_{wz_0}} \right) + \\ &+ n_{z_0} \left( \Delta z + n_{x_0} n_{z_0} z_0 \frac{\Delta k_{wx}}{k_{wz_0}} + n_{y_0} n_{z_0} z_0 \frac{\Delta k_{wy}}{k_{wz_0}} - (1 - n_{z_0}^2) z_0 \frac{\Delta k_{wz}}{k_{wz_0}} \right) = \\ &= n_{x_0} \Delta x + n_{y_0} \Delta y + n_{z_0} \Delta z \quad , \end{aligned} \quad (4.80)$$

where:

$$\left[ -n_{x_0} (1 - n_{x_0}^2) + n_{x_0} n_{y_0}^2 + n_{x_0} n_{z_0}^2 \right] z_0 \frac{\Delta k_{wx}}{k_{wz_0}} = 0 \quad , \quad (4.81)$$

---

<sup>22</sup>Same matrix can be directly derived from the linearization of the Hamiltonian dynamics of a photon in free space.

and coefficients in front of  $\frac{\Delta k_{wy}}{k_{wz_0}}$  and  $\frac{\Delta k_{wz}}{k_{wz_0}}$  disappear. Finally, one can rewrite the expression in Eq. (4.78) in terms of photon phase space at the source using matrix in Eq. (4.79):

$$\begin{aligned}
k_{wz}/n_z - k_{rad} &= \frac{k_{wz_0}}{z_0 (1 - \mathbf{n}_0 \boldsymbol{\beta}_0)} \cdot \\
&\cdot \left[ (n_{x_0} - \beta_{x_0}) (\Delta x^i - x_e) + (n_{y_0} - \beta_{y_0}) (\Delta y^i - y_e) + (n_{z_0} - \beta_{z_0}) (\Delta z^i - z_e) \right] + \\
&+ \frac{k_{wz_0}}{(1 - \mathbf{n}_0 \boldsymbol{\beta}_0)} \left[ \left( (n_{x_0} - \beta_{x_0}) \frac{\Delta k_{wx}}{k_{wz_0}} - \frac{n_{x_0}}{n_{z_0}} \Delta \beta_x \right) + \left( (n_{y_0} - \beta_{y_0}) \frac{\Delta k_{wy}}{k_{wz_0}} - \frac{n_{y_0}}{n_{z_0}} \Delta \beta_y \right) \right. \\
&\left. + \left( (n_{z_0} - \beta_{z_0}) \frac{\Delta k_{wz}}{k_{wz_0}} - \frac{n_{z_0}}{n_{z_0}} \Delta \beta_z \right) \right] . \tag{4.82}
\end{aligned}$$

Derived coefficients between photon and electron momenta are different. For a reference electron propagating along the  $z$ -axis ( $\beta_{x_0} = \beta_{y_0} = 0$ ) the multipliers in front of corresponding transverse momenta are the same, while the coefficients in front of longitudinal momenta are of the different order. This is because the frequency of the emitted radiation quadratically depends on the electron Lorentz factor. Each bi-quadratic form of the SWF components can be presented in a matrix form:

$$(a_1 x_1 + a_2 x_2 + \dots + a_n x_n)^2 = \mathbf{X}^T M_A \mathbf{X} \quad , \tag{4.83}$$

where  $\mathbf{X}^T = \{x_1, x_2, \dots, x_n\}$ ,  $\mathbf{A}^T = \{a_1, a_2, \dots, a_n\}$  and  $M_A = \mathbf{A} \mathbf{A}^T$ , while  $\det[A] = 0$ . Using this representation, we can rewrite each exponential function in a matrix form. Using Eq. (4.69) and Eq. (4.80), the space-time term becomes:

$$\frac{(r - ct)^2}{\sigma_{rad}^2} = (\zeta_{ph}^i - \zeta_e)^T M_t (\zeta_{ph}^i - \zeta_e) \quad , \tag{4.84}$$

where

$$M_t = \frac{1}{\sigma_{rad}^2} \begin{pmatrix} n_{x_0}^2 & 0 & n_{x_0}n_{y_0} & 0 & n_{x_0}n_{z_0} & 0 \\ 0 & 0 & 0 & 0 & 0 & 0 \\ n_{x_0}n_{y_0} & 0 & n_{y_0}^2 & 0 & n_{y_0}n_{z_0} & 0 \\ 0 & 0 & 0 & 0 & 0 & 0 \\ n_{x_0}n_{z_0} & 0 & n_{y_0}n_{z_0} & 0 & n_{z_0}^2 & 0 \\ 0 & 0 & 0 & 0 & 0 & 0 \end{pmatrix}. \quad (4.85)$$

Using (4.76), one can find for the  $k_x$ -interval:

$$\left( \frac{\frac{n_x}{n_z} k_{wz} - k_{wx}}{\delta_x} \right)^2 = (\zeta_{ph}^i - \zeta_e)^T M_x (\zeta_{ph}^i - \zeta_e) \quad , \quad (4.86)$$

where

$$M_x = \frac{k_{wz_0}^2}{\delta_x^2 z_0^2} \begin{pmatrix} 1 & 0 & 0 & 0 & \frac{n_{x0}}{n_{z0}} & 0 \\ 0 & 0 & 0 & 0 & 0 & 0 \\ 0 & 0 & 0 & 0 & 0 & 0 \\ 0 & 0 & 0 & 0 & 0 & 0 \\ \frac{n_{x0}}{n_{z0}} & 0 & 0 & 0 & \frac{n_{x0}^2}{n_{z0}^2} & 0 \\ 0 & 0 & 0 & 0 & 0 & 0 \end{pmatrix}. \quad (4.87)$$

Using Eq.(4.77), one can find the corresponding  $k_y$ -matrix:

$$M_y = \frac{k_{wz_0}^2}{\delta_y^2 z_0^2} \begin{pmatrix} 0 & 0 & 0 & 0 & 0 & 0 \\ 0 & 0 & 0 & 0 & 0 & 0 \\ 0 & 0 & 1 & 0 & \frac{n_{y0}}{n_{z0}} & 0 \\ 0 & 0 & 0 & 0 & 0 & 0 \\ 0 & 0 & \frac{n_{y0}}{n_{z0}} & 0 & \frac{n_{y0}^2}{n_{z0}^2} & 0 \\ 0 & 0 & 0 & 0 & 0 & 0 \end{pmatrix}. \quad (4.88)$$

Due to mismatching coefficients between photon and electron phase space, we introduce an effective coordinate system for electrons such that  $\zeta'_e = \Omega \zeta_e$ , where the transformation matrix is:

$$\Omega = \begin{pmatrix} 1 & 0 & 0 & 0 & 0 & 0 \\ 0 & \frac{n_{x0}}{n_{z0}(n_{x0}-\beta_{x0})} & 0 & 0 & 0 & 0 \\ 0 & 0 & 1 & 0 & 0 & 0 \\ 0 & 0 & 0 & \frac{n_{y0}}{n_{z0}(n_{y0}-\beta_{y0})} & 0 & 0 \\ 0 & 0 & 0 & 0 & 1 & 0 \\ 0 & 0 & 0 & 0 & 0 & \frac{n_{z0}}{n_{z0}(n_{z0}-\beta_{z0})} \end{pmatrix}. \quad (4.89)$$

Using Eq. (4.82), we find for  $k_z$ -term:

$$\left( \frac{k_{wz}/n_z - k_{rad}}{\sigma_{k_{rad}}} \right)^2 = (\zeta_{ph}^i - \zeta_e')^T M_\omega (\zeta_{ph}^i - \zeta_e') \quad , \quad (4.90)$$

where:

$$M_\omega = \left( \frac{k_{wz_0}}{z_0(1 - \mathbf{n}_0 \beta_0)} \right)^2 \mathbf{A}_\omega \mathbf{A}_\omega^T \quad , \quad (4.91)$$

$$\mathbf{A}_\omega = \begin{pmatrix} n_{x0} - \beta_{x0} \\ z_0(n_{x0} - \beta_{x0}) \\ n_{y0} - \beta_{y0} \\ z_0(n_{y0} - \beta_{y0}) \\ n_{z0} - \beta_{z0} \\ z_0(n_{z0} - \beta_{z0}) \end{pmatrix}. \quad (4.92)$$

All of the exponential functions can be combined together because matrices  $M_t$ ,  $M_x$ , and  $M_y$  are invariant under the introduced coordinate transformation described by  $\Omega$ -matrix. Thus, the single-electron Wigner function can be represented in a matrix form:

$$W_{1e} = \lim_{\delta_x, \delta_y \rightarrow 0} \left\{ \frac{W_1}{\pi \delta_x \delta_y} e^{-(\zeta_{ph}^i - \zeta_e^i)^T M_0 (\zeta_{ph}^i - \zeta_e^i)} \right\} , \quad (4.93)$$

where  $M_0 = M_t + M_x + M_y + M_\omega$ .

#### 4.6.2 Convolution of the single-electron Wigner function with an arbitrary electron distribution in 6D phase space

The Wigner function of radiation emitted by the electron bunch can be immediately found in the integral form by directly putting the matrix form of SWF in Eq. (4.93) in the convolution theorem in Eq. (4.63):

$$\begin{aligned} W_{beam} &= (\sqrt{\pi})^{-6} \sqrt{\det[\Sigma^{-1}]} \int W_{1e}(\zeta_e, \zeta_{ph}) e^{-\zeta_e^T \Sigma^{-1} \zeta_e} d^6 \zeta_e , \\ &= W_1 \frac{1}{\sqrt{\pi} \delta_x} \frac{1}{\sqrt{\pi} \delta_y} (\sqrt{\pi})^{-6} \sqrt{\det[\Sigma^{-1}]} \int e^{-(\zeta_{ph}^{(i)} - \zeta_e)^T M_0 (\zeta_{ph}^{(i)} - \zeta_e)} e^{-\zeta_e^T \Sigma^{-1} \zeta_e} d^6 \zeta_e . \end{aligned} \quad (4.94)$$

If the integrand can be represented in the following form:

$$e^{-(\zeta - \zeta_e)^T M (\zeta - \zeta_e) - X [M_0, \Sigma^{-1}, \zeta_{ph}^{(i)}]} , \quad (4.95)$$

the integral in Eq. (4.94) can be evaluated in a matrix form:

$$\int \dots = e^{-X [M_0, \Sigma^{-1}, \zeta_{ph}^{(i)}]} \int e^{-(\zeta_e - \zeta)^T M (\zeta_e - \zeta)} d^6 (\zeta_e - \zeta) = e^{-X [M_0, \Sigma^{-1}, \zeta_{ph}^{(i)}]} \frac{(\sqrt{\pi})^6}{\sqrt{\det[M]}} , \quad (4.96)$$

where  $\det[M] > 0$  is the condition required for convergence. One can immediately find the corresponding Wigner function:

$$W_{beam} = W_1 \frac{1}{\sqrt{\pi}\delta_x} \frac{1}{\sqrt{\pi}\delta_y} \frac{\sqrt{\det[\Sigma^{-1}]}}{\sqrt{\det[M]}} e^{-X[M_0, \Sigma^{-1}, \zeta_{ph}^{(i)}]} \quad (4.97)$$

Now, we only need to find  $X[M_0, \Sigma^{-1}, \zeta_{ph}^{(i)}]$  and  $\zeta[M_0, \Sigma^{-1}, \zeta_{ph}^{(i)}]$  to satisfy the assumption in Eq. (4.95), which is valid if the following is satisfied:

$$(\zeta_{ph}^{(i)} - \zeta_e)^T M_0 (\zeta_{ph}^{(i)} - \zeta_e) + \zeta_e^T \Sigma^{-1} \zeta_e = (\zeta - \zeta_e)^T M (\zeta - \zeta_e) - X \quad . \quad (4.98)$$

Since  $X$  and  $\zeta_{ph}^{(i)}$  are independent from  $\zeta_e$ , one can rewrite the condition in Eq. (4.98) as four independent equations:

$$\zeta_e^T M \zeta_e = M_0 \zeta_e + \zeta_e^T \Sigma^{-1} \zeta_e \quad , \quad (4.99)$$

$$\zeta_e^T M_0 \zeta_{ph}^{(i)} = \zeta_e^T M \zeta \quad , \quad (4.100)$$

$$(\zeta_{ph}^{(i)})^T M_0 \zeta_e = \zeta^T M \zeta_e \quad , \quad (4.101)$$

$$(\zeta_{ph}^{(i)})^T M_0 \zeta_{ph}^{(i)} = \zeta^T M \zeta + X \quad . \quad (4.102)$$

Equation (4.99) should be valid for  $\forall \zeta_e$ , consequently:

$$\zeta_e^T (M_0 + \Sigma^{-1} - M) \zeta_e = 0, \quad , \quad (4.103)$$

and one can immediately find the condition on  $M$ -matrix:

$$M = M_0 + \Sigma^{-1} \quad . \quad (4.104)$$

If matrix  $M^{-1}$  exists, which forces the condition  $\det[M] \neq 0$ , one can obtain from Equations (4.99 and 4.99):

$$\zeta = M^{-1}M_0\zeta_{ph}^{(i)} \quad . \quad (4.105)$$

Putting this result in Eq. (4.99), one can find  $X$ :

$$\begin{aligned} X &= (\zeta_{ph}^{(i)})^T M_0 \zeta_{ph}^{(i)} - \zeta^T M \zeta \\ &= (\zeta_{ph}^{(i)})^T M_0 \zeta_{ph}^{(i)} - (\zeta_{ph}^{(i)})^T M_0 (M^{-1} M M^{-1}) M_0 \zeta_{ph}^{(i)} \\ &= (\zeta_{ph}^{(i)})^T (M_0 - M_0 M^{-1} M_0) \zeta_{ph}^{(i)} \quad , \end{aligned} \quad (4.106)$$

which justifies the assumption made in Eq. (4.95). Correspondingly, the total Wigner function becomes:

$$W_{beam} = W_1 \cdot \lim_{\delta_x, \delta_y \rightarrow 0} \left\{ \frac{\sqrt{\det[\Sigma^{-1}]}}{\pi \delta_x \delta_y \sqrt{\det[M]}} e^{-(\zeta_{ph}^{(i)})^T (M_0 - M_0 M^{-1} M_0) \zeta_{ph}^{(i)}} \right\} \quad , \quad (4.107)$$

where  $M = M_0 + \Sigma^{-1}$  and  $\det[M] > 0$ . The limit should exist for any  $\zeta_{ph}^i$ . In particular, it should exist for  $\zeta_{ph}^i=0$ , which means the expression before the exponent converges itself, and defines the peak brightness of the source:

$$B_{peak} = W_1 \cdot \lim_{\delta_x, \delta_y \rightarrow 0} \left\{ \frac{\sqrt{\det[\Sigma^{-1}]}}{\pi \delta_x \delta_y \sqrt{\det[M]}} \right\} = \frac{W_1}{\pi \sqrt{\det[Q_0 M_0] \Sigma + Q_0}} \quad , \quad (4.108)$$

where the introduced matrix  $Q_0$  should not have any singularities. In addition, three other conditions should be satisfied:

$$Q_0 = \lim_{\delta_x, \delta_y \rightarrow 0} \{Q\} \quad , \quad (4.109)$$

$$Q_0 M_0 = \lim_{\delta_x, \delta_y \rightarrow 0} \{Q \cdot M_0\} \quad , \quad (4.110)$$

$$\det[Q] = (\delta_x \delta_y)^2 \quad . \quad (4.111)$$

The matrix  $\Sigma_{ph}^i = (M_0 - M_0 M^{-1} M_0)^{-1}$  is a corresponding matrix of the second order momentums for the initial distribution of emitted photons at the source. The similar matrix at the observer location defining the final distribution of photons in phase space can be found as following:

$$\Sigma_{ph}^f = D (M_0 - M_0 M^{-1} M_0)^{-1} D^T \quad . \quad (4.112)$$

## 4.7 Peak Brightness for the on-axis observer

For the simple case when an observer is located on-axis, also known as the “undulator” case, and an electron bunch traveling along the  $z$ -axis in the moment of interaction with the incoming laser pulse, one can find for the peak brightness of the radiation, defined by the maximum of the Wigner function<sup>23</sup>:

$$B_{peak} \sim \left[ \sigma_x^2 \sigma_y^2 \left( \frac{\sigma_z^2}{\sigma_{rad}^2} + k_{rad}^2 \epsilon_z^2 \right) \right]^{-1} \quad . \quad (4.113)$$

If emittances  $\epsilon_x$ ,  $\epsilon_y$  and  $\epsilon_z$  are fixed, one would have to squeeze the bunch in transverse directions by increasing the corresponding divergences in order to maximize the peak bright-

---

<sup>23</sup>In this simple model we assume no correlation between the transverse and longitudinal phase spaces of the electron beam.

ness. This can be realized by a set of quadrupoles separated by drifts which would compress the bunch simultaneously in  $x$ - and  $y$ -directions. Since  $k_{rad} \simeq 4\gamma_0^2 k_{z_{las}}$ ,  $\sigma_{rad} \simeq \frac{\sigma_z}{4\gamma_0^2}$  and quasi-monochromatic approximation for the incoming radiation  $k_{rad}\sigma_z \gg 1$ , the longitudinal emittance can dominate in the second term, if  $k_{rad}\sigma_z \frac{\Delta\gamma}{\gamma} \gg 1$  (approximation of the zero correlated energy spread). The regime dominated by the longitudinal bunch size would be observed under the opposite condition. In latter case, the peak beak brightness can be increased by applying a bunch compressor to the beam before interaction with a laser pulse.

## 4.8 Summary

In this Chapter we derived the 6-dimensional photon distribution of radiation emitted by an electron bunch while interacting with an incoming laser pulse. The Wigner function treatment was applied to characterize the produced radiation. First, we obtained the single-electron Wigner function, where variable approximations for the laser pulse were considered, such as continuous and time-limited plane-wave models. Alternatively, representing the incoming radiation as a superposition of plane waves produced the exact answer in the form of a multi-dimensional integral. This solution can be implemented in future ICS codes for an arbitrary-shaped laser pulse. In the Gaussian approximation of the laser pulse the single-electron Wigner function was further evaluated and expressed in a form of a 1-dimensional integral, where the integrand includes the special functions. Numerical integration of latter result justified legitimacy of the time-limited plane wave approximation for some configurations between the transverse and longitudinal sizes of the laser pulse. Further, the analytical solution derived in this approximation were convoluted with a 6D Gaussian distribution describing an electron bunch. The corresponding Wigner function characterizing radiation generated by the electron bunch arbitrary-shaped in 6D phase space was found in a matrix

form. Finally, the simple case for an on-axis observer was analyzed and conclusions how to properly shape an uncorrelated electron bunch in order to maximize the peak brightness of the emitted radiation were made. The detailed analysis of more complicated scenarios for an off-axis observer and arbitrary-shaped electron bunch is a subject of the future research.

## CHAPTER 5

### CONCLUSION

#### 5.1 Importance of this work for electron-beam-driven light sources

An electron moving on a curved trajectory emits synchrotron radiation. All light sources driven by an electron beam rely on this simple but important concept. The brightness of an electron bunch is limited by space charge forces and other collective effects, such as coherent synchrotron radiation, where the front of the beam interacts with a radiation produced by the tail of the beam; LSC-induced microbunch instabilities, in which an electron density noise present in the beam distribution can be amplified during propagation through the accelerator, etc. Simply speaking, it is quite complicated to create an electron bunch with all electrons having identical coordinates and velocity vectors, *i.e.* zero emittance bunch. As a result, individual electrons moving on distinct trajectories emit different photons compromising the brightness of all electron-driven light sources. For the last seventy years since first synchrotron radiation was detected, the significant progress towards creating cold electron beams and preserving their quality while accelerating to high energies have been maid. The practical limitations on the longitudinal bunch size, the energy spread, transverse and longitudinal emittances in order to reach high-brightness radiation in FELs have been explored theoretically, numerically and experimentally. Satisfying these requirements often relies on reshaping the beam phase space with a variety of available beam optics elements, since its overall 6-dimensional emittance practically defined at the source.

Phase-space manipulations in accelerators were initially applied individually for transverse and longitudinal phase spaces. For instance, a sequence of quadrupole magnets separated by drifts (FODO-lattice) is used for maintaining a reasonable transverse beam size while propagating in an accelerator. Shaping of the longitudinal phase space, in which the correlated energy spread imposed on or removed from the bunch, can be accomplished via an off-crest acceleration. Coupling of the transverse and longitudinal dynamics appeared to be useful for compressing an electron bunch in a dispersive beamline, chicane, contained of several bending magnets. A chicane relies on the principle that less energetic electrons travel through it slower than their high-energy counterpart, while the transverse and longitudinal beam dynamics are mixed in each bending magnet. The residual correlations in the transverse and longitudinal phase spaces at the exit of the scheme are typically undesired since it often results in the enlargement of corresponding emittances critical for the proper FEL-lasing. The chicane-based compressors were followed by even more advanced beamlines such as an emittance exchanger. This scheme intentionally mixes the transverse and longitudinal phase spaces of the beam in order to rotate its 6-dimensional distribution and eventually provide with an exchange. In this work, we push the limits of the advanced phase-space manipulations even further, predominantly for the sake of a degradation-free bunch compression. Short electron bunches are necessary to reach a high peak current which critically affects FELs' and ICS sources' performance.

Chapter 2 discusses a new type of a bunch compressor based on two transverse-to-longitudinal phase-space exchanges separated by transverse-optics elements. This scheme relies on completely different operational principles rather than conventional chicane-based bunch compressors. Therefore, it does not require upstream neither downstream energy-phase corrections such of whose necessary for the proper operation of a chicane. Furthermore, eliminating a chicane-type optics in the new compressor results in absence of the main amplification mechanism, chicane, driving the LCS-induced microbunching instabilities, which

are one of the two major factors degrading the beam quality and diluting transverse and longitudinal emittances. The second degradation factor, CSR effects, is mitigated by constructing a unique asymmetric beamline. The particular configuration of the scheme is found using a fast multi-dimensional optimization driven by a novel extremum seeking algorithm. Furthermore, it is demonstrated that the degradation of the longitudinal phase space due to nonlinear and CSR effects can be completely suppressed by turning the corresponding beam phase space around. This can be accomplished via proper transverse-optics insert in the middle of the scheme. The “mirrored” bunch additionally results in a partial compensation of the transverse phase-space dilution, which can be further minimized using the nonlinear optics elements (sextupoles). Overall, this results in a novel type of a bunch compressor capable to substitute chicane-based compressors in the existing and future accelerators. Chapter 2 is concluded with a complimentary emittance exchange technique requiring only two bending magnets if accompanied by two deflecting cavities and series of quadrupole magnets. This scheme might be of a big interest for the longitudinal beam shaping which would be extremely useful for advanced acceleration techniques such as dielectric or plasma wakefield acceleration.

In Chapter 3 we describe a novel beamline for imposing/removing the energy chirp along the bunch relying on the transverse-longitudinal mixing in transverse deflecting cavities separated by free-space propagation sections. Several realistic and ready-to-fit in the existing linacs designs have been developed and provide with an efficient alternative to the conventional technique based on the off-crest acceleration. The minimization of nonlinear effects at the exit of designed beamlines is accomplished by optimization of the input Twiss parameters and additionally by nonlinear optics elements (sextupoles). This results in the mutual cancellation of the nonlinear effects along the beamline and the overall good-quality bunch at the end. The proposed scheme is quite universal in an aspect of the beam energy and consequently can be placed at any location along the accelerator beamline.

Finally, the concept of the advanced phase-space manipulations is brought to the next level in Chapter 4. Shaping the electron beam in corresponding 6-dimensional phase space is discussed in an aspect of enhancing the peak brightness of an ICS source. The existing theoretical models are not capable to predict how the brightness of an ICS source would depend on the transverse-longitudinal correlations in phase space neither can suggest an optimal 6-dimensional shape of the bunch in order to reach the highest possible brightness if the overall 6D emittance is fixed. The novel approach is based on the Wigner function treatment used to characterize emitted radiation, first by a single electron for different approximations of the upcoming laser pulse and then by an electron bunch. For the latter case the Wigner function is found as a convolution of the single-electron Wigner function with an arbitrary 6-dimensional Gaussian distribution corresponding to the arbitrary-shaped electron bunch. It provides with an analytical solution in a matrix form for the 6-dimensional distribution of emitted photons in corresponding phase space. These theoretical results can be used to dramatically enhance the brightness of an ICS source by finding an optimal shape and constructing it using a variety of available beam optics elements.

## 5.2 Discussion

In the final section of the dissertation we speculate about next potential steps which can be made based of the results of this work. First, we emphasize that the experimental realization of the proposed schemes, in particular an alternative emittance exchanger, TDC-based chirper and dechirper, and a double emittance exchanger, would be very interesting to accomplish. In addition, the multi-dimensional ES algorithm and the eigen-emittance analysis can be applied for the start-to-end optimization of FELs' brightness and performance

of its structural components. Furthermore, it is extremely tempting to apply this approach for the feedback-aided electron beam diagnostics<sup>1</sup>.

Speaking of the novel 6-dimensional theory for an ICS source, there are many potential directions for the future work. First, the electron beam shaping for enhancing the brightness of emitted radiation should be precisely investigated. Second, the developed theory opens up the possibility for complete non-invasive electron beam diagnostics via analyzing photon distribution of produced radiation in the corresponding 6-dimensional phase space. This requires further theoretical and experimental work in the field of optical diagnostics. The developed theory for an ICS source can be extended numerically to consider higher orders correlations in phase space. This can become a novel simulation tool for ICS sources. Furthermore, it will be interesting to include effects of interaction with radiation when amplitude of the upcoming laser pulse is large. Adding quantum effects to the existing theory is also tempting. Finally, it will be extremely interesting and challenging to develop a similar analytical approach accounting for correlations in electron phase space for the free electron lasers. Although it might be impossible to accomplish this strictly from the theoretical perspective, we are convinced that the optimum shape of the electron beam phase space for an FEL can be found as a combination of both the theory in approximation of incoherent undulator radiation and powerful simulation tools, such as FEL code Genesis by Sven Reiche [116].

---

<sup>1</sup>In private communications with A. Scheinker

## REFERENCES

- [1] W. Crookes, “On the illumination of lines of molecular pressure, and the trajectory of molecule,” *Phil. Trans.* **170** 135, doi:10.1098/rstl.1879.0065 (1878).
- [2] R. Glocker and H. Schreiber, *Annalen der Physik.* **85**, 1089 (1928) (*in German*).
- [3] H.W. Koch and J.W. Motz, “Bremsstrahlung Cross-Section Formulas and Related Data,” *Rev. Mod. Phys.* **31**, 920 (1959).
- [4] J.A. Wheeler and W.E. Lamb, “Influence of Atomic Electrons on Radiation and Pair Production,” *Phys. Rev.* **55**, 858 (1939); *Erratum Phys. Rev.* **101**, 1836 (1956).
- [5] J. Joseph and F. Rohrlich, “Pair Production and Bremsstrahlung in the Field of Free and Bound Electrons,” *Rev. Mod. Phys.* **30**, 354 (1958).
- [6] R. C. Stabler, “Low-energy Electron-electron Bremsstrahlung,” *Nature* **206**, 922 (1965).
- [7] R. Giacconi, “Nobel Lecture: The dawn of X-ray astronomy,” *Rev. Mod. Phys.* **14** (3), 995 (2003).
- [8] J. Larmor, “On a Dynamical Theory of the Electric and Luminiferous Medium, Part 3, Relations with material media,” *Philosophical Transactions of the Royal Society* **190**, 205 (1897).
- [9] A.L. Robinson, “History of Synchrotron Radiation sources,” X-ray Data Booklet, LBNL (2009).
- [10] R. Wideröe, *Archiv f. Elektrotechnik* **21**, 387, <https://doi.org/10.1007/BF01656341> (1928) (*in German*).

- [11] D.W. Kerst, *Phys. Rev.* **60**, 47 (1941).
- [12] E.M. McMillan, “Radiation from a Group of Electrons Moving in a Circular Orbit,” *Phys. Rev.* **68**, 144 (1945).
- [13] J. Schwinger, “On the Classical Radiation of Accelerated Electrons,” *Phys. Rev.* **75**, 1912 (1949).
- [14] E.O. Lawrence and N.E. Edlefsen, *Science* **72**, 376 (1930).
- [15] E.O. Lawrence and M.S. Livingston, *Phys. Rev.* **40**, 19 (1932).
- [16] M. Conte, W.W. MacKay, “An Introduction to the Physics of Particle Accelerators,” Second Edition, *World Scientific Publishing Co. Pte. Ltd.*, Singapore (2009).
- [17] E.M. McMillan, “The Synchrotron - A Proposed High Energy Particle Accelerator,” *Phys. Rev.* **68**, 143 (1945).
- [18] V. Veksler, *Journal of Physics USSR* **9**, 153 (1945) (*in Russian*).
- [19] K.J. Kim, R. Lindberg, and Z. Huang, “Synchrotron Radiation and Free-Electron Lasers: Principles of Coherent X-Ray Generation,” *Cambridge University Press*, Cambridge (2017).
- [20] P. Schmöser, M. Dohlus, J. Rossbach, C. Behrens, “Free-Electron Lasers in the Ultra-violet and X-Ray Regime,” Second Edition, *Springer Tracts in Modern Physics* **258**, ISSN 0081-3869, Hamburg (October 2013).
- [21] G.R. Gordon (1959). “The LASER, Light Amplification by Stimulated Emission of Radiation,” *The Ann Arbor Conference on Optical Pumping*, 128, (1959).
- [22] J.M.J. Madey, “Stimulated emission of bremsstrahlung in a periodic magnetic field, *J. Appl. Phys.* **42**, 1906 (1971).

- [23] L.R. Elias et al., “Observation of stimulated emission of radiation by relativistic electrons in a spatially periodic transverse magnetic field,” *Phys. Rev. Lett.* **36**, 717 (1976).
- [24] D.A.G. Deacon et al., “First operation of a free-electron laser,” *Phys. Rev. Lett.* **38**, 892 (1977).
- [25] A.W. Chao and M. Tigner, “Handbook of Accelerator Physics and Engineering,” Second Printing, *World Scientific*, Singapore (2002).
- [26] J.D. Lawson, P.M. Lapostolle and R.L. Glukstern, “Emittance, Entropy and Information,” *Part. Acc.* **5**, 61 (1973).
- [27] T.R. Mazur, B. Klappauf and M.G. Raizen, “Demonstration of magnetically activated and guided isotope separation,” *Nat. phys.* **10**, 601 (2014).
- [28] C.J. Trahan and R.E. Wyatt, “Evolution of classical and quantum phase-space distributions: A new trajectory approach for phase space hydrodynamics,” *The Journal of Chemical Physics* **119**, 7017 (2003).
- [29] M.V. Berry, “Evolution of semiclassical quantum states in phase space,” *J. of Phys. A: Mathematical and General* **12** (5), 625 (1979).
- [30] L.D. Landau, E.M. Lifshitz, “Mechanics,” *Butterworth-Heinemann*, (1976).
- [31] Wolfram Research, Inc., Mathematica, Version 11.3, Champaign, IL (2018).
- [32] MATLAB, The MathWorks, Inc., Natick, Massachusetts, United States (2014).
- [33] J.H. Billen and L. Young. ”Parmela Users Manual,” LA-UR-96-1835 (1996).
- [34] K. Floettmann, ASTRA User’s Manual, 2000, [www.desy.de/~mpyflo/Astra dokumentation/](http://www.desy.de/~mpyflo/Astra_dokumentation/)

- [35] Ginger
- [36] M.J. de Loos and S.B. van der Geer, “General Particle Tracer: a New 3D Code for Accelerator and Beam Line Design,” *Proc. 5th European Part. Accel. Conf., Sitges, Barcelona*, 1241 (1996).
- [37] M. Borland, “Elegant: A flexible sdds-compliant code for accelerator simulation,” *Advanced Photon Source*, LS-287 (2000).
- [38] M. Borland and T. Berenc, “Users Manual for elegant,” [http://ops.aps.anl.gov/manuals/elegant\\_latest/elegant.html](http://ops.aps.anl.gov/manuals/elegant_latest/elegant.html) (2018).
- [39] Z. Huang et al, “Suppression of microbunching instability in the linac coherent light source,” *Phys. Rev. ST Accel. Beams* **7**, 074401 (2004).
- [40] A. Xiao et al., “Direct space-charge calculation in ELEGANT and its application to the ILC damping ring,” FERMILAB-CONF-07-702-AD (2007).
- [41] E.L. Saldin, E.A. Schneidmiller and M.V. Yurkov, “Klystron instability of a relativistic electron beam in a bunch compressor,” *Nucl. Instrum. Methods Phys. Res., Sect. A* **490**, 1 (2002).
- [42] B.E. Carlsten and T.O. Raubenheimer, “Emittance growth of bunched beams in bends,” *Phys. Rev. E* **51**, 1453 (1995).
- [43] J.D. Jackson, “Classical Electrodynamics”, Second Edition, *Wiley*, New York (1975).
- [44] Ya.S. Derbenev, J. Rossbach, E.L. Saldin, V.D. Shiltsev, “Microbunch Radiative Tail-Head Interaction,” TESLA-FEL 95-05 (1995).

- [45] E.L. Saldin, E.A. Schneidmiller and M.V. Yurkov, “On the coherent radiation of an electron bunch moving in arc of a circle,” *Nucl. Instrum. Methods Phys. Res., Sect. A* **398**, 373 (1997).
- [46] M. Borland, “Simple method for particle tracking with coherent synchrotron radiation,” *Phys. Rev. ST Accel. Beams* **4**, 070701 (2001).
- [47] G. Stupakov and P. Emma, **SLAC**, LCLS-TN-01-12 (2001).
- [48] M. Dohlus and T. Limberg, “CSRtrack Version 1.2 Users Manual,” [http://www.desy.de/fel-beam/csrtack/files/CSRtrack\\_User\\_Guide\\_\(actual\).pdf](http://www.desy.de/fel-beam/csrtack/files/CSRtrack_User_Guide_(actual).pdf) (2012).
- [49] M. Dohlus, “Two Methods for the Calculation of CSR Fields,” TESLA-FEL-2003-05 (2003).
- [50] M. Dohlus, A. Kabel, T. Limberg, “Efficient Field Calculation of 3D Bunches on General Trajectories,” *Nucl. Instrum. Methods Phys. Res., Sect. A* **445**, 338 (2000).
- [51] P. Emma et al, “First lasing and operation of an ångstrom-wavelength free-electron laser,” *Nat. Photonics* **4**, 641 (2010).
- [52] S. Schreiber and B. Faatz “The free-electron laser FLASH.” *High Power Laser Science and Engineering* **3**, e20 (2015).
- [53] T. Ishikawa et al., “A compact X-ray free-electron laser emitting in the sub-ångstrom region,” *Nat. Photonics* **6**, 540 (2012).
- [54] G. Geloni, “The European XFEL: Current status and self-seeding project.” Congresso Nazionale della Societ Italiana di Fisica, Trento, 13 September 2017.
- [55] <https://www.psi.ch/swissfel/first-pilot-experiment>

- [56] C.J. Milne Christopher et al., “SwissFEL: The Swiss X-ray Free Electron Laser,” *Applied Sciences* **7**, 720 (2017).
- [57] [https://portal.slac.stanford.edu/sites/lcls\\_public/lcls\\_ii/Pages/default.aspx](https://portal.slac.stanford.edu/sites/lcls_public/lcls_ii/Pages/default.aspx)
- [58] <http://www.lanl.gov/science-innovation/science-facilities/marie/index.php>
- [59] D. Möhl, G. Petrucci, L. Thorndahl, S. van der Meer, “Physics and technique of stochastic cooling,” *Physics Reports* **58** (2), 73 (1980).
- [60] H.-H. Braun, *48th ICFA Advanced Beam Dynamics Workshop on Future Light Sources*, Menlo Park (2010).
- [61] N. Yampolsky et al., *arXiv:1010.1558* (2010).
- [62] A.H. Compton, “A Quantum Theory of the Scattering of X-rays by Light Elements,” *Phys. Rev.* **21**, 483 (1923).
- [63] Cf. J. J. Thomson, “Conduction of Electricity through Gases,” Second Edition, *Cambridge University Press Warehouse*, Cambridge (1906).
- [64] M. Litos et al., “High-efficiency acceleration of an electron beam in a plasma wakefield accelerator,” *Nature* **515**, 92 (2014).
- [65] G.J. Caporaso, Y.J. Chen, S.E. Sampayan, “The dielectric wall accelerator,” LLNL-JRNL-416544 (2009).
- [66] C. Sun and Y.K. Wu, *Phys. Rev. ST Accel. Beams* **14**, 044701 (2011).
- [67] C. Curatolo, I. Drebot, V. Petrillo, and L. Serafini, *Phys. Rev. Accel. Beams* **20**, 081 (2017).
- [68] E. Wigner, *Phys. Rev.* **40**, 749 (1932).

- [69] A. Walther, *J. Opt. Soc. Am.* **58**, 1256 (1968).
- [70] K.-J. Kim, Report No. LBL-20181 (1985).
- [71] K.-J. Kim, *Nucl. Instrum. Methods Phys. Res., Sect. A* **246**, 71 (1986).
- [72] K.-J. Kim, *AIP Conf. Proc.* **184**, 565 (1989).
- [73] G. Geloni, E. Saldin, E. Schneidmiller, and M. Yurkov, *Nucl. Instrum. Methods Phys. Res., Sect. A* **588**, 463 (2008).
- [74] I.V. Bazarov, *Phys. Rev. ST Accel. Beams* **15**, 050703 (2012).
- [75] A. Gasbarro and I. Bazarov, *J. Synchrotron. Radiat.* **21**, 289 (2014).
- [76] T. Tanaka, *Phys. Rev. ST Accel. Beams* **17**, 060702 (2014).
- [77] R.R. Lindberg and K.-J. Kim, *Phys. Rev. ST Accel. Beams* **18**, 090702 (2015).
- [78] T. Tanaka, *Opt. Lett.* **42**, 1576 (2017).
- [79] F. Stulle et al., “Designing a bunch compressor chicane for a multi-TeV linear collider,” *Phys. Rev. Accel. Beams* **10**, 031001 (2007).
- [80] J.W. Lewellen, “MaRIE X-FEL Linac Design: Status and Plans,” *Los Alamos National Laboratory report*, LA-UR-15-21962 (2015).
- [81] R. Li, “Curvature-induced bunch self-interaction for an energy-chirped bunch in magnetic bends,” *Phys. Rev. ST Accel. Beams* **11**, 024401 (2008).
- [82] M. Borland et al., *Nucl. Instrum. Methods Phys. Res. Sect. A* **483**, 268 (2002).
- [83] M. Venturini et al., *Phys. Rev. ST Accel. Beams* **10**, 104401 (2007).

- [84] Z. Huang and K.J. Kim, “Formulas for coherent synchrotron radiation microbunching in a bunch compressor chicane,” *Phys. Rev. Accel. Beams* **5**, 074401 (2002).
- [85] E.L. Saldin, E.A. Schneidmiller, and M.V. Yurkov, *Nucl. Instrum. Methods Phys. Res. Sect. A* **528**, 355 (2004).
- [86] Z. Huang et al., *Phys. Rev. ST Accel. Beams* **13**, 020703 (2010).
- [87] C. Behrns, Z. Huang, and D. Xiang, *Phys. Rev. ST Accel. Beams* **15**, 022802 (2002).
- [88] J. Qiang, C.E. Mitchell, and M. Venturini, *Phys. Rev. Lett.* **111**, 054801 (2013).
- [89] A. Loulergue, A. Mosnier, “A simple S-chicane for the final bunch compressor of TTF-FEL,” *Proceedings of EPAC 2000, Vienna, Austria* CEA/DAPNIA/SEA France (2000).
- [90] B.E. Carlsten et al., “Using an emittance exchanger as a bunch compressor,” *Phys. Rev. Accel. Beams* **14**, 084403 (2011).
- [91] A.J Dragt, F. Neri, G. Rangarajan, “General moment invariants for linear hamiltonian systems,” *Phys. Rev. A* **45** (4), 2572 (1992).
- [92] A.J. Dragt, “Lie methods for nonlinear dynamics with applications to accelerator physics,” <http://www.physics.umd.edu/dsat/dsatliemethods.html> (2001).
- [93] M. Cornacchia and P. Emma, *Phys. Rev. Accel. Beams* **5**, 084001 (2002).
- [94] P. Emma et al., *Phys. Rev. Accel. Beams* **9**, 100702, (2006).
- [95] A. Malyzhenkov, B.E. Carlsten and N.A. Yampolsky, “Double emittance exchanger as a bunch compressor for the MaRIE XFEL electron beam line at 1 GeV,” *AIP Conference Proceedings* **1812**, 100009, doi: 10.1063/1.4975907 (2017).

- [96] A. Zholents and M. Zolotarev, “Collective effects in the double emittance exchange bunch compressor,” *Microbunching Workshop* (2012).
- [97] In private communications on microbunching instabilities in EEX-based bunch compressor with B.E. Carlsten and N. Yampolsky.
- [98] E.A. Nanni and W.S Graves, “Aberration corrected emittance exchange,” *Phys. Rev. Accel. Beams* **18**, 084401, (2015).
- [99] A. Scheinker and S. Gessner, “Adaptive method for electron bunch profile prediction,” *Phys. Rev. Accel. Beams* **18** (10), 102801 (2015).
- [100] A. Scheinker and D. Scheinker, “Bounded extremum seeking with discontinuous dithers,” *Automatica* **69**, 250 (2016).
- [101] A. Scheinker and M. Krstic, “Model-Free Stabilization by Extremum Seeking,” Springer (2017).
- [102] A. Scheinker et al., “Model-independent particle accelerator tuning,” *Phys. Rev. Accel. Beams* **16**, 102803 (2013).
- [103] S. Antipov et al., “IOTA (Integrable Optics Test Accelerator): facility and experimental beam physics program,” *JINST* **12**, T03002 (2017).
- [104] D.R. Douglas, “An Alternative to Conventional Transverse/Longitudinal Emittance Exchanges,” *JLAB-TN-12-014* (2010).
- [105] G. Ha et al. “Limiting effects in double EEX beamline,” *IOP Conf. Series: Journal of Phys.* **874**, 012061 (2017).
- [106] D.Yu. Shchegolkov et al. “Design of an emittance exchanger for production of special shapes of the electron beam current,” *Phys. Rev. Accel. Beams* **17** 041301 (2014).

- [107] A. Malyzhenkov and A. Scheinker, “Phase space exchange-based bunch compression with reduced CSR effects,” *arXiv:1809.05579* (2018).
- [108] N. Yampolsky, A. Malyzhenkov, E.I. Simakov, “Imposing strong correlated energy spread on relativistic bunches with transverse deflecting cavities,” (manuscript in preparation).
- [109] J. Arthur et al., “Linac Coherent Light Source (LCLS) Conceptual Design Report,” *SLAC* (2002).
- [110] A. Zholents and M. Zolotarev, “Collective Effects in the Double Emittance Exchange Bunch Compressor,” *ANL report* (2012).
- [111] CST MICROWAVE STUDIO, <http://www.cst.com/products/cstmws>
- [112] N. Yampolsky, A. Malyzhenkov, “Design of MITS de-chirper based on crab cavities,” *LANL report* (2014).
- [113] M. McAshan and R. Wanzenberg, “RF Design of a Transverse Mode Cavity for Kaon Separation,” *FERMILAB-TM-2144* (2001).
- [114] A. Malyzhenkov and N. Yampolsky, “6D photon phase space of an ICS source,” (manuscript in preparation).
- [115] A. Malyzhenkov and N. Yampolsky, “Optimization of Compton source performance through electron beam shaping,” *AIP Conference Proceedings* **1812**(1), 100008, DOI: 10.1063/1.4975906 (2017).
- [116] S. Reiche, *Nucl. Instrum. Methods Phys. Res., Sect. A* **429**, 243 (1999).